ÇUKUROVA UNIVERSITY
INSTITUTE OF NATURAL AND APPLIED SCIENCES

**PhD THESIS**

**Oğur İYNEN**

# MODELING OF POWER CONSUMPTION, CUTTING FORCE, SOUND, CURRENT, AND SURFACE ROUGHNESS DURING TURNING OF AISI 4340 STEEL WITH DIFFERENT HARDNESS

**DEPARTMENT OF MECHANICAL ENGINEERING**

**ADANA-2022**

ÇUKUROVA UNIVERSITY
INSTITUTE OF NATURAL AND APPLIED SCIENCES

**MODELING OF POWER CONSUMPTION, CUTTING FORCE, SOUND, CURRENT, AND SURFACE ROUGHNESS DURING TURNING OF AISI 4340 STEEL WITH DIFFERENT HARDNESS**

**Oğur İYNEN**

**PhD THESIS**

**DEPARTMENT OF MECHANICAL ENGINEERING**

We certify that the thesis titled above was reviewed and approved for the award of degree of the Doctoral of Science by the board of jury on 11 /02/ 2022.

| ………………………. | ………………………. | ………………………. | ………………………. |
|---|---|---|---|
| Prof. Dr.<br>Abdul Kadir EKŞİ<br>SUPERVISOR | Prof. Dr.<br>Ali Hamza TANRIKULU<br>MEMBER | Prof. Dr.<br>Necip Fazıl YILMAZ<br>MEMBER | Prof. Dr.<br>Ömer EYERCİOĞLU<br>MEMBER |

……………………….

Assist. Prof. Dr.
Mehmet İlteriş SARIGEÇİLİ
MEMBER

This PhD Thesis is written at the Department of Institute of Natural And Applied Sciences of Çukurova University.
**Registration Number**:

**Prof. Dr. Sadık DİNÇER**
**Director**
**Institute of Natural and Applied Sciences**

**ABSTRACT**

**PhD THESIS**

**MODELING OF POWER CONSUMPTION, CUTTING FORCE, SOUND, CURRENT, AND SURFACE ROUGHNESS DURING TURNING OF AISI 4340 STEEL WITH DIFFERENT HARDNESS**


**Oğur İYNEN**

**ÇUKUROVA UNIVERSITY**
**INSTITUTE OF NATURAL AND APPLIED SCIENCES**
**DEPARTMENT OF MECHANICAL ENGINEERING**

Supervisor : Prof. Dr. Abdul Kadir EKŞİ
: Year 2022, Page: 227
Jury : Prof. Dr. Abdul Kadir EKŞİ
: Prof. Dr. Ali Hamza TANRIKULU
: Prof. Dr. Necip Fazıl YILMAZ
: Prof. Dr. Ömer EYERCİOĞLU
: Asst. Prof. Dr. Mehmet İlteriş SARIGEÇİLİ

Up to now, a lot of research has been done on modeling and optimization of parameters like surface roughness, tool life, tool wear, cutting forces, vibration, and material removal rate influencing machining. However, little research has been done to optimize and model power consumption, sound, and current. To this aim, the effects of cutting parameters on power consumption, cutting forces, sound, current, and surface roughness were investigated. The present study focuses to obtain the optimal machining parameters leading to minimum power consumption, cutting forces, sound, current, and surface roughness during turning of AISI 4340 steel with different hardness (30, 35, 40 HRC) using ceramic, carbide, and CBN inserts. Predicted results with developed mathematical models for power consumption, cutting forces, sound, current, and surface roughness have been compared with experimental/calculated values. The results establish that there is a close relationship between the predicted values and experimental/calculated values. As a result of optimization, the most important parameter for power consumption, current, sound was found to be cutting speed. In addition to this, the most effective parameter for surface roughness was determined to be insert. The most effective parameter on radial force (Fx) and tangential force (Fy) is feed rate. And the most effective parameter on feed force (Fz) is depth of cut. Also, it has been observed that there is a strong relationship between the machining parameters and power consumption. In this way, it has been determined that power savings can be achieved by using optimal processing parameters.

**Key Words**: Power consumption, Cutting forces, Sound, Current, Surface roughness

# ÖZ

## DOKTORA TEZİ

**FARKLI SERTLİKTEKİ AISI 4340 ÇELİĞİNİN TORNALANMASI ESNASINDA GÜÇ TÜKETİMİ, KESME KUVVETİ, SES, AKIM VE YÜZEY PÜRÜZLÜLÜĞÜNÜN MODELLENMESİ**



**Oğur İYNEN**

**ÇUKUROVA ÜNİVERSİTESİ**
**FEN BİLİMLERİ ENSTİTÜSÜ**
**MAKİNA MÜHENDİSLİĞİ ANABİLİM DALI**



Danışman : Prof. Dr. Abdul Kadir EKŞİ
: Yıl 2022, Sayfa: 227
Jüri : Prof. Dr. Abdul Kadir EKŞİ
: Prof. Dr. Ali Hamza TANRIKULU
: Prof. Dr. Necip Fazıl YILMAZ
: Prof. Dr. Ömer EYERCİOĞLU
: Dr. Öğr. Üyesi Mehmet İlteriş SARIGEÇİLİ



Şimdiye kadar yüzey pürüzlülüğü, takım ömrü, takım aşınması, kesme kuvvetleri, titreşim ve talaş kaldırma oranı gibi talaşlı imalatı etkileyen parametrelerin modellenmesi ve optimizasyonu üzerine birçok araştırma yapılmıştır. Ancak güç tüketimini, sesi ve akımı optimize etmek ve modellemek için çok az araştırma yapılmıştır. Bu amaçla, bu çalışmada kesme parametrelerinin ses, akım, yüzey pürüzlülüğü, kesme kuvvetleri ve güç tüketimi üzerindeki etkileri araştırılmıştır. Bu çalışma, seramik, karbür ve CBN kesici uçlar kullanılarak AISI 4340 çeliğinin farklı sertlikte (30, 35, 40 HRC) tornalanması sırasında minimum güç tüketimine, kesme kuvvetlerine, sese, akıma ve yüzey pürüzlülüğüne yol açan en uygun talaşlı imalat parametrelerini elde etmeye odaklanmaktadır. Geliştirilen matematiksel modeller ile tahmin edilen sonuçlar, hesaplanan/deneysel değerlerle karşılaştırılmıştır. Sonuçlar; güç tüketimi, kesme kuvvetleri, yüzey pürüzlülüğü, ses ve akım için geliştirilen matematiksel modellerle tahmin edilen değerler, hesaplanan/deneysel değerler arasında yakın bir ilişki gösterdiğini ortaya koymaktadır. Optimizasyon sonucunda güç tüketimi, akım ve ses için en önemli parametrenin kesme hızı olduğu bulundu. Radyal kuvvet (Fx) ve teğetsel kuvvet (Fy) için en önemli parametrenin ilerleme; ilerleme kuvveti (Fz) için ise en önemli parametrenin kesme derinliği olduğu görülmüştür. Bunun yanı sıra yüzey pürüzlülüğüne en çok etki eden parametrenin kesici uç olduğu belirlenmiştir. Ayrıca güç tüketimi ile işleme parametreleri arasında güçlü bir ilişki olduğu tespit edilmiştir. Bu sayede optimum talaşlı imalat parametreleri kullanılarak güç tasarrufu sağlanabileceği belirlenmiştir.



**Anahtar Kelimeler:** Güç tüketimi, Kesme Kuvvetleri, Ses, Akım, Yüzey pürüzlülüğü

**EXTENDED SUMMARY**

More energy is needed in the world along with the increasing industrialization and human population. The manufacturing process is one of the most energy-consuming industries in the world. Machining is one of the most basic and major manufacturing processes. Most sectors in the manufacturing area are trying to improve their manufacturing processes in order to increase energy efficiency. The basic machining processes include turning, milling, shaping, boring, sawing, planing, grinding, broaching, and drilling operations. Turning process that is the most common machining operation is addressed in the present study. Power consumption that has an important place in the machining process is often used to analyze energy efficiency. The power consumption in the turning process is affected by many factors like cutting forces, metal removal rate, insert geometry, insert material, cutting speed, feed rate, and depth of cut. Also, Finite Element Method (FEM) can be used for finding machining parameters such as cutting forces, tool vibration, shear stress, strain rate, and temperature without making experiments. By this means, it is saved cost and time. For this purpose, this study focuses on optimizing and modeling machining parameters to ensure minimum power consumption, cutting forces, sound, current, and surface roughness during turning of AISI 4340 alloy steel using different insert materials and workpiece materials with different hardness.

The thesis presented consists of several steps. Initially, by applying different heat treatments on AISI 4340 alloy steel, workpieces with a hardness of 30, 35, 40 HRC were obtained. Next, cutting tools (inserts) manufactured from CBN, ceramic, and carbide material were supplied. The Design of Experiments (DOE) is used to minimize the number of total experiments and later for planning, conducting, analyzing, interpreting experiments. Thus, first of all, an experiment plan was prepared with Respond Surface Method (RSM) taking input machining parameters (insert, hardness, cutting speed, feed rate, depth of cut), and their levels (each with three levels). And then output machining parameters (power consumption, cutting forces, sound, current, surface roughness) were determined. Minitab 16 software was utilized to generate RSM in the DOE. In here, a Box-Behnken Design (BBD) was chosen. For this study, a Box-Behnken Design of 46 with 5 factors, 3 levels, and 1 single block was created. Experiments were conducted by using three levels of cutting speed (180, 220, 260 m/min), three levels of feed rate (0,03; 0,07; 0,11 mm/rev), three levels of depth of cut (0,08; 0,14; 0,20 mm), three levels of hardness (30, 35, 40 HRC), and three levels of insert (ceramic, carbide, CBN). Thirdly, experiments according

to experiment plan order were executed and results were evaluated. The target is to minimize all output parameters (response values). Accordingly, the experimental/calculated results were commented.

The results of ANOVA for radial force (Fx) show that feed rate is the most significant cutting parameter with 29,17% contribution. It was followed by insert of 26,46%, depth of cut of 25,66%, hardness of 9,03%, and cutting speed of 0,28%. From the analysis of the surface plot, it is seen that while cutting speed, depth of cut, feed rate, and hardness rise; Fx increases. The smaller Fx was got when ceramic insert was used. According to Signal-Noise ratios (SN), optimum Fx can be obtained at i = ceramic, h = 30 HRC, v = 180 m/min, f = 0,03 mm/rev, and a = 0,08 mm. It is predicted as 9,51 N according to these parameters in optimization plot.

The results of ANOVA for tangential force (Fy) show that feed rate is the most significant cutting parameter with 44,74% contribution. It is followed by depth of cut of 41,69%, insert of 7,06%, cutting speed of 0,19%, and hardness of 0,07%. It is seen from surface plot that as f and a increases, Fy also increases. Moreover, v has no effect or little effect on the Fy. Hardness has little influence on Fy. Fy changes little with the rise of hardness level and it can be neglected. Minimum Fy was achieved when ceramic insert was used in reference to surface plots. According to SN ratios, the minimum value of Fy was obtained at i = ceramic, h = 35 HRC, v = 220 m/min, f = 0,03 mm/rev, and a = 0,08 mm. It is predicted as 15,72 N according to these parameters in optimization plot.

From the results of ANOVA of the feed force (Fz), it can be seen that the depth of cut with 53,36% contribution are the most significant cutting parameter on Fz. It is followed by insert of 16,61%, feed rate of 10,52%, hardness of 1,57%, and cutting speed of 0,01%. Fz increases slightly or not changes with increasing cutting speed and feed rate levels. However, it was observed that the Fz increased strongly with increasing depth of cut value. As hardness the values increased, it was found that the Fz also increased. Furthermore, it was seen that the lowest Fz was observed when carbide inserts were used. When insert of carbide, hardness of 30 HRC, cutting speed of 180 m/min, feed rate of 0,03 mm/rev, and depth of cut of 0,08 mm was set according to SN ratios, the minimum value of Fz force was established. It is predicted as 29,25 N according to these parameters in optimization plot.

In the present research, the ANOVA analysis was used to indicate the percentage influence of cutting parameters on the surface roughness (Ra). According to percentage contribution of process parameters for Ra, it is concluded that insert with 51,52% is the most effect parameter on Ra. It is followed by hardness of 13,59%, feed rate of 1,86%, depth of cut of 0,47%, and cutting speed of 0,18%. Based on the surface plot results, the best Ra is obtained with the highest cutting speed in the pairwise interaction of the parameters v, f, a. The effect of depth of cut on the Ra was observed that it changed depending on the parameter interaction. It was observed that the value of Ra tends to increase with the combination of the highest feed rate and the lowest depth of cut. Besides, it was observed that the value of Ra tends to decrease with the combination of the highest cutting speed and the lowest depth of cut. Plus, with a rise in the feed rate, an increase of values in the Ra is observed. At the highest values of the hardness level, the lowest values of the Ra are generated. The minimum values of the Ra were obtained when CBN insert was used. From SN ratios for Ra, when i = CBN, h = 40 HRC, v = 180 m/min, f = 0,03 mm/rev, and a = 0,08 mm was set, the optimum value of Ra was established. It is predicted as 0,37 μm according to these parameters in optimization plot.

ANOVA table was used to determine the significance of cutting parameters on Total Current ($I_{total}$). Based on the ANOVA table, the most significant factor affecting $I_{total}$ is found to be cutting speed with 94,23% contribution. It is followed by depth of cut of 2,82%, insert of 0,83%, feed rate of 0,40%, hardness of 0,02%. According to surface plot for $I_{total}$, as the applied cutting speed increased, the $I_{total}$ increased linearly. Further, the effect of depth of cut and feed rate on the $I_{total}$ values was found to be changed. It was observed that the value of $I_{total}$ tends to increases with increases in the depth of cut and feed rate, but it decreases after peak point with further rises in depth of cut and feed rate. The $I_{total}$ increased at higher values of hardness. $I_{total}$ got its highest value when CBN insert used. From SN ratios for $I_{total}$, when i = ceramic, h = 30 HRC, v = 180 m/min, f = 0,03 mm/rev, and a = 0,08 mm was set, optimum value of $I_{total}$ was established. It is predicted as 4,83 A according to these parameters in optimization plot.

ANOVA method was applied for Total Sound ($S_{total}$) in order to statistically analyze the results. Based on the ANOVA table, the most significant factor affecting $S_{total}$ was cutting speed with 86,71% contribution. It is followed by feed rate of 2,14%, hardness of 1,75%, depth of cut of 0,09%, and insert of 0,06%. As depicted in the surface plot, it can be deduced that $S_{total}$ increases as cutting speed rise linearly. The effect of depth of cut on the $S_{total}$ values was seen to be changed. It was observed that the value of $S_{total}$ tends to increase with the combination of the highest feed rate and the lowest depth of cut. Besides, $S_{total}$ increases while depth of cut level rises in interaction of depth of cut and cutting speed. When the hardness values rise, $S_{total}$ increases. In addition, the $S_{total}$ was established the lowest when insert is used carbide. According to SN ratios, optimum $S_{total}$ level is generated at i = carbide, h = 30 HRC, v = 180 m/min, f = 0,07 mm/rev, and a = 0,08 mm. It is predicted as 77,48 dB according to these parameters in optimization plot.

From the results of ANOVA of the Total Power Consumption ($P_{total}$), it can be seen that the cutting speed with 94,23% contribution is the most significant cutting parameter. It is followed by depth of cut with 2,82%, insert of 0,83%, feed rate of 0,40%, and hardness of 0,02%. According to the surface plot of $P_{total}$, the effect of feed rate and depth of cut on the $P_{total}$ was found to be different. It was determined that the value of $P_{total}$ increased with risen of feed rate and depth of cut levels, but while feed rate and depth of cut levels rise further, $P_{total}$ after peak point decreased. Plus, it has been determined that the $P_{total}$ increases linearly as the cutting speed values increase. As the hardness level increases, $P_{total}$ usually increases. $P_{total}$ was reduced significantly when ceramic inserts instead of carbide or CBN inserts were used. For optimum $P_{total}$ according to SN ratios, the most appropriate process parameters are i = ceramic, h = 30 HRC, v = 180 m/min, f = 0,03 mm/rev, and a = 0,08 mm. It is predicted as 3178,60 W according to these parameters in optimization plot.

As a result, the mathematical model was developed as a formulation in order to obtain minimum $P_{total}$, Fx, Fy, Fz, Ra, $S_{total}$, and $I_{total}$. A maximum error between experimental/calculated and predicted values for $P_{total}$, Fx, Fy, Fz, Ra, $S_{total}$, and $I_{total}$ was found as 1,64%; 11,33%; 13,32%; 4,00%; 32,59,00%; 0,81%; and 1,64%, respectively. The results showed that the developed model is effective in order to obtain optimum power consumption of machine tools and can be used in industry.

## GENİŞLETİLMİŞ ÖZET

Artan sanayileşme ve insan nüfusu ile birlikte dünyada daha fazla enerjiye ihtiyaç duyulmaktadır. Üretim süreci, dünyanın en fazla enerji tüketen endüstrilerinden biridir. Talaşlı imalat, en temel ve ana üretim süreçlerinden biridir. Üretim alanındaki çoğu sektör, enerji verimliliğini artırmak için üretim süreçlerini iyileştirmeye çalışıyor. Temel talaşlı imalat yöntemleri; tornalama, frezeleme, şekillendirme, delme, testereyle kesme, planyalama, taşlama, broşlama ve delme işlemlerini içerir. Bu çalışmada, en yaygın talaşlı imalat yöntemi olan tornalama işlemi ele alınmıştır. Talaşlı imalat sürecinde önemli bir yere sahip olan güç tüketimi, enerji verimliliğini analiz etmek için sıklıkla kullanılmaktadır. Tornalama işlemindeki güç tüketimi, kesme kuvvetleri, talaş kaldırma oranı, kesici uç geometrisi, kesici uç malzemesi, kesme hızı, ilerleme ve kesme derinliği gibi birçok faktörden etkilenir. Ayrıca, kesme kuvvetleri, takım titreşimi, kesme gerilimi, gerinim hızı ve sıcaklık gibi işleme parametrelerinin deney yapmadan bulunması için Sonlu Elemanlar Metodu (SEM) kullanılabilir. Bu sayede maliyet ve zamandan tasarruf edilir. Bu amaçla bu çalışmada farklı kesici uç malzemeleri ve farklı sertlikteki iş parçası malzemeleri kullanılarak AISI 4340 alaşımlı çeliğin tornalanması sırasında minimum güç tüketimi, kesme kuvvetleri, ses, akım ve yüzey pürüzlülüğünü sağlamak için talaşlı imalatta işleme parametrelerinin optimize edilmesine ve modellenmesine odaklanmaktadır.

Sunulan tez, birkaç adımdan oluşmaktadır. İlk olarak AISI 4340 alaşımlı çelik üzerine farklı ısıl işlemler uygulanarak 30, 35, 40 HRC sertlikte iş parçaları elde edilmiştir. Ardından CBN, seramik ve karbür malzemeden üretilen kesici takımlar (uçlar) tedarik edildi. Deney Tasarımı (DT); toplam deney sayısını en aza indirmek ve daha sonra deneyleri planlamak, yürütmek, analiz etmek, yorumlamak için kullanılır. Bu yüzden öncelikle giriş işleme parametreleri (kesici uç, sertlik, kesme hızı, ilerleme, kesme derinliği) ve bunların seviyeleri (her biri üç seviyeli) alınarak Yanıt Yüzey Yöntemi (YYY) ile bir deney planı hazırlandı. Ardından çıktı işleme parametreleri (güç tüketimi, kesme kuvvetleri, ses, akım, yüzey pürüzlülüğü) belirlendi. Deney Tasarımında YYY oluşturmak için Minitab 16 yazılımı kullanıldı. Burada Box-Behnken deney tasarımı seçilmiştir. Bu çalışma için Box-Behnken Tasarımı (BBT) 5 faktörlü, 3 seviyeli ve 1 tek bloklu 46 deney seti oluşturulmuştur. Üç kesme hızı seviyesi (180, 220, 260 m/dak), üç ilerleme seviyesi (0,03; 0,07; 0,11 mm/dev), üç kesme derinliği seviyesi (0,08; 0,14; 0,20 mm), üç sertlik seviyesi (30, 35, 40 HRC) ve üç kesici uç seviyesi (seramik, karbür, CBN) kullanılarak deneyler yapılmıştır. Son olarak deney planı sırasına göre deneyler yapılmış ve sonuçlar değerlendirilmiştir. Hedef, tüm çıktı parametrelerini (yanıt değerleri) en aza indirmektir. Buna göre deneysel/hesaplanmış sonuçlar yorumlanmıştır.

Radyal kuvvet (Fx) için ANOVA sonuçları; %29,17 katkıyla ilerlemenin en önemli kesme parametresi olduğunu göstermektedir. Bunu %26,46 ile kesici uç, %25,66 ile kesme derinliği, %9,03 ile sertlik ve %0,28 ile kesme hızı takip etmektedir. Yüzey grafik analizlerinden kesme hızı, kesme derinliği, ilerleme ve sertlik arttıkça Fx'nin arttığı görülmektedir. Seramik uç kullanıldığında daha düşük Fx elde edildi. Sinyal-Gürültü oranlarına (SG) göre optimum Fx; i = seramik, h = 30 HRC, v = 180 m/dak, f = 0,03 mm/dev ve a = 0,08 mm'de elde edilebilir. Bu parametrelerde optimizasyon grafiğine göre Fx; 9,51 N tahmin edilmiştir.

Teğetsel kuvvet (Fy) için ANOVA sonuçları; %44,74 katkı ile ilerlemenin en önemli kesme parametresi olduğunu göstermektedir. Bunu %41,69 ile kesme derinliği, %7,06 ile kesici uç, %0,19 ile kesme hızı ve %0,07 ile sertlik takip etmektedir. Yüzey grafiğinden f ve a arttıkça Fy'nin de arttığı görülmektedir. Ayrıca, v'nin Fy üzerinde etkisi çok az veya hiç yoktur. Sertliğin Fy üzerinde çok az etkisi vardır. Fy, sertlik seviyesinin artmasıyla çok az değişir ve ihmal edilebilir. Bu durum sertlik skalaları arasında çok büyük fark olmamasından dolayı olmuş olabilir. Yüzey grafiklerine göre seramik kesici uç kullanıldığında minimum Fy elde edildi. SG oranlarına göre; minimum Fy değeri i = seramik, h = 35 HRC, v = 220 m/dak, f = 0,03 mm/dev ve a = 0,08 mm'de elde edilmiştir. Bu parametrelerde optimizasyon grafiğine göre Fy; 15,72 N tahmin edilmiştir.

İlerleme kuvveti (Fz)'nin ANOVA sonuçlarından; %53,36 katkı ile kesme derinliğinin Fz üzerinde en önemli kesme parametresi olduğu görülebilir. Bunu %16,61 ile kesici uç, %10,52 ile ilerleme, %1,57 ile sertlik ve %0,01 ile kesme hızı takip etmektedir. Fz, artan kesme hızı ve ilerleme seviyeleri ile biraz artar veya değişmez. Bununla birlikte, artan kesme derinliği değeri ile Fz'nin kuvvetli bir şekilde arttığı gözlemlenmiştir. Sertlik değerleri arttıkça Fz'nin de arttığı tespit edilmiştir. Ayrıca en düşük Fz, karbür kesici uç kullanıldığında görüldü. SG oranlarına göre; karbür uç, 30 HRC sertlik, 180 m/dk kesme hızı, 0,03 mm/dev ilerleme ve 0,08 mm kesme derinliği ayarlandığında, optimum Fz değeri tespit edilir. Bu parametrelerde optimizasyon grafiğine göre Fz; 29,25 N tahmin edilmiştir.

Bu araştırmada, kesme parametrelerinin yüzey pürüzlülüğü (Ra) üzerindeki yüzde etkisini göstermek için ANOVA analizi kullanılmıştır. Ra için süreç parametrelerinin yüzde katkısına göre, Ra üzerinde en fazla etkiye sahip parametrenin %51,52 ile kesici uç olduğu sonucuna varılmıştır. Bunu %13,59 ile sertlik, %1,86 ile ilerleme, %0,47 ile kesme derinliği ve %0,18 ile kesme hızı takip etmektedir. Yüzey grafiği sonuçlarına göre; a, f, v parametrelerinin ikili etkileşiminde en yüksek kesme hızıyla en iyi yüzey pürüzlülüğü elde edilir. Kesme derinliğinin Ra üzerindeki etkisinin parametre etkileşimine bağlı olarak değişkenlik gösterdiği bulunmuştur. En yüksek ilerleme ve en düşük kesme derinliği kombinasyonu ile Ra değerinin artma eğiliminde olduğu gözlemlenmiştir. Ayrıca, en yüksek kesme hızı ve en düşük kesme derinliği kombinasyonu ile Ra değerinin düşme eğiliminde olduğu gözlemlenmiştir. Bunlarla birlikte, ilerlemenin artmasıyla Ra değerlerinde bir artış gözlemlenir. Sertlik seviyesinin en yüksek değerlerinde, en düşük Ra değerleri üretilir. En düşük Ra değerleri, CBN kesici uç kullanıldığında elde edilmiştir. Ra için SG oranlarına göre; i = CBN, h = 40 HRC, v = 180 m/dak, f = 0,03 mm/dev ve a = 0,08 mm ayarlandığında, optimum Ra değeri belirlendi. Bu parametrelerde optimizasyon grafiğine göre Ra; 0,37 µm tahmin edilmiştir.

Kesme parametrelerinin Toplam Akım ($I_{toplam}$) üzerindeki önemini belirlemek için ANOVA tablosu kullanılmıştır. ANOVA tablosuna göre $I_{toplam}$'ı etkileyen en önemli faktörün %94,23 katkı ile kesme hızı olduğu görülmüştür. Bunu %2,82 ile kesme derinliği, %0,83 ile kesici uç, %0,40 ile ilerleme, ve %0,02 ile sertlik takip ediyor. $I_{toplam}$ için yüzey grafiğine bakıldığında, uygulanan kesme hızı arttıkça $I_{toplam}$ doğrusal olarak arttı. Ayrıca, kesme derinliği ve ilerlemenin $I_{toplam}$ değerleri üzerindeki etkisinin değişken olduğu bulunmuştur. $I_{toplam}$ değerinin kesme derinliği ve ilerlemedeki artışlarla artma eğiliminde olduğu, ancak kesme derinliği ve ilerlemedeki artışlarla tepe noktasından sonra azaldığı gözlemlendi. $I_{toplam}$, daha yüksek sertlik değerlerinde arttı. $I_{toplam}$, CBN uç kullanıldığında en yüksek değerini almıştır. $I_{toplam}$ için SG oranlarına göre; i = seramik, h = 30 HRC, v = 180 m/dak, f = 0,03 mm/dev ve a = 0,08 mm olarak ayarlandığında optimum $I_{toplam}$ değeri tespit edilmiştir. Bu parametrelerde optimizasyon grafiğine göre $I_{toplam}$; 4,83 A tahmin edilmiştir.

Sonuçların istatistiksel olarak analiz edilebilmesi amacıyla Toplam Ses ($S_{toplam}$) için ANOVA yöntemi uygulandı. ANOVA tablosuna göre $S_{toplam}$'i etkileyen en önemli faktör; %86,71 katkı ile kesme hızıdır. Bunu %2,14 ile ilerleme, %1,75 ile sertlik, %0,09 ile kesme derinliği ve %0,06 ile kesici uç takip etmektedir. Yüzey grafiğinde gösterildiği gibi, kesme hızı lineer olarak arttıkça $S_{toplam}$'in arttığı açıkça çıkarılabilir. Kesme derinliğinin $S_{toplam}$ değerleri üzerindeki etkisinin değişken olduğu görülmüştür. En yüksek ilerleme ve en düşük kesme derinliği kombinasyonu ile $S_{toplam}$ değerinin artma eğiliminde olduğu gözlemlenmiştir. Ayrıca, kesme derinliği ve kesme hızının etkileşiminde kesme derinliğinin seviyesi yükselirken $S_{toplam}$ arttı. Sertlik değerleri yükseldiğinde $S_{toplam}$'in artığı görülmüştür. Tüm bunların yanı sıra; karbür kesici uç kullanıldığında $S_{toplam}$, en düşük seviyesini almıştır. SG oranlarına göre minimum $S_{toplam}$ seviyesi kombinasyonu; i = karbür, h = 30 HRC, v = 180 m/dak, f = 0,07 mm/dev ve a = 0,08 mm'de oluşturulur. Bu parametrelerde optimizasyon grafiğine göre $S_{toplam}$; 77,48 dB tahmin edilmiştir.

Toplam Güç Tüketiminin ($P_{toplam}$) ANOVA sonuçlarından, %94,23 katkı ile kesme hızının en önemli kesme parametresi olduğu görülebilir. Bunu %2,82 ile kesme derinliği, %0,83 ile kesici uç, %0,40 ile ilerleme ve %0,02 ile sertlik takip ediyor. $P_{toplam}$'nin yüzey grafiğine göre, ilerleme ve kesme derinliğinin $P_{toplam}$ üzerindeki etkisinin etkileşim parametresine bağlı olarak değişkenlik gösterdiği bulundu. İlerleme ve kesme derinliği seviyeleri arttıkça $P_{toplam}$ değerinin arttığı, ancak ilerleme ve kesme derinliği seviyeleri daha fazla arttıkça $P_{toplam}$'nin tepe noktasından sonra düştüğü belirlendi. Ayrıca kesme hızı değerleri arttıkça $P_{toplam}$'nin lineer olarak arttığı tespit edilmiştir. Sertlik seviyesi arttıkça $P_{toplam}$ genellikle artmıştır. CBN kesici uç yerine karbür veya seramik kesici uç kullanıldığında $P_{toplam}$ önemli ölçüde azaldı. SG oranlarına göre optimum $P_{toplam}$ için en uygun süreç parametreleri; i = seramik, h = 30 HRC, v = 180 m/dk, f = 0,03 mm/dev ve a = 0,08 mm'dir. Bu parametrelerde optimizasyon grafiğine göre $P_{toplam}$; 3178,60 W tahmin edilmiştir.

Sonuç olarak optimum $P_{toplam}$, Fx, Fy, Fz, Ra, $S_{toplam}$ ve $I_{toplam}$'ı elde etmek için formülasyon olarak matematiksel modeller geliştirilmiştir. $P_{toplam}$, Fx, Fy, Fz, Ra, $S_{toplam}$ ve $I_{toplam}$ için deneysel/hesaplanmış ve tahmin edilen değerler arasındaki maksimum hata; sırasıyla %1,64; %11,33; %13,32; %4,00; %32,59; %0,81 ve %1,64 bulunmuştur. Sonuçlar; geliştirilen modelin takım tezgâhlarının optimum güç tüketimini elde etmede etkili olduğunu ve endüstride kullanılabileceğini göstermiştir.

**ACKNOWLEDGEMENTS**

At first, I would like to thank Prof. Dr. Abdul Kadir EKŞİ who has been my thesis main supervisor for their motivation, encouragement, and guidance. Also, I would like to thank my co-supervisor Prof. Dr. Hamza Kemal AKYILDIZ for his constant support, availability, and constructive suggestions.

Furthermore, I would like to thank my thesis committee members Prof. Dr. Ali Hamza TANRIKULU, Prof. Dr. Necip Fazıl YILMAZ, Prof. Dr. Ömer EYERCİOĞLU, and Assist. Prof. Dr. Mehmet İlteriş SARIGEÇİLİ, and for their many helpful suggestions.

I wish to thank to Prof. Dr. İlhami YİĞİT, Prof. Dr. Yusuf USTA, Assoc. Prof. Dr. Mustafa ÖZDEMİR, Assoc. Prof. Dr. Sertan OZAN, Assist. Prof. Dr. Durmuş Ali BİRCAN, Assist. Prof. Dr. Abidin ŞAHİNOĞLU, Assist. Prof. Dr. Mohammad RAFİGHİ, Lecturer. Dr. Mehmet Akif DÜNDAR, and Mehmet Tuncay KAYA for their endless support.

In addition, I would like to thank Çukurova University and all staff of The Mechanical Engineering Department at Çukurova University for their continuous support and motivation. I acknowledge Yozgat Bozok University Scientific Research Projects (BAP) coordination unit for supporting financial during my thesis.

Finally, my sincere appreciation goes to my supervisor Prof. Dr. Abdul Kadir EKŞİ who provides full academic and spiritual support. I am also very grateful to my father, my mother, my wife, and my children for their endless spiritual support.

**CONTENTS** **PAGES**

ABSTRACT .......... I
ÖZ .......... II
EXTENDED SUMMARY .......... III
GENİŞLETİLMİŞ ÖZET .......... VII
ACKNOWLEDGEMENTS .......... XI
CONTENTS .......... XII
LIST OF TABLES .......... XIV
LIST OF FIGURES .......... XVI
NOMENCLATURES .......... XXV
1. INTRODUCTION .......... 1
2. PREVIOUS STUDIES .......... 15
  2.1. Studies related to power consumption, cutting forces, sound, current, surface roughness, DOE, and FEM .......... 15
3. MATERIAL AND METHODS .......... 31
  3.1. Material .......... 31
  3.2. Micro Hardness Test .......... 34
  3.3. Macro Hardness Test .......... 38
  3.4. X-Ray Diffraction (XRD) Analysis .......... 40
  3.5. Metallographic Analysis .......... 43
  3.6. Tensile Test Analysis .......... 46
  3.7. Surface Roughness Measurement .......... 48
  3.8. Cutting Force Measurement .......... 49
  3.9. Current Measurement .......... 50
  3.11. Sound Measurement .......... 52
  3.12. Methods .......... 52

3.12.1. Taguchi Method (TM) ..... 54
3.12.2. Respond Surface Method (RSM) ..... 55
3.12.3. Analysis of Variance (ANOVA) ..... 57
3.12.4. Finite Element Method (FEM) ..... 57
3.12.5. Turning Experiments ..... 59
4. RESULTS AND DISCUSSION ..... 67
4.1. Analysis with RSM and Taguchi Method of Experimental Results ..... 68
4.1.1. Radial Force (Fx) Analysis ..... 76
4.1.2. Tangential Force (Fy) Analysis ..... 87
4.1.3. Feed Force (Fz) Analysis ..... 99
4.1.4. Surface Roughness (Ra) Analysis ..... 110
4.1.5. Total Electric Current ($I_{total}$=$I_{unloaded}$+ $I_{cutting}$) Analysis ..... 122
4.1.6. Total Sound ($S_{total}$= $S_{machine}$+ $S_{cutting}$) Analysis ..... 133
4.1.7. Total Power Consumption ($P_{total}$=$P_{unloaded}$+$P_{cutting}$) Analysis ..... 145
4.2. Comparison of Dynamometer Cutting Power and Electric Cutting Power during the Turning Process ..... 157
4.3. Comparison of Experimental and FEM Cutting Forces ..... 160
5. CONCLUSIONS AND RECOMMENDATIONS FOR FUTURE WORK ..... 175
5.1. Conclusions ..... 175
5.2. Recommendations for Future Studies ..... 180
REFERENCES ..... 181
CURRICULUM VITAE (CV) ..... 215
APPENDIX ..... 216

**LIST OF TABLES** **PAGES**


| | | |
|---|---|---|
| Table 1.1. | Specific cutting energy ofmaterials……………………… | 8 |
| Table 3.1. | Chemical composition of AISI 4340 alloy steel used in this study…………………………………………………. | 31 |
| Table 3.2. | Physical properties of AISI 4340 alloy steel used in this study (Alimardani et al., 2010; Khatir et al., 2021; Elsheikh et al., 2021)………………………………….. | 32 |
| Table 3.3. | Role of statistics in engineering and experimentation…… | 53 |
| Table 3.4. | Kennametal/CNMG120408/RP/KU30T (Kennametal master catalog, 2018; Akko catalog, 2021)……………… | 62 |
| Table 3.5. | Sumitomo electric/CNGA120408/NB100C (Akko catalog, 2021; Sumitomo catalog, 2021)………………… | 63 |
| Table 3.6. | Sumitomo electric/2NCCNGA120408HS/BNC2010 (Akko catalog, 2021, 2018; Sumitomo catalog, 2021)….. | 64 |
| Table 3.7. | Kennametal/TPGN160304/KC5010 (Kennametal master catalog, 2018)…………………………………............ | 65 |
| Table 4.1. | Process factors and selected levels were used for machining parameters in this experimental study……….. | 67 |
| Table 4.2. | Percent ratios of Power consumption of CNC machine tool used in the study………………………………….. | 70 |
| Table 4.3. | Box-Behnken Design test plan…………………………... | 72 |
| Table 4.4. | Experiment design of RSM (L46), experimental results, and calculated results………………………………….. | 74 |
| Table 4.5. | Analysis of variance for Fx……………………………… | 76 |
| Table 4.6. | Comparison of experimental and predicted results for Fx. | 87 |
| Table 4.7. | Analysis of variance for Fy……………………………… | 88 |
| Table 4.8. | Comparison of experimental and predicted results for Fy. | 98 |

| | | |
|---|---|---|
| Table 4.9. | Analysis of variance for Fz………………………………. | 99 |
| Table 4.10. | Comparison of experimental and predicted results for Fz.. | 109 |
| Table 4.11. | Analysis of variance for Ra……………………………… | 110 |
| Table 4.12. | Comparison of experimental and predicted results for Ra. | 121 |
| Table 4.13. | Analysis of variance for $I_{total}$…………………………... | 122 |
| Table 4.14. | Comparison of experimental and predicted results for $I_{total}$…………………………………………………….. | 133 |
| Table 4.15. | Analysis of variance for $S_{total}$………………………….. | 134 |
| Table 4.16. | Comparison of experimental and predicted results for $S_{total}$……………………………………………………. | 145 |
| Table 4.17. | Analysis of variance for $P_{total}$………………………….. | 146 |
| Table 4.18. | Comparison of calculated and predicted results for Ptotal…………………………………………………... | 156 |
| Table 4.19. | Comparison of dynamometer cutting power ($P_{cuttingD}$) and electric cutting power ($P_{cuttingE}$)…………………………... | 159 |
| Table 4.20. | Physical properties for AISI 4340 steel with 30 HRC…... | 164 |
| Table 4.21. | Strength constants for AISI 4340 steel with 30 HRC……. | 164 |
| Table 4.22. | Fracture constants for AISI4340 steel with 30 HRC…….. | 164 |
| Table 4.23. | Physical properties for cutting tool (Carbide insert)…….. | 164 |
| Table 4.24. | Experimental and simulated forces on cylindrical tubes… | 171 |
| Table 4.25. | Experimental and simulated cutting forces results for cylindrical bars…………………………………………... | 173 |
| Table 5.1. | Confirmation test results for Fx, Fy, Fz, Ra, $I_{total}$, $S_{total}$ and $P_{total}$……………………………………………………. | 179 |

**LIST OF FIGURES** **PAGES**


| | | |
|---|---|---|
| Figure 1.1 | Surface roughness profile……………………………….. | 2 |
| Figure 1.2. | Primary world energy consumption……………………... | 3 |
| Figure 1.3. | Energy flow for manufacturing processes……………….. | 4 |
| Figure 1.4. | Consumption percentage of electrical energy used by each sector………………………………………….…... | 4 |
| Figure 1.5. | Total energy consumption; a) Energy used for machining during turning of the workpiece, b) Energy used for an automobile production line……………………………… | 5 |
| Figure 1.6. | Characteristic power need of a machine tool…………… | 6 |
| Figure 1.7. | The power profile of the turning process………………... | 7 |
| Figure 2.1. | Energy consumption levels……………………………… | 19 |
| Figure 2.2. | Strategies for energy efficiency………………………….. | 21 |
| Figure 2.3. | Power flow of machine tool machining process ($P_{start}$: start state power, $P_{standby}$: standby state power, $P_{no-load}$: no-load state power, $P_{load}$: load state power)………………… | 24 |
| Figure 3.1. | Photos of AISI 4340 steel test material; a) Front view, b) Side view………………………………………………… | 31 |
| Figure 3.2. | Thermo Scientific ARL PERFORM'X XRF Sequential X-Ray Fluorescence Spectrometer used for material analysis in this study……………………….................. | 32 |
| Figure 3.3. | Heat cycle of normalizing of AISI 4340 steel…………… | 33 |
| Figure 3.4. | The heat cycle of quenching and tempering of AISI 4340 steel used in this study…………………………………… | 34 |
| Figure 3.5. | Metkon MH3 microhardness tester used in this study…... | 35 |

| | | |
|---|---|---|
| Figure 3.6. | FEI Quanta FEG 450 including Field Emission Gun-Scanning Electron Microscope with Environmental Scanning Electron Microscope (ESEM) used for the imageVickerskers hardness specimens in this study…….. | 35 |
| Figure 3.7. | SEM images belonging to the different magnification of Vickers Microhardness indents the of the cylindrical specimen with the size of Ø40x10mm; a) Photo of front view, b) Photo of side view, c) 100X magnification, d) 1000X magnification……………….................................. | 36 |
| Figure 3.8. | Vickers microhardness mean values for AISI 4340 steel specimens tempered at 610ºC (for material with 30 HRC)………………………………………………….... | 37 |
| Figure 3.9. | Vickers microhardness mean values for AISI 4340 steel specimens tempered at 560ºC (for material with 35 HRC)………………………………………………….... | 37 |
| Figure 3.10. | Vickers microhardness mean values for AISI 4340 steel specimens tempered at 510ºC (for material with 40 HRC)................................................................................ | 38 |
| Figure 3.11. | BMS 200-RB Analog Rockwell & Brinell Hardness Tester used in this study…………………………………. | 39 |
| Figure 3.12. | HRC image of the cylindrical specimen with 30±1 HRC……………………………………………………… | 39 |
| Figure 3.13. | Mean hardness values measured in Rockwell C scale HRC (Note: The term as-rolled condition stems from the fact that the product is not heat-treated)………………… | 40 |
| Figure 3.14. | Photos of specimens used in this study for crystalline phase analysis; a) Front view of specimen, b) Side view of the specimen………………………………………….... | 41 |

| | | |
|---|---|---|
| Figure 3.15. | PANalytical Empyrean X-ray diffractometer used in the study………………………………………………... | 42 |
| Figure 3.16. | X-ray diffraction patterns from the surface of the specimen tempered at 610 ºC (for material with 30 HRC)………………………………………………... | 42 |
| Figure 3.17. | X-ray diffraction patterns from the surface of the specimen tempered at 560 ºC (for material with 35 HRC)………………………………………………... | 43 |
| Figure 3.18. | X-ray diffraction patterns from the surface of the specimen tempered at 510 ºC (for material with 40 HRC)………………………………………………... | 43 |
| Figure 3.19. | SEM image of a specimen of tempered at 610 ºC……….. | 44 |
| Figure 3.20. | SEM image of a specimen tempered at 560 ºC………….. | 45 |
| Figure 3.21. | SEM image of a specimen of tempered at 510 ºC……….. | 45 |
| Figure 3.22. | Experimental setup of the tensile test machine………….. | 46 |
| Figure 3.23. | Photos and schematic of technical drawing tensile specimen; a) Machined, b) Technical drawing G—Gage length (62,5 ± 0,1 mm), D—Diameter (12,5 ± 0,2 mm), R—Radius of fillet (10 mm), A—Length of reduced section (75 mm), c) Front view of broken tensile specimen, d) Broken surfaces of tensile specimen……… | 47 |
| Figure 3.24. | The results obtained from tensile tests…………………... | 48 |
| Figure 3.25. | Mitutoyo SJ211 Surftest Surface Roughness Tester; a) Setup, b) Close-up shot…………………………………... | 49 |
| Figure 3.26. | Calibration of Surftest Surface Roughness Tester; a) Setup, b) Reference specimen…………………………… | 49 |

| | | |
|---|---|---|
| Figure 3.27. | Experimental setup for force measurement used in this work; a) Goodway 260Y CNC Lathe, b) Kistler 9129AA model piezoelectric dynamometer, c) Kistler 5070A model amplifier, d) Kistler 5697 model data acquisition box, e) Computer, f) Dynoware software, g) Screenshot of cutting forces………………………………………… | 50 |
| Figure 3.28. | Setup for current measurement used in this work; a) Electric panel of CNC lathe, b) Digital Clamp Multimeter, c) Cable color of electrical phases………….. | 51 |
| Figure 3.29. | Labels of the CNC lathe used in this work; a) Feature nameplate, b) Electrical nameplate………………………. | 51 |
| Figure 3.30. | Setup for sound level measurement used in this work; a) Sound level measurement in CNC lathe, b) Close-up shot, c) Sound Level Meter……………………………… | 52 |
| Figure 3.31. | Process procedure……………………………………... | 54 |
| Figure 3.32. | Stages of Abaqus analysis (Abaqus, 2021)……………… | 59 |
| Figure 3.33. | CNC lathe………………………………………………... | 60 |
| Figure 3.34. | Experimental setup on CNC lathe……………………….. | 60 |
| Figure 3.35. | Schematic representation of the machined test specimen; a) General drawing, b) Close-up (dimensions are mm)…. | 61 |
| Figure 4.1. | Fishbone diagram of factors affecting $P_{total}$, Fx, Fy, Fz, Ra, $S_{total}$, and $I_{total}$………………………………………… | 68 |
| Figure 4.2. | Power consumption of 5 axis CNC turning machine tool used in this study……………………………………….. | 69 |
| Figure 4.3. | Cutting forces on the symbolic cutting tool (insert)........... | 71 |
| Figure 4.4. | Residual plots for Fx……………………………......... | 77 |
| Figure 4.5. | Surface plot of Fx vs a;f……………………………........ | 78 |
| Figure 4.6. | Surface plot of Fx vs a;v…………………………………. | 79 |

| | | |
|---|---|---|
| Figure 4.7. | Surface plot of Fx vs f;v………………………………… | 79 |
| Figure 4.8. | Surface plot of Fx vs a;h………………………………… | 80 |
| Figure 4.9. | Surface plot of Fx vs f;h………………………………… | 81 |
| Figure 4.10. | Surface plot of Fx vs v;h………………………………… | 81 |
| Figure 4.11. | Surface plot of Fx vs a;i……………………………......... | 82 |
| Figure 4.12. | Surface plot of Fx vs f;i……………………………......... | 83 |
| Figure 4.13. | Surface plot of Fx vs v;i………………………………… | 84 |
| Figure 4.14. | Surface plot of Fx vs h;i……………………………......... | 84 |
| Figure 4.15. | Main effects plot for SN ratios of Fx…………………….. | 85 |
| Figure 4.16. | Optimization plot for Fx………………………………… | 86 |
| Figure 4.17. | Residual plots for Fy……………………………......... | 89 |
| Figure 4.18. | Surface plot of Fy vs a;f……………………………......... | 90 |
| Figure 4.19. | Surface plot of Fy vs a;v………………………………… | 90 |
| Figure 4.20. | Surface plot of Fy vs f;v………………………………… | 91 |
| Figure 4.21. | Surface plot of Fy vs a;h……………………………......... | 92 |
| Figure 4.22. | Surface plot of Fy vs f;h………………………………… | 92 |
| Figure 4.23. | Surface plot of Fy vs v;h………………………………… | 93 |
| Figure 4.24. | Surface plot of Fy vs a;i………………………………….. | 94 |
| Figure 4.25. | Surface plot of Fy vs f;i……………………………......... | 94 |
| Figure 4.26. | Surface plot of Fy vs v;i……………………………......... | 95 |
| Figure 4.27. | Surface plot of Fy vs h;i……………………………......... | 95 |
| Figure 4.28. | Main effects plot for SN ratios of Fy……………….......... | 96 |
| Figure 4.29. | Optimization plot for Fy………………………………… | 96 |
| Figure 4.30. | Residual plot for Fz……………………………………… | 100 |
| Figure 4.31. | Surface plot of Fz vs a;f………………………………….. | 101 |
| Figure 4.32. | Surface plot of Fz vs a;v………………………………… | 101 |
| Figure 4.33. | Surface plot of Fz vs f;v……………………………......... | 102 |
| Figure 4.34. | Surface plot of Fz vs a;h………………………………… | 103 |

Figure 4.35. Surface plot of Fz vs f;h……………………………........ 103
Figure 4.36. Surface plot of Fz vs v;h…………………………………. 104
Figure 4.37. Surface plot of Fz vs a;i………………………….......... 105
Figure 4.38. Surface plot of Fz vs f;i…………………………….......... 105
Figure 4.39. Surface plot of Fz vs v;i…………………………….......... 106
Figure 4.40. Surface plot of Fz vs h;i…………………………….......... 106
Figure 4.41. Main effects plot for SN ratios of Fz……………........ 107
Figure 4.42. Optimization plot for Fz…………………………………. 107
Figure 4.43. Residual plot for Ra……………………………………… 111
Figure 4.44. Surface plot of Ra vs a;f…………………………………. 112
Figure 4.45. Surface plot of Ra vs a;v………………………………… 113
Figure 4.46. Surface plot of Ra vs f;v…………………………………. 113
Figure 4.47. Surface plot of Ra vs a;h………………………………… 114
Figure 4.48. Surface plot of Ra vs f;h…………………………………. 115
Figure 4.49. Surface plot of Ra vs v;h………………………………… 115
Figure 4.50. Surface plot of Ra vs a;i…………………………………. 117
Figure 4.51. Surface plot of Ra vs f;i……………………………......... 117
Figure 4.52. Surface plot of Ra vs v;i…………………………………. 118
Figure 4.53. Surface plot of Ra vs h;i…………………………………. 118
Figure 4.54. Main effects plot for SN ratios of Ra………………........ 119
Figure 4.55. Optimization plot for Ra…………………………………. 119
Figure 4.56. Residual plot for $I_{total}$…………………………….............. 123
Figure 4.57. Surface plot of $I_{total}$ vs a;f………………………………… 124
Figure 4.58. Surface plot of $I_{total}$ vs a;v……………………………......... 125
Figure 4.59. Surface plot of $I_{total}$ vs f;v………………………………... 125
Figure 4.60. Surface plot of $I_{total}$ vs a;h………………………….......... 126
Figure 4.61. Surface plot of $I_{total}$ vs f;h……………………………... 127
Figure 4.62. Surface plot of $I_{total}$ vs v;h…………………………......... 127

| | | |
|---|---|---|
| Figure 4.63. | Surface plot of $I_{total}$ vs a;i…………………………… | 128 |
| Figure 4.64. | Surface plot of $I_{total}$ vs f;i………………………………… | 129 |
| Figure 4.65. | Surface plot of $I_{total}$ vs v;i………………………………… | 129 |
| Figure 4.66. | Surface plot of $I_{total}$ vs h;i………………………………… | 130 |
| Figure 4.67. | Main effects plot for SN ratios of $I_{total}$…………………… | 131 |
| Figure 4.68. | Optimization plot for $I_{total}$……………………………… | 131 |
| Figure 4.69. | Residual plot for $S_{total}$…………………………………… | 135 |
| Figure 4.70. | Surface plot of $S_{total}$ vs a;f……………………………… | 137 |
| Figure 4.71. | Surface plot of $S_{total}$ vs a;v……………………………… | 137 |
| Figure 4.72. | Surface plot of $S_{total}$ vs f;v……………………………… | 138 |
| Figure 4.73. | Surface plot of $S_{total}$ vs a;h……………………………… | 139 |
| Figure 4.74. | Surface plot of $S_{total}$ vs f;h……………………………… | 139 |
| Figure 4.75. | Surface plot of $S_{total}$ vs v;h……………………………… | 140 |
| Figure 4.76. | Surface plot of $S_{total}$ vs a;i……………………………… | 140 |
| Figure 4.77. | Surface plot of $S_{total}$ vs f;i……………………………… | 141 |
| Figure 4.78. | Surface plot of $S_{total}$ vs v;i……………………………… | 142 |
| Figure 4.79. | Surface plot of $S_{total}$ vs h;i……………………………… | 142 |
| Figure 4.80. | Main effects plot for SN ratios of $S_{total}$…………………… | 143 |
| Figure 4.81. | Optimization plot for $S_{total}$……………………………… | 143 |
| Figure 4.82. | Residual plot for $P_{total}$…………………………………… | 147 |
| Figure 4.83. | Surface plot of $P_{total}$ vs a;f……………………………… | 148 |
| Figure 4.84. | Surface plot of $P_{total}$ vs a;v……………………………… | 148 |
| Figure 4.85. | Surface plot of $P_{total}$ vs f;v……………………………… | 149 |
| Figure 4.86. | Surface plot of $P_{total}$ vs a;h……………………………… | 149 |
| Figure 4.87. | Surface plot of $P_{total}$ vs f;h……………………………… | 150 |
| Figure 4.88. | Surface plot of $P_{total}$ vs v;h……………………………… | 151 |
| Figure 4.89. | Surface plot of $P_{total}$ vs a;i……………………………… | 151 |
| Figure 4.90. | Surface plot of $P_{total}$ vs f;i……………………………… | 152 |

| | | |
|---|---|---|
| Figure 4.91. | Surface plot of $P_{total}$ vs v;i…………………………......... | 152 |
| Figure 4.92. | Surface plot of $P_{total}$ vs h;i…………………………......... | 153 |
| Figure 4.93. | Main effects plot for SN ratios of $P_{total}$…………….......... | 154 |
| Figure 4.94. | Optimization plot for $P_{total}$…………………………......... | 154 |
| Figure 4.95. | Symbolic schematic design of the turning process………. | 158 |
| Figure 4.96. | Turning process of cylindrical bar specimens; a) Experimental setup, b) Close-up, c) Depicted schema…... | 160 |
| Figure 4.97. | Turning process of cylindrical tube specimens; a) Experimental setup, b) Close-up, c) Depicted schema…... | 161 |
| Figure 4.98. | Force measurement system used in this study; a) Goodway 260Y CNC Lathe, b) Kistler 9129AA model piezoelectric dynamometer, c) Kistler 5070 model amplifier, d) Kistler 5697 model data acquisition box, e) Computer, f) Dynoware software, g) Screenshot of cutting forces………………………………………….. | 162 |
| Figure 4.99. | Measured feed, radial, and tangential force components for a cylindrical bar specimen…………………………… | 163 |
| Figure 4.100. | Measured feed, radial, and tangential force components for a cylindrical tube specimen…………………………... | 163 |
| Figure 4.101. | Iteration of friction coefficient for F…………………….. | 165 |
| Figure 4.102. | Finite element model of cylindrical bar workpiece prepared by means of HyperMesh software; a) Full image, b) Close-up……………………………………… | 167 |
| Figure 4.103. | Finite element model of cylindrical tube workpiece prepared by means of HyperMesh software; a) Full image, b) Close-up……………………………………… | 167 |

| | | |
|---|---|---|
| Figure 4.104. | First step of Von-Mises Stress Contour in ABAQUS/Explicit for 3D cylindrical tube (feed rate: 0,1 mm/rev); a) Full image, b) Close-up. …………………… | 168 |
| Figure 4.105. | Final step of Von-Mises Stress Contour in ABAQUS/Explicit for 3D cylindrical tube (feed rate: 0,1 mm/rev)……………………………………………….. | 168 |
| Figure 4.106. | First step of Von-Mises Stress Contour in ABAQUS/Explicit for 3D cylindrical bar (feed rate: 0,2 mm/rev) ; a) Full image, b) Close-up……………………. | 169 |
| Figure 4.107. | Final step of Von-Mises Stress Contour in ABAQUS/Explicit for 3D cylindrical bar (feed rate: 0,2 mm/rev); a) Full image, b) Close-up…………………….. | 169 |
| Figure 4.108. | Comparison of experimental and simulated forces on the cylindrical tube for feed rate of 0,1 mm/rev during the turning process………………………………………… | 170 |
| Figure 4.109. | Comparison of experimental and simulated forces on the cylindrical tube for feed rate of 0,2 mm/rev during the turning process………………………………………… | 170 |
| Figure 4.110. | Comparison of experimental and simulated forces on the cylindrical tube for feed rate of 0,3 mm/rev during the turning process………………………………………… | 171 |
| Figure 4.111. | Comparison of experimental and simulated forces on the cylindrical bar for feed rate of 0,1 mm/rev during the turning process………………………………………… | 172 |
| Figure 4.112. | Comparison of experimental and simulated forces on the cylindrical bar for feed rate of 0,2 mm/rev during the turning process………………………………………… | 172 |

Figure 4.113. Comparison of experimental and simulated forces on the cylindrical bar for feed rate of 0,3 mm/rev during the turning process…………………………………………… 173

**NOMENCLATURES**

| | |
|---|---|
| AISI | : American iron and steel institute |
| DOE | : Design of experiment |
| RSM | : Response surface methodology |
| FFD | : Full factorial design |
| ANOVA | : Analysis of variance |
| CNC | : Computer numerical control |
| HRC | : Rockwell C hardness scale |
| OP | : Optical microscope |
| SEM | : Scanning electron microscope |
| MOPSO | : Multiple objective particle swarm optimization algorithm |
| EC | : Energy consumption |
| MTEC | : Machine tool energy consumption |
| NC | : Numerical control |
| EN | : Europe norm |
| ASP | : Acoustic sound pressure |
| RAM | : Random access memory |
| MQL | : Minimum quantity lubricating |
| PCBN | : Polycrystalline cubic boron nitride |
| i | : Insert |
| h | : Hardness (HRC) |
| v | : Cutting speed (m/min) |
| f | : Feed rate (mm/rev) |
| a | : Depth of cut (mm) |
| Ra | : Arithmetical mean height surface roughness (µm) |
| Rz | : Maximum height of profile surface roughness (µm) |
| Rq | : Root mean square deviation surface roughness (µm) |

| | |
|---|---|
| Fx | : Radial force (N) |
| Fy | : Tangential force (N) |
| Fz | : Feed force (N) |
| F | : Resultant force (N) |
| SN | : Signal noise ratio (dB) |
| P | : Power consumption (W) |
| $P_{total}$ | : Total power consumption (W) |
| $P_{idle}$ | : Idle power consumption (W) |
| $P_{cutting}$ | : Cutting power (W) |
| $P_{unloaded}$ | : Power calculated without cutting the workpiece |
| $I_{cutting}$ | : Electric cutting current |
| $I_{total}$ | : Total current consumption |
| $I_{unloaded}$ | : Current measured without cutting the workpiece |
| $P_{cuttingD}$ | : Dynamometer cutting power |
| $P_{cuttingE}$ | : Electric cutting power |
| $S_{total}$ | : Total sound |
| $S_{machine}$ | : Sound formed without cutting the workpiece |
| $S_{cutting}$ | : Cutting sound of the workpiece |
| V | : Voltage (V) |
| I | : Amper (A) |
| cosφ | : Power factor |
| BUE | : Built-up edge |
| MRR | : Material removal rate ($mm^3/s$) |
| CBN | : Cubic boron nitride |
| 3D | : Three dimensional |
| 2D | : Two dimensional |
| CLA | : Centre line average |
| yi | : Vertical deviations (µm) |

| | |
|---|---|
| Lm | : Evaluation length (µm) |
| SCE | : Specific cutting energy (k, W.s/$mm^3$) |
| min | : Minute |
| rev | : Revolution |
| m | : Meter |
| mm | : Millimeter |
| ASTM | : American society for testing and materials |
| ESEM | : Environmental scanning electron microscope |
| HV | : Vickers hardness |
| UTS | : Ultimate tensile strength (MPa) |
| YS | : Yield strength (MPa) |
| RS | : Rupture strength (MPa) |
| TM | : Taguchi method |
| OA | : Orthogonal arrays |
| AD | : Anderson-Darling statistic |
| Mean | : Arithmetic average of the sum of all observations |
| StDev, S | : Standard deviation |
| N | : Number of total observations |
| P-Value, P | : Probability |
| R-Sq | : Accuracy value |
| R-Sq(pred) | : Predicted $R^2$ |
| R-Sq(adj) | : Adjusted $R^2$ |
| DF | : Degree of freedom |
| Seq SS | : Sequential sum of squares |
| Adj SS | : Adjusted sum of square |
| Adj MS | : Adjusted mean square |
| F | : Fisher test value |
| % Cont. | : Percent contribution |

CI : Confidence interval

* : Asterisk (*) is a star-shaped character and it denotes multiplication operation in this study.

# 1. INTRODUCTION

AISI (American Iron and Steel Institute) 4340 steel is known for its low alloy, medium carbon, and heat treatable. It is also a type of nickel-chromium-molybdenum steel. High toughness, strength, and perfect fatigue resistance are obtained when it is subjected to heat treatment. It is used in many applications like aircraft, automobiles, engine parts, gears, camshafts, crankshafts, steering arms, and sleeves (Fakir et al., 2018; Atlas Specialty Metals, 2005; Lee and Su, 1999; Suresh et al, 2012). Thanks to these properties, it has become attractive for use in the aeronautical, marine, and automotive industries. Therefore, it was decided to use AISI 4340 steel material in this study.

Surface roughness is widely used in engineering design and industry. That is, surface roughness has a significant effect on mechanical properties such as fatigue behavior, corrosion resistance, and creep life. Besides, it influences the functional properties of machine components such as friction, wear, light reflection, lubrication, electrical conductivity, corrosion resistance, and conduction of heat. On the other hand, in the turning process, surface quality is can vary significantly by many factors such as depth of cut, cutting speed, feed rate, material properties, insert geometry, a built-up edge (BUE), cutting fluid, and stability of the machine-tool-workpiece system. Turning operations are very precise and have a tolerance of 0,05 mm. For this reason, it is extremely important to optimize the parameters chosen during the turning of the workpiece and to provide suitable process conditions. Various parameters like Ra (roughness average), Rz (average maximum height of the profile), and Rq (root mean square roughness) are available to interpret the surface quality. Today, average surface roughness (Ra) known as the Centre Line Average (CLA) and broadly accepted in the industry were chosen to use in this work. Visually, the measurement procedure is indicated in Figure 1.1 (Groover, 2010; Davim and Jackson, 2011; Rao et al., 2013; Sumardiyanto et al., 2018; Tanikić and Marinković, 2012).

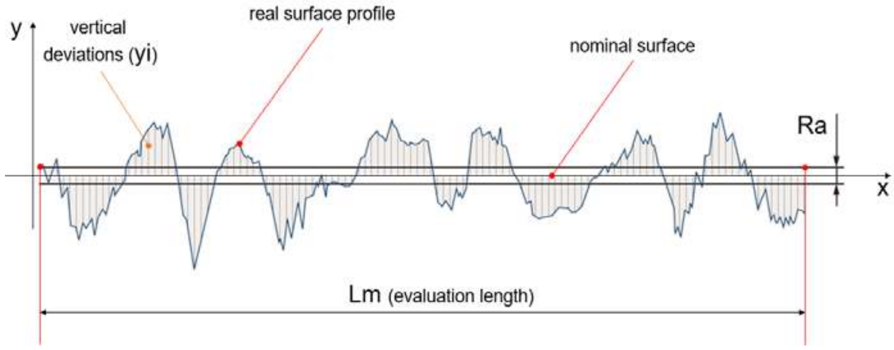


Figure 1.1. Surface roughness profile

Surface roughness can be approximately calculated using the following Equation 1.1.

$$Ra = \sum_{i=1}^{n} \frac{|yi|}{n} \text{ or } Ra = \int_{0}^{Lm} \frac{|y|}{Lm} \qquad (1.1)$$

Average roughness, vertical deviation from nominal surface, evaluation length, number of deviations included in Lm, and vertical deviations (absolute value) identified by subscript i are symbolized with Ra, y, Lm, n, and yi, respectively. The units in these equations are micrometers (µm).

Energy and materials are two key components that need the growth of the economy. These are provided by using natural resources such as fossil fuels and underground ores (Kant and Sangwan, 2015).

Energy consumption has increased due to the growth of industrialization and the increase in human population in the world as shown in Figure 1.2 (bp, 2020; Moradnazhad and Unver, 2016).

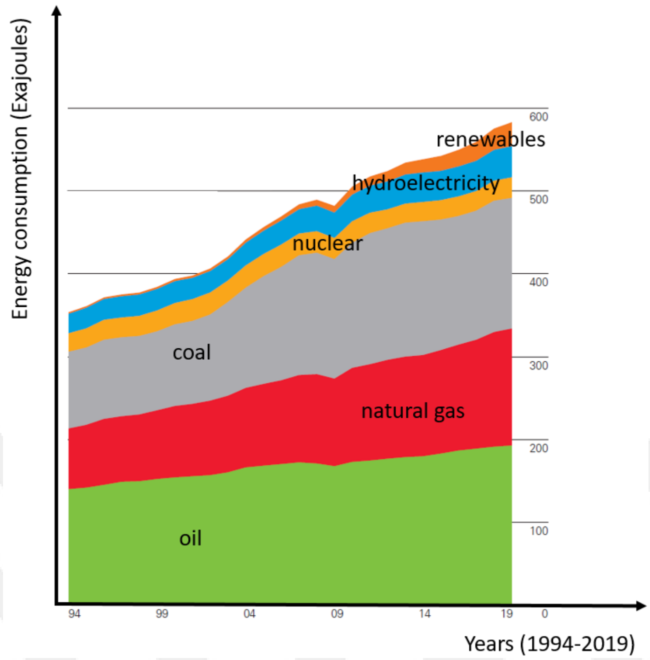


Figure 1.2. Primary world energy consumption

The environmental damages of greenhouse gas generated during electrical power production from fossil fuels and total energy cost affect energy consumption. An increase in greenhouse gas emissions will cause global warming in the atmosphere. Apart from this, the decrease in underground resources significantly affects energy consumption. If the electricity consumption is reduced, greenhouse gas emissions ($CO_2$, $CH_4$, …) will decrease (Şahinoğlu and Rafighi, 2019; Kara et al., 2011).

There is material input in these manufacturing processes and these materials are converted into products. These processes need energy and generally, this energy is supplied by electrical power as shown in Figure 1.3 (Gutowski et al., 2006; Herrmann et al., 2011).

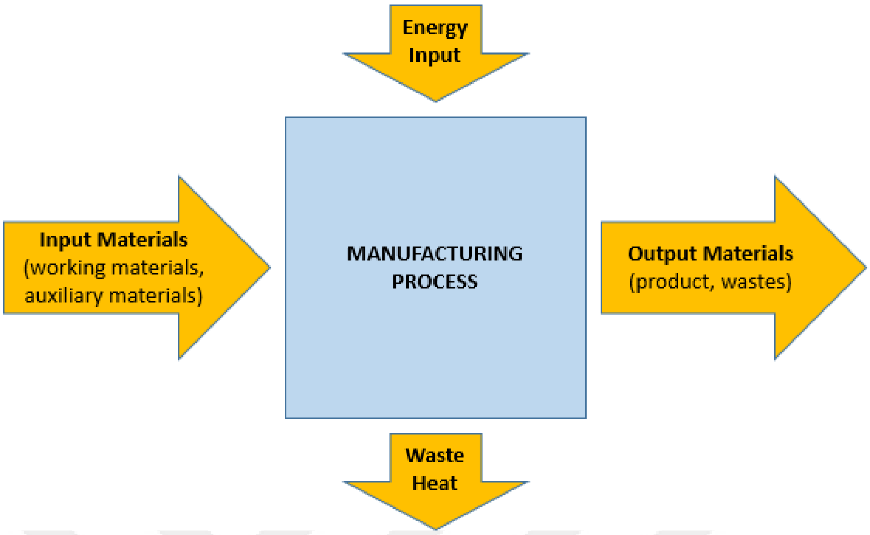


Figure 1.3. Energy flow for manufacturing processes

Machining has an important energy consumption area in the manufacturing industry as shown in Figure 1.4 (eia, 2013; Lv et al., 2018; Moradnazhad and Unver, 2016).

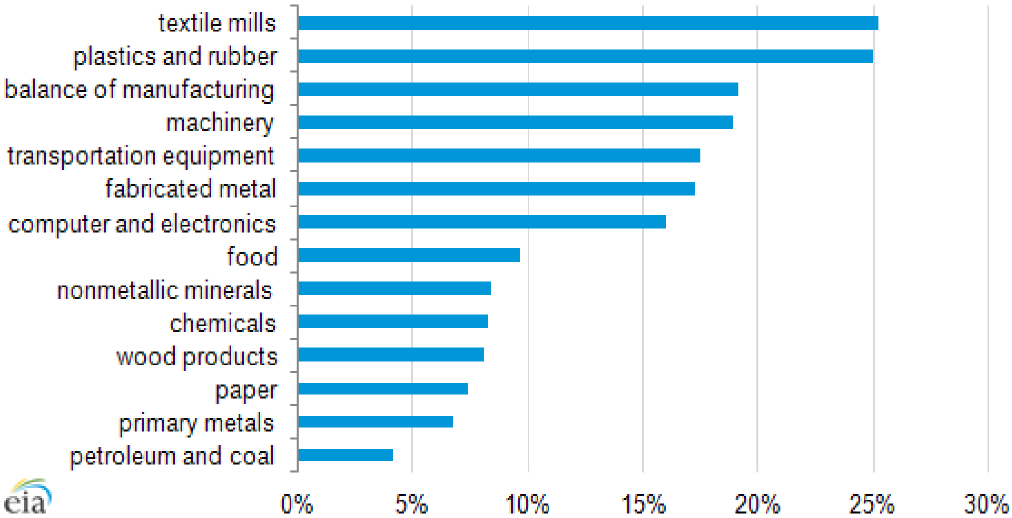


Figure 1.4. Consumption percentage of electrical energy used by each sector

Machine tools need great energy during machining to run motors and auxiliary equipment as shown in Figure 1.5a. They have various stages: an idle state by non-cutting operations, removal material along the cutting process, and post-machining (Abele et al., 2011; Kant and Sangwan, 2015). As shown in Figure 1.5b, although a lot of energy is consumed when the machine is idle in an automobile production line, a significant amount of energy is also consumed during machining (Gutowski et al., 2005).

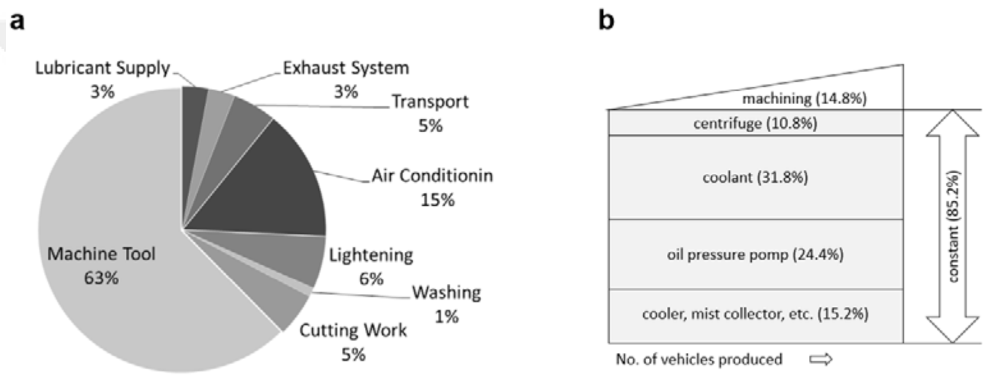


Figure 1.5. Total energy consumption; a) Energy used for machining during turning of the workpiece, b) Energy used for an automobile production line

In another sense, the power requirement of a machine tool is examined in three stages as fixed, variable, and cutting power. Fixed power is due to auxiliary components like computers and lights. Variable power consists of components such as spindle and drives motors. Cutting power is the power required during the metal removal process. Whether cutting process or not, the sum of fixed and variable power is the minimum amount of power required to operate the machine tool. And they're called tare power together as shown in Figure 1.6 (Helu et al., 2011).

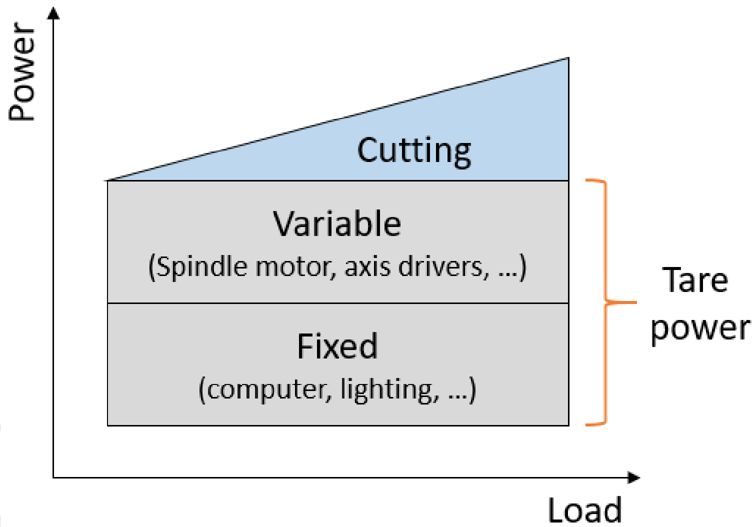

Figure 1.6. Characteristic power need of a machine tool

As mentioned above, the manufacturing industry consumes significant amounts of power and leads to an increase in global greenhouse gases. Furthermore, the increasing cost due to the excessive consumption of energy and natural underground resources seriously affects the manufacturing companies in the world. Therefore, energy consumption should be minimized (Warsi et al., 2015; Guo et al., 2012; Zhao et al., 2016).

The least energy can be consumed by reducing the electrical energy needed during machining. This can be achieved by increasing the energy efficiency of machining processes. For example, energy conservation could be provided by choosing the best cutting parameters for the machining process. That is, the cutting parameters need to be optimized (Şahinoğlu and Rafighi, 2020; Nur et al., 2015; Campatelli et al., 2014; Li and Kara, 2014). Optimization criteria that are usually examined in machining operations are material removal rate, surface roughness, tool life, cutting force, and power consumption (Zhang et al., 2017).

In addition to these, sound and current measurements of the machine tool can be taken as alternative optimization criteria to minimize energy consumption in the manufacturing industry (Karaaslan and Şahinoğlu, 2020).

Turning is a vital machining process practiced using a single-point cutting tool. In the turning process, cylindrical parts are machined with the help of a lathe. While the workpiece rotates steadily, the tool moves linearly and the material is removed from the workpiece surface. The turning process depends on many parameters such as spindle speed, feed rate, and depth of cut. Changes in these parameters affect power consumption. In other words, power consumption may increase if the appropriate parameters are not selected. Therefore, the parameters need to be optimized. In this way, power consumption is reduced (Abhang and Hameedullah, 2010; Valera and Bhavsar, 2014; Bagaber and Yusoff, 2017). The power profile curve of a typical turning process is shown in Figure 1.7 (Nur et al., 2017; Li et al., 2011).

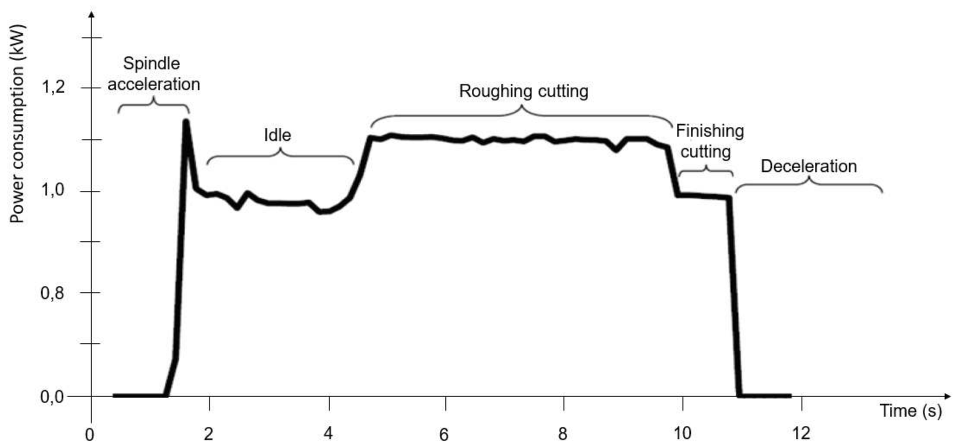

Figure 1.7. The power profile of the turning process

The electric power of the lathe can be calculated with the following Equation 1.2 (Shokoohi et al. 2015; Öztürk and Kara, 2020).

$$P = \sqrt{3}.V.I.\cos\varphi \ (watt) \tag{1.2}$$

Here, V is the voltage (volt), I is the current (amper), and cosϕ is the power factor (-).

Besides, the total electric power expended by machine tools is found with helping the following Equation 1.3 (Jiang et al., 2018; Mativenga and Rajemi, 2011; Rajemi et al., 2010; Serin et al., 2019; Zhong et al., 2015).

$$P_{total} = P_{idle} + P_{cutting}(k.\dot{v}) \tag{1.3}$$

In here, $P_{total}$ is total electric power (W), $P_{idle}$ is idle power (W) that keeps only auxiliary equipment running, $P_{cutting}$ is cutting power (W), $\dot{v}$ is the rate of material removal ($mm^3/s$), and k is specific cutting energy ($W.s/mm^3$). Specific cutting energy values are given in Table 1.1 (Kalpakjian and Schmid, 2010).

Table 1.1. Specific cutting energy of materials

| **Material** | **Specific cutting energy ($W.s/mm^3$)** |
|---|---|
| Aluminum alloys | 0,4-1 |
| Cast irons | 1,1-5,4 |
| Copper alloys | 1,4-3,2 |
| High-temperature alloys | 3,2-8 |
| Magnesium alloys | 0,3-0,6 |
| Nickel alloys | 4,8-6,7 |
| Refractory alloys | 3-9 |
| Stainless steels | 2-5 |
| Steels | 2-9 |
| Titanium alloys | 2-5 |

Also, the cutting power requirement can be calculated by the basic physical relationship between the cutting force and the cutting speed given in Equation 1.4 (Korkmaz and Günay, 2018; Nur et al., 2014).

$$P_{cutting} = F_c.v/60\ (watt, \frac{Nm}{s}) \tag{1.4}$$

In here, $P_{cutting}$ is cutting power (W), Fc is main cutting force (N), and v is cutting speed (m/min). The main cutting force in turning refers tangential and often the largest force (except hard turning) (Kistler, 2021).

Amongst many manufacturing processes, the machining process expends a significant amount of Specific Cutting Energy (SCE). SCE is described as the power required to remove material per unit volume and is a level of resistance against cutting. Furthermore, it gives information about the effectiveness of cutting conditions. SCE can be calculated using Equation 1.5. $\dot{v}$ is Material Removal Rate (MRR) and it is found as shown in Equation 1.6 (Black et al., 2002; Liu et al., 2016; Cica et al., 2020).

$$SCE = P_{cutting} / \dot{v}\ (W.s/mm^3) \tag{1.5}$$

$$\dot{v} = MRR = 1000.v.f.a\ (mm^3/\min) \tag{1.6}$$

Here f is feed rate (mm/rev), a is the depth of cut (mm), and v is cutting speed (m/min).

In addition, SCE involves the relationship between energy consumption and machining parameters that represent the energy efficiency of machine tools. Also, it is widely used in the literature because it is easy to determine (Zhou et al., 2015).

In the manufacturing industry, many machine operators may be exposed to high machine noise when machine tools are running. If the limit rises above the levels, it can harm human health. There are some reference values related to this. The European Parliament and the Council of The European Union issued a

Directive 2003/10/EC on noise levels covering the protection of workers' health and safety. For the purposes of this Directive, the physical parameters used as risk predictors are defined as follows:
Daily noise exposure level is a time-weighted average of the noise exposure levels for a nominal eight-hour (8h) working day.
Weekly noise exposure level is a time-weighted average of the daily noise exposure levels for a nominal week of five eight-hour (8h) working days.

a. Protection is not recommended if the daily noise exposure level is below 80 dB.
b. Protection is required if the daily noise exposure level is above 85 dB and the company should initiate a program to reduce the sound level emission.
c. If the daily noise exposure level is between 80 and 85 dB, the company should offer individual protection to operators and test their hearing capacity annually.
d. The weekly noise exposure level as shown by adequate monitoring does not exceed the exposure limit value of 87 dB (Albayrak et al., 2020; Government gazette, 2013; Directive of the European Parliament and of the Council, 2003; Karabulut and Şahinoğlu, 2018; Józwik et al., 2018). Generally, the daily noise exposure level (85 dB) in the manufacturing industries is exceeded (Rech et al., 2017).

Vibrations that are occurred during machining lead to different effects such as deterioration of surface quality, reduction in tool life, a decrease of the rigidity of the machine, decrease of machine maintenance times, high-pitched sound noise affecting workers (Şahinoğlu et al., 2019; Siddhpura and Paurobally, 2012).

There is a strong relationship between sound and vibration occurred during machining processes (Şahinoğlu and Güllü, 2019). For example, in a turning process, cutting force, vibration, surface roughness, and sound level have increased in parallel with the increase in feed rate (Tekiner and Yeşilyurt, 2004). Namely, the machining process can be characterized by analyzing sound received during the cutting process (Seemuang et al., 2016).

Predicting production performance is difficult and time-consuming, especially for the machining process. Theoretical and empirical methods are widely utilized. Theoretical or experimental models have some problems. For example, theoretical results sometimes do not reflect the actual production process. Experimental models are valid only for the same situations. That's why, analytical models can be used to eliminate these problems (Shin et al., 2014). In addition to these findings, due to the complexity of computer numerical control (CNC) machines, it is difficult to achieve many parameters like cutting energy, power, and force with theoretical models. And they consume too much energy (Lv et al., 2015). By determining optimum cutting parameters, energy consumption, power consumption, sound level, and surface roughness can be minimized (Şahinoğlu and Ulas, 2020).

Recently, the statistical Design of Experiments (DOE) has been widely used in manufacturing research to develop, improve and optimize products and processes. Moreover, DOE methods like Full Factorial Design (FFD), Response Surface Methodology (RSM), and Taguchi Method (TM) have benefited in terms of cost and time (Selvamuthu and Das, 2018; Aggarwal et al., 2008).

When the present literature study considers, the main purpose of this thesis is to make investigations to minimize the power consumed during the machining process and greenhouse gases generated. This thesis aims to fill the gap in this subject by applying the studies listed below comprehensively:

i. Firstly, cylindrical steel materials with a diameter of 40 mm and a length of 250 mm AISI 4340 alloy were purchased. Later, these materials were subjected to heat treatment.

ii. After heat treatment, micro and macro hardness tests were carried out. Materials of approximately 30, 35, and 40 HRC hardness (Hardness with Rockwell C scale) were obtained.

iii. Tensile tests were performed to determine the mechanical properties of materials with different hardness.

iv. Then, metallographic analyses were performed with the help of Optical microscopes (OP) and Scanning Electron Microscope (SEM) devices.

v. Ceramic, carbide, and CBN (cubic boron nitride) inserts were supplied to compare the performance of different insert materials on the cutting process.

vi. A Response Surface Methodology (RSM) experiment design with 46 simulations was created to establish a connection between input variables and output variables. The orthogonal array has 5 factors (insert, hardness, cutting speed, feed rate, and depth of cut) and each of these factors has 3 levels. After the experiment design has been performed, turning operations on the CNC lathe were carried out to compare three different insert materials (ceramic, carbide, CBN). Also, it was compared materials that have three different hardness (30, 35, 40 HRC).

vii. After the experiment design has been performed, turning operations on the CNC lathe were carried out. Insert material, hardness of the material, cutting speed, feed rate, and depth of cut were taken as input variables. Power consumption, cutting forces, instantaneous current, sound level, and surface roughness were taken as output variables. Then mathematical models were developed for the prediction of output variables using regression analysis.

viii. After completing all the experiments prepared with RSM, the optimum cutting conditions for the output variables were established with the help of Signal to Noise (SN) ratios based on the Taguchi method. Also, Analysis of Variance (ANOVA) was applied to the experimental data to evaluate the contribution of input variables on the output variables.

ix. Finally, confirmation experiments were performed and a comparison was made between the experimental/calculated values and the predicted experiments. There are many ways to calculate the power consumed during machining. Another way to find the power consumption for machining is to calculate it by cutting force. Furthermore, to reduce time and cost spent in experimental studies, it was benefited from ABAQUS/Explicit Finite Element Method (FEM) software. So, the cutting forces were found with the ABAQUS/Explicit FEM software.

# 2. PREVIOUS STUDIES

The main objective of this study is based on the optimization of cutting parameters to minimize power consumption during machining using DOE methods. The study investigates effects of insert material, hardness of workpiece, cutting speed, depth of cut, and feed rate cutting parameters on power consumption, cutting forces, and current, sound, and surface roughness during the turning process of AISI 4340 alloy steels with different hardness. Also, to find cutting forces, it was benefited from ABAQUS/Explicit Finite Element Method (FEM) software. Some of the works related to the thesis subject are summarized the following:

## 2.1. Studies related to power consumption, cutting forces, sound, current, surface roughness, DOE, and FEM

Pervaiz et al. (2016) investigated energy consumed during turning of AISI 1045 material using uncoated tungsten carbide tool by DEFORM finite element software. They stated that energy used in the machining operation influences greenhouse gas emissions. Simulated cutting forces by DEFORM software were used to predict power and energy consumed in the cutting process. They calculated that $CO_2$ emissions decreased with increasing feed rate under the same conditions.

Li et al. (2016) presented a method for optimization of cutting parameters to evaluate energy efficiency using the Taguchi method, Response Surface Method, and Multi-Objective Particle Swarm optimization algorithm (MOPSO). They stated that as energy resources and environmental problems are becoming more and more serious, solutions should be sought to reduce the energy consumption of machine tools. However, they noted that significant energy savings will be achieved by selecting optimal cutting parameters. Specific energy consumption has been chosen to assess the energy efficiency of the milling process. They used AISI 1045 steel as a workpiece and high-speed steel as an end milling cutter. As a result, they revealed that using sustainable optimization methods has benefits such as energy savings and production efficiency.

Li et al. (2015) investigated the energy consumption of machining manufacturing systems. They state that energy consumption in machining systems is getting more and more attention due to global climate change and production sustainability. For this purpose, they reported that energy flow of energy consumption in machining manufacturing systems has three layers involving machine tool layer, task layer, and auxiliary production layer. Energy consumers of machine tools can be classified into three categories: constant (fan motors, servos, and cool pump, etc.), variable (spindle motors and feed motors, etc.), and cutting power.

Zhang et al. (2013) proposed a methodology for estimating the power consumption of numerically controlled machining. They noted that they studied the energy consumption (EC) of the production system due to insufficient energy supply during production and low energy efficiency. This methodology consists of four stages. These are machine tool energy consumption (MTEC) database, numerical control (NC) code analyzer, virtual cutting simulator, and MTEC calculator. The energy model was tested on a milling center to predict the power consumed using a carbide end mill. They reported that the error between the estimated EC and the measured energy was 11,3%.

Meng et al. (2016) studied the estimation of power consumption during the turning process using the DOE method. They stated that different manufacturers have been forced to reduce their energy consumption due to high energy costs, increasing production demands, and environmental problems. To optimize processing parameters and thus ensure precise energy consumption, the experiments were carried out using the Full Factorial experiment design method. 45 steel as workpiece and carbide as the insert was used in the turning process.

Rawat and Potdar (2014) presented a review on the optimization of cutting parameters by the Taguchi method in machining. They stated that the Taguchi method is a powerful statistical approach for the optimization of process parameters. The influence of process factors and optimum cutting conditions can be determined from the Signal-to-Noise ratio plots. In addition, it is possible to obtain reliable results by decreasing the number of tests with the Taguchi method. And so the experimental cost is reduced. They observed that generally, the researchers used the cutting speed, feed rate, and depth of cut as input parameters. Few researchers evaluated nose radius, tool material, and hardness as input parameters. The output parameters were taken cutting force, surface roughness, material removal rate, tool wear, environmental impact, power consumption, and machinability.

Dahmus and Gutowski (2004) investigated the environmental analysis of machining. They stated that the power required during the operation of the machine tools is supplied from the electricity grid. For this reason, the material removal process should be performed considering the electrical energy consumption. Because electrical energy is provided by coal, nuclear, and natural gas. As a result, it causes emissions of mercury, chromium, and lead materials.

Özdemir et al. (2020) studied the analysis of surface roughness and cutting forces performed during hard turning of 42CrMo4 material with 52 HRC. They took advantage of the Taguchi method and RSM. They used parameters that were cutting speeds (200, 250, 300 m/min), feed rates (0,05; 0,1; 0,15 mm/rev), depths of cut (0,1; 0,25; 0,4 mm), and tool nose radiuses (0,8; 1,2 mm). The most important parameters were determined to be depth of cut and feed rate according to ANOVA.

Özdemir (2019) studied the effect of cutting parameters on surface roughness with helping RSM. He used cutting speed, feed rate, depth of cut, tool nose radius as independent variables, and surface roughness as a dependent variable during the turning of C45 material. He found that the most important parameters on surface roughness were feed rate and tool nose radius. It was determined that the surface roughness value increased as the feed rate increased, but decreased as the tool nose radius increased.

Frigieri et al. (2017) investigated the correlation between sound intensity and machining parameters during the turning of AISI 52100 steel material that had hardness between 49 and 52 HRC. The linear relationship between sound and machining parameters has been commented on with Pearson correlation analysis. They stated that there were strong correlations.

Gok et al. (2012) studied the correlation between surface roughness and Acoustic Sound Pressure (ASP) occurring during milling of EN X40CrMoV5-1 material. Experiment results showed that there is a rise of surface roughness with rising of acoustic sound pressure. They stated that surface roughness could be formed out with acoustic sound pressure levels.

Garg et al. (2017) conducted an experimental study on optimization of cutting parameters to minimize power consumption during turning of AISI 6061 Aluminum material. They found a sufficient relationship between power consumption and cutting parameters (cutting speed, feed rate, depth of cut) using ANOVA. With the help of the RSM optimization technique, a model has been developed that can be used in the industry to ensure the minimum power consumption of machine tools.

Warsi et al. (2017) studied the effect on energy consumption of different cutting parameters (feed rate and cutting speed) during machining of Al 6061-T6 alloy. It was found important relation between specific cutting energy consumption and cutting conditions. They stated that SCE decreased with the choosing of suitable cutting parameters. For example, the feed rate was found to be the strongest parameter, and SCE consumption decreased as the feed rate increased.

Velchev et al. (2014) studied the optimization of cutting parameters for minimizing energy consumption during turning of steel 40X material. They reported that effects of insert grade, feed rate, and depth of cut parameters on the minimum energy consumption have been found. It has been determined that lesser energy is consumed when the maximum possible feed rate and cutting depth values were chosen under the machining conditions.

Anderberg and Kara (2009) compared energy and cost efficiency in CNC machining. They stated that if production efficiency was be improved through optimization of process parameters, cost, and energy savings could be achieved.

Zhao et al. (2017) classified energy consumption in machining as a process, machine, and system-level as shown in Figure 2.1. They noted that consumed energy during machining comprises an important portion of the cost of production and has a large impact on the environment. Energy-saving could be provided with optimization of machining parameters, shorten of the transition phase of the machine tool's spindle, optimization of the energy components of the machine tool such as spindle motor transmission system, and improvement of peripheral equipment such as coolant pumps.

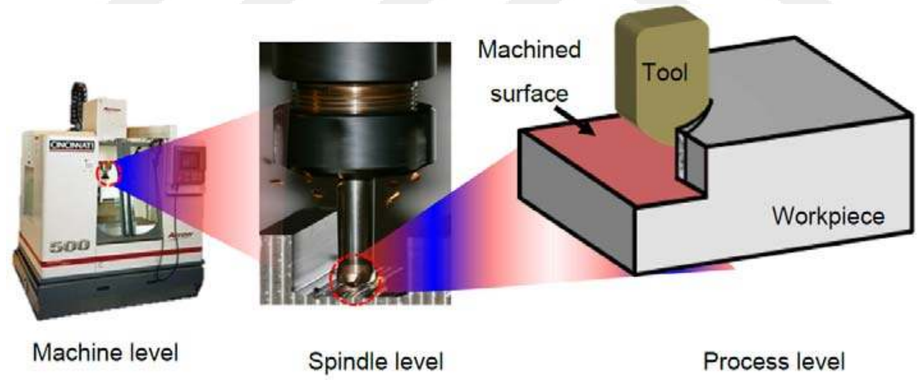

Figure 2.1. Energy consumption levels

Pawanr et al. (2021) investigated the modeling of variable energy consumption for CNC machine tools. They stated that machining is a common process in manufacturing industries. It also consumes a significant amount of energy and causes negative environmental effects. An experimental model was generated between cutting parameters and energy consumed during the turning process using Response Surface Methodology. It is seen that there was a strong relationship between cutting parameters and energy consumed. They reported that the developed model would predict energy consumption with 94,70% accuracy.

Wirtz et al. (2019) studied the electric power consumption of machine tools. Energy efficiency became more and more important owing to increasing energy costs and consumption in manufacturing industries. Thus, an empirical approach to determine the power consumption of machine tools developed and they take advantage of the Kienzle method to calculate cutting forces that occurred in the milling process. They stated that experimental measurements and predicted results of cutting power occurring in the finishing milling process presented a good concordance.

Cui et al. (2019) evaluated specific cutting energy considering the impacts of tool geometry during the micro-milling process of AerMet100 material. Power consumptions were measured using a power analysis system including voltage sensor and current sensor. They stated that cutting tool geometry during the cutting process has a notable effect on the consumption of SCE. That is, the more chips the cutting tool removes during the cutting process, the lower the SCE consumption. And, they stated that the need for energy in the manufacturing industry could be achieved by optimizing cutting conditions.

Khanna et al. (2020) investigated tool wear, energy consumption, and surface roughness during the turning of Inconel 718. They stated that energy consumption, chip reduction coefficient, and surface roughness are machinability indicators related to the industry. Furthermore, energy consumption changes markedly depending on input process parameters (cutting speed, feed rate, depth of cut, etc.) and cutting conditions (dry turning, wet turning, cryogenic turning, etc.).

Akkuş and Yaka (2021) investigated as experimental and statistical the effect of cutting parameters on surface roughness, vibration, and energy consumption in turning of 6Al-4V ELI titanium alloy. They were benefited from Taguchi method, ANOVA analysis, and Pareto analysis to detect suitable cutting conditions. It was determined that the most powerful parameter in surface roughness, vibration, and energy consumption was feed rate.

Li et al. (2017) investigated the energy performance development of CNC machining. They stated that CNC machining consumes a significant amount of energy in industrial production. It is among the most important production methods. Strategies shown in Figure 2.2 can be suggested to develop the energy efficiency of CNC machining.

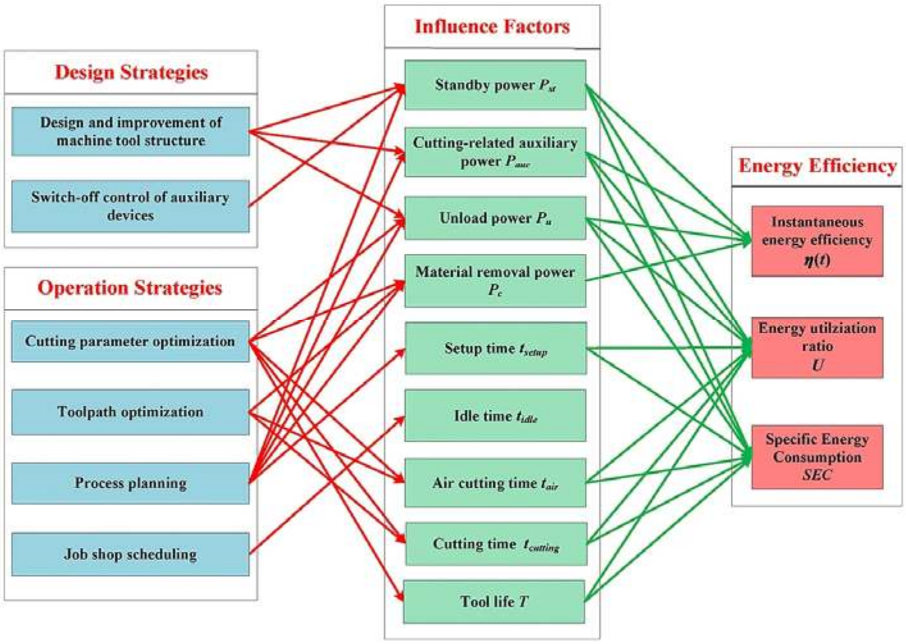


Figure 2.2. Strategies for energy efficiency

Shoba et al. (2018) investigated surface roughness, power consumption, material removal rate, and tool wear while hybrid composite materials are turned. Power consumption was calculated by taking the cutting force. They reported that power consumption increased with cutting speed, feed rate, and depth of cut.

Arrazola (2011) studied finite element modeling and simulation. The finite element method can present support for experimental, mechanical, or analytical approaches to construct the machining process. He noted that the material removal process can be simulated in a computer environment with the help of FEM without an experimental process. In this way, problems that may arise during actual machining operations can be reduced or eliminated.

Nur et al. (2015) studied effects on cutting force, surface roughness, power consumption, and tool life of machining parameters while AISI 316L stainless steel is dry turned using coated carbide tools. The design of the experiments was created with RSM and then the results were evaluated by ANOVA. It has been found that the parameters of feed rate and cutting speed are effective on power consumption. Therefore, they noted that power consumption is a notable factor in sustainable production.

LMalghan et al. (2018) studied the effects of machining parameters on the responses like cutting force, surface roughness, and power consumption using RSM and particle swarm optimization during milling of AA6061material. They showed that cutting force and power consumption increased as spindle speed, feed speed, and cutting depth increased. Out of these, surface roughness value decreased while spindle speed increased.

Phate and Tatwawadi (2015) studied mathematical modeling of MRR and power consumption while dry turning of ferrous material was conducted using dimensional analysis. They reported that MRR and power consumption dimensional analysis models reveal that the feed rate is the most significant variable in determining surface roughness value. A researcher can choose the best combination of design variables with the model equations created for providing optimum MRR and power consumption. Most notably, this will improve productivity.

Kaladhar (2020) studied modeling and optimization of surface roughness and tool flank wear in turning of AISI 4340 steel utilizing TiSiN-TiAlN nanolaminate coated insert. Parameters were evaluated by Taguchi method, RSM, Pareto diagram, ANOVA, and Tukey's test. He reported that the most significant factor is feed rate for good surface finish and cutting speed for tool wear.

Ahilan et al. (2013) worked on intelligent hybrid decision-making tools to model and estimate machining characteristics in the CNC lathe process. They used AISI 304 stainless steel with 70 HRC hardness, different machining parameters (cutting speed, feed rate, depth of cut, nose radius), and carbide inserts. They stated that the most critical factor for power consumption is the cutting speed, the depth of cut, feed rate, and nose radius (in the order of importance), respectively. Feed rate was important for surface roughness.

Lv et al. (2020) investigated modeling of energy consumption of machine tool mechanism. They stated that machine tool energy consumption has been a research topic in the international manufacturing industry. Energy-saving must be provided. To achieve this, an energy consumption model of the machining process must first be created. The definition of machine state according to the international organization for standardization and the actual basic structure of machine tools, the machining process can be divided into states including starting, standby, no-load, load, and closed as shown in Figure 2.3. They reported that the method used with integrated mechanisms and data is suitable for grinding and other types of machine tools. A more sensitive mathematical model could be created for future energy consumption.

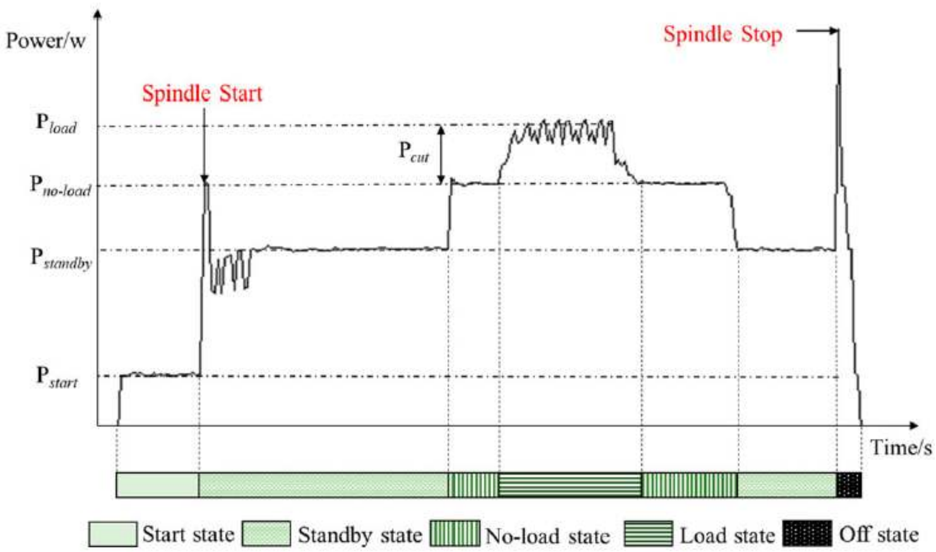


Figure 2.3. Power flow of machine tool machining process ($P_{start}$: start state power, $P_{standby}$: standby state power, $P_{no-load}$: no-load state power, $P_{load}$: load state power)

Kambagowni et al. (2018) investigated the effect on surface roughness of different material hardness during hard turning using AISI 4340 alloy steel. They planned experiments based on RSM and conducted a turning process on materials at 45, 50, and 55 HRC with ceramic cutting inserts. They stated that feed rate has the most significant parameter for surface roughness and typically, surface roughness decrease as hardness increase.

Kumar et al. (2020) investigated influences of cutting conditions, tool geometry, material hardness (45, 50, 55 HRC) on surface roughness, and cutting forces of AISI H13 material using CBN inserts. They noticed that surface roughness and cutting forces were affected by work material hardness. The result that the higher work material hardness produced the higher cutting forces and better surface roughness shows.

He et al. (2012) studied the energy consumption of numerical control machining. They stated that carbon dioxide emissions are directly related to the manufacturing industry and machining is one of the fundamental manufacturing technologies. Also, the energy-consuming components of NC (numerical control) machine tools generally consist of spindle speed, axis feed, servos system, tool change system, and other auxiliary equipment such as coolant pump and fans. Thus, the energy consumption of machine tools and their machining processes must be considered for reducing energy consumption in the industry.

Bagci (2011) investigated the effects of cutting conditions using acoustic sound pressure levels in milling. He stated that machining sound pressure levels increased with the increase of feed rate, cutting force, and cutting tool deflection. Also, he presented that a powerful, positive, and linear relationship was observed among feed rate, sound pressure level, and tool deflection.

Kumar et al. (2021) investigated energy efficiency in finish turning of EN 353 alloy steel material. They stated that first of all, Taguchi method was used to optimize energy efficiency. Then ANOVA was used to find important variables influencing energy efficiency. Finally, an experimental model was obtained using RSM. They reported that there is a 78,92% improvement in energy efficiency when finish turning settings utilized in industries compared.

Luan et al. (2016) founded optimal cutting parameters with the help of RSM and ANOVA methods to reduce power consumption in face milling of cast iron alloy. Results indicated that higher power consumption becomes while depth of cut and cutting speed was at a higher value. They indicate that power consumption could be saved under the optimized cutting condition and at the same time, surface quality could be better.

Gürbüz and Gönülaçar (2020) investigated effects of dry and Minimum Quantity Lubricating (MQL) properties on machinability of AISI 4140 using Taguchi and ANOVA methods. According to SN ratios, MQL than dry machining had a more significant influence on cutting force and surface roughness. ANOVA results demonstrated that feed rate was the most influential on cutting force and surface roughness. Finally, they reported that the Taguchi was a highly achieved method in the optimization of variables.

Negrete et al. (2015) analyzed by Taguchi method effect of cutting parameters to reduce energy consumption in turning of AISI 1018 steel. It was stated that feed rate and depth of cut were the most influential parameters on energy consumption. They reported that as the depth of cut increased, the force value needed to remove the material increased, and therefore the system had to expend more energy.

In the work presented by Sangwan and Kant (2017), optimization of machining parameters for developing energy efficiency was studied using RSM and genetic algorithm approach. They were revealed that power consumption increased with the rise in cutting parameters during the turning of AISI 1045 steel with a tungsten carbide tool. It was found that depth of cut had more impact on power consumption against cutting speed and feed rate. Also, generated optimal data would be helpful for the industry during the selection of machine tools to provide needed power consumption.

Frifita et al. (2020) studied the effects of machining parameters to generate surface roughness, cutting force and power, specific energy, and maximum productivity in turning of Inconel 718 material. They stated that according to ANOVA method, the most important factor affecting surface quality and cutting forces was nose radius. Moreover, developed mathematical models by RSM showed close prediction values.

The aim of the work published by Khanna et al. (2019) was to optimize power consumption and surface roughness in ultrasonic-assisted turning of Nimonic-90 with the aid of Taguchi and ANOVA methods. It has been seen that feed rate was the major factor affecting surface roughness values whereas cutting speed was the most significant for power consumption.

The aim of the work published by Anand et al. (2016) is to investigate the optimization of machining parameters for green manufacturing. They mentioned that developed and developing countries continue to expand over time. This leads to higher energy use and consequently, it causes higher $CO_2$ emissions. They stated that corrective measures must be taken to reduce the energy consumption of the manufacturing industry. Here, studies were laid particularly on the turning operation to optimize cutting parameters. They reported that all the values show an appreciable reduction in energy consumption.

Kuntoğlu et al. (2021) investigated the optimization of cutting forces and MRR via Taguchi and RSM methods in the turning of AISI 5140. They noted that optimization was one of the significant approaches to solve many problems and had many advantages. For example, it provided a reduction in costs and contribution to productivity.

Khan et al. (2019) investigated energy consumption, tool wear, and surface roughness in turning Titanium alloy under dry, wet, and cryogenic conditions. Cutting speed had contributed at a high rate towards specific cutting energy and surface roughness was significantly influenced by feed rate. Finally, they presented that reduction in energy consumption could be achieved by the use of generated optimum machining parameters.

Panda et al. (2019) analyzed surface roughness with the aid of RSM in hard turning of AISI 4340 steel with a ceramic tool. From analysis results, it was shown that feed rate was the most significant contribution to surface roughness. With the rise in feed rate, surface roughness increased; but it decreased with the rise of cutting speed. They stated that generated results by the developed model have been perfectly in conformity with responses.

Kechagias et al. (2019) used Taguchi Experimental Design (TED) and Full Factorial Design for the machinability of material in turning titanium alloy. They stated that cutting force and surface roughness was selected as the output machinability parameters and spindle speed, feed rate, depth of cut as input cutting variables. According to FFD and TED, the most important parameter for Ra is the feed rate, and the least important parameter is the cutting depth. Speed does not have any important effect and the most important cutting parameters that affect cutting force (Fc) are depth of cut and feed rate. They reported that TED and FFD methodologies could apply to machinability studies.

The work presented by Sarıkaya and Güllü (2014) investigated the analysis of machining parameters via Taguchi method and RSM in turning of AISI 1050 steel by using minimum Quantity Lubrication System (MQL). Their findings indicated that the most influential parameters were feed rate and MQL on the surface roughness. Finally, they showed that the developed mathematical models through RSM could be used because there was a high correlation between the experimental value and predicted value.

Ng and Aspinwall (2002) investigated the effect of different workpiece hardness (28, 35, 42, 49 HRC) and cutting speed on machinability of AISI H13 steel when polycrystalline cubic boron nitride (PCBN) tool was used. Cutting forces were generated lower when machining was executed at a higher cutting speed. They stated that this could be explained by forming sufficient high heat in the shear zone to plasticize workpiece material. In other words, a decrease in the strength of the workpiece was happened by producing high heat during machining. Shear angle increased as workpiece hardness value risen, but values of cutting force failed between 35 and 49 HRC. They reported that higher shear angle was associated with lower cutting forces.

Abbas et al. (2021) studied the effect of different cooling strategies on surface quality and power consumption in the milling of 316 stainless steel. They reported that power consumption was determined to increase with increasing cutting speed and feed rate, and the effect of cutting speed was higher than that occurred by feed rate at whole coolant types. At the end of experiments, the influence of feed rate on power consumption was detected neglectable at dry conditions.

Nur et al. (2021) investigated energy consumption via RSM and ANOVA method during the turning of AISI 420 hardened stainless steel. They stated that reduction of energy consumption during machining of metal materials was all-important in sustainable production. They showed that lower machining energy could be obtained by taking a higher feed rate (f) and higher cutting speed (v).

# 3. MATERIAL AND METHODS

## 3.1. Material

AISI 4340 high strength alloy steel is supplied in the form of a cylindrical extruded bar of 40 mm diameter and length of 250 mm as shown in Figure 3.1. Its chemical composition and physical properties are given in Table 3.1, Table 3.2, respectively. Chemical analysis was executed using Thermo Scientific ARL PERFORM'X XRF Sequential X-Ray Fluorescence Spectrometer in Yozgat Bozok University Science and Technology Application and Research Centre, Yozgat/TURKEY as indicated in Figure 3.2.


Figure 3.1. Photos of AISI 4340 steel test material; a) Front view, b) Side view

Table 3.1. Chemical composition of AISI 4340 alloy steel used in this study

| Elements | Content (% of weight) |
|---|---|
| Fe | 95,1700 |
| Cr | 1,58000 |
| Ni | 1,48000 |
| Mn | 0,58700 |
| C | 0,34780 |
| Mo | 0,18800 |
| Si | 0,17900 |
| Cu | 0,17700 |
| Al | 0,07460 |
| Ca | 0,04990 |
| Co | 0,04940 |
| Mg | 0,04450 |
| P | 0,02230 |
| Others | 0,05050 |

Table 3.2. Physical properties of AISI 4340 alloy steel used in this study (Alimardani et al., 2010; Khatir et al., 2021; Elsheikh et al., 2021)

| | |
|---|---|
| **Density, kg/m3** | 7850 |
| **Melting temperature, K** | 1695 |
| **Specific heat capacity, J/kgK** | 475 |
| **Modulus of elasticity, GPa** | 205 |
| **Bulk modulus, GPa** | 140 |
| **Poisson's ratio** | 0,29 |
| **Shear modulus, GPa** | 80 |
| **Thermal conductivity, W/mK** | 44,5 |
| **Coefficient of thermal expansion, μm/mK** | 12,3 |
| **Latent heat, J/kg** | 272000 |
| **Electrical conductivity, S/m** | 4,032×106 |
| **Relative permittivity, -** | 1 |
| **Relative permeability, -** | 1 |


Figure 3.2. Thermo Scientific ARL PERFORM'X XRF Sequential X-Ray Fluorescence Spectrometer used for material analysis in this study

Firstly, cylindrical bars with a diameter of 40 mm and a length of 250 mm were normalized to improve ductility and toughness properties and also to eliminate dendritic segregation that could remain from the casting process. The specimens were normalized, quenched, and tempered in Metalurji Akdağ Heat Treatment Limited Company (Ankara/Turkey), respectively. To this end, materials were annealed at 840 ºC for 1,5 h (hours) utilizing atmosphere controlled furnace and then cooled in still air at ambient temperature (about 20 ºC and 5 hours) as shown in Figure 3.3. Thus, the hardness of the specimens reached 38±1 HRC.

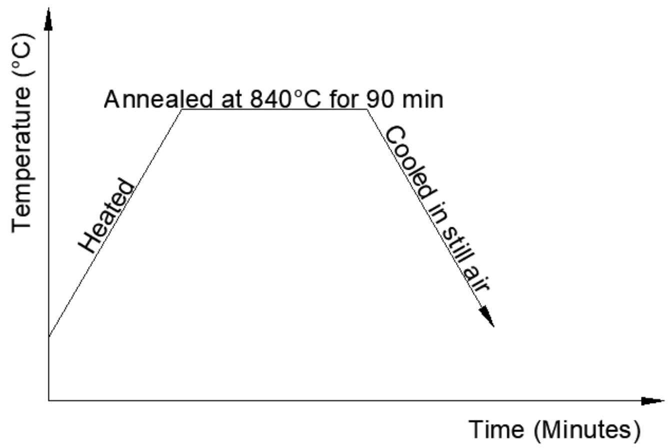


Figure 3.3. Heat cycle of normalizing of AISI 4340 steel

Then the samples were austenitized at 860 ºC for 90 min (minutes) utilizing atmosphere controlled furnace to obtain different quenched and tempered martensite structures. After this, it was left to cool in oil (about 20 ºC and 5 hours). Hence the hardness of the specimens reached 55±1 HRC. Finally, the specimens were kept constant at 510 ºC, 560 ºC, and 610 ºC for 1,5 h utilizing a tempering furnace to perform a quenched martensite structure, respectively. Also, the furnace temperature was increased at a heating rate of 70-75 °C/h. All other specimens cooled in still air at ambient temperature (about 20 ºC and 5 hours). As a result of this, specimens with 40±1 HRC, 35±1 HRC, and 30±1 HRC hardness were obtained, respectively. Schematic illustration of heat cycle for quenching and tempering of AISI 4340 steel is given in Figure 3.4.

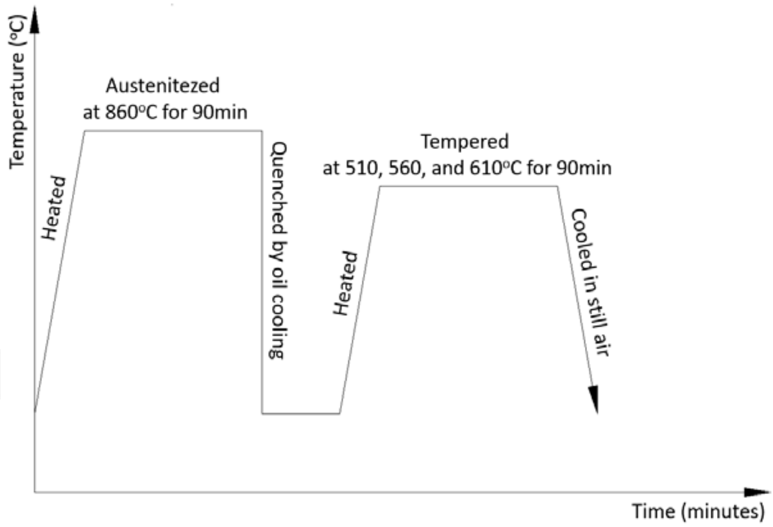


Figure 3.4. The heat cycle of quenching and tempering of AISI 4340 steel used in this study

**3.2. Micro Hardness Test**

Vickers Microhardness test was used to describe fine-scale changes in hardness. Vickers Microhardness tests were completed using Metkon MH3 microhardness tester as shown in Figure 3.5. The microhardness tests were conducted according to ASTM E92 with 100 g load with a duration time of 15 seconds (ASTM standard: E92-82, 2004).

Figure 3.5. Metkon MH3 microhardness tester used in this study


Figure 3.6. FEI Quanta FEG 450 including Field Emission Gun-Scanning Electron Microscope with Environmental Scanning Electron Microscope (ESEM) used for the imageVickerskers hardness specimens in this study

The images of micro-Vickers indents were observed by using FEI Quanta FEG 450 operating with Field Emission Gun (FEG)-Scanning Electron Microscope (SEM) in Yozgat Bozok University Science and Technology Application and Research Center, Yozgat/TURKEY as shown in Figure 3.6. SEM images belonging to the different magnification of the micro-Vickers hardness indents are shown in Figure 3.7.

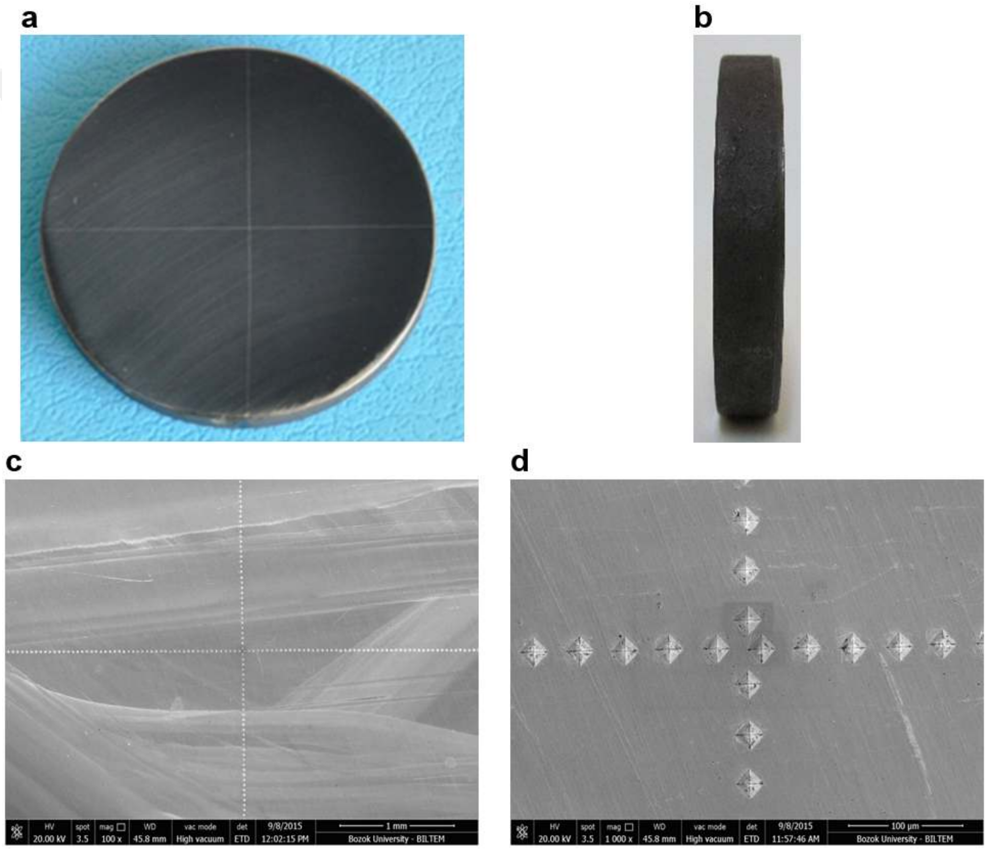


Figure 3.7. SEM images belonging to the different magnification of Vickers Microhardness indents the of the cylindrical specimen with the size of Ø40x10mm; a) Photo of front view, b) Photo of side view, c) 100X magnification, d) 1000X magnification

Vickers microhardness mean values for AISI 4340 steel specimens tempered at different temperatures are shown in Figures 3.8-3.10.

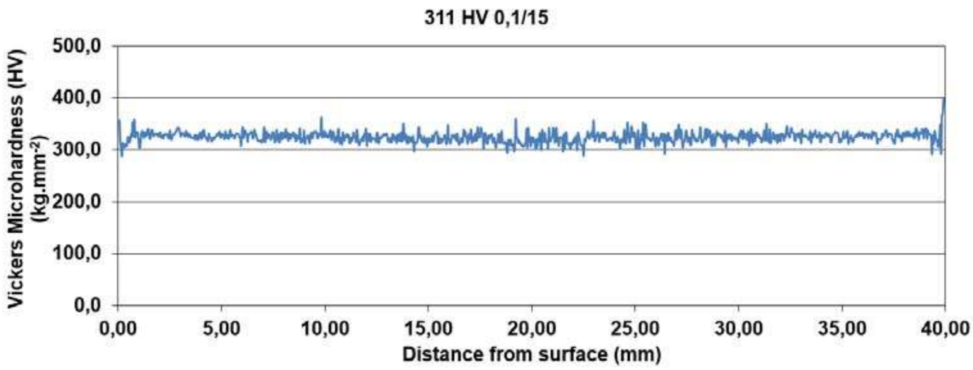


Figure 3.8. Vickers microhardness mean values for AISI 4340 steel specimens tempered at 610°C (for material with 30 HRC)

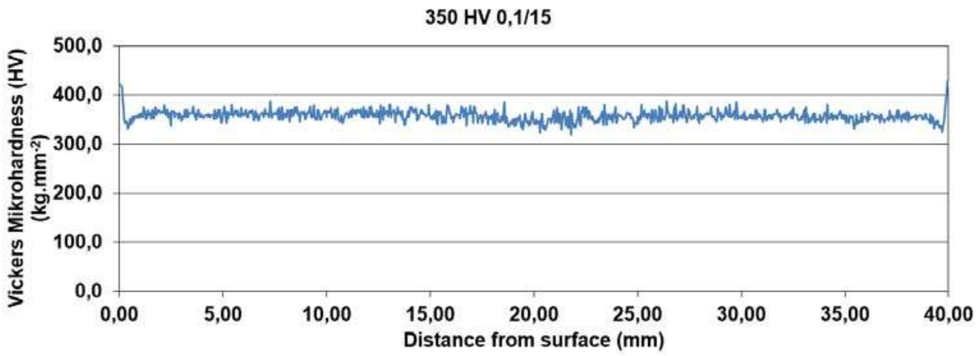


Figure 3.9. Vickers microhardness mean values for AISI 4340 steel specimens tempered at 560°C (for material with 35 HRC)

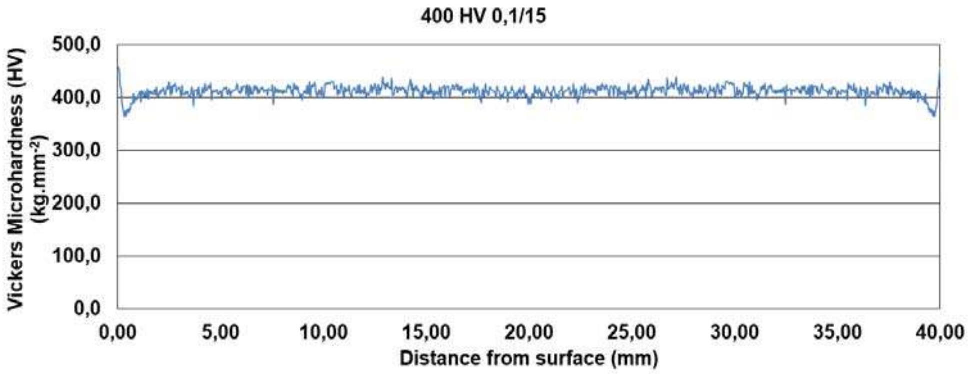


Figure 3.10. Vickers microhardness mean values for AISI 4340 steel specimens tempered at 510$^{o}$C (for material with 40 HRC)

### 3.3. Macro Hardness Test

Macro hardness tests were performed on a Rockwell C (HRC) scale. Rockwell hardness tests were carried out using BMS 200-RB Analog Rockwell & Brinell Hardness Tester according to ASTM E18 with a load of 150 kg and a load time of 15 seconds (ASTM standard: E18-15, 2015). BMS 200-RB Analog Rockwell & Brinell Hardness Tester is shown in Figure 3.11. Photo of Rockwell hardness indents of specimens with 30±1 HRC is shown in Figure 3.12. The mean hardness value was measured around 30±1, 35±1, 40±1 HRC, and a uniform microstructure is seen as shown Figure 3.13. Also, the surface hardness of the product not heat-treated was found about 15 HRC.

Figure 3.11. BMS 200-RB Analog Rockwell & Brinell Hardness Tester used in this study

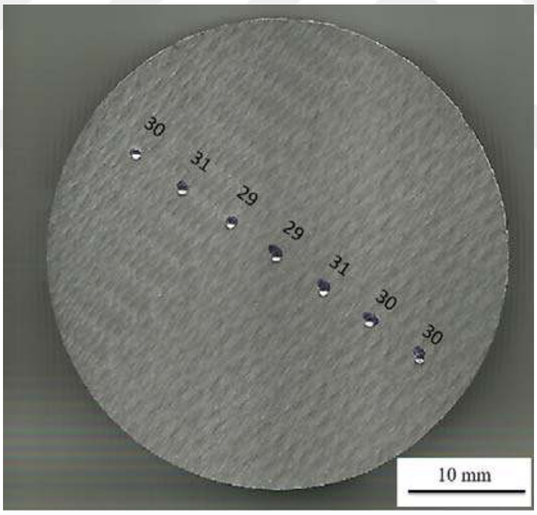


Figure 3.12. HRC image of the cylindrical specimen with 30±1 HRC

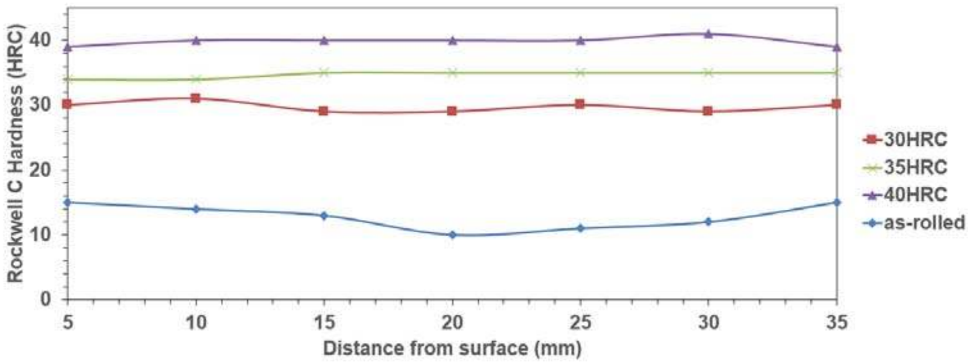


Figure 3.13. Mean hardness values measured in Rockwell C scale HRC (Note: The term as-rolled condition stems from the fact that the product is not heat-treated)

As shown in Figure 3.7 and Figure 3.12, it was found that there was no significant difference between the sizes of micro and macro indents when the sizes of the indents of the specimens were compared separately. In other words, it has been observed that the samples have a uniform microstructure after heat treatment.

### 3.4. X-Ray Diffraction (XRD) Analysis

Firstly, the surface of the specimen was ground by using 120, 320, 500, 1000 SiC grinding papers gradually. Then the ground specimens were polished with 3, 1, and 0,25 µm diamond suspension gradually as shown in Figure 3.14.

Figure 3.14. Photos of specimens used in this study for crystalline phase analysis; a) Front view of specimen, b) Side view of the specimen

PANalytical Empyrean X-ray diffractometer shown in Figure 3.15 was used to measure the pattern of the specimens in Yozgat Bozok University Science and Technology Application and Research Center (Yozgat/TURKEY). To identify the existing phases in the microstructure, specimens were characterized through X-ray diffraction analysis with Cu Kα radiation (wave-length of $\lambda$=1,54060 Å) in a 2θ range from 40º to 105º generated at 45 kV, 40 mA and data was collected at every 0,01º interval.


Figure 3.15. PANalytical Empyrean X-ray diffractometer used in the study

The XRD plots of the AISI 4340 steel are shown in Figures 3.16-3.18. Ferrite (α-Fe), martensite, and cementite ($Fe_3C$) phases were identified from the XRD patterns. No retained austenite was observed in the XRD patterns.

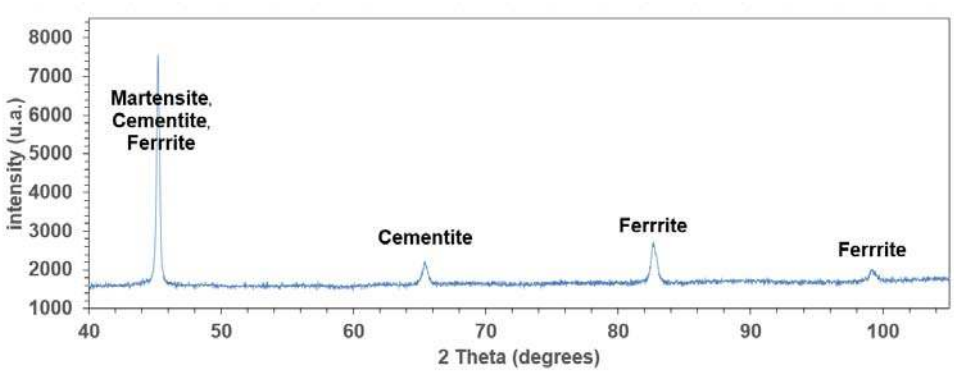


Figure 3.16. X-ray diffraction patterns from the surface of the specimen tempered at 610 ºC (for material with 30 HRC)

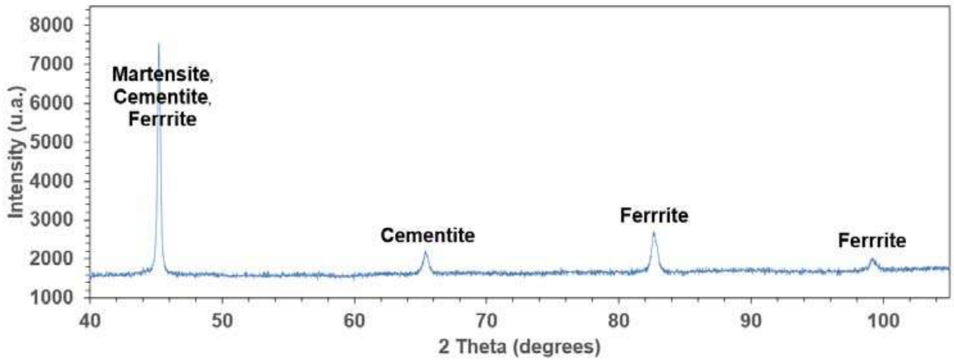


Figure 3.17. X-ray diffraction patterns from the surface of the specimen tempered at 560 $^{o}$C (for material with 35 HRC)

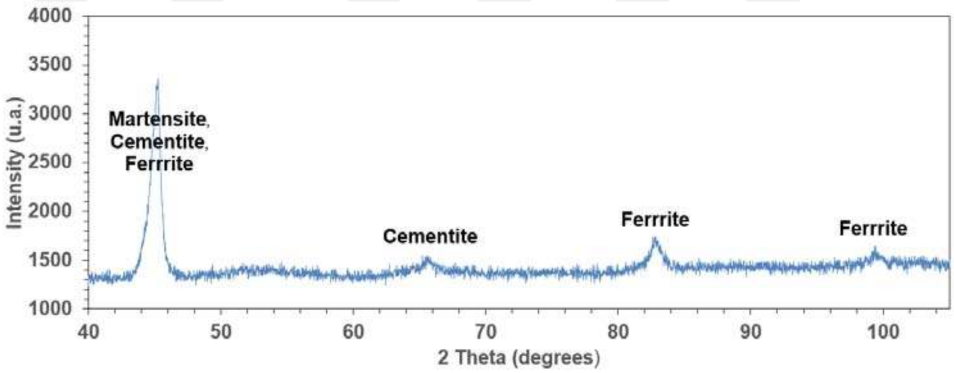


Figure 3.18. X-ray diffraction patterns from the surface of the specimen tempered at 510 $^{o}$C (for material with 40 HRC)

### 3.5. Metallographic Analysis

The polished specimens were etched using Nital solution that is a combination of nitric acid and ethanol. Nital etching (2cc $HNO_3$ + 98cc Ethyl alcohol) was prepared according to ASTM standard (ASTM standard: E407-99, 1999). Nital etching was conducted by immersing the specimen face in the glass container for 10-15 seconds. After Nital exposure, the specimen was immediately washed with water to cease the etching reaction.

Micrograph images of each specimen were taken by FEI Quanta FEG 450 operating with Field Emission Gun (FEG)-Scanning Electron Microscope (SEM) in Yozgat Bozok University Science and Technology Application and Research Center (Yozgat/TURKEY). Micrographs were revealed at magnifications of 10,00 KX for every specimen. As mentioned above, AISI 4340 steel is widely used for rod and shaft parts that require high strength and toughness. To this end, to create very good mechanical properties, specimens must be subjected to a heat treatment for quenching and tempering. As shown in Figures 3.19-3.21, it was observed that the microstructure of the tempered specimens was martensite, ferrite, and cementite. The results are similar to the literature (Lianget et al., 2020; Saeidi and Ekrami, 2009).

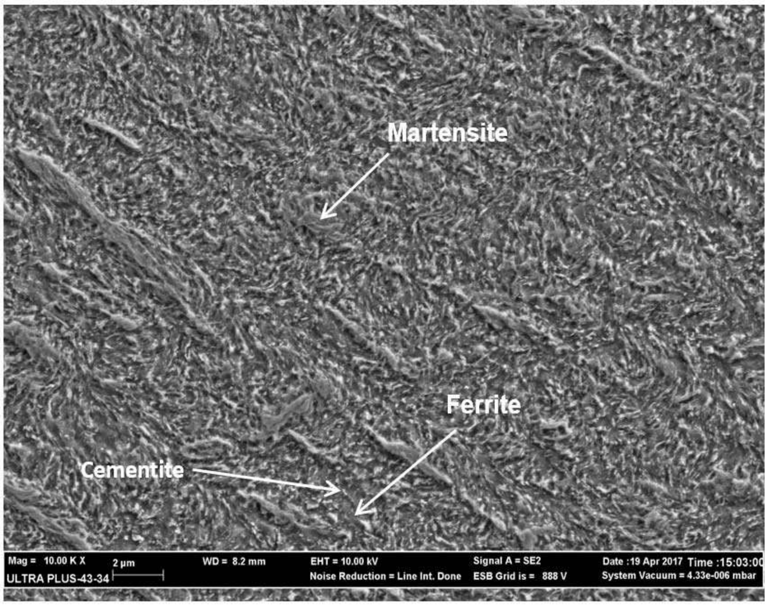


Figure 3.19. SEM image of a specimen of tempered at 610 °C

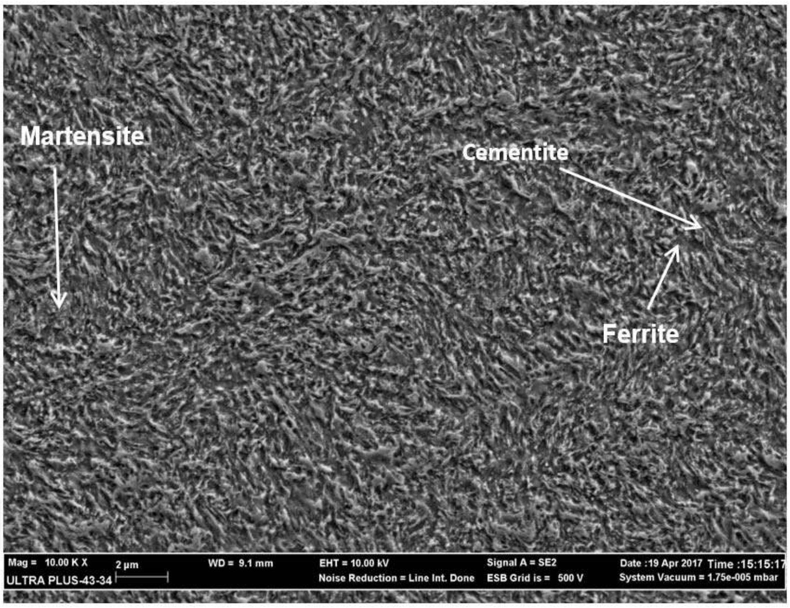


Figure 3.20. SEM image of a specimen tempered at 560 ºC

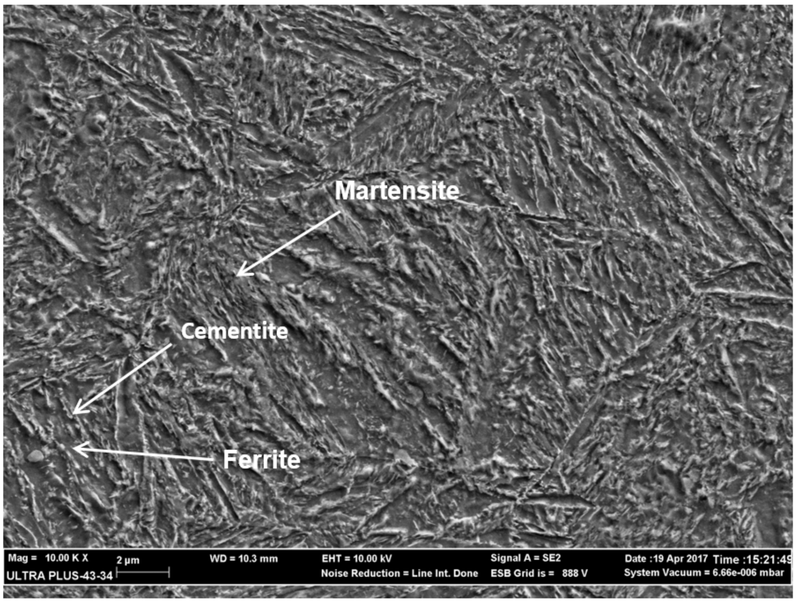


Figure 3.21. SEM image of a specimen of tempered at 510 ºC

**3.6. Tensile Test Analysis**

The tensile test is one of the most common types of mechanical tests used to characterize the mechanical behavior of engineering material. Tensile test of AISI 4340 alloy steel was conducted by using a digitally-controlled servo-hydraulic DARTEC tensile test machine with a 600 kN tensile and compressive force in Gazi University Department of Mechanical Engineering Mechanical-Strength Laboratory (Ankara/TURKEY). In this test, a specimen was prepared suitable for gripping into the jaws of the testing machine type. The experimental setup is shown in Figure 3.22.

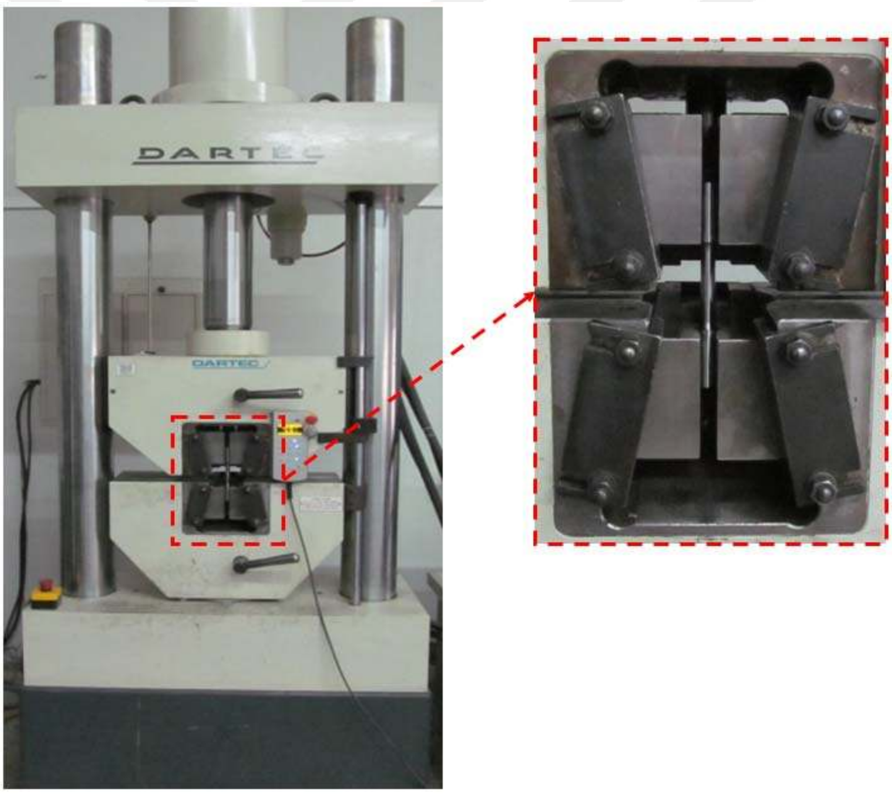


Figure 3.22. Experimental setup of the tensile test machine

Tensile tests were performed by the information ASTM standard (ASTM standard: E8/E8M-09, 2009). The test specimens were produced in the form of cylindrical with 75 mm reduced section length, 62,5 mm thickness length, and 12,5 mm inner diameter. The tests were carried out quasi-static at room temperature. The test speed was set at 0,05 mm·s$^{-1}$. The results revealed that a ductile fracture happens. Also, the photos and schematic of the technical drawing tensile specimen are shown in Figure 3.23.

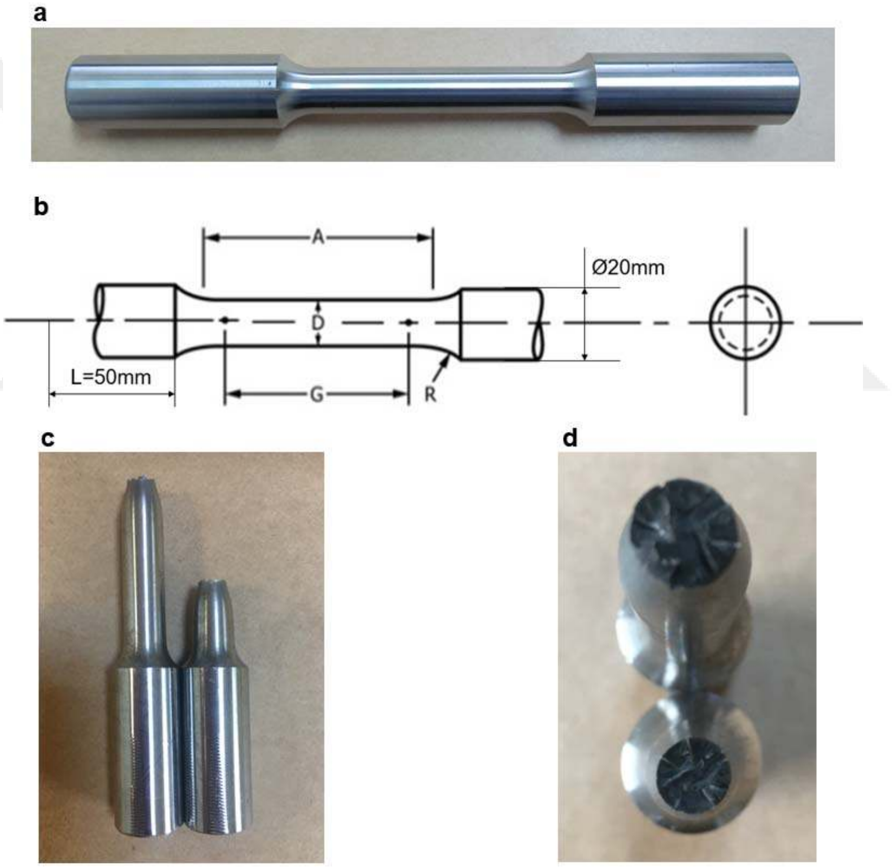


Figure 3.23. Photos and schematic of technical drawing tensile specimen; a) Machined, b) Technical drawing G—Gage length (62,5 ± 0,1 mm), D—Diameter (12,5 ± 0,2 mm), R—Radius of fillet (10 mm), A—Length of reduced section (75 mm), c) Front view of broken tensile specimen, d) Broken surfaces of tensile specimen

Elastic modulus obtained from the tensile test is 202 MPa. As shown in Figure 3.24, ultimate tensile strength (UTS), yield strength (YS), and rupture strength (RS) increased, and elongation of rupture reduced while hardness value is increased.

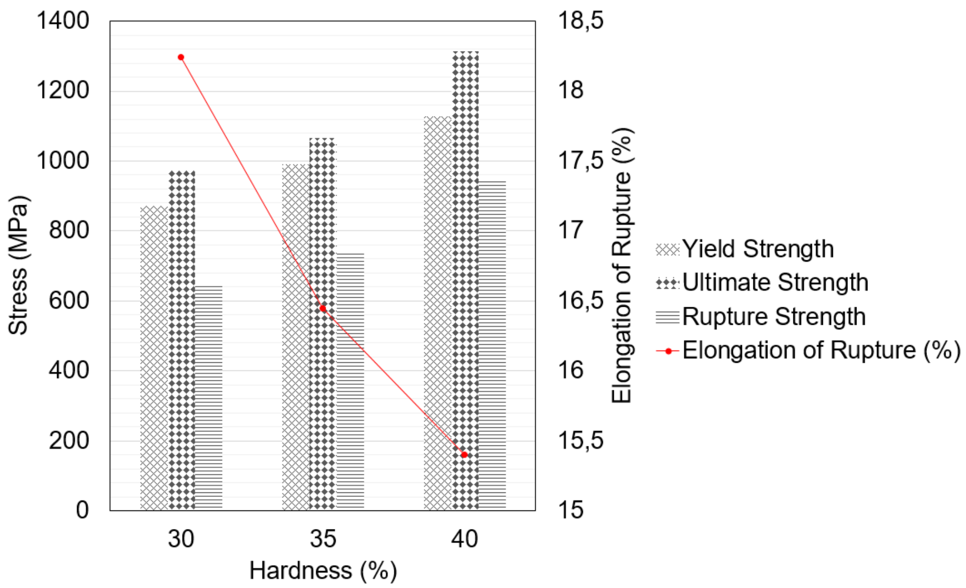


Figure 3.24. The results obtained from tensile tests

### 3.7. Surface Roughness Measurement

In this study, Mitutoyo SJ211 Surftest Surface Roughness Tester shown in Figure 3.25 below was used. Each specimen was measured three times, then the average of the three measurements was taken as the roughness value (Ra). Cut-off length, sampling length, and driving speed of stylus were fixed as 0,8 mm, 4 mm, and 0,5 mm/rev, respectively. Before the roughness device was used, it was calibrated with a reference specimen shown in Figure 3.26.


Figure 3.25. Mitutoyo SJ211 Surftest Surface Roughness Tester; a) Setup, b) Close-up shot.

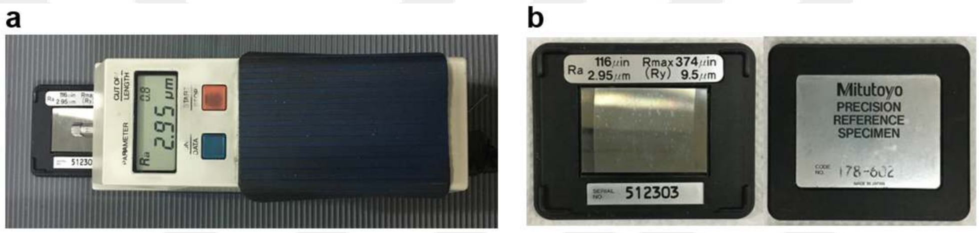


Figure 3.26. Calibration of Surftest Surface Roughness Tester; a) Setup, b) Reference specimen

### 3.8. Cutting Force Measurement

Experiments were conducted in the Manufacturing Laboratory of the Mechanical Engineering Department at the University of Yozgat Bozok in Yozgat/Turkey. The cutting forces that occurred in the experiments conducted under each cutting condition have been measured by a KISTLER 9129AA piezoelectric dynamometer. Machining force measurement is provided by Kistler 3 component piezoelectric dynamometer that measures averaged tangential, feed, and radial forces during turning processes. Graphical displays of force outputs are recorded using Data Acquisition Card (DAC) and Dynoware software at the end of each experiment. The experimental setup of force measurement used to perform the tests are illustrated in Figure 3.27.

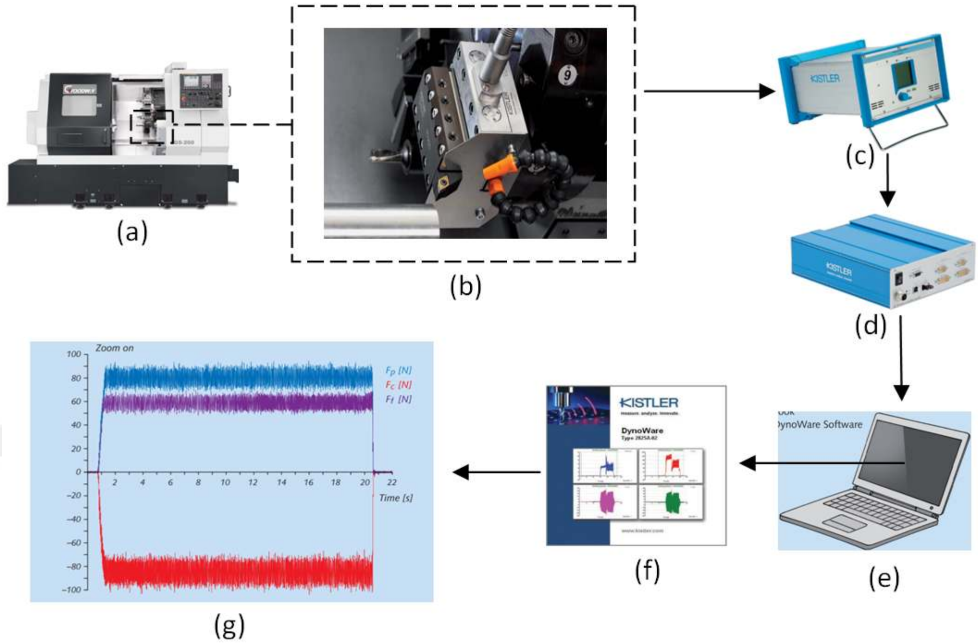


Figure 3.27. Experimental setup for force measurement used in this work; a) Goodway 260Y CNC Lathe, b) Kistler 9129AA model piezoelectric dynamometer, c) Kistler 5070A model amplifier, d) Kistler 5697 model data acquisition box, e) Computer, f) Dynoware software, g) Screenshot of cutting forces

### 3.9. Current Measurement

In this study, UNI-T UT 201 Digital Clamp Multimeter was used to measure the current. Total current measurement is provided by the instantaneous electrical current taken from the electrical panel of the machine during the operation of the lathe. Instantaneous electric current was recorded for the machine running in cutting and non-cutting modes. Current flowing through one phase of the servo motors in the CNC lathe was measured by the clamp amperemeter and multiplied by three as shown in Figure 3.28 below. In addition, labels of the CNC lathe used in this work are shown in Figure 3.29.

a b c


Figure 3.28. Setup for current measurement used in this work; a) Electric panel of CNC lathe, b) Digital Clamp Multimeter, c) Cable color of electrical phases.

a b


Figure 3.29. Labels of the CNC lathe used in this work; a) Feature nameplate, b) Electrical nameplate

### 3.10. Power Consumption Calculation

All current measurements were converted into power consumption using the electrical power formula given in Equation 1.2.

$$Power\,consumption = \sqrt{3}.V.I.\cos\varphi \;(watt) \tag{1.2}$$

### 3.11. Sound Measurement

Sound in this study is total noise emitted by machine tools and the cutting process during the turning process. Lutron SL-401 sound level meter was used to measure sound. The sound level meter was placed in the closest position to the cutting tool as shown in Figure 3.30.

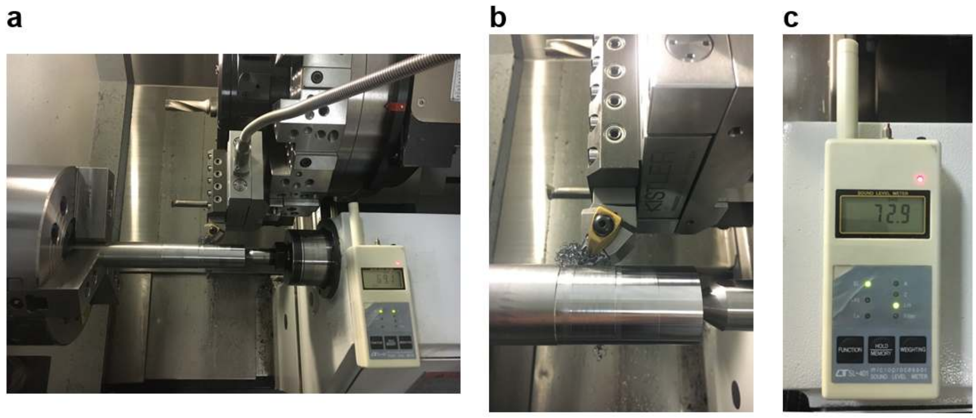


Figure 3.30. Setup for sound level measurement used in this work; a) Sound level measurement in CNC lathe, b) Close-up shot, c) Sound Level Meter

### 3.12. Methods

The scientific discipline applied by obtaining valid inferences from experimental or observational data is called statistics. In engineering and scientific experiments, statistic has three phases: project planning, experimental design, and data analysis phase as given in Table 3.3 (Mason et al., 2003).

Table 3.3. Role of statistics in engineering and experimentation

| Project planning phase | Experimental design phase | Data analysis phase |
|---|---|---|
| •What is to be measured?<br>•How large is the likely variation?<br>•What are the influential factors? | •Control known sources of variation<br>•Allow estimation of the size of the uncontrolled variation<br>•Permit an investigation of suitable models | •Make inferences on design factors<br>•Guide subsequent designs<br>•Suggest more appropriate models |

If meaningful results are to be drawn from the data, a statistical approach is needed for experimental design. Research in engineering, science, and industry is often experimental and has intensive experimental work. The efficiency of experiments can largely improve with the help of statistical methods, and the results obtained with this method can become more meaningful (Montgomery, 2001). Because of this, Design of Experiment methods such as Full Factor Design, Response Surface Methodology, and Taguchi Method (TM) are widely used (Raman et al., 2021).

In this study, turning was carried out on a CNC lathe. Firstly, cutting parameters were determined as cutting speed (v, m/min), feed rate (f, mm/rev), cutting depth (a, mm), hardness of workpiece (30, 35, 40 HRC), and insert material (ceramic, carbide, CBN). Then, experiments were designed with TM, and mathematical formulas were obtained with RSM. Finally, an Analysis of Variance was performed to examine the effect of each parameter. The process procedure is shown in the following Figure 3.31.

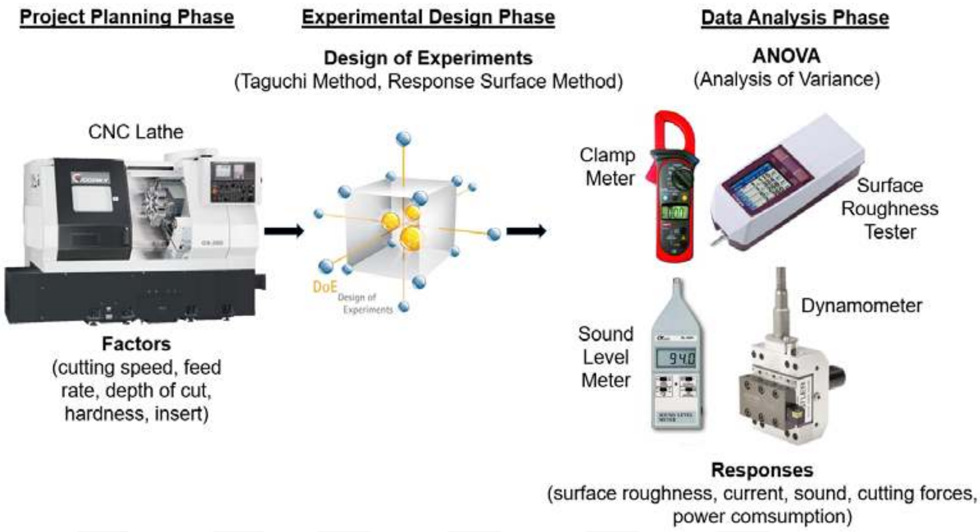


Figure 3.31. Process procedure

### 3.12.1. Taguchi Method (TM)

Taguchi is an experimental design method that is significantly decreasing the number of experiments by use of orthogonal arrays (OA), and also attempts to minimize impacts of out-of-control factors. The biggest advantages of the Taguchi Method are listed in the following. It shortens the experimental time, reduces the cost, and reveals important factors in less time (Asiltürk and Akkuş, 2011; Gaitonde et al., 2009; Antony, 2003). The purpose of the Taguchi Method is to determine control factor settings that present acceptable responses even though there are the natural environment and process variability. In the Taguchi Method, two designs called inner and outer arrays are used. Orthogonal arrays have two-level, three-level, four-level, five-level, and mixed-level designs. Control factors and Noise factors build up the inner array and the outer array, respectively. This approach benefits from signal and noise factors, inner and outer arrays, and signal-to-noise ratios (Davis and John, 2018; Negrete, 2015; Mori, 2011). If experimental runs are properly selected using the Taguchi experiment design, there will be no need to conduct full factorial experiments. Taguchi Signal-to-Noise (SN) Ratios are a function of the monitored responses on an outer array as given in Equations 3.1, 3.2, and 3.3. For each factor value, the optimal level of a process parameter is the level that offers the highest value of the SN ratio conversion (Minitab, 2021; Deepanraj et al., 2020; Negrete, 2013; Bilga et al., 2016).

Larger is better (the response is maximized; for instance, flavor),

$$SN = -10\log\left(\frac{1}{n}\sum_{i=1}^{n}\frac{1}{Y_i^2}\right)\ (dB) \tag{3.1}$$

Nominal is best (the response is targeted; for instance, part dimension),

$$SN = 10\log\left(\frac{\mu^2}{\sigma^2}\right)\ (dB) \tag{3.2}$$

Smaller is better (the response is minimized; for instance, cost),

$$SN = -10\log\left(\frac{1}{n}\sum_{i=1}^{n}Y_i^2\right)\ (dB) \tag{3.3}$$

Here; $Y_i$ symbolizes observations of response variable at the ith test, and $\mu^2$ symbolizes the square of the mean. Furthermore, $\sigma^2$ symbolizes the variance of the observations of the replicated response values, and n is the total number of the tests.

### 3.12.2. Respond Surface Method (RSM)

Response Surface Method (RSM) is an approach based on statistical and mathematical techniques used to develop, improve and optimize processes. In addition to the improvement of existing products, it has important applications such as the design, development, and formulation of new products. The relation of a product, process, or system with a y response dependent on controllable input variables $(\xi_1, \xi_2, \xi_3, ..., \xi_k)$ can be formulated as given in Equation 3.4 below.

$$y = f(\xi_1, \xi_2, \xi_3, ..., \xi_k) + \varepsilon \tag{3.4}$$

These input variables can be called factors, independent variables, or process variables. $\varepsilon$ represents variables that are not calculated in the function f. That is, $\varepsilon$ contains impacts like measurement error on the response, change of existing natural resources in the process or system, and influence of unknown variables. It is usually considered a statistical error and zero. If $\varepsilon$ is zero, the new equation can be written as given in Equation 3.5.

$$y = f(\xi_1, \xi_2, \xi_3, ..., \xi_k) \tag{3.5}$$

Variables in Equation 3.5 are often called natural variables such as degrees, pounds, or grams. Since the form of the actual response function f is unknown, accomplished application of the RSM depends on the experimenter's skill to improve a proper approach for f. Generally, a second-order mathematical model given in Equation 3.6 created by regression analysis is used in the RSM.

$$y = \beta_0 + \sum_{i=1}^{k} \beta_i x_i + \sum_{i=1}^{k} \beta_{ii} x_i^2 + \sum_{i \neq j=1}^{k} \beta_{ij} x_i x_j \tag{3.6}$$

Here, y represents the predicted response. $\beta_0$ is a constant term called intercept of the regression equation. $\beta_i$, $\beta_{ii}$, and $\beta_{ij}$ are the regression coefficients for the linear, quadratic, and interactive impacts of the model, respectively. $x_i$ and $x_j$ are the factors and k is the number of factors. i and j are the index of summation (Myers et al., 2016; Bouzid et al., 2015; Sahoo and Sahoo, 2013; Ozturk, 2019).

### 3.12.3. Analysis of Variance (ANOVA)

Analysis of variance is widely used in many fields such as psychology, biology, medicine, education, sociology, anthropology, economics, political science, industry, and commerce (Rutherford, 2011; Kaufmann and Schering, 2014). ANOVA is a statistical approach used to show interactions between factors and responses affecting the performance of the machining process. ANOVA has a table that includes degrees of freedom (DF), sum of squares (SS), mean of squares (MS), Fisher (F) values, probability (P) values, and percentage of contributions (C%) (Das et al., 2017; Dutta and Narala, 2021). In ANOVA analysis, some values are checked to see the effects of the parameters. One of these values, P (probability or significance) values indicate the performance of factors. If the P-value of parameters is less than or equal to the confidence level, they are significant. If the P-value of parameters is greater than the confidence level, they are not significant. In this study, the confidence level was accepted as 95 percent (95%) and the significance level as 5 percent (5%) considering the literature (Qasim et al., 2015; Bhushan, 2013; Cardoso et al., 2021; Aouici et al., 2012; Deepak and Rajendra, 2016; Basmacı, 2018; Nguyen, 2019). Another important value in terms of statistics is the F value. Generally, if the F-value of any parameter in the process is greater than 4, it means that this parameter has a significant impact on process performance (Yang and Tarng, 1998; Kant and Sangwan, 2014). That is, if $P<0,05$ or $F>4$, the parameter is meaningful, otherwise, it is meaningless.

### 3.12.4. Finite Element Method (FEM)

Abaqus is a forceful simulation tool based on the Finite Element Method that could conduct linear and nonlinear problems. Some features of Abaqus are given below (Abaqus, 2021):

- Virtually any geometry can be modelled,
- The behavior of engineering materials such as metals, rubber, polymers, composites, reinforced concrete, crushable, resilient foams, geotechnical materials, soils, and rock could be simulated,
- It could be utilized for stress/displacement problems,
- Problems like heat transfer, mass diffusion, thermal analysis, acoustics, soil mechanics, piezoelectric analysis, electromagnetic analysis, and fluid dynamics could be simulated.

Abaqus analysis usually takes place in 3 stages. These are preprocessing, simulation and postprocessing as shown in Figure 3.32 below. First of all, the model of the physical problem is identified and formed an Abaqus input file. Later, the simulation is run as a background process in Abaqus/Standard or Abaqus/Explicit to be solved the numerical problem defined in the model. After the simulation has been completed, the results are evaluated with visualization module, animations, and X–Y plots (Abaqus, 2021):

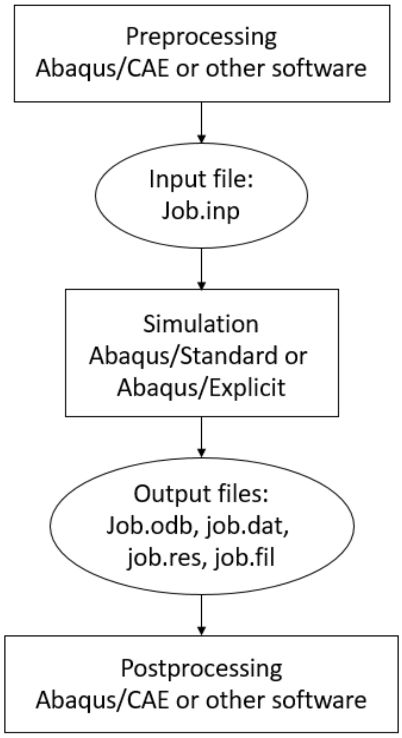


Figure 3.32. Stages of Abaqus analysis (Abaqus, 2021)

### 3.12.5. Turning Experiments

Cutting experiments were carried out using a lathe with Computer Numerical Control (CNC) that has Goodway brand (GS-260Y model, made in Taiwan) and 5 axes technical properties. Also, the CNC machine tool has 15 kW spindle power, high rigidly, and a maximum spindle speed of 4000 rpm as shown in Figure 3.33. The experimental setup is represented in Figure 3.34.


Figure 3.33. CNC lathe

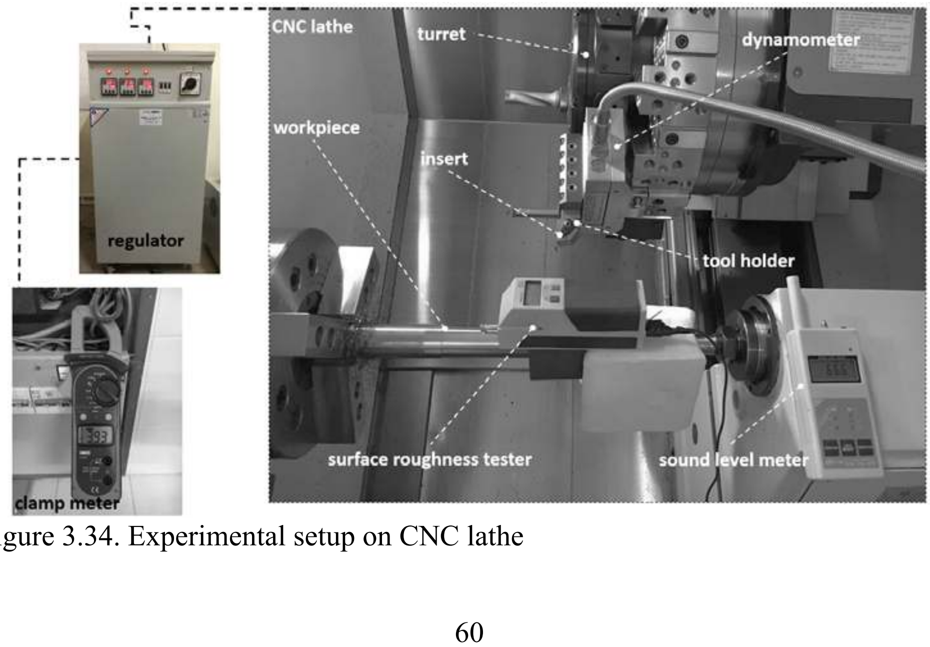


Figure 3.34. Experimental setup on CNC lathe

In the experiments, AISI 4340 alloy steel specimens with three different hardness that are 30 HRC, 35 HRC, and 40 HRC (hardness scale C) were used. The experiments were executed under dry-cutting conditions. The initial diameter of the test specimen is 40 mm and the length is 250 mm. The workpiece was cleaned by removing the 0,5 mm thickness material of the surface from the workpiece to eliminate any surface defects and wobbling. Before performing experiments, the workpiece was divided into sections 15 mm in length. Then workpiece was positioned between tailstock and chuck. A schematic representation of the machined test specimen is shown in Figure 3.35.

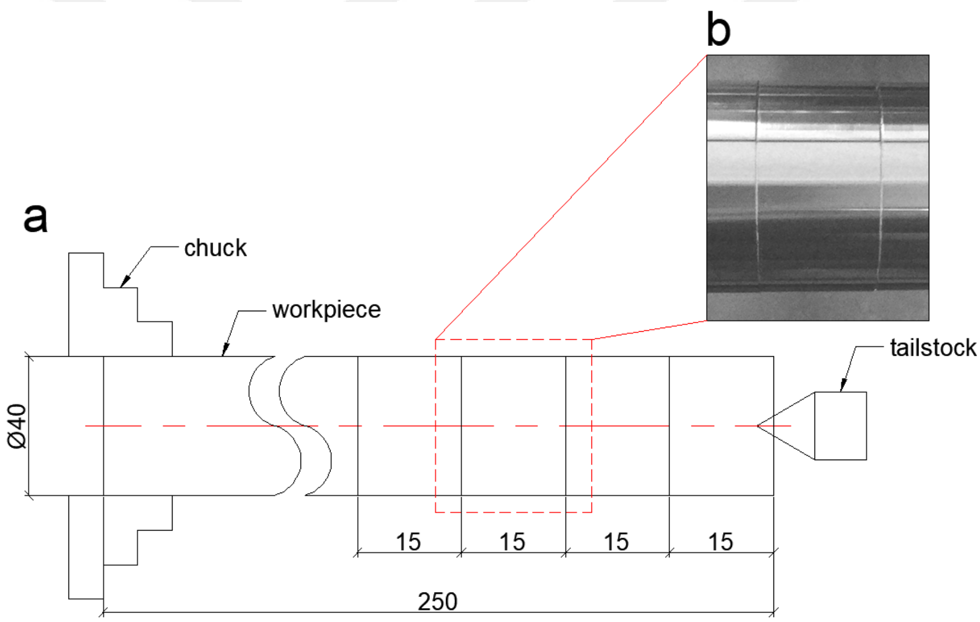


Figure 3.35. Schematic representation of the machined test specimen; a) General drawing, b) Close-up (dimensions are mm)

Properties of inserts (cutting tool) and tool holder are used as given in Tables 3.4-3.7.

Table 3.4. Kennametal/CNMG120408/RP/KU30T (Kennametal master catalog, 2018; Akko catalog, 2021)

| **Trademark/ISO Catalog Number/Grade** | Kennametal/CNMG120408/RP/KU30T |
|---|---|
| **Insert material** | Carbide |
| **Insert geometry** | 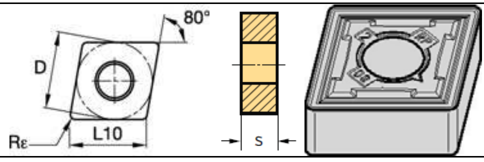 |
| **Grade** | 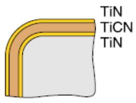<br>KU30T<br>Composition: A tough cobalt-enriched substrate with a multilayered CVD coating.<br>Application: KU30T is a new grade designed specifically for the job shop industry where a wide range of workpiece materials is employed. With its tough cobalt-enriched substrate, KU30T performs very effectively in roughing through finishing operations. The post-coat grinding of the insert permits stable insert seating while the post-coat treatment resists workpiece build-up and microchipping. For machining steels, cast irons, and stainless steels, first choices are the -RN, -MN, and the -RP geometries. For medium machining and finishing, the -MP and -FP geometries with a positive rake are suggested. |
| **Geometric data and specifications** | Inscribed circle (IC) diameter (D): 12,7 mm<br>Insert cutting edge length (L10): 12,896 mm<br>Insert thickness (S): 4,7620 mm<br>Corner radius ($R_{\varepsilon}$): 0,7940 mm<br>Chip breaker: RP<br>Shape: Rhombic |
| **Toll holder** | AKKO brand TCLNL 25x25 M12<br>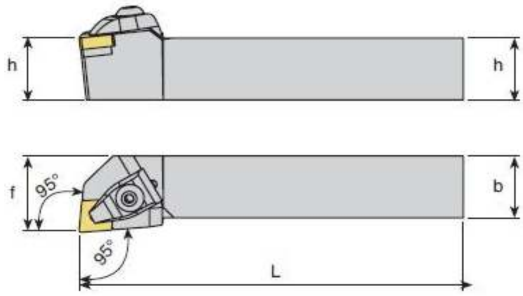<br>L: 150 mm, h: b: 25 mm, f: 32 mm |
| **Features and benefits** | Roughing geometry with positive rake face for chip control in difficult materials |
| **Working process** | External turning |
| **Workpiece materials** | Steel, Stainless Steel, Cast Iron, High-Temp Alloys |

Table 3.5. Sumitomo electric/CNGA120408/NB100C (Akko catalog, 2021; Sumitomo catalog, 2021)

| | |
|---|---|
| **Trademark/ISO Catalog Number/Grade** | Sumitomo electric/CNGA120408/NB100C |
| **Insert material** | Ceramic |
| **Insert geometry** | 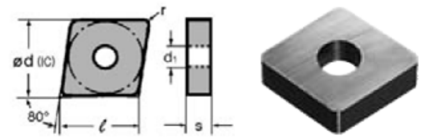 |
| **Grade** | NB100C<br>$Al_2O_3$-based high strength ceramic with ZX Coat. Low-speed/continuous light cutting of hardened steel. Main Coating Components are TiAIN Type. |
| **Geometric data and specifications** | Inscribed circle (IC): 12,7 mm<br>Cutting edge length (l): 12,9 mm<br>Thickness (S): 4,76 mm<br>Corner radius (r): 0,8 mm<br>Shape: Rhombic<br>Relief Angle: 0°<br>$d_1$: 5,16 mm |
| **Toll holder** | AKKO brand TCLNL 25x25 M12<br>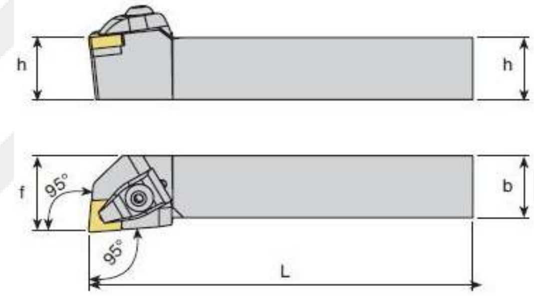<br>L: 150 mm<br>h: b: 25 mm<br>f: 32 mm |
| **Field of applications** | Finishing to Light Cutting. Superb wear resistance enables ultra-high-speed machining. |
| **Working process** | External turning |
| **Workpiece materials** | Hardened steel |

Table 3.6. Sumitomo electric/2NCCNGA120408HS/BNC2010 (Akko catalog, 2021, 2018; Sumitomo catalog, 2021)

| **Trademark/ISO Catalog Number/Grade** | Sumitomo electric/2NCCNGA120408HS/BNC2010 |
|---|---|
| **Insert material** | CBN (cubic boron nitride) |
| **Insert geometry** | 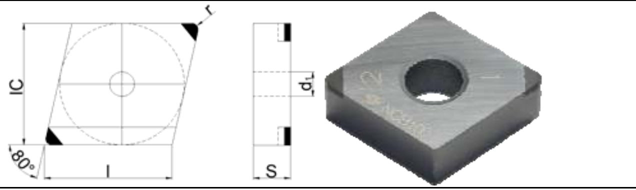 |
| **Grade** | BNC2010<br>A newly developed tough CBN substrate coated with a highly wear-resistant TiAlN layer. Achieves more stable machining and longer tool life by employing a highly adhesive layer to reduce delamination. |
| **Geometric data and specifications** | Inscribed circle (IC): 12,7 mm<br>Cutting edge length (l): 12,9 mm<br>Thickness (S): 4,76 mm<br>Corner radius (r): 0,8 mm<br>Shape: Rhombic<br>Relief Angle: 0°<br>$d_1$: 5,5 mm |
| **Toll holder** | AKKO brand TCLNL 25x25 M12<br>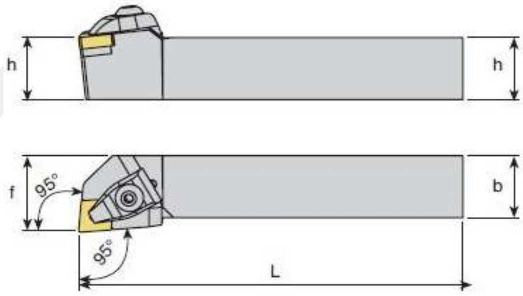<br>L: 150 mm<br>h: b: 25 mm<br>f: 32 mm |
| **Field of applications** | A grade for high-precision machining applicable to finishing requiring good surface roughness and dimensional accuracy. Provides further improved wear resistance thanks to a newly developed CBN substrate coated with a TiCN layer. Reduces boundary wear and stably achieves excellent surface finish thanks to newly developed special multi-layered coating. |
| **Working process** | External turning |
| **Workpiece materials** | A general-purpose grade applicable to general hardened steel machining. |

Table 3.7. Kennametal/TPGN160304/KC5010 (Kennametal master catalog, 2018)

| **Trademark/ISO Catalog Number/Grade** | Kennametal/TPGN160304/KC5010 |
|---|---|
| **Insert material** | Carbide |
| **Insert geometry** | 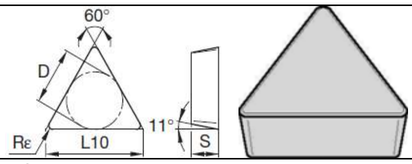 |
| **Grade** | KC5010<br>An advanced PVD AlTiN coating over a very deformation-resistant unalloyed carbide substrate. The new and improved coating enables speeds to be increased by 50–100%. |
| **Geometric data and specifications** | Inscribed circle (D): 9,5300 mm<br>Cutting edge length (L10): 16,5000 mm<br>Thickness (S): 3,1800 mm<br>Corner radius ($R_\varepsilon$): 0,4000 mm<br>Shape: Triangular<br>Relief angle: 11°<br>Rake angle: 5°<br>Nose angle: 60° |
| **Toll holders** | Kennametal brand CTGPL2525M16<br>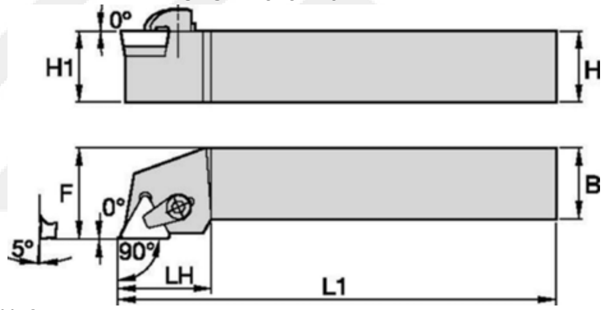<br>H: 25 mm<br>H1: 25 mm<br>B: 25 mm<br>F: 32 mm<br>L1: 150 mm<br>LH: 26 mm |
| **Field of applications** | Excellent for machining most steels, stainless steels, cast irons, non-ferrous materials, and superalloys under stable conditions. It also performs well machining hardened and short chipping materials. |
| **Working process** | External turning. |
| **Workpiece materials** | Ideal for finishing to general machining of most workpiece materials at higher speeds. |

# 4. RESULTS AND DISCUSSION

In this study, three different inserts, three different material hardness, three different cutting speeds, three different feed rates, and three different depths of cut were used. Factors and levels are given in Table 4.1. The symbols and numerical values expressed in the created design were performed by considering the literature (Öztürk and Kara, 2020; Kıvak, 2014; Akgün and Kara, 2021). Also, parameter levels were taken from insert catalogs (Kennametal catalog, 2018; Sumitomo catalog, 2021). Taguchi Method, RSM, and ANOVA were executed to find the optimum parameters. Analyzes were performed utilizing Minitab 16 software. The relationship between cutting parameters and Total Power Consumption ($P_{total}$), Cutting forces (Fx, Fy, Fz), Total Sound ($S_{total}=S_{machine}+S_{cutting}$), Total Current ($I_{total}= I_{unloaded}+I_{cutting}$), Surface roughness (Ra) values are examined. Later, the relationships between these values are explained. Finally, a mathematical model is developed using regression analysis for each response prediction based on the experimental results.

Table 4.1. Process factors and selected levels were used for machining parameters in this experimental study

| Factors | Symbols (Units) | Levels (uncoded) | | | Levels (coded) | | |
|---|---|---|---|---|---|---|---|
| | | 1 | 2 | 3 | 1 | 2 | 3 |
| Insert (i, cutting tool) | A (-) | 1: Ceramic | 2: Carbide | 3: CBN | -1 | 0 | 1 |
| Material hardness (h) | B (HRC) | 30 | 35 | 40 | -1 | 0 | 1 |
| Cutting speed (v) | C (m/min) | 180 | 220 | 260 | -1 | 0 | 1 |
| Feed rate (f) | D (mm/rev) | 0,03 | 0,07 | 0,11 | -1 | 0 | 1 |
| Depth of cut (a) | E (mm) | 0,08 | 0,14 | 0,20 | -1 | 0 | 1 |

The Fishbone diagram is one of the outputs in experimental design. A fishbone diagram can be created to see exactly how the identified factors relate to each other. This diagram indicates all factors that represent product or process quality. And it affects the experimental values. With the help of the fishbone diagram, variable and fixed factors were decided. Factors affecting $P_{total}$, Fx, Fy, Fz, Ra, $S_{total}$, and $I_{total}$ are collected under six main categories as shown in Figure 4.1.

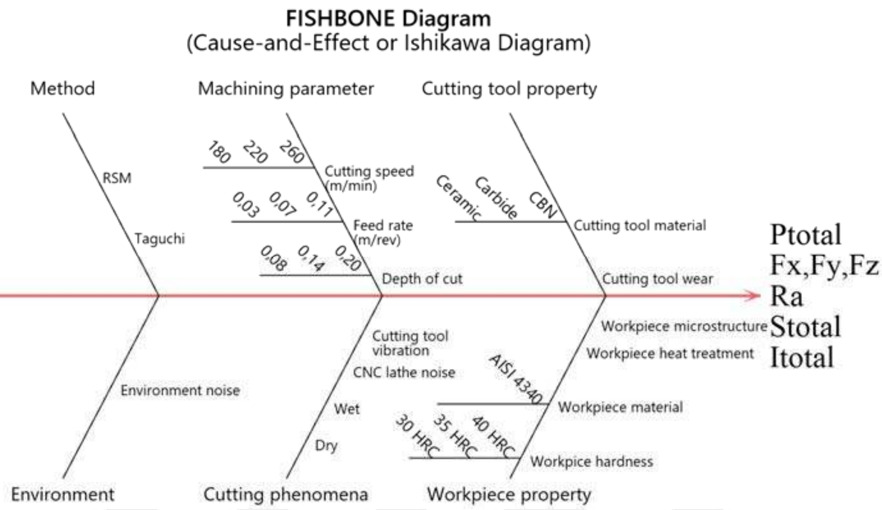


Figure 4.1. Fishbone diagram of factors affecting $P_{total}$, Fx, Fy, Fz, Ra, $S_{total}$, and $I_{total}$

Also, mathematical models are subjected to constraints in the following involving ceramic, carbide, and CBN inserts:

$30 \text{ HRC} \leq h \leq 40 \text{ HRC}$,
$180 \text{ m/min} \leq v \leq 260 \text{ m/min}$,
$0{,}03 \text{ mm/rev} \leq f \leq 0{,}11 \text{ mm/rev}$,
$0{,}08 \text{ mm} \leq a \leq 0{,}20 \text{ mm}$.

### 4.1. Analysis with RSM and Taguchi Method of Experimental Results

The power consumed of 5 axis CNC machine tool used in this study can be divided into parts as shown in Figure 4.2. Constant power consumption in machine tools comprises machine axes, spindle, pumps, hydraulic system, CNC controller, automated tool changer, control panel, and so on. Variable power consumption comprises machining of the workpiece, the influence of feed rate, cutting speed, material removal rate, and so on.

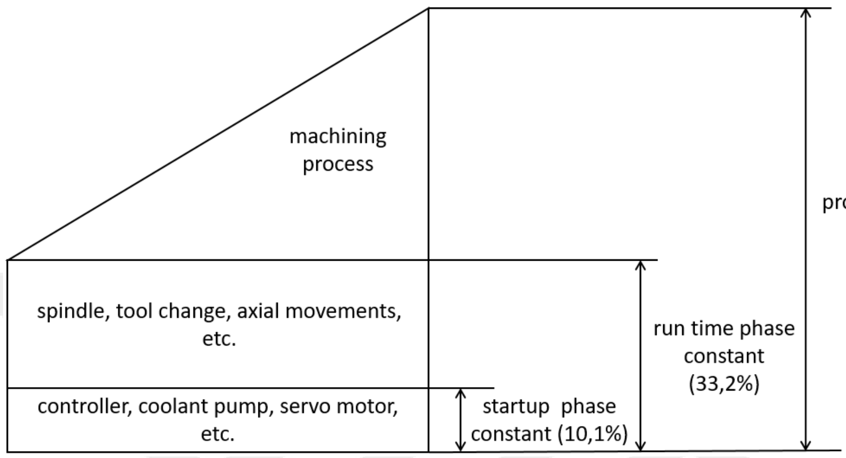


Figure 4.2. Power consumption of 5 axis CNC turning machine tool used in this study

The power consumption for the line current of the CNC lathe can be calculated with the following Equation 1.2. The power factor and voltage of CNC lathe used in this study are read as PF=1 and V=380 volt from the machine tool catalog, respectively.

$$Power\,consumption = \sqrt{3}.V.I.\cos\varphi \;\; (watt) \tag{1.2}$$

Here V is the voltage (volt), I is the current (amper), and cost ϕ is the power factor (PF) (-). Power consumption for every phase is calculated in the following.

$Power\,consumption = \sqrt{3}.V.I.\cos\varphi$ = 1,73x380x1,09x1 = 717,4 watt for startup phase.

$Power\,consumption = \sqrt{3}.V.I.\cos\varphi$ = 1,73x380x3,58x1 = 2356,3 watt for run time phase.

$Power\,consumption = \sqrt{3}.V.I.\cos\varphi$ = 1,73x380x6,12x1 = 4023,3 watt for process phase.

Here, the current value for process phase is taken as the arithmetic mean of 46 experiment results. % ratios of power consumption are given in Table 4.2. Percent ratios of power consumption are found with Equation 4.1.

$$\%\,Ratio = \frac{Phase\ power\,consumption}{Total\ power\,consumption} x100\ (\%) \tag{4.1}$$

Table 4.2. Percent ratios of Power consumption of CNC machine tool used in the study

| **Phases** | **Power consumption (W)** | **% Ratio** |
|---|---|---|
| startup phase | 717,4 | 10,1 |
| run time phase | 2356,3 | 33,2 |
| process phase | 4023,3 | 56,7 |
| total | 7097,0 | 100,0 |

To evaluate experimental and predicted results, the following Equations of 4.2 and 4.3 are used.

$$\%\,Contribution = (SeqSS/Total)x100\ (\%) \tag{4.2}$$

$$\%\,Error = \left|\frac{Experimental\,value - Predicted\,value}{Experimental\,value}\right| x100\ (\%) \tag{4.3}$$

When the % Error formula given in Equation 4.3 is used, the simulated value can be taken instead of the predicted value, and the calculated value can be taken instead of the experimental value.

Three cutting forces happened on the cutting tool as shown in Figure 4.3. These are radial force (Fx), tangential force (Fy), and feed force (Fz). The resultant cutting force (F) is shown in Equation 4.4 (Altintas, 2012; Kistler, 2021).

$$F = \sqrt{F_x^2 + F_y^2 + F_z^2} \tag{4.4}$$

Fz is viewed in the direction of the thickness of the uncut chip and is influenced mainly by the feed rate. However, the feed force increases as the feed rate increases. Fy acts on the cutting speed direction. Fx is a radial force that moves the tool away from the workpiece and acts along the radial direction of the workpiece.

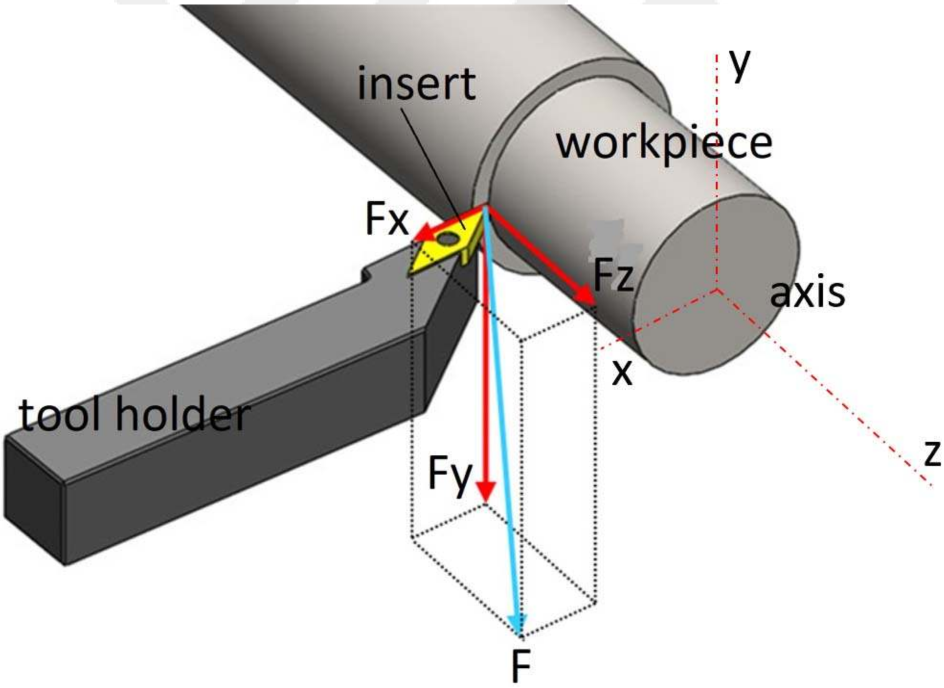


Figure 4.3. Cutting forces on the symbolic cutting tool (insert)

Table 4.3. Box-Behnken Design test plan

| Runs | Coded values | | | | | Real (Uncoded) values | | | | |
|---|---|---|---|---|---|---|---|---|---|---|
| | A | B | C | D | E | i (-) | h (HRC) | v (m/min) | f (mm/rev) | a (mm) |
| **1** | -1 | -1 | 0 | 0 | 0 | Ceramic | 30 | 220 | 0,07 | 0,14 |
| **2** | 1 | -1 | 0 | 0 | 0 | CBN | 30 | 220 | 0,07 | 0,14 |
| **3** | -1 | 1 | 0 | 0 | 0 | Ceramic | 40 | 220 | 0,07 | 0,14 |
| **4** | 1 | 1 | 0 | 0 | 0 | CBN | 40 | 220 | 0,07 | 0,14 |
| **5** | 0 | 0 | -1 | -1 | 0 | Carbide | 35 | 180 | 0,03 | 0,14 |
| **6** | 0 | 0 | 1 | -1 | 0 | Carbide | 35 | 260 | 0,03 | 0,14 |
| **7** | 0 | 0 | -1 | 1 | 0 | Carbide | 35 | 180 | 0,11 | 0,14 |
| **8** | 0 | 0 | 1 | 1 | 0 | Carbide | 35 | 260 | 0,11 | 0,14 |
| **9** | 0 | -1 | 0 | 0 | -1 | Carbide | 30 | 220 | 0,07 | 0,08 |
| **10** | 0 | 1 | 0 | 0 | -1 | Carbide | 40 | 220 | 0,07 | 0,08 |
| **11** | 0 | -1 | 0 | 0 | 1 | Carbide | 30 | 220 | 0,07 | 0,2 |
| **12** | 0 | 1 | 0 | 0 | 1 | Carbide | 40 | 220 | 0,07 | 0,2 |
| **13** | -1 | 0 | -1 | 0 | 0 | Ceramic | 35 | 180 | 0,07 | 0,14 |
| **14** | 1 | 0 | -1 | 0 | 0 | CBN | 35 | 180 | 0,07 | 0,14 |
| **15** | -1 | 0 | 1 | 0 | 0 | Ceramic | 35 | 260 | 0,07 | 0,14 |
| **16** | 1 | 0 | 1 | 0 | 0 | CBN | 35 | 260 | 0,07 | 0,14 |
| **17** | 0 | 0 | 0 | -1 | -1 | Carbide | 35 | 220 | 0,03 | 0,08 |
| **18** | 0 | 0 | 0 | 1 | -1 | Carbide | 35 | 220 | 0,11 | 0,08 |
| **19** | 0 | 0 | 0 | -1 | 1 | Carbide | 35 | 220 | 0,03 | 0,2 |
| **20** | 0 | 0 | 0 | 1 | 1 | Carbide | 35 | 220 | 0,11 | 0,2 |
| **21** | 0 | -1 | -1 | 0 | 0 | Carbide | 30 | 180 | 0,07 | 0,14 |
| **22** | 0 | 1 | -1 | 0 | 0 | Carbide | 40 | 180 | 0,07 | 0,14 |
| **23** | 0 | -1 | 1 | 0 | 0 | Carbide | 30 | 260 | 0,07 | 0,14 |
| **24** | 0 | 1 | 1 | 0 | 0 | Carbide | 40 | 260 | 0,07 | 0,14 |
| **25** | -1 | 0 | 0 | -1 | 0 | Ceramic | 35 | 220 | 0,03 | 0,14 |
| **26** | 1 | 0 | 0 | -1 | 0 | CBN | 35 | 220 | 0,03 | 0,14 |
| **27** | -1 | 0 | 0 | 1 | 0 | Ceramic | 35 | 220 | 0,11 | 0,14 |
| **28** | 1 | 0 | 0 | 1 | 0 | CBN | 35 | 220 | 0,11 | 0,14 |
| **29** | 0 | 0 | -1 | 0 | -1 | Carbide | 35 | 180 | 0,07 | 0,08 |
| **30** | 0 | 0 | 1 | 0 | -1 | Carbide | 35 | 260 | 0,07 | 0,08 |
| **31** | 0 | 0 | -1 | 0 | 1 | Carbide | 35 | 180 | 0,07 | 0,2 |
| **32** | 0 | 0 | 1 | 0 | 1 | Carbide | 35 | 260 | 0,07 | 0,2 |
| **33** | -1 | 0 | 0 | 0 | -1 | Ceramic | 35 | 220 | 0,07 | 0,08 |
| **34** | 1 | 0 | 0 | 0 | -1 | CBN | 35 | 220 | 0,07 | 0,08 |
| **35** | -1 | 0 | 0 | 0 | 1 | Ceramic | 35 | 220 | 0,07 | 0,2 |
| **36** | 1 | 0 | 0 | 0 | 1 | CBN | 35 | 220 | 0,07 | 0,2 |
| **37** | 0 | -1 | 0 | -1 | 0 | Carbide | 30 | 220 | 0,03 | 0,14 |
| **38** | 0 | 1 | 0 | -1 | 0 | Carbide | 40 | 220 | 0,03 | 0,14 |
| **39** | 0 | -1 | 0 | 1 | 0 | Carbide | 30 | 220 | 0,11 | 0,14 |
| **40** | 0 | 1 | 0 | 1 | 0 | Carbide | 40 | 220 | 0,11 | 0,14 |
| **41** | 0 | 0 | 0 | 0 | 0 | Carbide | 35 | 220 | 0,07 | 0,14 |
| **42** | 0 | 0 | 0 | 0 | 0 | Carbide | 35 | 220 | 0,07 | 0,14 |
| **43** | 0 | 0 | 0 | 0 | 0 | Carbide | 35 | 220 | 0,07 | 0,14 |
| **44** | 0 | 0 | 0 | 0 | 0 | Carbide | 35 | 220 | 0,07 | 0,14 |
| **45** | 0 | 0 | 0 | 0 | 0 | Carbide | 35 | 220 | 0,07 | 0,14 |
| **46** | 0 | 0 | 0 | 0 | 0 | Carbide | 35 | 220 | 0,07 | 0,14 |

The experiment design of Respond Surface Method (L46) and experimental results are given in Table 4.3. Since the Box-Behnken Design (BBD) is considered more competent and the most powerful than other designs, such as the three-level Full Factorial Design (FFD), the Central Composite Design (CCD), the Design of Experiment (DOE) is done using a Box-Behnken design.

Box-Behnken designs do not have axial points and Central Composite Designs usually have axial points outside the "cube". Due to fact that all design points fall within the safe operating zone in Box-Behnken design, BBD was selected. A total number of 46 runs of experimental conditions including six replicates at center points (runs between 41-46) were performed for different combinations according to BBD. Terms that represent factors were selected as full quadratic in analyze response surface design.

In the traditional cutting theory, the main cutting force (tangential force) is the largest in the three-component forces (Fx, Fy, Fz). However, this relationship is different in the present study. Fx, Fy, and Fz are reported in Table 4.4. It was observed that the radial force component was dominant rather than the tangential force during turning. This increase in radial force can be explained by the rising of ploughing effect between insert and workpiece that prevails under small feed rate, and small depth of cut conditions when it is compared to nose radius (Azizi et al., 2012; Bartarya and Choudhury, 2012; Lalwani et al., 2008; Yao et al., 2017). Besides; experiment design of RSM (L46), experimental results, and the calculated results are given in Table 4.4. Here, power consumption that is found using instantaneous electric current are the calculated results.

Table 4.4. Experiment design of RSM (L46), experimental results, and calculated results

| Runs | Inputs (Factors) | | | | | Outputs (Responses) | | | | | | |
|---|---|---|---|---|---|---|---|---|---|---|---|---|
| | | | | | | Experimental values | | | | | | Calculated values |
| | A | B | C | D | E | Fx (N) | Fy (N) | Fz (N) | Ra (µm) | $I_{total}$ (A) | $S_{total}$ (dB) | $P_{total}$ (W) |
| **1** | -1 | -1 | 0 | 0 | 0 | 38,20 | 36,37 | 41,25 | 0,90 | 6,00 | 83,30 | 3949,08 |
| **2** | 1 | -1 | 0 | 0 | 0 | 68,96 | 49,30 | 54,74 | 0,34 | 6,17 | 82,25 | 4060,97 |
| **3** | -1 | 1 | 0 | 0 | 0 | 52,26 | 38,87 | 44,88 | 0,63 | 6,12 | 83,40 | 4028,06 |
| **4** | 1 | 1 | 0 | 0 | 0 | 79,37 | 52,68 | 54,21 | 0,25 | 6,27 | 83,10 | 4126,78 |
| **5** | 0 | 0 | -1 | -1 | 0 | 33,74 | 23,81 | 38,86 | 0,38 | 5,20 | 80,20 | 3422,53 |
| **6** | 0 | 0 | 1 | -1 | 0 | 42,55 | 21,50 | 40,36 | 0,27 | 6,89 | 88,30 | 4534,86 |
| **7** | 0 | 0 | -1 | 1 | 0 | 65,86 | 55,33 | 48,60 | 0,38 | 5,42 | 77,90 | 3567,33 |
| **8** | 0 | 0 | 1 | 1 | 0 | 68,26 | 52,59 | 47,68 | 0,56 | 6,95 | 87,40 | 4574,35 |
| **9** | 0 | -1 | 0 | 0 | -1 | 26,25 | 24,37 | 32,49 | 0,56 | 5,98 | 81,30 | 3935,91 |
| **10** | 0 | 1 | 0 | 0 | -1 | 47,59 | 27,67 | 34,67 | 0,15 | 6,00 | 83,10 | 3949,08 |
| **11** | 0 | -1 | 0 | 0 | 1 | 53,73 | 53,07 | 51,04 | 0,45 | 6,28 | 82,30 | 4133,37 |
| **12** | 0 | 1 | 0 | 0 | 1 | 72,87 | 53,25 | 54,38 | 0,31 | 6,25 | 83,40 | 4113,62 |
| **13** | -1 | 0 | -1 | 0 | 0 | 46,11 | 37,60 | 44,28 | 0,65 | 5,26 | 78,60 | 3462,02 |
| **14** | 1 | 0 | -1 | 0 | 0 | 75,25 | 51,81 | 56,45 | 0,20 | 5,48 | 78,50 | 3606,82 |
| **15** | -1 | 0 | 1 | 0 | 0 | 45,60 | 37,17 | 43,60 | 0,75 | 6,94 | 87,30 | 4567,76 |
| **16** | 1 | 0 | 1 | 0 | 0 | 72,12 | 47,42 | 53,79 | 0,20 | 6,90 | 87,30 | 4541,44 |
| **17** | 0 | 0 | 0 | -1 | -1 | 26,07 | 15,69 | 33,00 | 0,14 | 5,93 | 83,00 | 3903,00 |
| **18** | 0 | 0 | 0 | 1 | -1 | 44,54 | 32,72 | 34,87 | 0,47 | 5,95 | 83,80 | 3916,17 |
| **19** | 0 | 0 | 0 | -1 | 1 | 41,71 | 31,20 | 44,49 | 0,49 | 6,20 | 85,51 | 4080,71 |
| **20** | 0 | 0 | 0 | 1 | 1 | 79,20 | 75,42 | 59,45 | 0,33 | 6,21 | 81,80 | 4087,29 |
| **21** | 0 | -1 | -1 | 0 | 0 | 43,67 | 44,05 | 40,23 | 0,45 | 5,32 | 77,80 | 3501,51 |
| **22** | 0 | 1 | -1 | 0 | 0 | 59,70 | 41,54 | 44,96 | 0,30 | 5,35 | 78,80 | 3521,26 |
| **23** | 0 | -1 | 1 | 0 | 0 | 44,19 | 37,84 | 41,08 | 0,52 | 6,83 | 86,80 | 4495,36 |
| **24** | 0 | 1 | 1 | 0 | 0 | 64,25 | 40,14 | 45,57 | 0,22 | 6,79 | 88,20 | 4469,04 |
| **25** | -1 | 0 | 0 | -1 | 0 | 29,74 | 19,77 | 39,15 | 0,70 | 5,95 | 83,80 | 3916,17 |
| **26** | 1 | 0 | 0 | -1 | 0 | 51,19 | 29,87 | 47,37 | 0,32 | 6,20 | 85,20 | 4080,71 |
| **27** | -1 | 0 | 0 | 1 | 0 | 55,19 | 49,90 | 46,21 | 0,83 | 6,06 | 83,70 | 3988,57 |
| **28** | 1 | 0 | 0 | 1 | 0 | 93,13 | 67,11 | 58,63 | 0,34 | 6,20 | 82,90 | 4080,71 |
| **29** | 0 | 0 | -1 | 0 | -1 | 30,17 | 23,88 | 32,84 | 0,36 | 5,18 | 78,60 | 3409,37 |
| **30** | 0 | 0 | 1 | 0 | -1 | 38,91 | 25,50 | 34,54 | 0,22 | 6,70 | 87,50 | 4409,80 |
| **31** | 0 | 0 | -1 | 0 | 1 | 62,00 | 52,98 | 50,98 | 0,22 | 5,40 | 77,80 | 3554,17 |
| **32** | 0 | 0 | 1 | 0 | 1 | 64,55 | 52,34 | 53,13 | 0,42 | 7,10 | 87,00 | 4673,07 |
| **33** | -1 | 0 | 0 | 0 | -1 | 30,06 | 21,66 | 37,81 | 0,61 | 5,98 | 83,10 | 3935,91 |
| **34** | 1 | 0 | 0 | 0 | -1 | 49,04 | 28,79 | 40,15 | 0,28 | 6,05 | 82,50 | 3981,98 |
| **35** | -1 | 0 | 0 | 0 | 1 | 53,48 | 55,45 | 51,59 | 0,73 | 6,14 | 83,90 | 4041,22 |
| **36** | 1 | 0 | 0 | 0 | 1 | 92,22 | 69,98 | 69,41 | 0,19 | 6,35 | 83,50 | 4179,44 |
| **37** | 0 | -1 | 0 | -1 | 0 | 28,71 | 24,01 | 36,45 | 0,58 | 6,01 | 81,30 | 3955,66 |
| **38** | 0 | 1 | 0 | -1 | 0 | 40,39 | 22,80 | 39,97 | 0,28 | 6,02 | 87,20 | 3962,24 |
| **39** | 0 | -1 | 0 | 1 | 0 | 54,03 | 52,87 | 43,79 | 0,59 | 6,22 | 83,87 | 4093,88 |
| **40** | 0 | 1 | 0 | 1 | 0 | 76,03 | 54,85 | 48,83 | 0,36 | 6,20 | 81,90 | 4080,71 |
| **41** | 0 | 0 | 0 | 0 | 0 | 56,06 | 38,50 | 45,31 | 0,28 | 6,29 | 82,60 | 4139,95 |
| **42** | 0 | 0 | 0 | 0 | 0 | 56,52 | 38,31 | 43,33 | 0,21 | 6,10 | 82,30 | 4014,89 |
| **43** | 0 | 0 | 0 | 0 | 0 | 56,56 | 37,76 | 44,19 | 0,23 | 6,22 | 82,80 | 4093,88 |
| **44** | 0 | 0 | 0 | 0 | 0 | 53,84 | 38,88 | 44,60 | 0,27 | 6,19 | 82,80 | 4074,13 |
| **45** | 0 | 0 | 0 | 0 | 0 | 53,92 | 39,12 | 44,64 | 0,29 | 6,18 | 82,80 | 4067,55 |
| **46** | 0 | 0 | 0 | 0 | 0 | 54,18 | 39,39 | 44,60 | 0,32 | 6,22 | 82,70 | 4093,88 |

The expressions of i, h, v, f, a, Fx, Fy, Fz, Ra, $I_{total}$, $S_{total}$, and $P_{total}$ denote insert, hardness, cutting speed, feed rate, depth of cut, radial force, tangential force, feed force, surface roughness, total electric current, total sound level, and total electric power consumption, respectively. Cutting forces, surface roughness values, current values, and sound values are average values.

Experimental results are analyzed with ANOVA to determine factors that markedly affect machining process performance. In this study, significance level and confidence level are taken as $\alpha = 0,05$ and 95%, respectively when ANOVA is investigated. The prediction power of developed regression model is stated with $R^2$ value. $R^2$ takes values between 0-100% and its precision of prediction increases as its value rises. Then contribution, residuals, and possibilities of the process parameters are examined. Residual is the difference between the experimental value and predicted value. Four-in-one residual plots are Histogram, Normal Probability Plot, Versus Fits, and Versus Order. These residual plots play an important role in assessing the fit of the developed model (Mia et al., 2017; Seçkin, 2020). Additionally, surface plots are practical for determining desirable response values and operating requirements. Therefore, surface plots are examined. The signal-to-noise (SN) ratio is a robustness measure that can be used to determine control factor settings that minimize the impact of noise on response. The SN ratios are assessed according to the smaller the better characteristic. Because the target of experiments is to minimize parameters in the machining process. Besides, SN ratios are utilized to detect the optimum levels of factors. In Main Effects Plot for SN ratios, x-axis indicates a level value of machining process parameters and y-axis indicates response values. The horizontal line indicates the mean value of the response. Afterward, SN ratio analysis using Taguchi Method for “smaller is better” characteristic is investigated. And finally, the optimization plot and comparison of results are analyzed. The Optimization Plot displays the effect of each factor (columns) on the responses or composite desirability (rows). The Optimization Plot is used to detect the optimal settings and optimized response values. Boundary values are shown with High and Low. The vertical red lines on the plot symbolize the present factor settings. The horizontal lines and numbers symbolize the responses for the present factor level. And, optimum (present) values are represented in red color. y indicates predicted optimum value as d states the desirability for each parameter. The target in the present study is to minimize responses.

### 4.1.1. Radial Force (Fx) Analysis

Table 4.5. Analysis of variance for Fx

| Source | DF | Seq SS | Adj SS | Adj MS | F | P | % Cont. |
|---|---|---|---|---|---|---|---|
| **Regression** | 20 | 12407,2 | 12407,2 | 620,36 | 98,47 | 0,000 | 98,75 |
| **Linear** | 5 | 11383,5 | 11383,5 | 2276,71 | 361,38 | 0,000 | 90,60 |
| **i** | 1 | 3324,7 | 3324,7 | 3324,68 | 527,72 | 0,000 | 26,46 |
| **h** | 1 | 1134,3 | 1134,3 | 1134,34 | 180,05 | 0,000 | 9,03 |
| **v** | 1 | 35,8 | 35,8 | 35,79 | 5,68 | 0,025 | 0,28 |
| **f** | 1 | 3664,5 | 3664,5 | 3664,49 | 581,65 | 0,000 | 29,17 |
| **a** | 1 | 3224,3 | 3224,3 | 3224,25 | 511,78 | 0,000 | 25,66 |
| **Square** | 5 | 710,8 | 710,8 | 142,17 | 22,57 | 0,000 | 5,66 |
| **i*i** | 1 | 498,2 | 260,9 | 260,95 | 41,42 | 0,000 | 3,97 |
| **h*h** | 1 | 0,1 | 15,7 | 15,71 | 2,49 | 0,127 | 0,00 |
| **v*v** | 1 | 6,7 | 5,3 | 5,32 | 0,85 | 0,367 | 0,05 |
| **f*f** | 1 | 29,6 | 78,4 | 78,38 | 12,44 | 0,002 | 0,24 |
| **a*a** | 1 | 176,2 | 176,2 | 176,16 | 27,96 | 0,000 | 1,40 |
| **Interaction** | 10 | 312,8 | 312,8 | 31,28 | 4,97 | 0,001 | 2,49 |
| **i*h** | 1 | 3,3 | 3,3 | 3,33 | 0,53 | 0,474 | 0,03 |
| **i*v** | 1 | 1,7 | 1,7 | 1,72 | 0,27 | 0,606 | 0,01 |
| **i*f** | 1 | 68,0 | 68,0 | 67,98 | 10,79 | 0,003 | 0,54 |
| **i*a** | 1 | 97,6 | 97,6 | 97,61 | 15,49 | 0,001 | 0,78 |
| **h*v** | 1 | 4,1 | 4,1 | 4,06 | 0,64 | 0,430 | 0,03 |
| **h*f** | 1 | 26,6 | 26,6 | 26,63 | 4,23 | 0,050 | 0,21 |
| **h*a** | 1 | 1,2 | 1,2 | 1,21 | 0,19 | 0,665 | 0,01 |
| **v*f** | 1 | 10,3 | 10,3 | 10,27 | 1,63 | 0,213 | 0,08 |
| **v*a** | 1 | 9,6 | 9,6 | 9,58 | 1,52 | 0,229 | 0,08 |
| **f*a** | 1 | 90,4 | 90,4 | 90,44 | 14,36 | 0,001 | 0,72 |
| **Residual Error** | 25 | 157,5 | 157,5 | 6,30 | | | 1,25 |
| **Lack-of-Fit** | 20 | 148,6 | 148,6 | 7,43 | 4,20 | 0,059 | 1,18 |
| **Pure Error** | 5 | 8,9 | 8,9 | 1,77 | | | 0,07 |
| **Total** | 45 | 12564,7 | | | | | 100,00 |
| **Model summary** S = 2,51001; R-Sq = 98,75%; R-Sq(pred) = 95,17%; R-Sq(adj) = 97,74% | | | | | | | |

The percentage contributions of machining parameters on Fx are shown in Table 4.5. Percentage contributions of insert (i), hardness (h), cutting speed (v), feed rate (f), depth of cut (a), and on Fx were found to be 26,46%, 9,03%, 0,28%, 29,17%, and 25,66%, respectively. It appears that feed rate is the most significant parameter. In addition to these, other contributions on Fx are square, interaction, and residual error. These are 5,66, 2,49, and 1,25 percent, respectively.

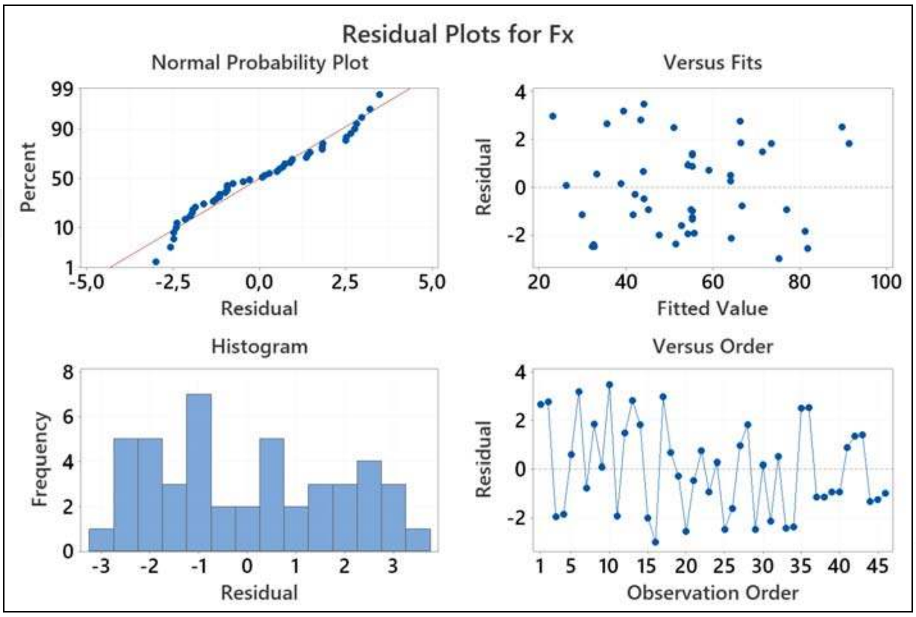

Figure 4.4. Residual plots for Fx

As shown of Residual plots for Fx in Figure 4.4, the residuals are normally distributed if the points on the Normal Probability Plot form an approximately linear line. The residuals have constant variance because residuals are scattered randomly around zero on the Versus Fits graph. In this case, the model is valid. The Histogram chart is used to evaluate the shape and spread of data. The Histogram chart below shows that the data is normally distributed such as bell shape. Ideally, the residuals on Versus Order plot should occur randomly around the zero line. The residuals in this plot are appeared to fluctuate in a down and up around the zero line. From the investigation of the Residual Plots for Fx, it is concluded that the model can accurately predict Fx.

Figures 4.5-4.7 surface plots show that the highest Fx is obtained when f and a level is the highest. This result can be explained by the simultaneous increase of amount of material removed from the workpiece per unit time with the rise of f and a (Özdemir et al., 2020). There appears to be a peak at about f = 0,10 and a = 0,20. It is determined that the cutting speed is not as effective as feed rate (f) and depth of cut (a) on Fx.

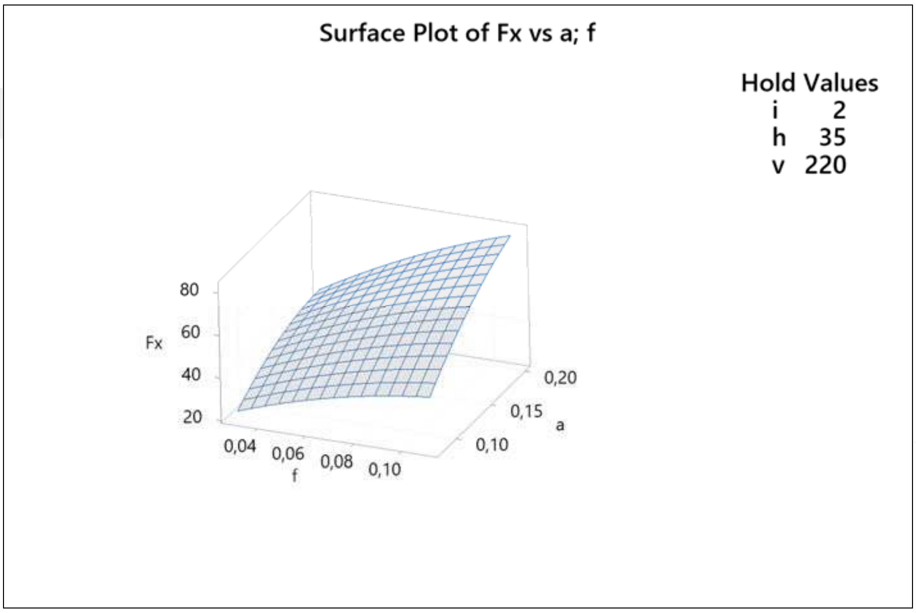

Figure 4.5. Surface plot of Fx vs a;f

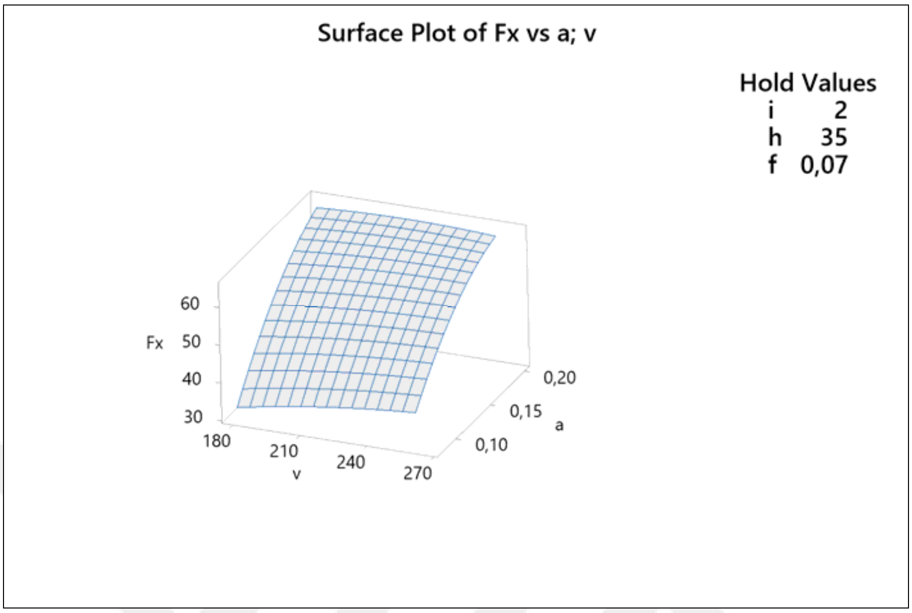


Figure 4.6. Surface plot of Fx vs a;v

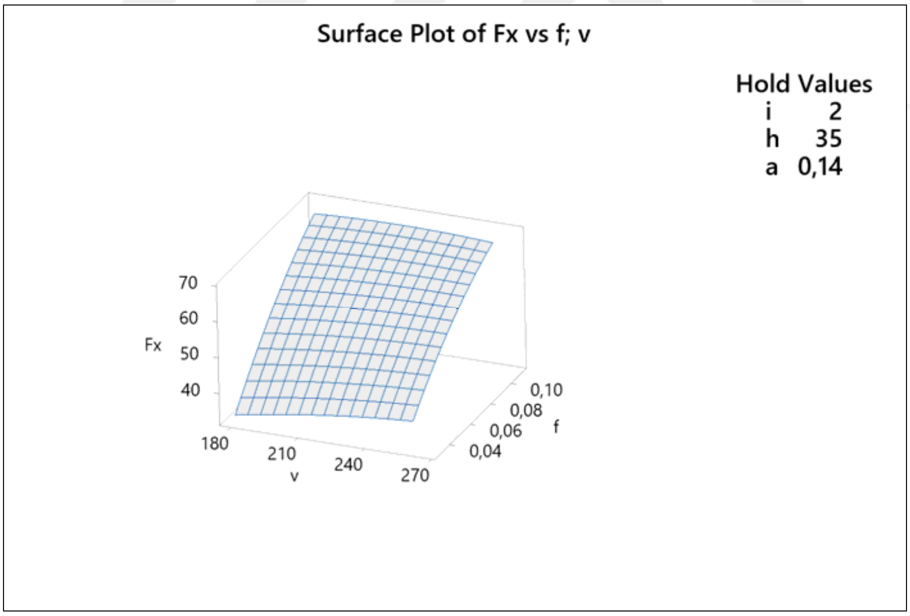


Figure 4.7. Surface plot of Fx vs f;v

Effects of process parameters of h, a, v, and f on Fx are depicted using surface plots in Figures 4.8-4.10. The lowest Fx values are found at the points that h and a both have the lowest values as shown in Figure 4.8. As h and a or h and f move toward their high values, values for Fx increase steadily. The following surface plots from Figure 4.8 to Figure 4.10 show that feed rate is the most influential machining parameter affecting the Fx. Workpiece hardness has a significant effect on the cutting forces in the machining process. The more workpiece hardness increases, the higher the cutting forces. It can be said that materials with lower hardness have higher toughness, lower strength, and therefore less cutting force is needed during the process (Zhang et al., 2016). The surface plots for Fx below confirm this.

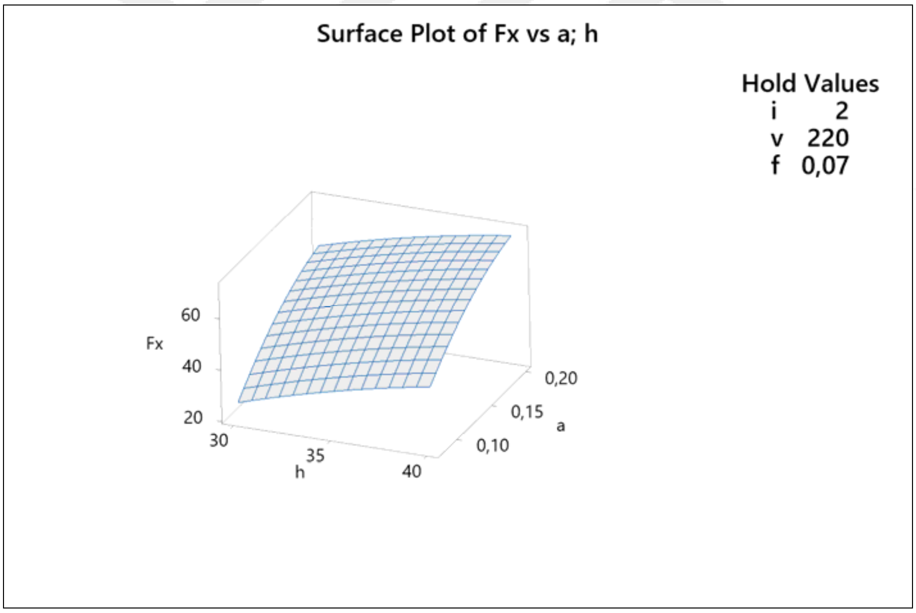


Figure 4.8. Surface plot of Fx vs a;h

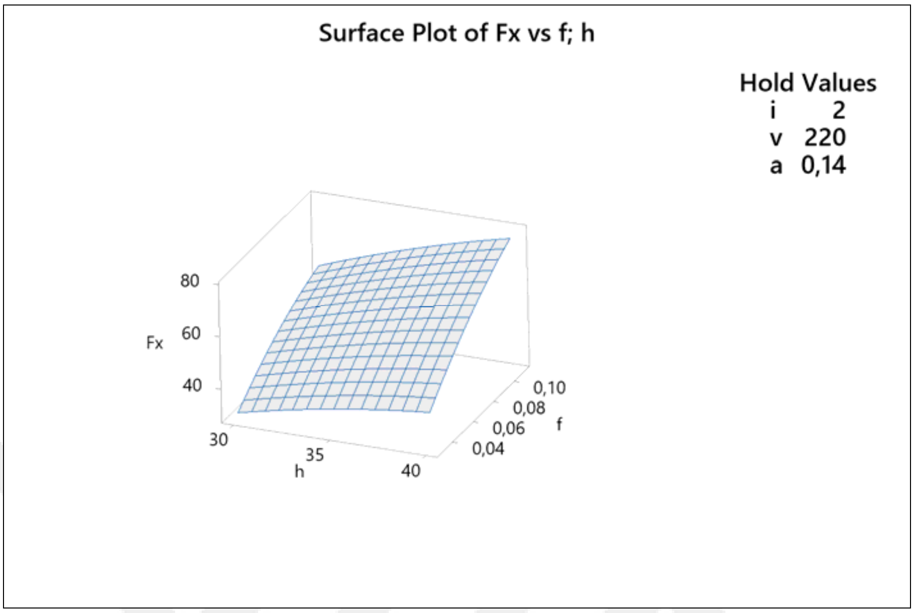


Figure 4.9. Surface plot of Fx vs f;h

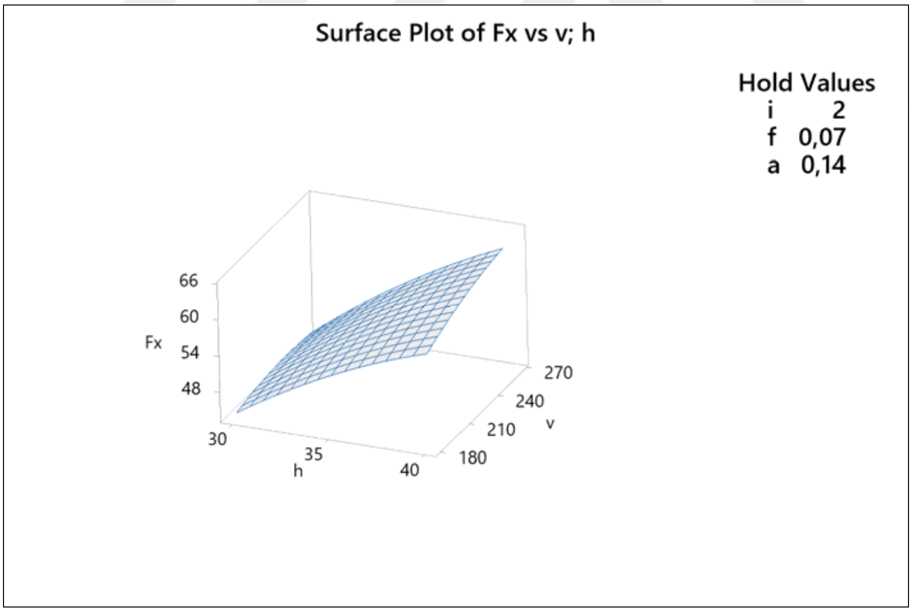


Figure 4.10. Surface plot of Fx vs v;h

The variation of the Fx depending on i, h, f, a, and v machining parameters is shown in Figures 4.11-4.14 with surface plots. The following surface plots depicted in Figures 4.11, 4.12, 4.14 show that Fx increases as levels of machining parameters rise. However, Fx increases a little whereas i and v levels rise significantly as shown in Figure 4.13. It has been determined that the cutting speed has almost no effect or little effect on the Fx. In this study, three different inserts (1: ceramic, 2: carbide, and 3: CBN) were used. The surface plots from Figure 4.11 to Figure 4.14 show that the highest Fx occurred using the CBN insert.

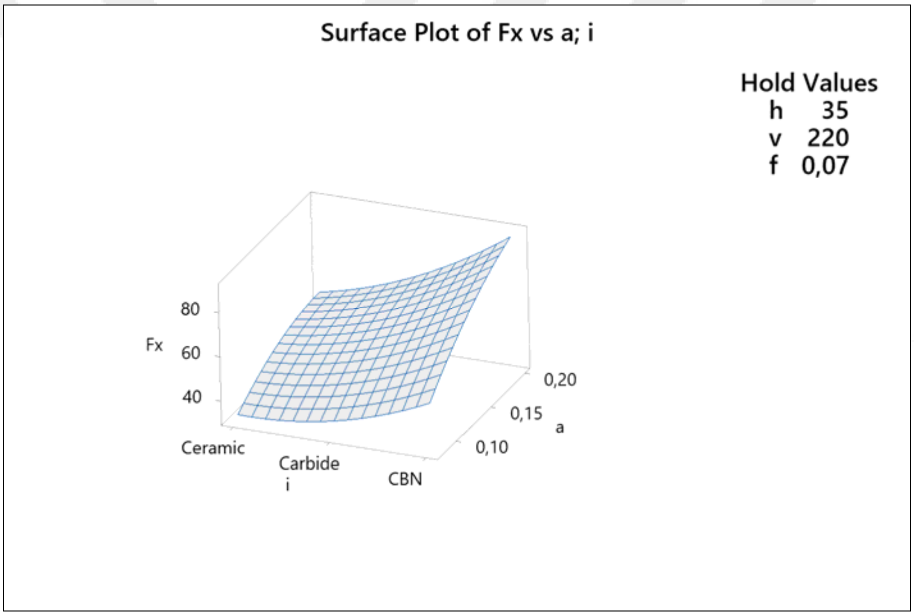


Figure 4.11. Surface plot of Fx vs a;i

The lowest Fx was obtained when the ceramic insert was used. Looking at the results, forces are affected by cutting tool materials. CBN insert caused greater forces during machining when CBN compared to the ceramic and carbide insert. When the cutting tool materials are ordered from hardest to softest, the hardest material is CBN. Carbide has the highest toughness (Smith, 2008). This case can be explained by the high hardness of CBN insert according to ceramic and carbide inserts (Rafighi et al., 2021).

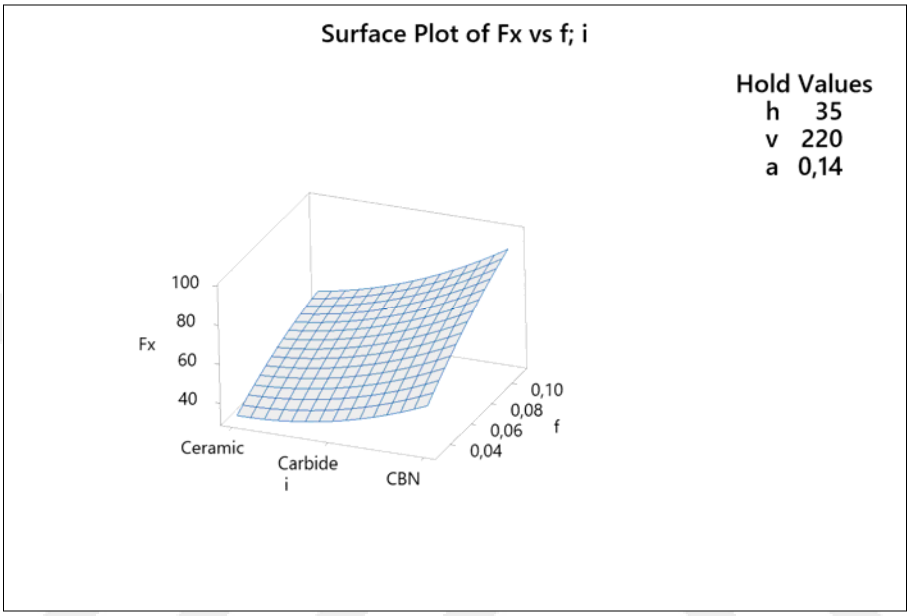


Figure 4.12. Surface plot of Fx vs f;i

In addition, the wear properties of CBN, ceramic, and carbide inserts are opposite to the hardness property. The carbide insert wears the most and the CBN insert wears the least. It can be said that the increase in cutting forces is due to the wear on the carbide insert during turning. Likewise, factors such as negative rake angle, vibration, plastic deformation of the tool, chip jamming, BUE, temperature, friction in the tool-chip interface can result in higher cutting forces. So, when carbide is used, it may have generated more force due to the above reasons.

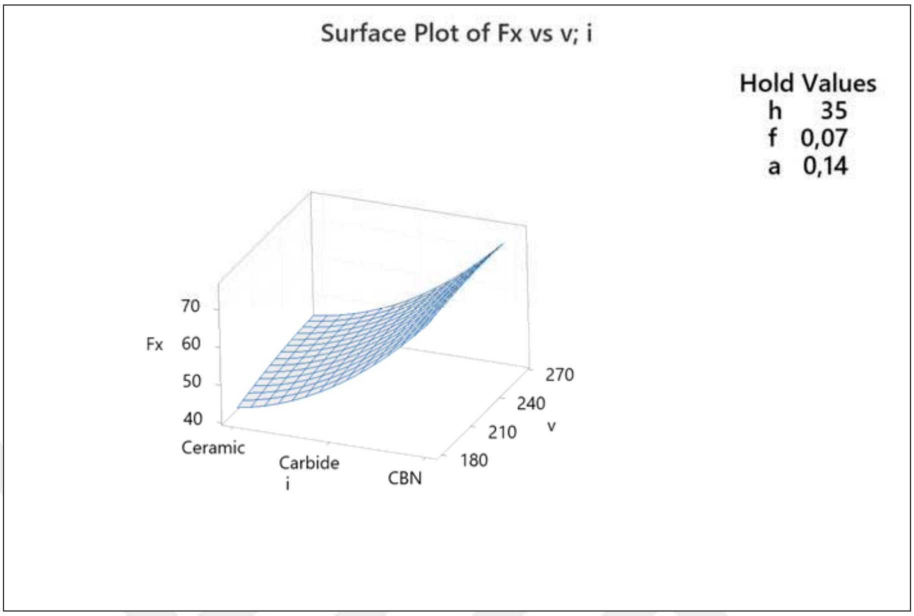


Figure 4.13. Surface plot of Fx vs v;i

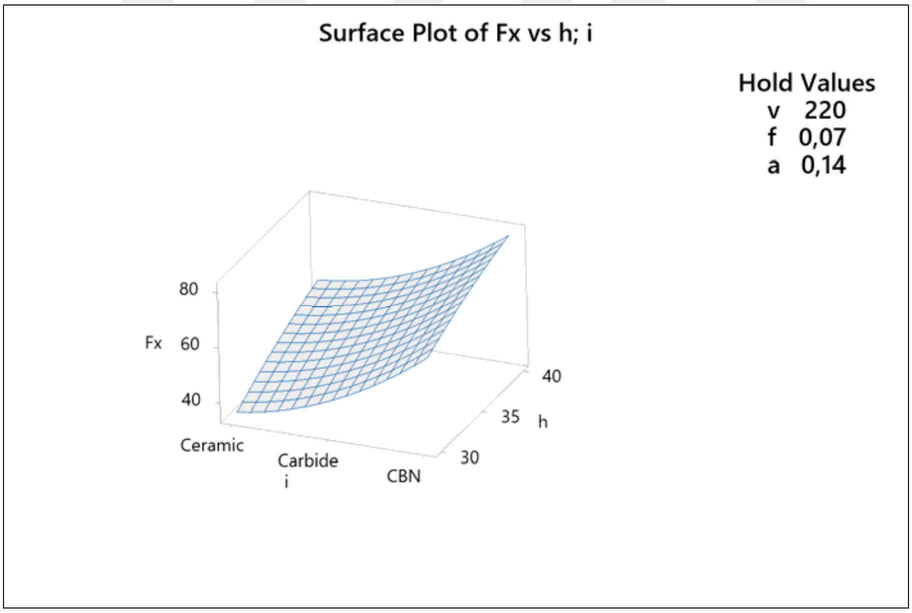


Figure 4.14. Surface plot of Fx vs h;i

Taguchi experiments, it always is maximized the SN ratio. Taguchi design method shows that the optimum levels of factors for Fx values can be determined. The optimum level for factors is achieved according to the highest SN ratio in all levels of those factors. The levels of the factors giving the optimum Fx value are seen as i1 (Level 1), h1 (Level 1), v1 (Level 1), f1 (Level 1), and a1 (Level 1). That is to say, the optimum Fx value is found with ceramic insert (i1), 30 HRC hardness (h1), 180 m/min cutting speed (v1), 0,03 mm/rev feed rate (f1), and 0,08 mm depth of cut (a1) as shown in Figure 4.15.

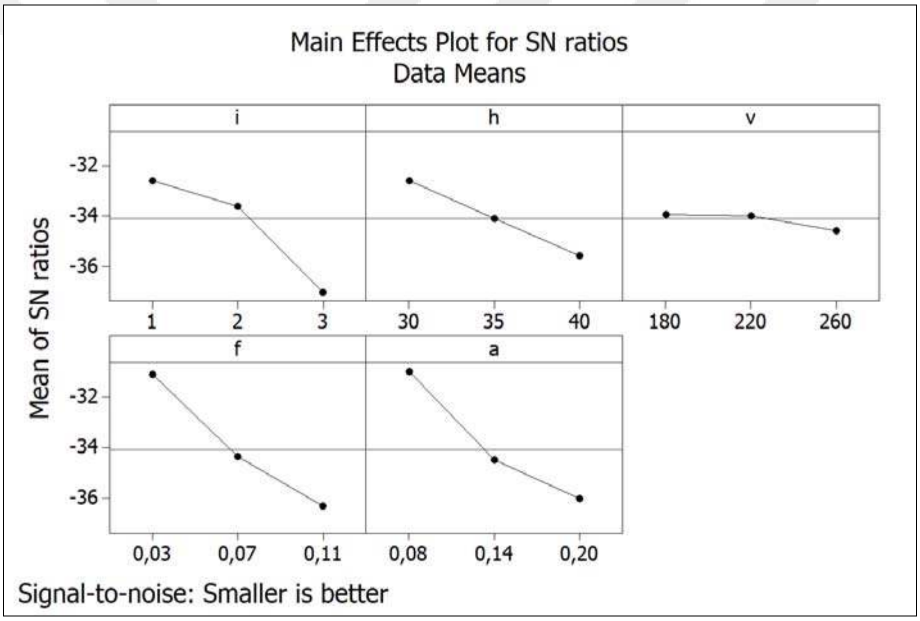

Figure 4.15. Main effects plot for SN ratios of Fx

After optimum parameters are read from the Main effects plot for SN ratios of Fx, optimization Plot is run for optimum level (A1B1C1D1E1) of Fx as shown in Figure 4.16. The optimum value of Fx is predicted as 9,51 N.

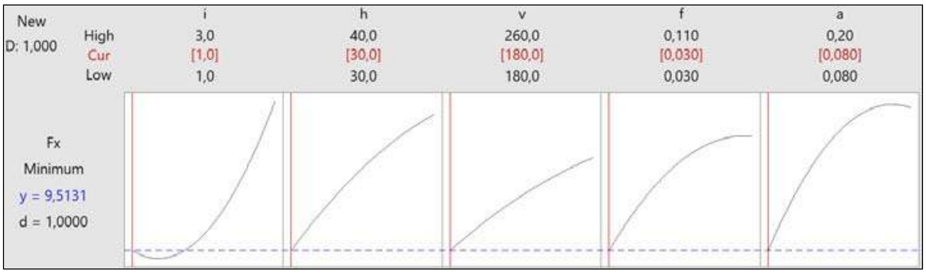

Figure 4.16. Optimization plot for Fx

Experimental modeling equations in coded and uncoded formats are given in Equation 4.5 and Equation 4.6, respectively. They have been developed considering the relationship between Fx and machining parameters (i, h, v, f, a).

$$Fx = 55,1800 + 14,4150\ A + 8,4200\ B + 1,4956\ C + 15,1338\ D + 14,1956\ E + 5,4681\ A*A - 1,3419\ B*B - 0,7810\ C*C - 2,9969\ D*D - 4,4927\ E*E - 0,9125\ A*B - 0,6550\ A*C + 4,1225\ A*D + 4,9400\ A*E + 1,0075\ B*C + 2,5800\ B*D - 0,5500\ B*E - 1,6025\ C*D - 1,5475\ C*E + 4,7550\ D*E \quad (4.5)$$

$$Fx = -138,5 - 16,2\ i + 4,05\ h + 0,269\ v - 74\ f + 489\ a + 5,468\ i*i - 0,0537\ h*h - 0,000488\ v*v - 1873\ f*f - 1248\ a*a - 0,182\ i*h - 0,0164\ i*v + 103,1\ i*f + 82,3\ i*a + 0,00504\ h*v + 12,90\ h*f - 1,83\ h*a - 1,002\ v*f - 0,645\ v*a + 1981\ f*a \quad (4.6)$$

A comparison of experimental and predicted Fx values is shown in Table 4.6. Fx is predicted using developed experimental modeling equations. An error is found in a range of 0,27-11,33 percent. When Table 4.6 is analyzed, it is seen that % Error are obtained within acceptable limits (Kuntoğlu et al., 2020; Laghari et al., 2020).

Table 4.6. Comparison of experimental and predicted results for Fx

| Runs | Experimental value | Predicted value | Error (%) |
|---|---|---|---|
| 1 | 38,20 | 35,56 | 6,91 |
| 2 | 68,96 | 66,21 | 3,98 |
| 3 | 52,26 | 54,22 | 3,76 |
| 4 | 79,37 | 81,23 | 2,34 |
| 5 | 33,74 | 33,17 | 1,69 |
| 6 | 42,55 | 39,37 | 7,48 |
| 7 | 65,86 | 66,64 | 1,19 |
| 8 | 68,26 | 66,43 | 2,68 |
| 9 | 26,25 | 26,18 | 0,27 |
| 10 | 47,59 | 44,12 | 7,29 |
| 11 | 53,73 | 55,67 | 3,61 |
| 12 | 72,87 | 71,41 | 2,00 |
| 13 | 46,11 | 43,30 | 6,09 |
| 14 | 75,25 | 73,44 | 2,40 |
| 15 | 45,60 | 47,60 | 4,39 |
| 16 | 72,12 | 75,12 | 4,16 |
| 17 | 26,07 | 23,12 | 11,33 |
| 18 | 44,54 | 43,87 | 1,50 |
| 19 | 41,71 | 42,00 | 0,69 |
| 20 | 79,20 | 81,77 | 3,25 |
| 21 | 43,67 | 44,15 | 1,10 |
| 22 | 59,70 | 58,97 | 1,22 |
| 23 | 44,19 | 45,13 | 2,12 |
| 24 | 64,25 | 63,98 | 0,42 |
| 25 | 29,74 | 32,23 | 8,36 |
| 26 | 51,19 | 52,81 | 3,16 |
| 27 | 55,19 | 54,25 | 1,71 |
| 28 | 93,13 | 91,32 | 1,94 |
| 29 | 30,17 | 32,67 | 8,28 |
| 30 | 38,91 | 38,75 | 0,40 |
| 31 | 62,00 | 64,15 | 3,47 |
| 32 | 64,55 | 64,05 | 0,77 |
| 33 | 30,06 | 32,48 | 8,07 |
| 34 | 49,04 | 51,43 | 4,88 |
| 35 | 53,48 | 51,00 | 4,64 |
| 36 | 92,22 | 89,71 | 2,73 |
| 37 | 28,71 | 29,87 | 4,03 |
| 38 | 40,39 | 41,55 | 2,87 |
| 39 | 54,03 | 54,98 | 1,75 |
| 40 | 76,03 | 76,98 | 1,24 |
| 41 | 56,06 | 55,18 | 1,57 |
| 42 | 56,52 | 55,18 | 2,37 |
| 43 | 56,56 | 55,18 | 2,44 |
| 44 | 53,84 | 55,18 | 2,49 |
| 45 | 53,92 | 55,18 | 2,34 |
| 46 | 54,18 | 55,18 | 1,85 |

### 4.1.2. Tangential Force (Fy) Analysis

Percentage contributions of machining parameters on Fy are shown in Table 4.7. Percentage contributions of insert (i), hardness (h), cutting speed (v), feed rate (f), and depth of cut (a) on Fy were found to be 7,06%, 0,07%, 0,19%, 44,74%, and 41,69%, respectively. It appears that feed rate is the most significant parameter. In addition to these, other contributions on Fy are square, interaction, and residual error. These are 2,48, 2,56, and 1,20 percent, respectively.

Table 4.7. Analysis of variance for Fy

| Source | DF | Seq SS | Adj SS | Adj MS | F | P | % Cont. |
|---|---|---|---|---|---|---|---|
| **Regression** | 20 | 8774,76 | 8774,76 | 438,74 | 102,50 | 0,000 | 98,80 |
| **Linear** | 5 | 8326,73 | 8326,73 | 1665,35 | 389,08 | 0,000 | 93,75 |
| **i** | 1 | 627,13 | 627,13 | 627,13 | 146,52 | 0,000 | 7,06 |
| **h** | 1 | 6,15 | 6,15 | 6,15 | 1,44 | 0,242 | 0,07 |
| **v** | 1 | 17,02 | 17,02 | 17,02 | 3,98 | 0,057 | 0,19 |
| **f** | 1 | 3973,41 | 3973,41 | 3973,41 | 928,33 | 0,000 | 44,74 |
| **a** | 1 | 3703,03 | 3703,03 | 3703,03 | 865,16 | 0,000 | 41,69 |
| **Square** | 5 | 220,68 | 220,68 | 44,14 | 10,31 | 0,000 | 2,48 |
| **i*i** | 1 | 194,14 | 173,45 | 173,45 | 40,52 | 0,000 | 2,19 |
| **h*h** | 1 | 13,40 | 10,93 | 10,93 | 2,55 | 0,123 | 0,15 |
| **v*v** | 1 | 3,14 | 1,67 | 1,67 | 0,39 | 0,538 | 0,04 |
| **f*f** | 1 | 9,16 | 7,09 | 7,09 | 1,66 | 0,210 | 0,10 |
| **a*a** | 1 | 0,84 | 0,84 | 0,84 | 0,20 | 0,662 | 0,01 |
| **Interaction** | 10 | 227,35 | 227,35 | 22,74 | 5,31 | 0,000 | 2,56 |
| **i*h** | 1 | 0,19 | 0,19 | 0,19 | 0,05 | 0,833 | 0,00 |
| **i*v** | 1 | 3,92 | 3,92 | 3,92 | 0,92 | 0,348 | 0,04 |
| **i*f** | 1 | 12,64 | 12,64 | 12,64 | 2,95 | 0,098 | 0,14 |
| **i*a** | 1 | 13,69 | 13,69 | 13,69 | 3,20 | 0,086 | 0,15 |
| **h*v** | 1 | 5,78 | 5,78 | 5,78 | 1,35 | 0,256 | 0,07 |
| **h*f** | 1 | 2,54 | 2,54 | 2,54 | 0,59 | 0,448 | 0,03 |
| **h*a** | 1 | 2,43 | 2,43 | 2,43 | 0,57 | 0,458 | 0,03 |
| **v*f** | 1 | 0,05 | 0,05 | 0,05 | 0,01 | 0,918 | 0,00 |
| **v*a** | 1 | 1,28 | 1,28 | 1,28 | 0,30 | 0,590 | 0,01 |
| **f*a** | 1 | 184,82 | 184,82 | 184,82 | 43,18 | 0,000 | 2,08 |
| **Residual Error** | 25 | 107,00 | 107,00 | 4,28 | | | 1,20 |
| **Lack-of-Fit** | 20 | 105,25 | 105,25 | 5,26 | 15,03 | 0,003 | 1,19 |
| **Pure Error** | 5 | 1,75 | 1,75 | 0,35 | | | 0,02 |
| **Total** | 45 | 8881,76 | | | | | 100,00 |
| **Model summary**<br>S = 2,06886, R-Sq = 98,80%, R-Sq(pred) = 95,23%, R-Sq(adj) = 97,83% | | | | | | | |

Four-in-one Residual Plots for Fy: Histogram, Normal Probability Plot, Versus Fits, and Versus Order are shown in Figure 4.17. The residuals are normally distributed if the points on the Normal Probability Plot form an approximately linear line as shown in Figure 4.17. The residuals have constant variance because residuals are scattered randomly around zero on the Versus Fits graph. In this case, the model is valid. The Histogram chart is used to evaluate the shape and spread of data. The histogram chart below shows that the data is normally distributed such as bell shape. Ideally, the residuals on Versus Order plot should occur randomly around zero line. The residuals in this plot are appeared to fluctuate in a down and up around the zero line. From the investigation of the Residual Plots, it is concluded that the model can accurately predict Fy.

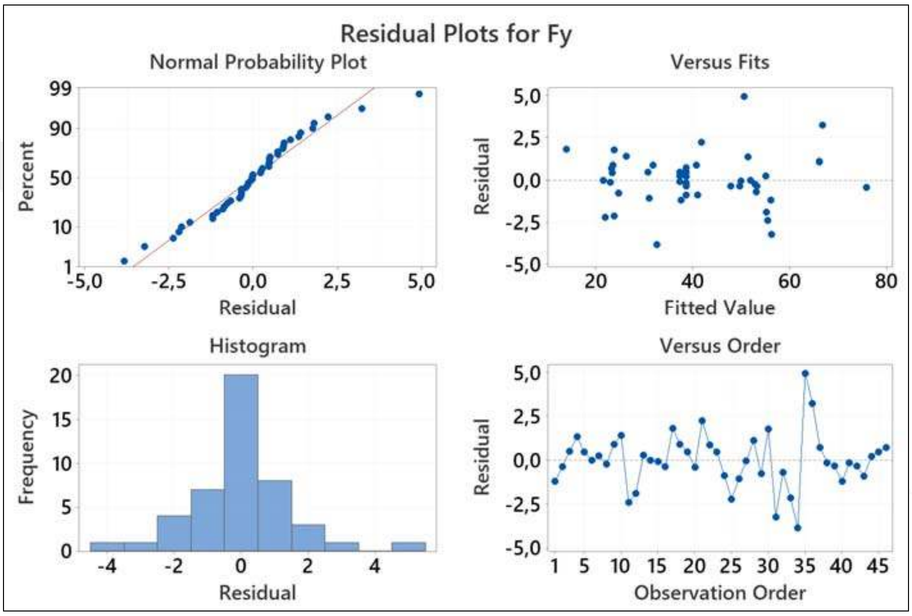


Figure 4.17. Residual plots for Fy

Figures 4.18-4.20 Surface Plots show that the highest Fy is obtained when f and a levels are the highest. There appears to be a peak at about f = 0,10 and a = 0,20. It is determined that the cutting speed is not as effective as feed rate (f) and depth of cut (a) on Fy.

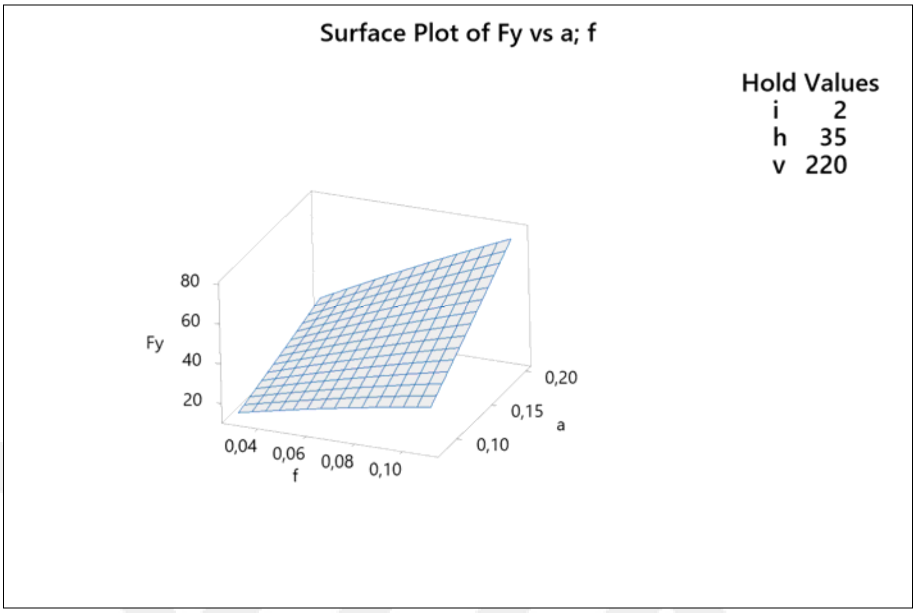


Figure 4.18. Surface plot of Fy vs a;f

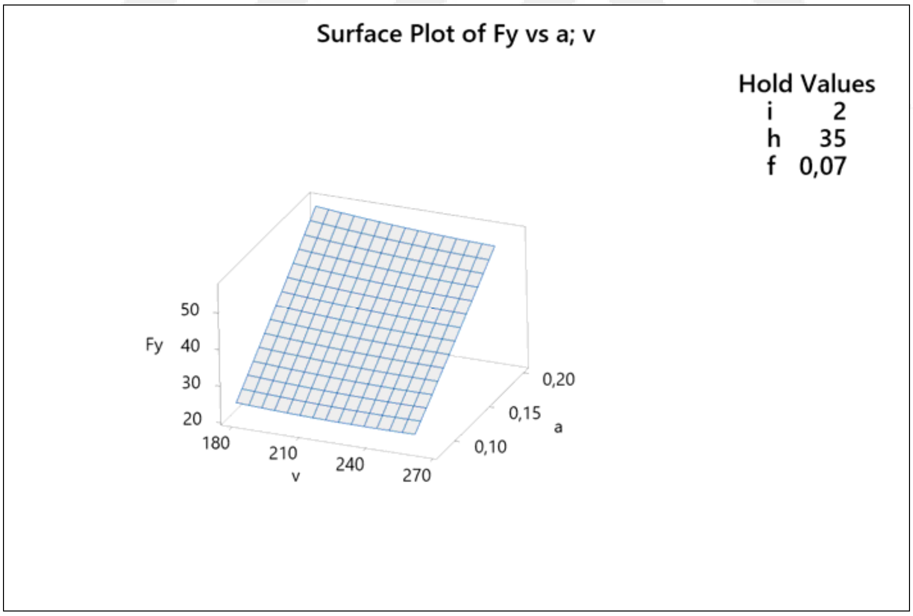


Figure 4.19. Surface plot of Fy vs a;v

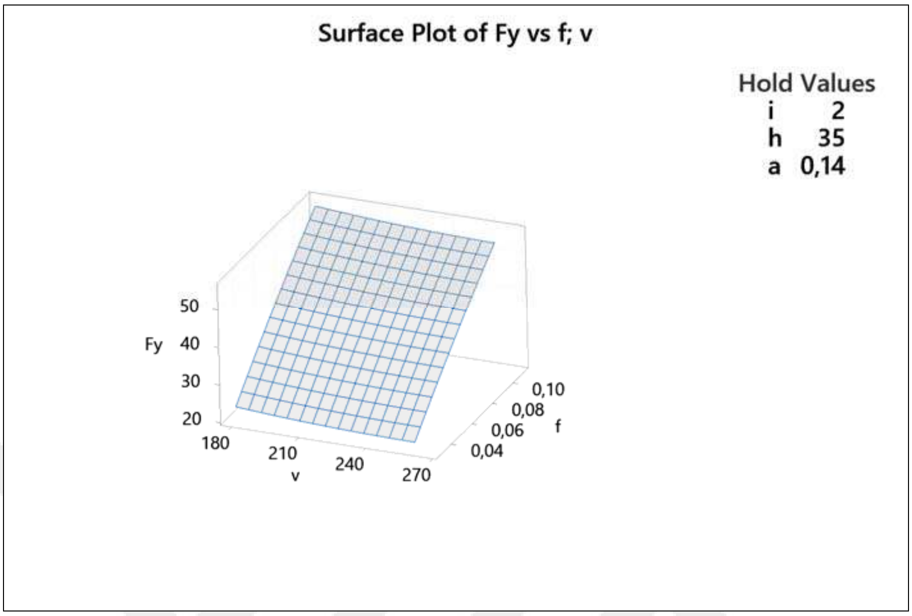


Figure 4.20. Surface plot of Fy vs f;v

Effects of process parameters of h, a, v, and f on Fy are depicted using Surface Plots in Figure 4.21-4.23. The lowest Fy values are found at the points that h;f or h;a both have the lowest values as shown in Figures 4.21, 4.22. As feed rate and depth of cut values move toward their high values, values for Fy increase steadily. The following Surface Plots from Figure 4.21 to Figure 4.23 show that feed rate and depth of cut are the most influential machining parameters affecting the Fy.

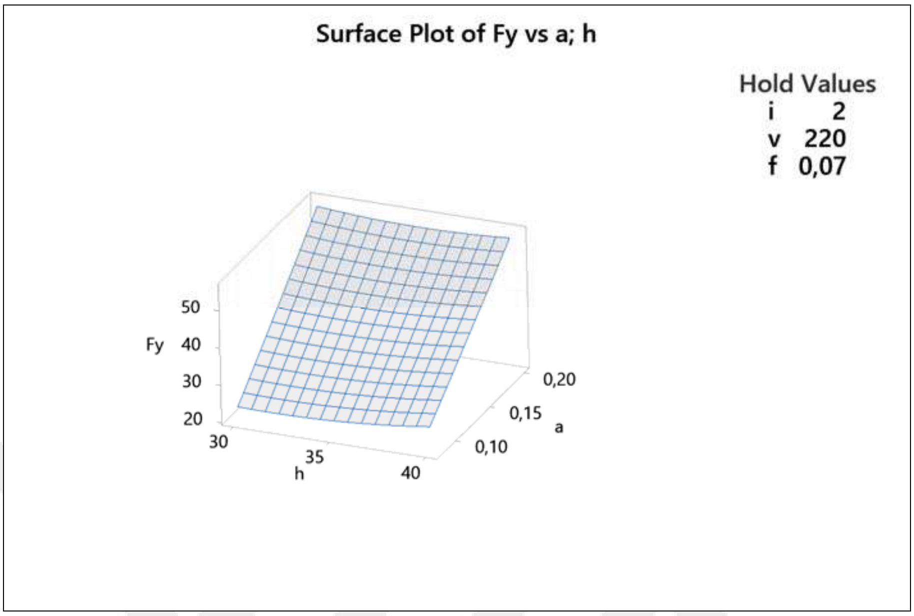


Figure 4.21. Surface plot of Fy vs a;h

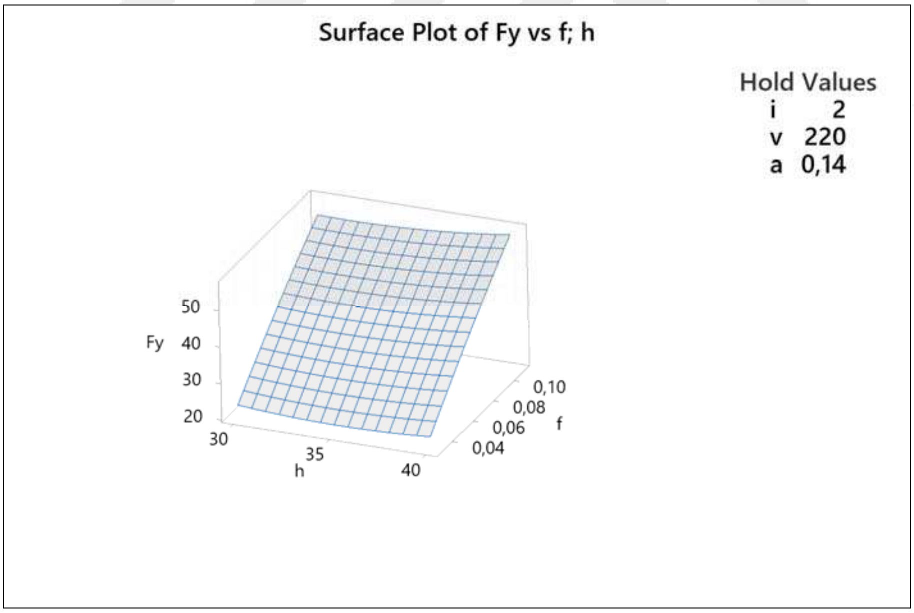


Figure 4.22. Surface plot of Fy vs f;h

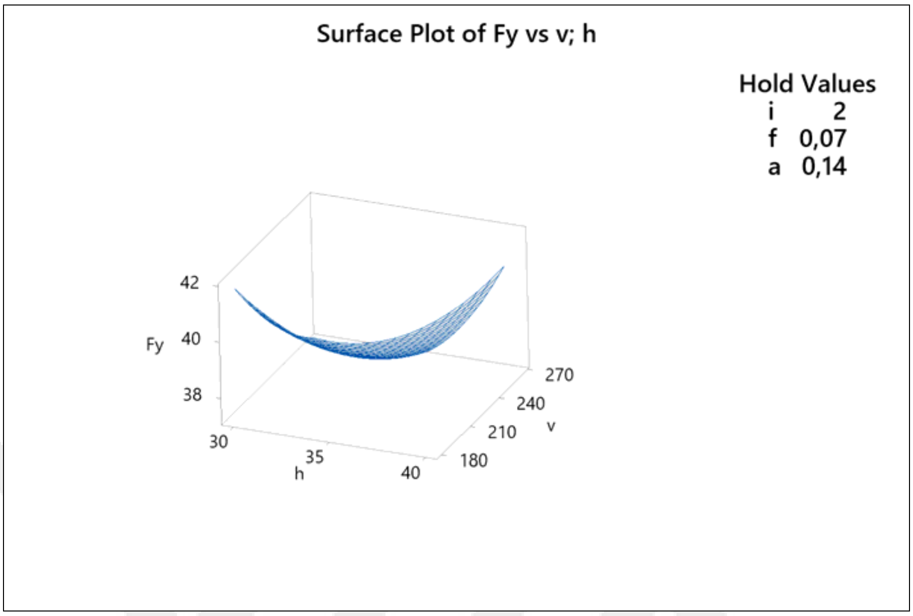


Figure 4.23. Surface plot of Fy vs v;h

The variations of the Fy depending on i, h, f, a, and v machining parameters are shown in Figures 4.24-4.27 with Surface Plots. The following Surface Plots depicted in Figures 4.24, 4.25, 4.26 show that Fy increases as levels of machining parameters rise. However, Fy increases a little whereas i and v levels rise significantly as shown in Figure 4.26. It has been determined that the cutting speed has almost no effect or little effect on the Fy. The Surface Plots from Figure 4.24 to Figure 4.27 show that the highest Fy has occurred using the CBN insert.

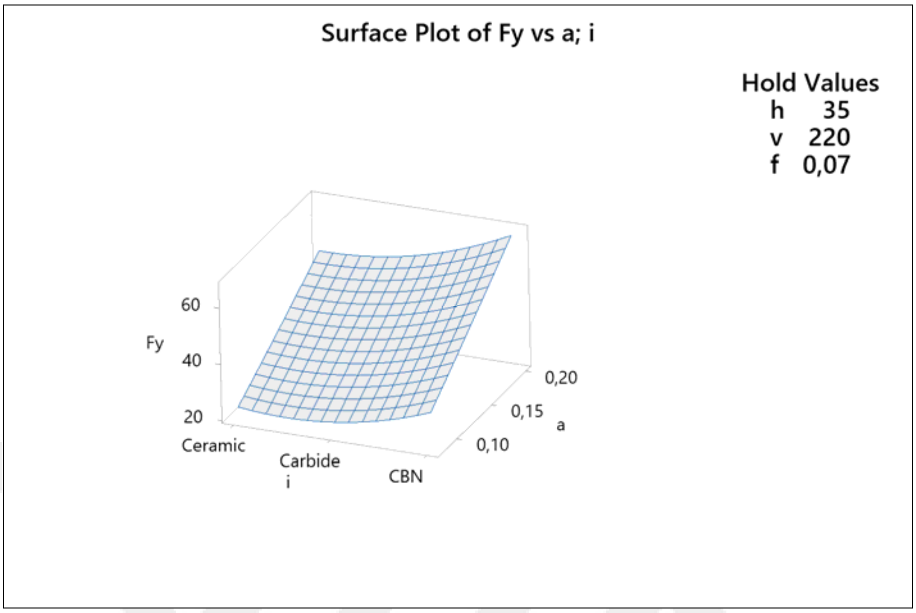


Figure 4.24. Surface plot of Fy vs a;i

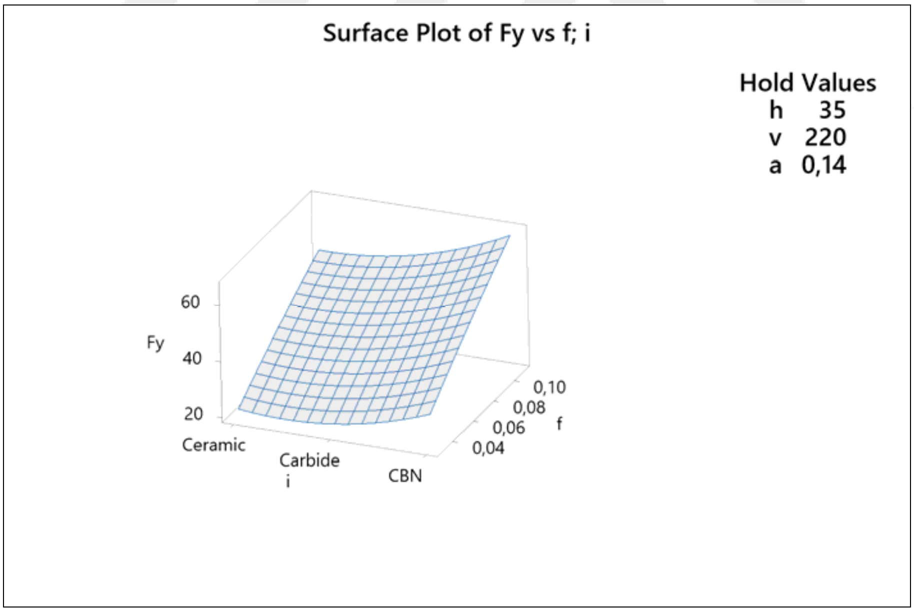


Figure 4.25. Surface plot of Fy vs f;i

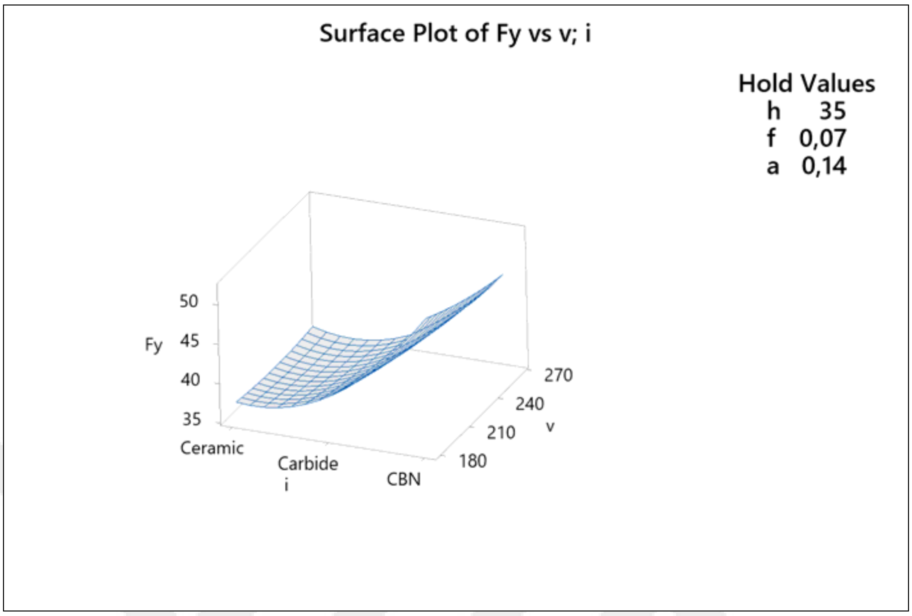


Figure 4.26. Surface plot of Fy vs v;i

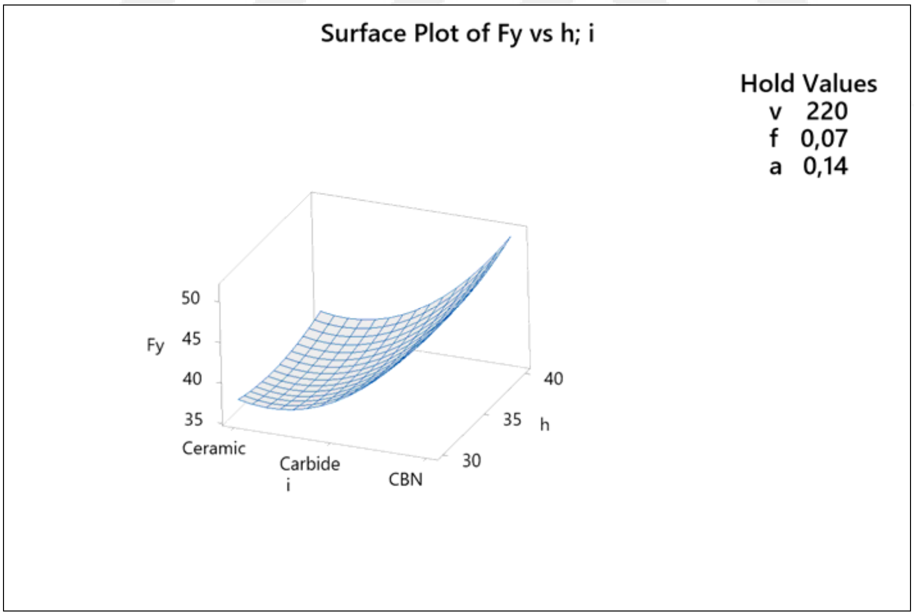


Figure 4.27. Surface plot of Fy vs h;i

The optimum level for factors is achieved according to the highest SN ratio in all levels of those factors. The levels of the factors giving the optimum Fy value are seen as i1 (Level 1), h2 (Level 2), v2,3 (Level 2,3), f1 (Level 1), and a1 (Level 1). That is to say, the optimum Fy value is found with ceramic insert (i1), 35 HRC hardness (h2), 220, 260 m/min cutting speed (V2,3), 0,03 mm/rev feed rate (f1), and 0,08 mm depth of cut (a1) as shown in Figure 4.28.

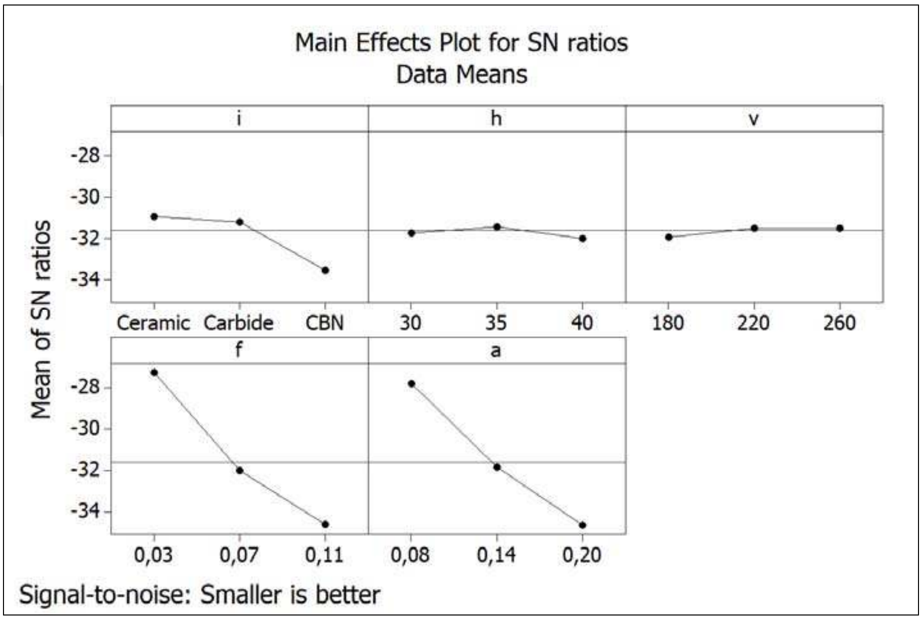

Figure 4.28. Main effects plot for SN ratios of Fy

Figure 4.29. Optimization plot for Fy

After optimum parameters are read from the Main effects plot for SN ratios of Fy, optimization Plot is run for optimum level (A1B2C2D1E1) of Fy as shown in Figure 4.29. The optimum value of Fy is predicted as 15,72 N.

An experimental modeling equation has been developed via the relationship between Fy and machining parameters (i, h, v, f, a). Experimental modeling equations of Fy in coded and uncoded formats are given in Equation 4.7 and Equation 4.8, respectively.

$$Fy = 38{,}6600 + 6{,}2606\ A + 0{,}6200\ B - 1{,}0312\ C + 15{,}7588\ D + 15{,}2131\ E + 4{,}4581\ A*A + 1{,}1190\ B*B + 0{,}4373\ C*C - 0{,}9010\ D*D + 0{,}3098\ E*E + 0{,}2200\ A*B - 0{,}9900\ A*C + 1{,}7775\ A*D + 1{,}8500\ A*E + 1{,}2025\ B*C + 0{,}7975\ B*D - 0{,}7800\ B*E - 0{,}1075\ C*D - 0{,}5650\ C*E + 6{,}7975\ D*E \quad (4.7)$$

$$Fy = 119{,}1 - 15{,}1\ i - 4{,}33\ h - 0{,}269\ v - 137\ f + 112\ a + 4{,}458\ i*i + 0{,}0448\ h*h + 0{,}000273\ v*v - 563\ f*f + 86\ a*a + 0{,}044\ i*h - 0{,}0248\ i*v + 44{,}4\ i*f + 30{,}8\ i*a + 0{,}00601\ h*v + 3{,}99\ h*f - 2{,}60\ h*a - 0{,}067\ v*f - 0{,}235\ v*a + 2832\ f*a \quad (4.8)$$

A comparison of experimental and predicted Fy values is shown in Table 4.8. Fy is predicted using a developed experimental modeling equation. An error is found in a range of 0,05-13,32 percent. When Table 4.8 is analyzed, it is seen that % Error are obtained within acceptable limits (Kuntoğlu et al., 2020; Laghari et al., 2020).

Table 4.8. Comparison of experimental and predicted results for Fy

| Runs | Experimental value | Predicted value | Error (%) |
|---|---|---|---|
| **1** | 36,37 | 37,58 | 3,32 |
| **2** | 49,3 | 49,66 | 0,73 |
| **3** | 38,87 | 38,38 | 1,27 |
| **4** | 52,68 | 51,34 | 2,55 |
| **5** | 23,81 | 23,36 | 1,88 |
| **6** | 21,5 | 21,51 | 0,06 |
| **7** | 55,33 | 55,09 | 0,43 |
| **8** | 52,59 | 52,82 | 0,43 |
| **9** | 24,37 | 23,48 | 3,67 |
| **10** | 27,67 | 26,28 | 5,04 |
| **11** | 53,07 | 55,46 | 4,51 |
| **12** | 53,25 | 55,14 | 3,55 |
| **13** | 37,6 | 37,34 | 0,70 |
| **14** | 51,81 | 51,84 | 0,05 |
| **15** | 37,17 | 37,25 | 0,22 |
| **16** | 47,42 | 47,79 | 0,79 |
| **17** | 15,69 | 13,89 | 11,44 |
| **18** | 32,72 | 31,82 | 2,76 |
| **19** | 31,2 | 30,73 | 1,52 |
| **20** | 75,42 | 75,84 | 0,55 |
| **21** | 44,05 | 41,83 | 5,04 |
| **22** | 41,54 | 40,67 | 2,11 |
| **23** | 37,84 | 37,36 | 1,26 |
| **24** | 40,14 | 41,01 | 2,16 |
| **25** | 19,77 | 21,98 | 11,15 |
| **26** | 29,87 | 30,94 | 3,59 |
| **27** | 49,9 | 49,94 | 0,08 |
| **28** | 67,11 | 66,01 | 1,63 |
| **29** | 23,88 | 24,66 | 3,27 |
| **30** | 25,5 | 23,73 | 6,95 |
| **31** | 52,98 | 56,22 | 6,11 |
| **32** | 52,34 | 53,02 | 1,31 |
| **33** | 21,66 | 23,80 | 9,90 |
| **34** | 28,79 | 32,63 | 13,32 |
| **35** | 55,45 | 50,53 | 8,87 |
| **36** | 69,98 | 66,75 | 4,61 |
| **37** | 24,01 | 23,30 | 2,97 |
| **38** | 22,8 | 22,94 | 0,62 |
| **39** | 52,87 | 53,22 | 0,66 |
| **40** | 54,85 | 56,05 | 2,20 |
| **41** | 38,5 | 38,66 | 0,42 |
| **42** | 38,31 | 38,66 | 0,91 |
| **43** | 37,76 | 38,66 | 2,38 |
| **44** | 38,88 | 38,66 | 0,57 |
| **45** | 39,12 | 38,66 | 1,18 |
| **46** | 39,39 | 38,66 | 1,85 |

### 4.1.3. Feed Force (Fz) Analysis

The percentage contributions of machining parameters on Fz are shown in Table 4.9. Percentage contributions of insert (i), hardness (h), cutting speed (v), feed rate (f), and depth of cut (a) on Fz were found to be 16,61%, 1,57%, 0,01%, 10,52%, and 53,36%, respectively. It appears that depth of cut is the most significant parameter. In addition to these, other contributions on Fz are square, interaction, and residual error. These are 12,61, 4,13, and 1,19 percent, respectively.

Table 4.9. Analysis of variance for Fz

| Source | DF | Seq SS | Adj SS | Adj MS | F | P | % Cont. |
|---|---|---|---|---|---|---|---|
| Regression | 20 | 2748,44 | 2748,44 | 137,42 | 103,43 | 0,000 | 98,81 |
| Linear | 5 | 2282,67 | 2282,67 | 456,53 | 343,62 | 0,000 | 82,06 |
| i | 1 | 462,04 | 462,04 | 462,04 | 347,76 | 0,000 | 16,61 |
| h | 1 | 43,56 | 43,56 | 43,56 | 32,79 | 0,000 | 1,57 |
| v | 1 | 0,41 | 0,41 | 0,41 | 0,31 | 0,585 | 0,01 |
| f | 1 | 292,50 | 292,50 | 292,50 | 220,15 | 0,000 | 10,52 |
| a | 1 | 1484,18 | 1484,18 | 1484,18 | 1117,10 | 0,000 | 53,36 |
| Square | 5 | 350,86 | 350,86 | 70,17 | 52,82 | 0,000 | 12,61 |
| i*i | 1 | 335,74 | 239,82 | 239,82 | 180,51 | 0,000 | 12,07 |
| h*h | 1 | 4,68 | 8,84 | 8,84 | 6,65 | 0,016 | 0,17 |
| v*v | 1 | 0,01 | 0,81 | 0,81 | 0,61 | 0,441 | 0,00 |
| f*f | 1 | 8,41 | 10,09 | 10,09 | 7,60 | 0,011 | 0,30 |
| a*a | 1 | 2,02 | 2,02 | 2,02 | 1,52 | 0,229 | 0,07 |
| Interaction | 10 | 114,90 | 114,90 | 11,49 | 8,65 | 0,000 | 4,13 |
| i*h | 1 | 4,33 | 4,33 | 4,33 | 3,26 | 0,083 | 0,16 |
| i*v | 1 | 0,98 | 0,98 | 0,98 | 0,74 | 0,399 | 0,04 |
| i*f | 1 | 4,41 | 4,41 | 4,41 | 3,32 | 0,080 | 0,16 |
| i*a | 1 | 59,91 | 59,91 | 59,91 | 45,09 | 0,000 | 2,15 |
| h*v | 1 | 0,01 | 0,01 | 0,01 | 0,01 | 0,918 | 0,00 |
| h*f | 1 | 0,58 | 0,58 | 0,58 | 0,43 | 0,516 | 0,02 |
| h*a | 1 | 0,34 | 0,34 | 0,34 | 0,25 | 0,619 | 0,01 |
| v*f | 1 | 1,46 | 1,46 | 1,46 | 1,10 | 0,304 | 0,05 |
| v*a | 1 | 0,05 | 0,05 | 0,05 | 0,04 | 0,847 | 0,00 |
| f*a | 1 | 42,84 | 42,84 | 42,84 | 32,24 | 0,000 | 1,54 |
| Residual Error | 25 | 33,21 | 33,21 | 1,33 | | | 1,19 |
| Lack-of-Fit | 20 | 31,07 | 31,07 | 1,55 | 3,63 | 0,079 | 1,12 |
| Pure Error | 5 | 2,14 | 2,14 | 0,43 | | | 0,08 |
| Total | 45 | 2781,65 | | | | | 100,00 |
| Model summary<br>S = 1,15265, R-Sq = 98,81%, R-Sq(pred) = 95,42%, R-Sq(adj) = 97,85% | | | | | | | |

As shown of Residual plots for Fz in Figure 4.30, the residuals are normally distributed if the points on the Normal Probability Plot form an approximately linear line. The residuals have constant variance because of the fact that residuals are scattered randomly around zero on the Versus Fits graph. In this case, the model has been found to be valid. The Histogram chart below shows that the data is normally distributed such as bell shape. Ideally, the residuals on Versus Order plot should occur randomly around zero line. The residuals in this plot are appeared to fluctuate in a down and up around the zero line. From the investigation of the Residual Plots of Fz, it is concluded that the model has the ability to accurately predict Fz.

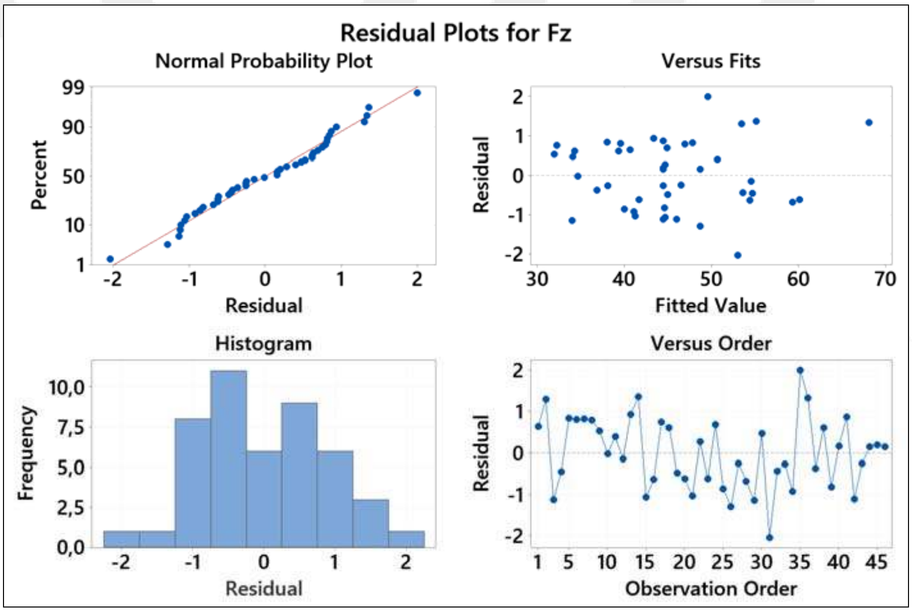


Figure 4.30. Residual plot for Fz

Surface Plots in Figures 4.31-4.33 show that the highest Fz is obtained when f and a levels are the highest. There appears to be a peak at about f = 0,10 and a = 0,20. It is determined that the cutting speed and feed rate (f) is not as effective as depth of cut (a) on Fz.

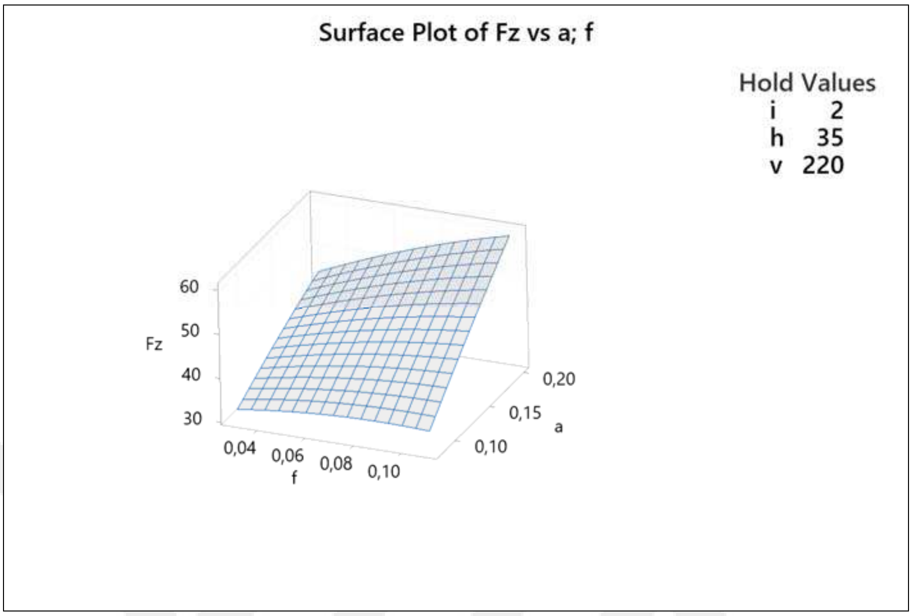


Figure 4.31. Surface plot of Fz vs a;f

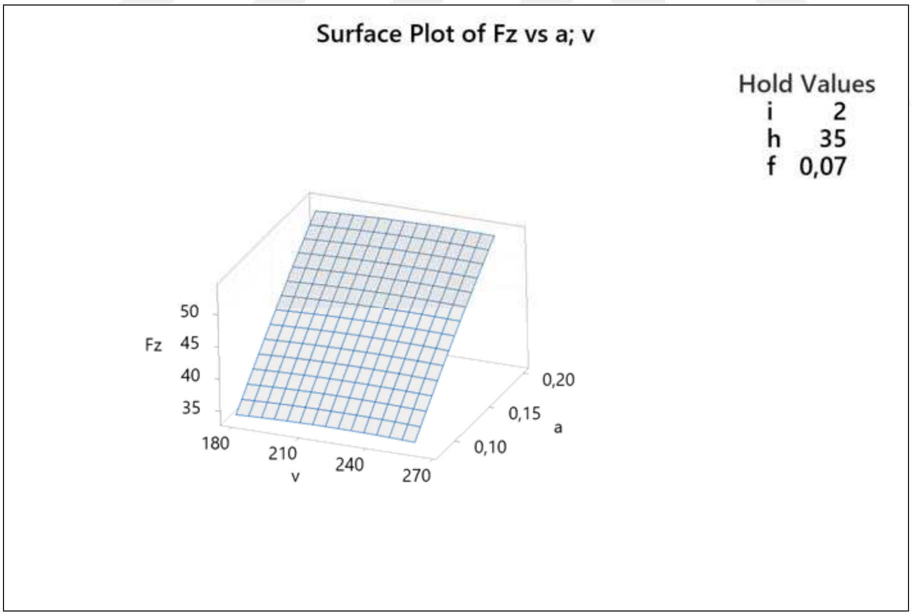


Figure 4.32. Surface plot of Fz vs a;v

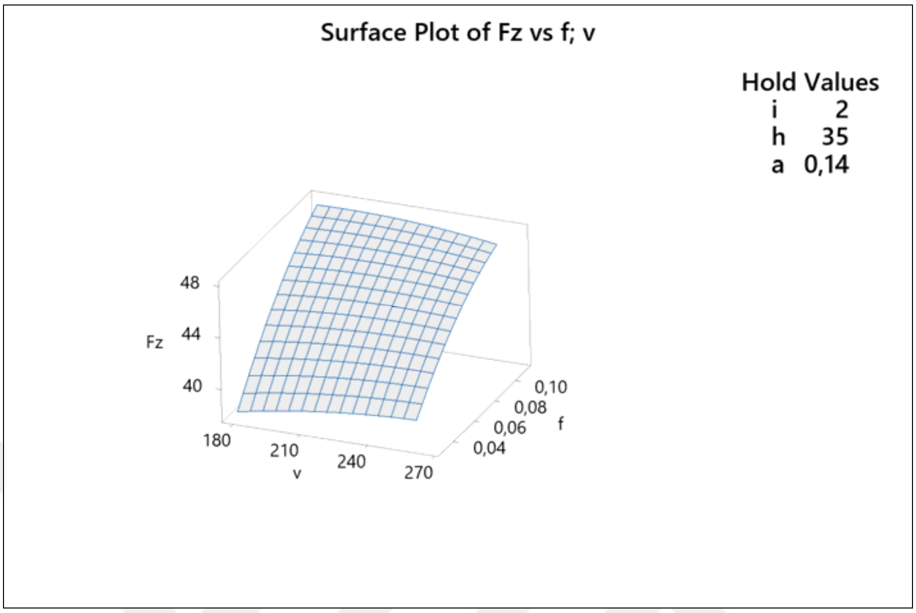

Figure 4.33. Surface plot of Fz vs f;v

Effects of process parameters of h, a, v, and f on Fz are depicted using Surface Plots in Figures 4.34-4.36. The lowest Fz values are found at the points that h;v or h;f both have the lowest values as shown in Figures 4.35, 4.36. As h and a or h and f move toward their high values, values for Fz increase steadily. The following Surface Plots from Figure 4.34 to Figure 4.36 show that depth of cut is the most influential machining parameter affecting the Fz.

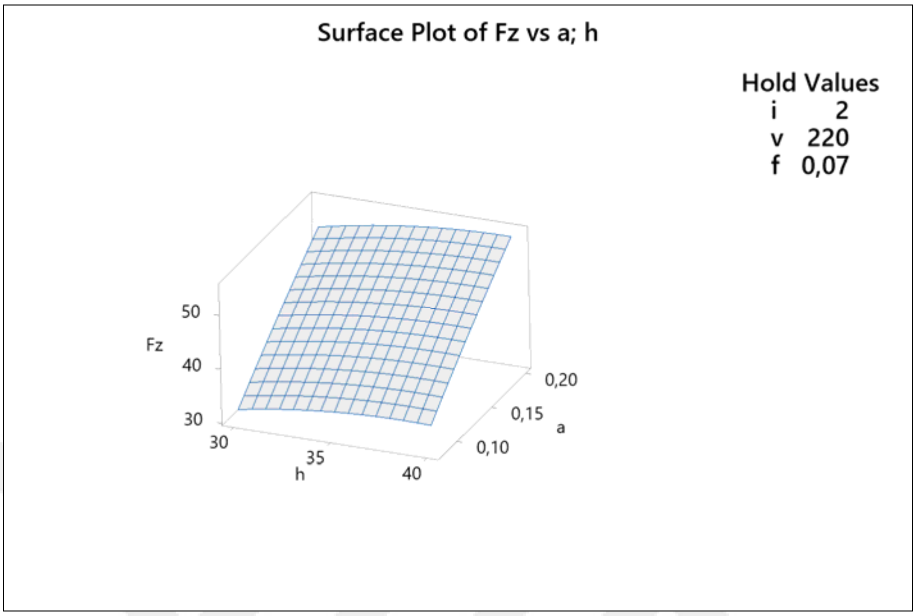


Figure 4.34. Surface plot of Fz vs a;h

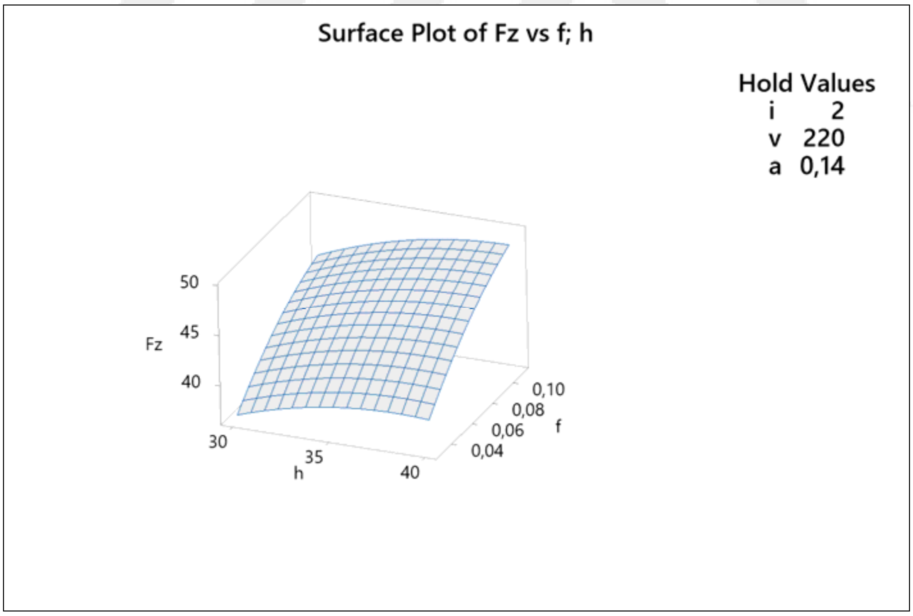


Figure 4.35. Surface plot of Fz vs f;h

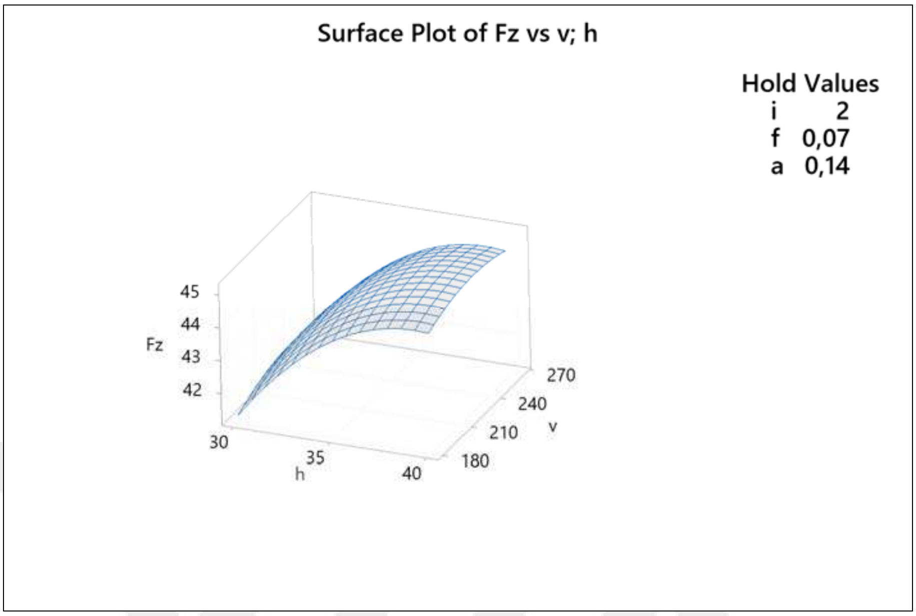


Figure 4.36. Surface plot of Fz vs v;h

The variations of the Fz depending on i, h, f, a and v machining parameters are shown in Figures 4.37-4.40 with Surface Plots. The following Surface Plots depicted in Figures 4.37, 4.38, 4.40 show that Fz increases as levels of machining parameters rise. However, Fz increases a little while i with v and i with h levels rise significantly as shown in Figures 4.39, 4.40. It has been determined that the cutting speed and hardness have little effect on the Fz. The Surface Plots from Figure 4.37 to Figure 4.40 show that the highest Fz has occurred using the CBN insert.

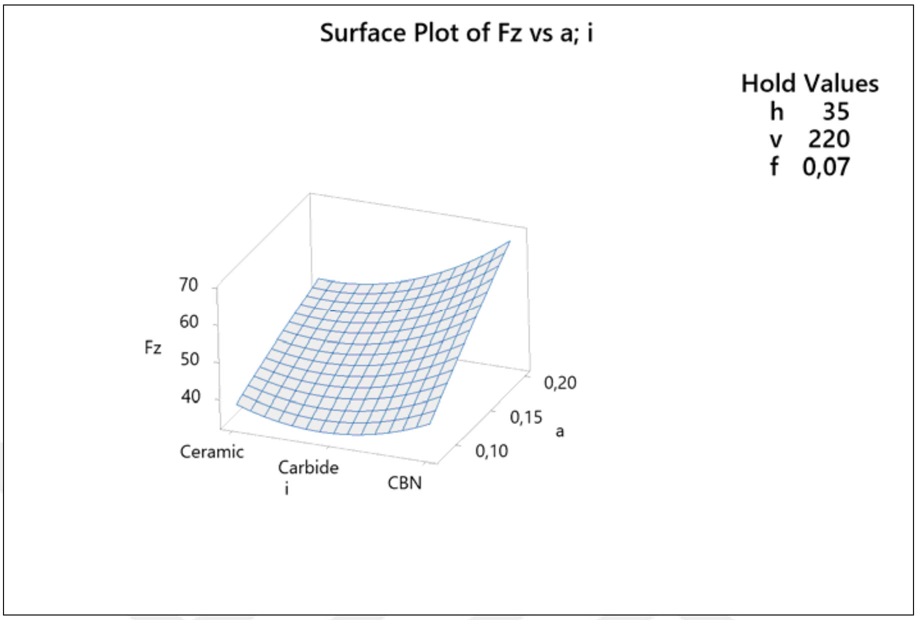


Figure 4.37. Surface plot of Fz vs a;i

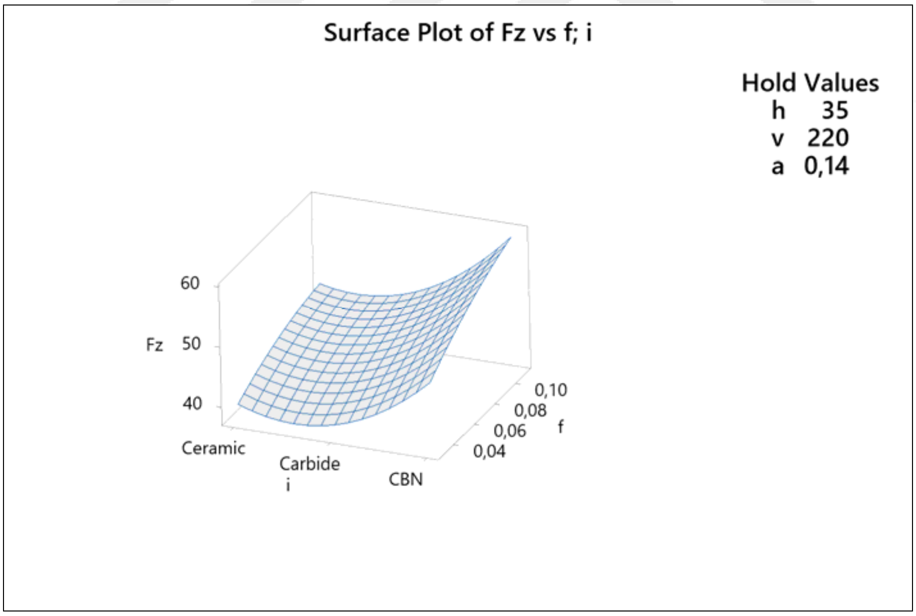


Figure 4.38. Surface plot of Fz vs f;i

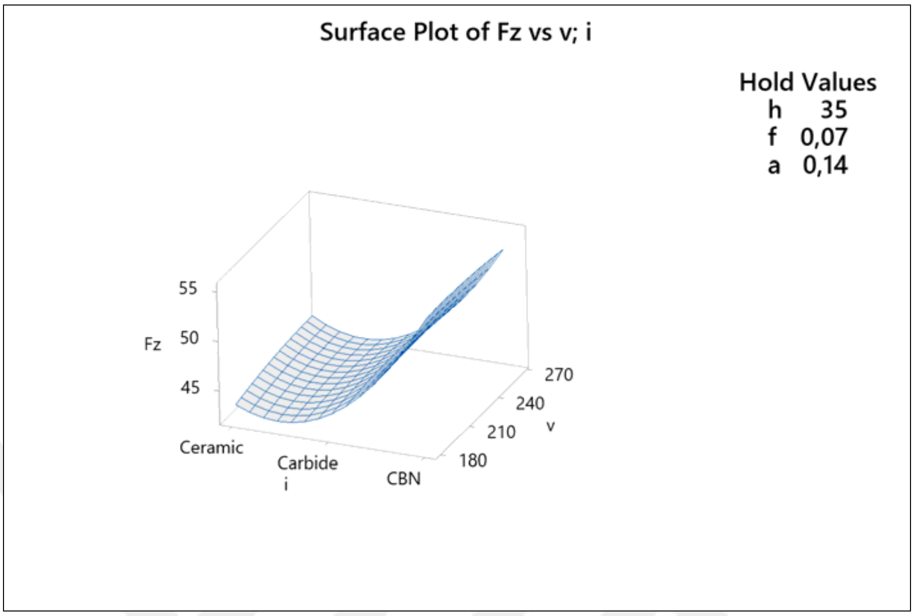


Figure 4.39. Surface plot of Fz vs v;i

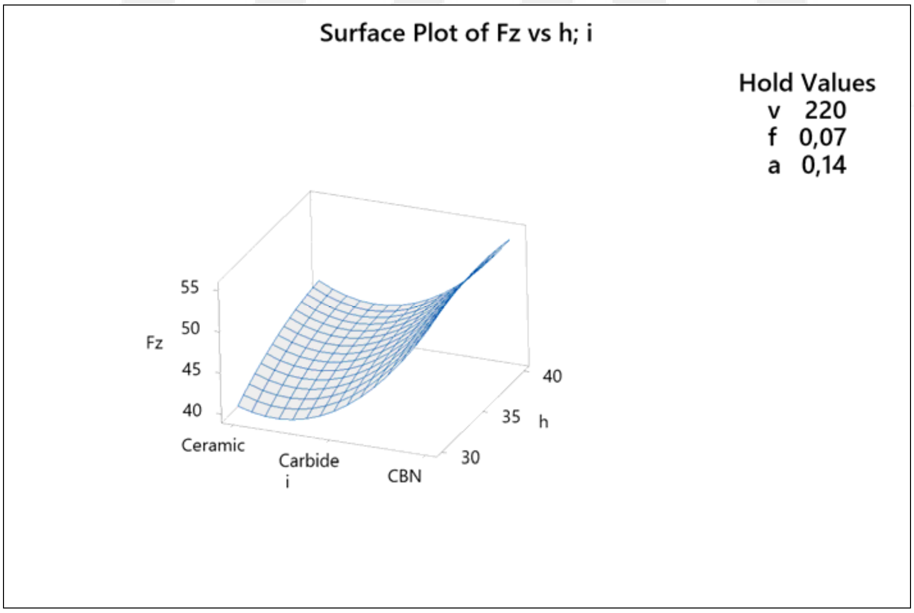


Figure 4.40. Surface plot of Fz vs h;i

Main Effects Plot for SN ratios of Fz is shown in Figure 4.41. The levels of the factors giving the optimum Fz value are seen as a1 (Level 1), i2 (Level 2), f1 (Level 1), h1 (Level 1), and v1 (Level 1). That is to say, the optimum Fz value is found with carbide insert (i2), 30 HRC hardness (h1), 180 m/min cutting speed (v1), 0,03 mm/rev feed rate (f1), and 0,08 mm depth of cut (a1) as shown in Figure 4.41.

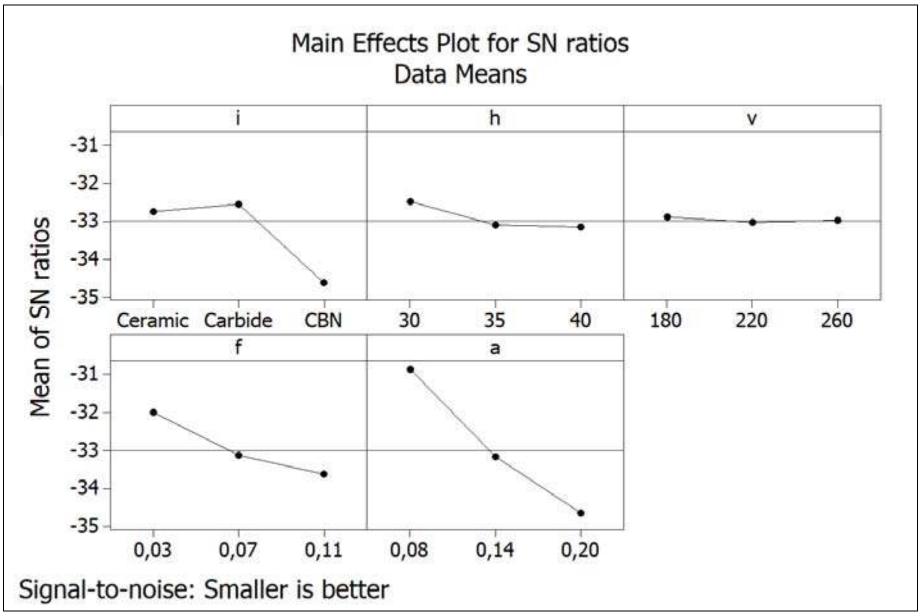


Figure 4.41. Main effects plot for SN ratios of Fz

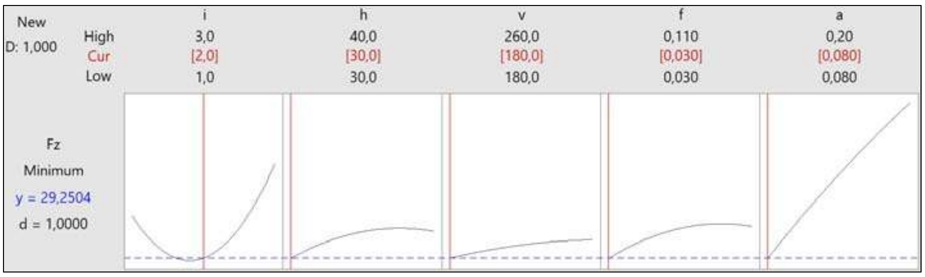


Figure 4.42. Optimization plot for Fz

After optimum parameters are read from the Main effects plot for SN ratios of Fz, optimization Plot is run for optimum level (A2B1C1D1E1) of Fz as shown in Figure 4.42. The optimum value of Fz is predicted as 29,25 N.

Experimental modeling equations of Fz in coded and uncoded formats are given in Equation 4.9 and Equation 4.10, respectively. Fz is predicted using a developed experimental modeling equations. Maximum error (%) between the experimental and predicted Fz are obtained as 4,00 as shown in Table 4.10.

$$Fz = 44,4450 + 5,3737\ A + 1,6500\ B + 0,15938\ C + 4,27563\ D + 9,63125\ E + 5,24208\ A*A - 1,00625\ B*B - 0,30542\ C*C - 1,07542\ D*D - 0,48125\ E*E - 1,04000\ A*B - 0,49500\ A*C + 1,05000\ A*D + 3,87000\ A*E - 0,06000\ B*C + 0,38000\ B*D + 0,29000\ B*E - 0,60500\ C*D + 0,11250\ C*E + 3,27250\ D*E \quad (4.9)$$

$$Fz = - 34,4 - 16,46\ i + 3,36\ h + 0,143\ v - 26\ f - 70,6\ a + 5,242\ i*i - 0,0403\ h*h - 0,000191\ v*v - 672\ f*f - 134\ a*a - 0,208\ i*h - 0,0124\ i*v + 26,3\ i*f + 64,50\ i*a - 0,00030\ h*v + 1,90\ h*f + 0,97\ h*a - 0,378\ v*f + 0,047\ v*a + 1364\ f*a \quad (4.10)$$

Table 4.10. Comparison of experimental and predicted results for Fz

| Runs | Experimental value | Predicted value | Error (%) |
|---|---|---|---|
| **1** | 41,25 | 40,62 | 1,53 |
| **2** | 54,74 | 53,44 | 2,37 |
| **3** | 44,88 | 46,00 | 2,49 |
| **4** | 54,21 | 54,66 | 0,84 |
| **5** | 38,86 | 38,02 | 2,15 |
| **6** | 40,36 | 39,55 | 2,00 |
| **7** | 48,6 | 47,79 | 1,68 |
| **8** | 47,68 | 46,89 | 1,65 |
| **9** | 32,49 | 31,97 | 1,61 |
| **10** | 34,67 | 34,69 | 0,05 |
| **11** | 51,04 | 50,65 | 0,77 |
| **12** | 54,38 | 54,53 | 0,27 |
| **13** | 44,28 | 43,35 | 2,09 |
| **14** | 56,45 | 55,09 | 2,41 |
| **15** | 43,6 | 44,66 | 2,44 |
| **16** | 53,79 | 54,42 | 1,17 |
| **17** | 33 | 32,25 | 2,26 |
| **18** | 34,87 | 34,26 | 1,75 |
| **19** | 44,49 | 44,97 | 1,08 |
| **20** | 59,45 | 60,07 | 1,04 |
| **21** | 40,23 | 41,26 | 2,57 |
| **22** | 44,96 | 44,68 | 0,61 |
| **23** | 41,08 | 41,70 | 1,52 |
| **24** | 45,57 | 44,88 | 1,51 |
| **25** | 39,15 | 40,01 | 2,20 |
| **26** | 47,37 | 48,66 | 2,72 |
| **27** | 46,21 | 46,46 | 0,55 |
| **28** | 58,63 | 59,31 | 1,16 |
| **29** | 32,84 | 33,98 | 3,47 |
| **30** | 34,54 | 34,07 | 1,35 |
| **31** | 50,98 | 53,02 | 4,00 |
| **32** | 53,13 | 53,56 | 0,81 |
| **33** | 37,81 | 38,07 | 0,69 |
| **34** | 40,15 | 41,08 | 2,31 |
| **35** | 51,59 | 49,59 | 3,87 |
| **36** | 69,41 | 68,08 | 1,91 |
| **37** | 36,45 | 36,82 | 1,01 |
| **38** | 39,97 | 39,36 | 1,53 |
| **39** | 43,79 | 44,61 | 1,87 |
| **40** | 48,83 | 48,67 | 0,33 |
| **41** | 45,31 | 44,45 | 1,91 |
| **42** | 43,33 | 44,45 | 2,57 |
| **43** | 44,19 | 44,45 | 0,58 |
| **44** | 44,6 | 44,45 | 0,35 |
| **45** | 44,64 | 44,45 | 0,44 |
| **46** | 44,6 | 44,45 | 0,35 |

### 4.1.4. Surface Roughness (Ra) Analysis

The percentage contributions of machining parameters on Ra is shown in Table 4.11. Percentage contributions of insert (i), hardness (h), cutting speed (v), feed rate (f), and depth of cut (a) on Ra were found to be 51,52%, 13,59%, 0,18%, 1,86%, and 0,47%, respectively. It appears that insert is the most significant parameter on Ra. In addition to these, other contributions on Ra are square, interaction, and residual error. These are 20,74; 9,72; and 1,92 percent, respectively.

Table 4.11. Analysis of variance for Ra

| Source | DF | Seq SS | Adj SS | Adj MS | F | P | % Cont. |
|---|---|---|---|---|---|---|---|
| **Regression** | 20 | 1,61138 | 1,61138 | 0,080569 | 63,84 | 0,000 | 98,08 |
| **Linear** | 5 | 1,11096 | 1,11096 | 0,222192 | 176,06 | 0,000 | 67,62 |
| **i** | 1 | 0,84640 | 0,84640 | 0,846400 | 670,68 | 0,000 | 51,52 |
| **h** | 1 | 0,22326 | 0,22326 | 0,223256 | 176,91 | 0,000 | 13,59 |
| **v** | 1 | 0,00303 | 0,00303 | 0,003025 | 2,40 | 0,134 | 0,18 |
| **f** | 1 | 0,03062 | 0,03062 | 0,030625 | 24,27 | 0,000 | 1,86 |
| **a** | 1 | 0,00766 | 0,00766 | 0,007656 | 6,07 | 0,021 | 0,47 |
| **Square** | 5 | 0,34075 | 0,34075 | 0,068149 | 54,00 | 0,000 | 20,74 |
| **i*i** | 1 | 0,20844 | 0,20844 | 0,264100 | 209,27 | 0,000 | 12,69 |
| **h*h** | 1 | 0,04349 | 0,04349 | 0,067776 | 53,71 | 0,000 | 2,65 |
| **v*v** | 1 | 0,00000 | 0,00000 | 0,004337 | 3,44 | 0,076 | 0,00 |
| **f*f** | 1 | 0,08824 | 0,08824 | 0,085464 | 67,72 | 0,000 | 5,37 |
| **a*a** | 1 | 0,00058 | 0,00058 | 0,000576 | 0,46 | 0,505 | 0,04 |
| **Interaction** | 10 | 0,15967 | 0,15967 | 0,015967 | 12,65 | 0,000 | 9,72 |
| **i*h** | 1 | 0,00810 | 0,00810 | 0,008100 | 6,42 | 0,018 | 0,49 |
| **i*v** | 1 | 0,00250 | 0,00250 | 0,002500 | 1,98 | 0,172 | 0,15 |
| **i*f** | 1 | 0,00302 | 0,00302 | 0,003025 | 2,40 | 0,134 | 0,18 |
| **i*a** | 1 | 0,01103 | 0,01103 | 0,011025 | 8,74 | 0,007 | 0,67 |
| **h*v** | 1 | 0,00563 | 0,00563 | 0,005625 | 4,46 | 0,045 | 0,34 |
| **h*f** | 1 | 0,00122 | 0,00122 | 0,001225 | 0,97 | 0,334 | 0,07 |
| **h*a** | 1 | 0,01823 | 0,01823 | 0,018225 | 14,44 | 0,001 | 1,11 |
| **v*f** | 1 | 0,02102 | 0,02102 | 0,021025 | 16,66 | 0,000 | 1,28 |
| **v*a** | 1 | 0,02890 | 0,02890 | 0,028900 | 22,90 | 0,000 | 1,76 |
| **f*a** | 1 | 0,06002 | 0,06002 | 0,060025 | 47,56 | 0,000 | 3,65 |
| **Residual Error** | 25 | 0,03155 | 0,03155 | 0,001262 | | | 1,92 |
| **Lack-of-Fit** | 20 | 0,02342 | 0,02342 | 0,001171 | 0,72 | 0,730 | 1,43 |
| **Pure Error** | 5 | 0,00813 | 0,00813 | 0,001627 | | | 0,49 |
| **Total** | 45 | 1,64293 | | | | | 100,00 |
| **Model summary** | | | | | | | |
| S = 0,0355246, R-Sq = 98,08%, R-Sq(pred) = 93,59%, R-Sq(adj) = 96,54% | | | | | | | |

As shown of Residual plots for Ra in Figure 4.43, The residuals are normally distributed if the points on the normal probability plot form an approximately linear line. The residuals have constant variance because of the fact that residuals scattered randomly around zero on the Versus Fits graph. In this case, the model has been found to be valid. The Histogram chart is used to evaluate the shape and spread of data. The Histogram chart below shows that the data is normally distributed such as bell shape. Ideally, the residuals on Versus Order plot should occur randomly around zero line. The residuals in this plot are appeared to fluctuate in a down and up around the zero line. From investigation the Residual Plots, it is concluded that the model has the ability to accurately predict Ra.

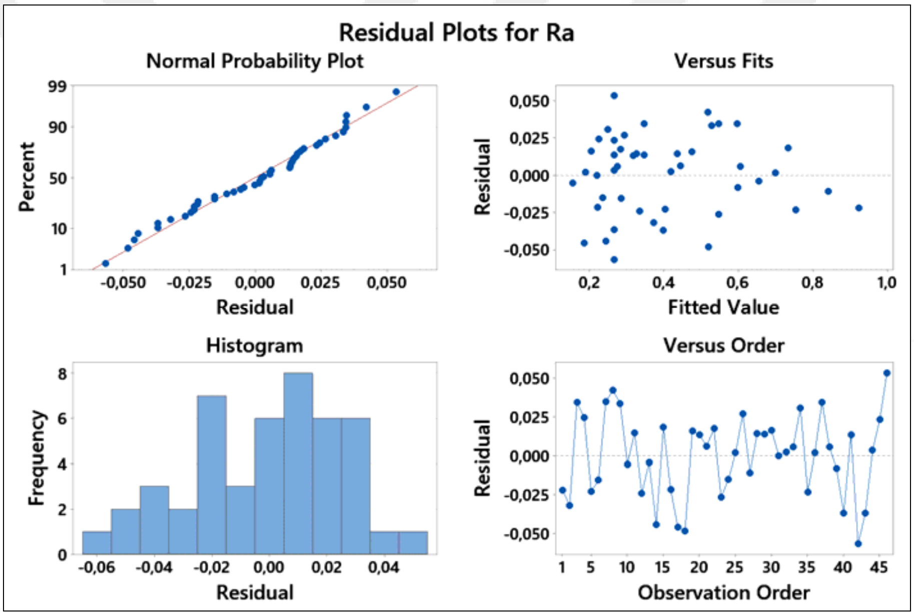


Figure 4.43. Residual plot for Ra

Figures 4.44-4.46 Surface Plots show the effects of the machining parameters on Ra. It is observed that the highest Ra is obtained when f levels are high (f = 0,10 mm/rev) as shown in Figure 4.46. Later on, the lowest Ra is generated in the lowest f level (f = 0,04 m/rev) and the highest v level (v = 270 m/min) as shown in Figures 4.44,4.45. In other words, surface roughness falls while cutting speed increases or feed rate decreases. This result can be explained by the effects of the formation of high temperatures in the cutting zone when the cutting speed increases. In this context heat generated by the high temperature stays on the workpiece due to the characteristic of low thermal conductivity of the workpiece material. This result can cause thermal softening of the workpiece and, consequently, elastic deformation on the workpiece surface is taken place. Thusly, the surface of the workpiece deteriorates. It appeared that when the depth of cut is processed in the range of from 0,1 mm to 0,2 mm, the Ra increased in a and v pairs interaction as shown in Figures 4.45. And, the Ra decreased while cutting speed increases as shown in Figures. Another factor to consider is feed rate. When Figures are examined, it is understood that feed rate has the biggest effect on Ra. The least Ra occurred at the smallest feed rate level (f = 0,04 mm/rev). This issue can be explained by the decrease in cutting forces as a result of the decrease in feed rate. Smaller cutting forces lead less vibration and ensure better surface finish (Özdemir, 2019; Özdemir, 2020; Sahu and Andhare, 2017; Davoodi and Tazehkandi, 2014; Çelik et al., 2016; Cakir et al., 2009).

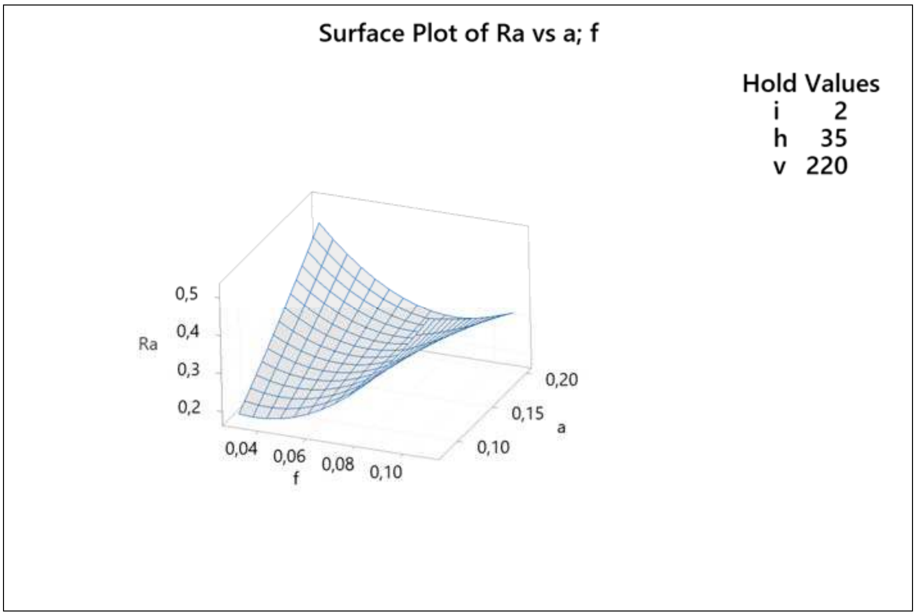


Figure 4.44. Surface plot of Ra vs a;f

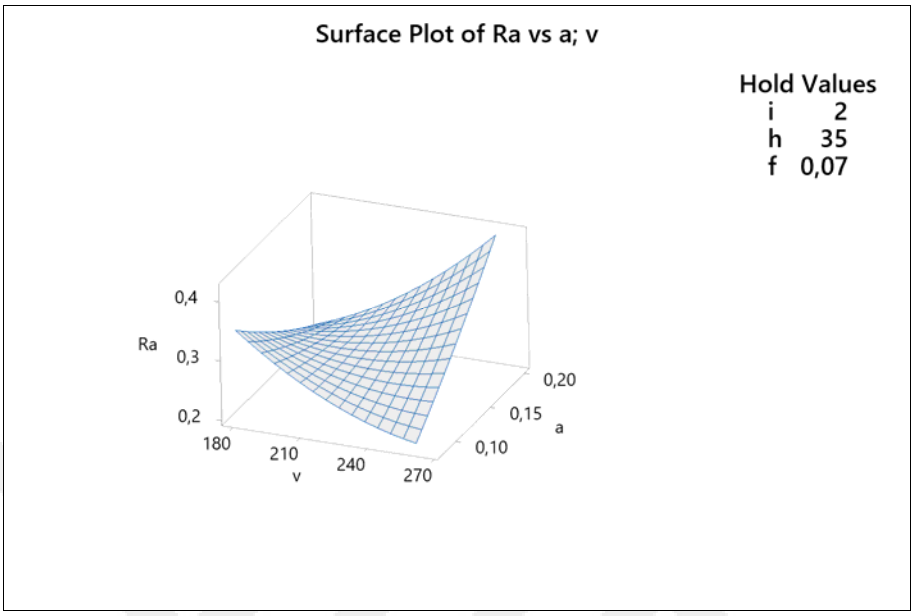


Figure 4.45. Surface plot of Ra vs a;v

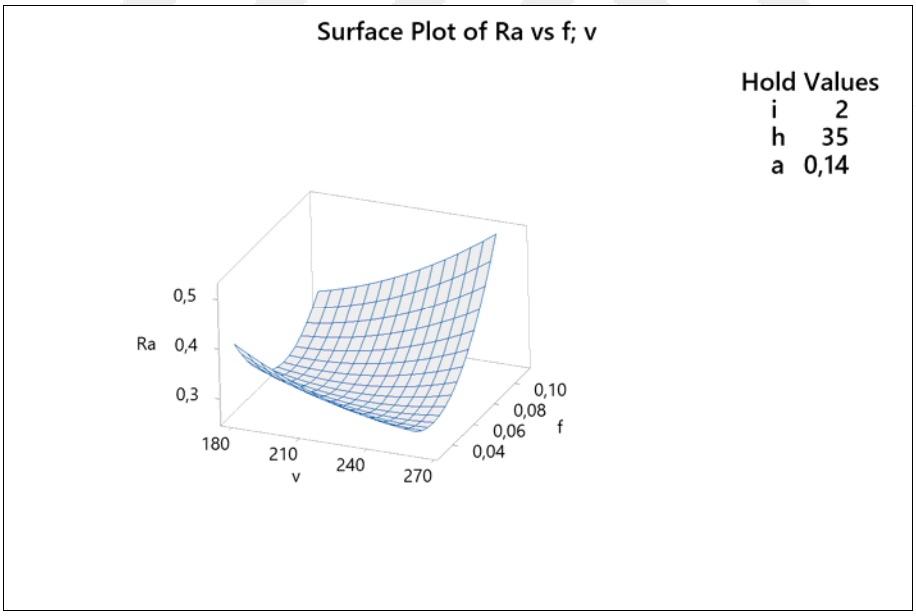


Figure 4.46. Surface plot of Ra vs f;v

Three-dimensional (3D) Surface Plots given in Figures 4.47-4.49 are shown to assess the effect of cutting parameters on Ra. Ra is diminished as hardness level rises. The lowest Ra occurs at 40 HRC. Machining of workpiece makes difficult as a result of the increase in the hardness of the workpiece. This situation can be explained by the fact that the workpiece faces more cutting resistance during machining. Afterward, a high-temperature rise generates at the tool and workpiece interface. The high temperatures at tool and workpiece interface can lead to thermal softening of the workpiece. And hence lower Ra values can occur while hardness levels rise during the machining of hard materials in the range of from 30 HRC to 40 HRC. These findings are compatible with the literature (Subbaiah et al., 2020; Azizi et al., 2012). These results can be explained in another respect: as the hardness level of the workpiece increases, the plasticity of the material decreases. As a result, the plastic flow decreases, and then the Ra value decreases (Kumar et al., 2019).

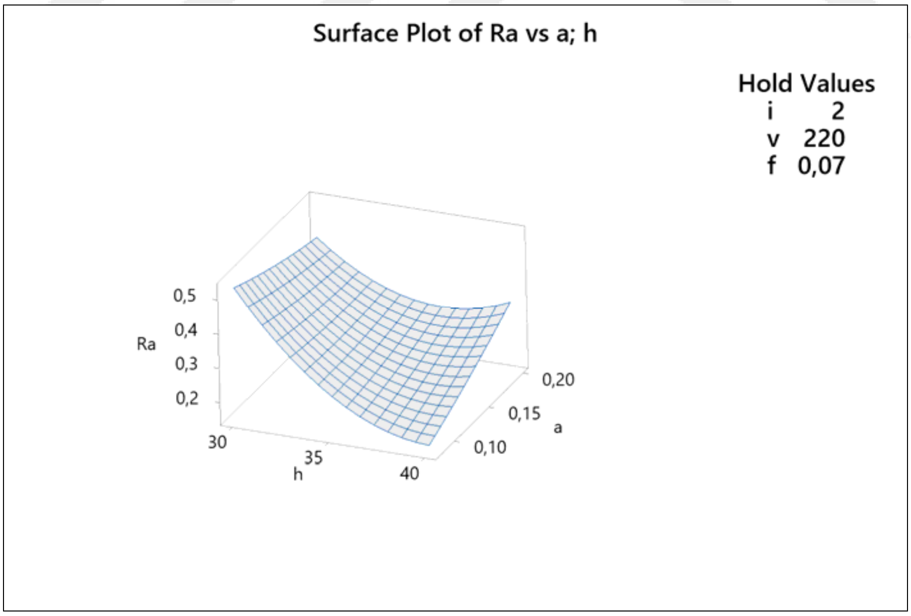


Figure 4.47. Surface plot of Ra vs a;h

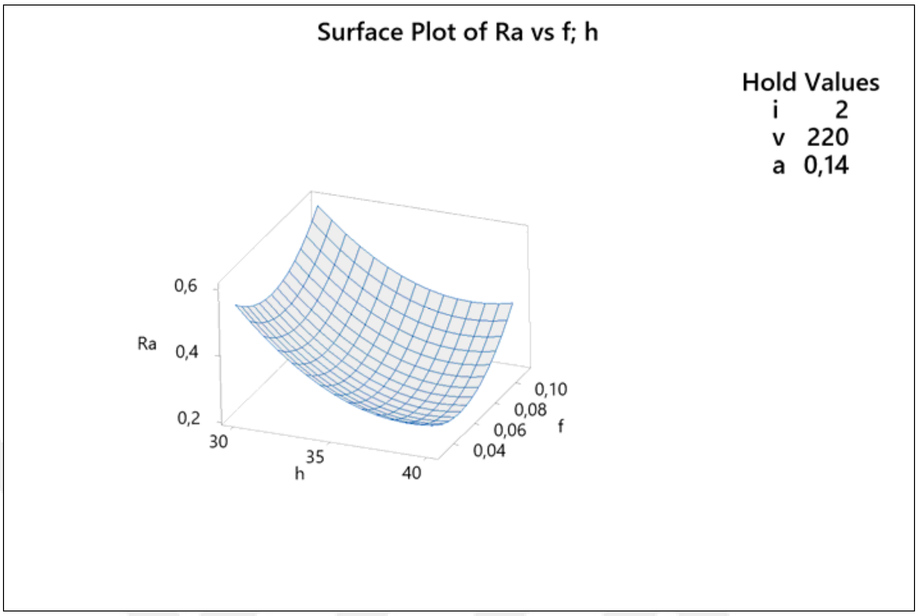


Figure 4.48. Surface plot of Ra vs f;h

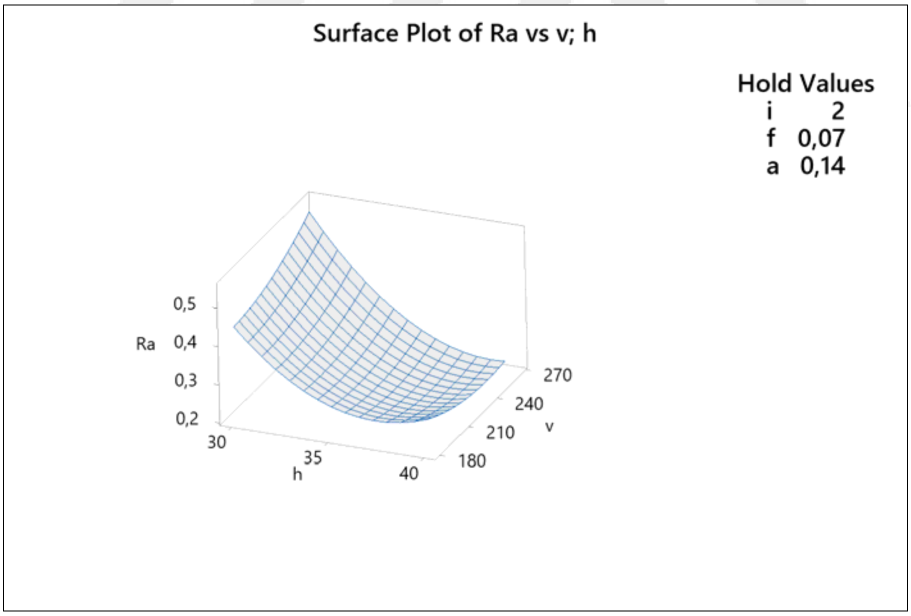


Figure 4.49. Surface plot of Ra vs v;h

Other Surface Plots of Ra are shown in Figures 4.50-4.53. Figures indicate that the lowest Ra value is obtained when CBN insert (3) is used. That is, the analysis revealed that ceramic insert (1) and carbide insert (2) gave surfaces with higher roughness than CBN insert (3). This situation might be explained by the high hardness of insert, the strength of insert, and the shape chip produced. CBN inserts provide a better wear resistance than carbide and ceramic inserts because of fact that they have a higher hardness (Akhtar et al., 2014; Motorcu, 2011). This case can be explained from another point of view. Ceramic insert has less thermally conductive than CBN insert. Higher thermal conductivity decreases cutting temperatures close to the tool edge. Lower thermal conductivity leads to tool thermal softening and rise of abrasive wear rate. Tool materials with higher thermal conductivity enable to eliminate the heat generated in the cutting zone during machining. Ra surface roughness immediately remains constant or decreases when CBN insert is used, but the Ra increases when ceramic insert is used. It is noted that these effects can be related to worn tool nose shape. In literature, it stated that ceramic inserts exhibited a wavy shape on the cutting edge, while CBN inserts conserved their shape very close to the original one (Godoy and Diniz, 2011; Yallese et al., 2005). Therefore, based on the above explanation, it can be said that a better surface can be obtained when a CBN insert is used.

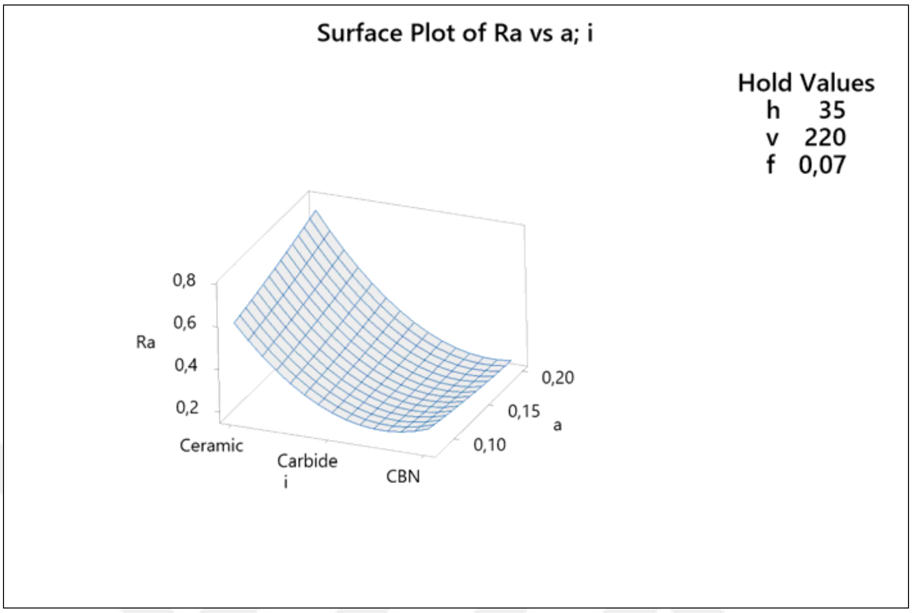


Figure 4.50. Surface plot of Ra vs a;i

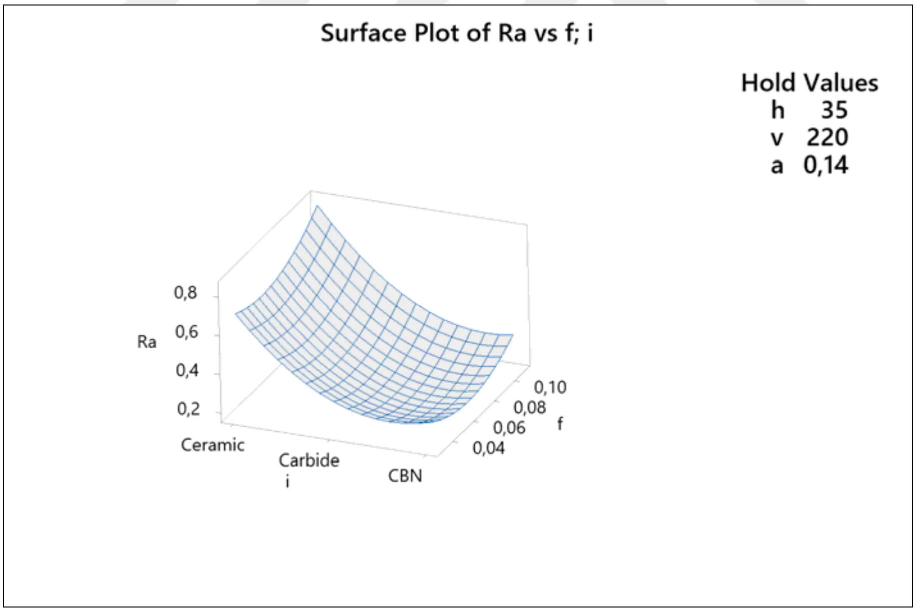


Figure 4.51. Surface plot of Ra vs f;i

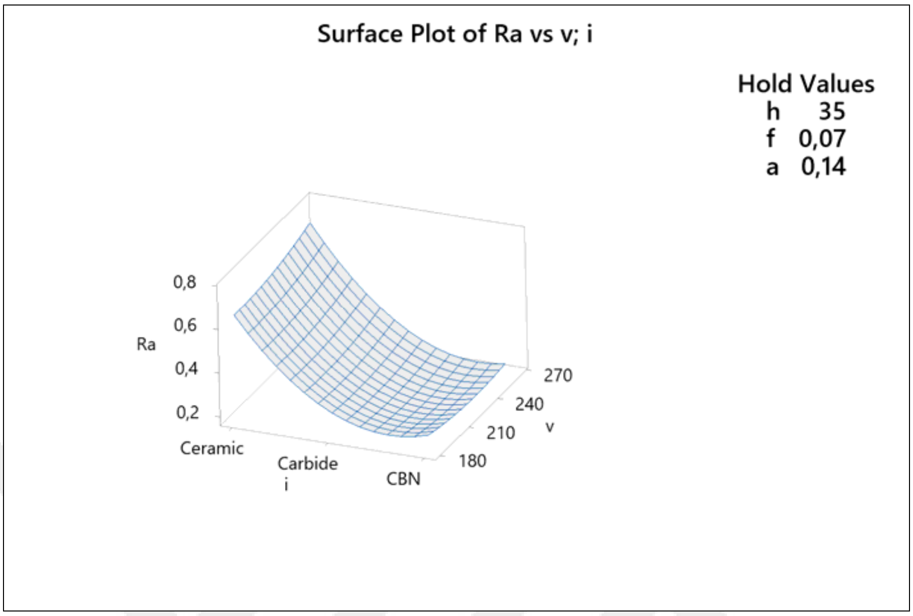

Figure 4.52. Surface plot of Ra vs v;i

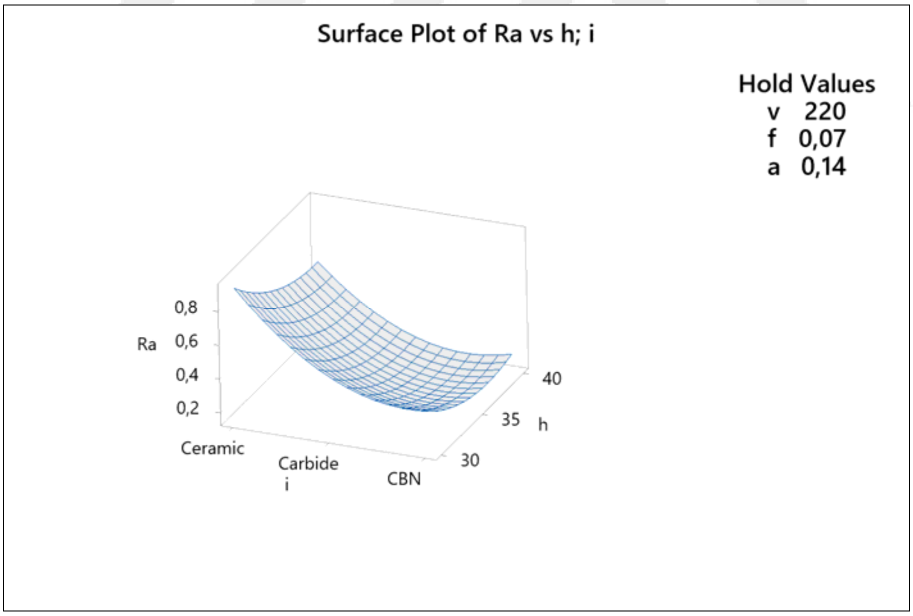

Figure 4.53. Surface plot of Ra vs h;i

The Main Effects Plot for SN ratio of Ra indicates that insert has the largest effect on the Signal-to-Noise ratio. The levels of the factors giving the optimum Ra value are seen as i3 (Level 3), h3 (Level 3), a1 (Level 1), f1 (Level 1), and v1 (Level 1). That is to say, the optimum Ra value is found with CBN insert (i3), 40 HRC hardness (h3), 180 m/min cutting speed (v1), 0,03 mm/rev feed rate (f1), and 0,08 mm depth of cut (a1) as shown in Figure 4.54.

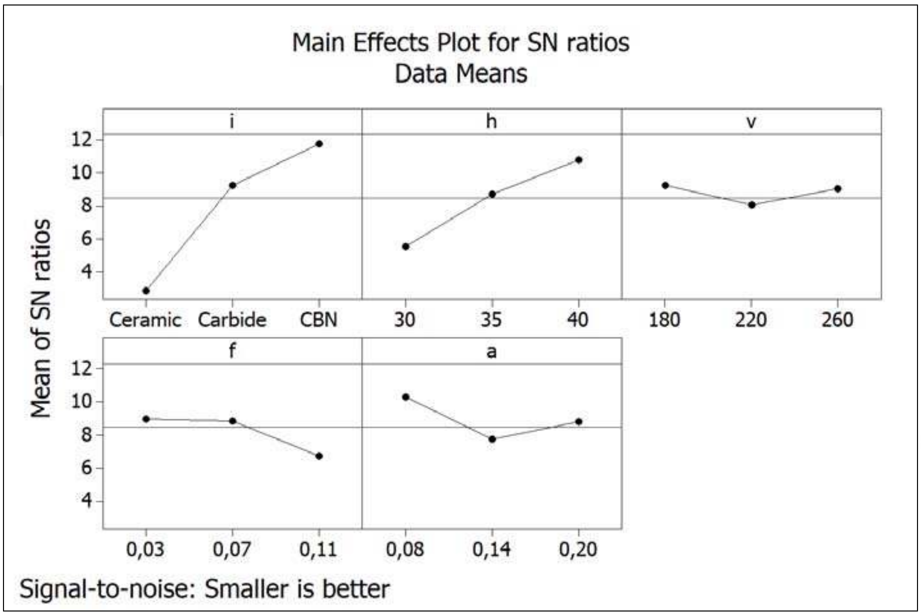

Figure 4.54. Main effects plot for SN ratios of Ra

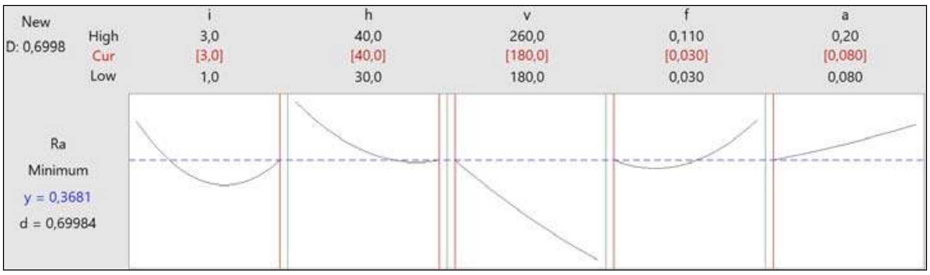

Figure 4.55. Optimization plot for Ra

After optimum parameters are read from the response table for SN ratios of Ra, optimization Plot is run for optimum level (A3B3C1D1E1) of Ra as shown in Figure 4.55. The optimum value of Ra is predicted as 0,37 µm.

An experimental modeling equation has been developed via the relationship between Ra and machining parameters (i, h, v, f, a). Experimental modeling equations of Ra in coded and uncoded formats are given in Equation 4.11 and Equation 4.12, respectively. Ra is calculated using a developed experimental modeling equation.

$$\begin{aligned} Ra = {} & 0{,}266667 - 0{,}230000\, A - 0{,}118125\, B + \\ & 0{,}013750\, C + 0{,}043750\, D + 0{,}021875\, E + 0{,}173958 \\ & A*A + 0{,}088125\, B*B + 0{,}022292\, C*C + 0{,}098958 \\ & D*D + 0{,}008125\, E*E + 0{,}045000\, A*B - 0{,}025000 \\ & A*C - 0{,}027500\, A*D - 0{,}052500\, A*E - 0{,}037500 \\ & B*C + 0{,}017500\, B*D + 0{,}067500\, B*E + 0{,}072500 \\ & C*D + 0{,}085000\, C*E - 0{,}122500\, D*E \end{aligned} \tag{4.11}$$

$$\begin{aligned} Ra = {} & 8{,}56 - 0{,}933\, i - 0{,}2848\, h - 0{,}00610\, v - 12{,}08\, f - \\ & 10{,}61\, a + 0{,}1740\, i*i + 0{,}003525\, h*h + 0{,}000014\, v*v \\ & + 61{,}85\, f*f + 2{,}26\, a*a + 0{,}00900\, i*h - 0{,}000625\, i*v - \\ & 0{,}687\, i*f - 0{,}875\, i*a - 0{,}000187\, h*v + 0{,}0875\, h*f \\ & + 0{,}2250\, h*a + 0{,}0453\, v*f + 0{,}03542\, v*a - 51{,}04\, f*a \end{aligned} \tag{4.12}$$

A comparison of experimental and predicted Ra values are shown in Table 4.12. An error is found in a range of 0,09-32,59 percent. When Table 4.12 is analyzed, it is seen that % Error are found within acceptable limits.

Table 4.12. Comparison of experimental and predicted results for Ra

| Runs | Experimental Value | Predicted Value | Error (%) |
|---|---|---|---|
| 1 | 0,9 | 0,92 | 2,43 |
| 2 | 0,34 | 0,37 | 9,37 |
| 3 | 0,63 | 0,60 | 5,46 |
| 4 | 0,25 | 0,23 | 9,75 |
| 5 | 0,38 | 0,40 | 6,03 |
| 6 | 0,27 | 0,29 | 5,71 |
| 7 | 0,38 | 0,35 | 9,10 |
| 8 | 0,56 | 0,52 | 7,51 |
| 9 | 0,56 | 0,53 | 5,95 |
| 10 | 0,15 | 0,16 | 3,61 |
| 11 | 0,45 | 0,44 | 3,24 |
| 12 | 0,31 | 0,33 | 7,80 |
| 13 | 0,65 | 0,65 | 0,64 |
| 14 | 0,2 | 0,24 | 22,08 |
| 15 | 0,75 | 0,73 | 2,44 |
| 16 | 0,2 | 0,22 | 10,83 |
| 17 | 0,14 | 0,19 | 32,59 |
| 18 | 0,47 | 0,52 | 10,24 |
| 19 | 0,49 | 0,47 | 3,19 |
| 20 | 0,33 | 0,32 | 3,98 |
| 21 | 0,45 | 0,44 | 1,34 |
| 22 | 0,3 | 0,28 | 5,76 |
| 23 | 0,52 | 0,55 | 5,09 |
| 24 | 0,22 | 0,24 | 6,91 |
| 25 | 0,7 | 0,70 | 0,24 |
| 26 | 0,32 | 0,29 | 8,33 |
| 27 | 0,83 | 0,84 | 1,31 |
| 28 | 0,34 | 0,33 | 4,17 |
| 29 | 0,36 | 0,35 | 3,76 |
| 30 | 0,22 | 0,20 | 7,29 |
| 31 | 0,22 | 0,22 | 0,09 |
| 32 | 0,42 | 0,42 | 0,55 |
| 33 | 0,61 | 0,60 | 0,92 |
| 34 | 0,28 | 0,25 | 10,94 |
| 35 | 0,73 | 0,75 | 3,17 |
| 36 | 0,19 | 0,19 | 0,99 |
| 37 | 0,58 | 0,55 | 5,93 |
| 38 | 0,28 | 0,27 | 2,01 |
| 39 | 0,59 | 0,60 | 1,38 |
| 40 | 0,36 | 0,40 | 10,24 |
| 41 | 0,28 | 0,27 | 4,76 |
| 42 | 0,21 | 0,27 | 26,98 |
| 43 | 0,23 | 0,27 | 15,94 |
| 44 | 0,27 | 0,27 | 1,23 |
| 45 | 0,29 | 0,27 | 8,05 |
| 46 | 0,32 | 0,27 | 16,67 |

### 4.1.5. Total Electric Current ($I_{total}$=$I_{unloaded}$+ $I_{cutting}$) Analysis

Percentage contributions of machining parameters on $I_{total}$ are shown in Table 4.13. Percentage contributions of insert (i), hardness (h), cutting speed (v), feed rate (f), and depth of cut (a) on $I_{total}$ were found to be 0,83%, 0,02%, 94,23%, 0,40, and 2,82%, respectively. It appears that cutting speed is the most significant parameter. In addition to these, other contributions on $I_{total}$ are square, interaction, and residual error. These are 0,50, 0,40, and 0,81 percent, respectively.

Table 4.13. Analysis of variance for $I_{total}$

| Source | DF | Seq SS | Adj SS | Adj MS | F | P | % Cont. |
|---|---|---|---|---|---|---|---|
| Regression | 20 | 10,2635 | 10,2635 | 0,51317 | 153,00 | 0,000 | 99,19 |
| Linear | 5 | 10,1704 | 10,1704 | 2,03409 | 606,44 | 0,000 | 98,29 |
| i | 1 | 0,0856 | 0,0856 | 0,08556 | 25,51 | 0,000 | 0,83 |
| h | 1 | 0,0023 | 0,0023 | 0,00226 | 0,67 | 0,420 | 0,02 |
| v | 1 | 9,7500 | 9,7500 | 9,75001 | 2906,83 | 0,000 | 94,23 |
| f | 1 | 0,0410 | 0,0410 | 0,04101 | 12,23 | 0,002 | 0,40 |
| a | 1 | 0,2916 | 0,2916 | 0,29160 | 86,94 | 0,000 | 2,82 |
| Square | 5 | 0,0515 | 0,0515 | 0,01031 | 3,07 | 0,027 | 0,50 |
| i*i | 1 | 0,0011 | 0,0036 | 0,00356 | 1,06 | 0,313 | 0,01 |
| h*h | 1 | 0,0019 | 0,0153 | 0,01530 | 4,56 | 0,043 | 0,02 |
| v*v | 1 | 0,0071 | 0,0220 | 0,02200 | 6,56 | 0,017 | 0,07 |
| f*f | 1 | 0,0188 | 0,0299 | 0,02991 | 8,92 | 0,006 | 0,18 |
| a*a | 1 | 0,0227 | 0,0227 | 0,02274 | 6,78 | 0,015 | 0,22 |
| Interaction | 10 | 0,0415 | 0,0415 | 0,00415 | 1,24 | 0,316 | 0,40 |
| i*h | 1 | 0,0001 | 0,0001 | 0,00010 | 0,03 | 0,864 | 0,00 |
| i*v | 1 | 0,0169 | 0,0169 | 0,01690 | 5,04 | 0,034 | 0,16 |
| i*f | 1 | 0,0030 | 0,0030 | 0,00302 | 0,90 | 0,351 | 0,03 |
| i*a | 1 | 0,0049 | 0,0049 | 0,00490 | 1,46 | 0,238 | 0,05 |
| h*v | 1 | 0,0012 | 0,0012 | 0,00122 | 0,37 | 0,551 | 0,01 |
| h*f | 1 | 0,0002 | 0,0002 | 0,00022 | 0,07 | 0,798 | 0,00 |
| h*a | 1 | 0,0006 | 0,0006 | 0,00062 | 0,19 | 0,670 | 0,01 |
| v*f | 1 | 0,0064 | 0,0064 | 0,00640 | 1,91 | 0,179 | 0,06 |
| v*a | 1 | 0,0081 | 0,0081 | 0,00810 | 2,41 | 0,133 | 0,08 |
| f*a | 1 | 0,0000 | 0,0000 | 0,00003 | 0,01 | 0,932 | 0,00 |
| Residual Error | 25 | 0,0839 | 0,0839 | 0,00335 | | | 0,81 |
| Lack-of-Fit | 20 | 0,0645 | 0,0645 | 0,00322 | 0,83 | 0,657 | 0,62 |
| Pure Error | 5 | 0,0194 | 0,0194 | 0,00388 | | | 0,19 |
| Total | 45 | 10,3473 | 10,3473 | | | | 100,00 |
| **Model summary**<br>S = 0,0579152, R-Sq = 99,19%, R-Sq(pred) = 97,24%, R-Sq(adj) = 98,54 | | | | | | | |

Four-in-one residual plots for $I_{total}$: Histogram, Normal Probability Plot, Residuals Versus Fits and Residuals Versus Order are shown in Figure 4.56. The residuals are normally distributed if the points on the Normal Probability Plot form an approximately linear line. The residuals have constant variance because of the fact that residuals scattered randomly around zero on the Versus Fits graph. In this case, the model has been found to be valid. The Histogram chart is used to evaluate the shape and spread of data. The Histogram chart below shows that the data is normally distributed such as bell shape. Ideally, the residuals on Versus Order plot should occur randomly around zero line. The residuals in this plot are appeared to fluctuate in a down and up around the zero line. From investigation the Residual Plots of $I_{total}$, it is concluded that the model has the ability to accurately predict $I_{total}$.

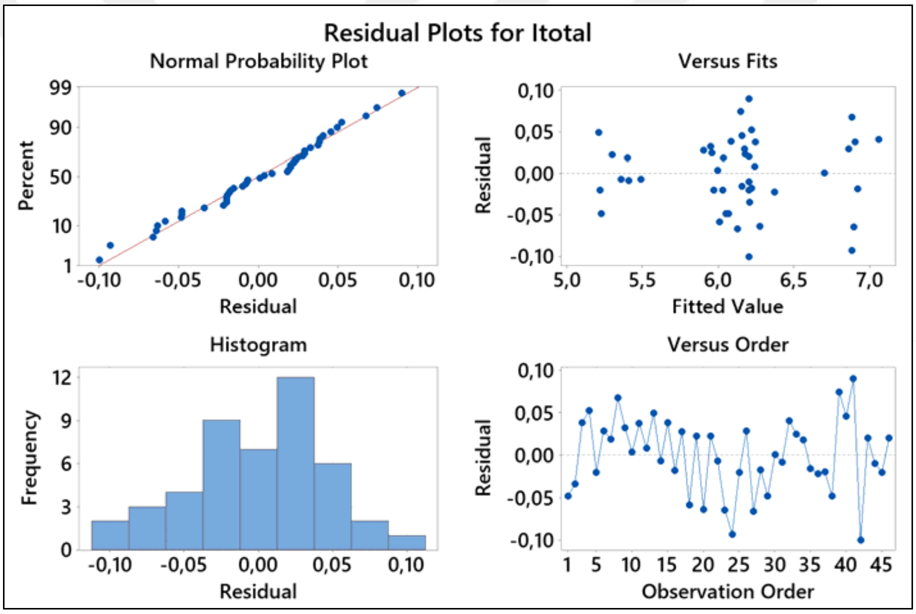


Figure 4.56. Residual plot for $I_{total}$

Surface Plots of $I_{total}$ against a;f, a;v, and v;f are presented in Figures 4.57-4.59. The observation results of these plots show that the highest values of $I_{total}$ were achieved at high cutting speed values. When depth of cut and feed rate was changed from minimum to maximum, $I_{total}$ values mostly are risen. As seen in the Figures, minimum $I_{total}$ is reached once cutting speed, feed rate, and depth of cut are taken at the smallest level. The Surface Plots show that $I_{total}$ continuously increases with rising in cutting speed. Results show that $I_{total}$ increases as the chip depth and feed rate levels increase, and decreases after the optimum level is reached. This situation can be explained by a built-up edge (BUE) that occurs at the chip and insert interface. When formula of P = 1,73*V*I*cosφ is considered, it can be seen that electric current (I) is directly proportional with electric power (P).

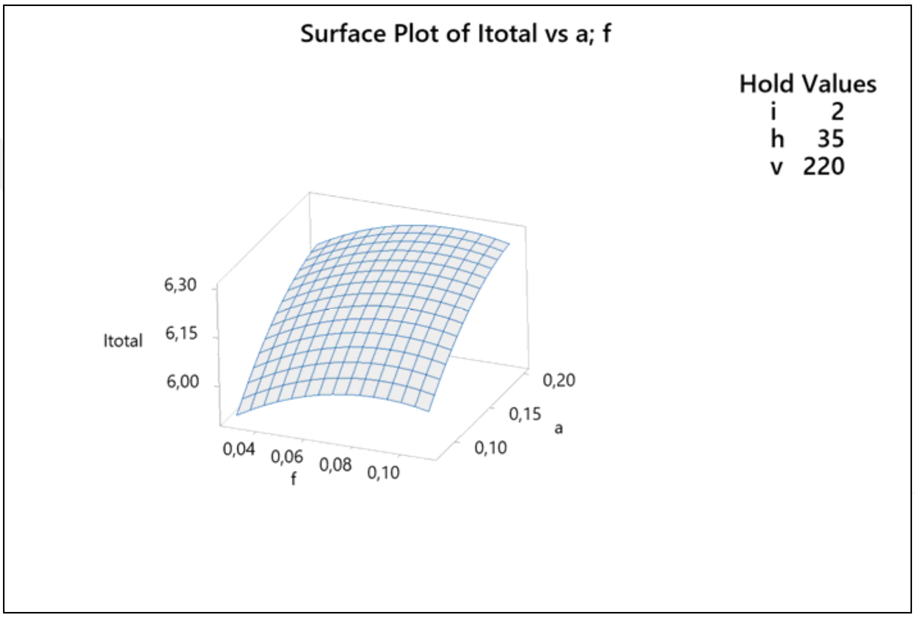

Figure 4.57. Surface plot of $I_{total}$ vs a;f

Figure 4.57 clearly shows that the maximum power consumption ($I_{total}$) decreases gradually after depth of cut of 0,14 mm and feed rate of 0,07 mm/rev. As seen in the Figures, while the feed rate and depth of cut were higher, the presence of BUE may have been observed more. That is, during machining at low cutting speeds, the workpiece material tends to stick to the insert due to BUE formation. Therefore, the machine tool is loaded more, and power consumption ($I_{total}$) increases. On the contrary, the power consumed by the machine tool decreases as BUE formation is reduced at high cutting speeds (Bhattacharya et al., 2009). These results agree with the knowledge of literature (Warsi et al., 2020; Tamang et al., 2018; Abbas et al., 2019; Al-Sulaiman et al., 2005).

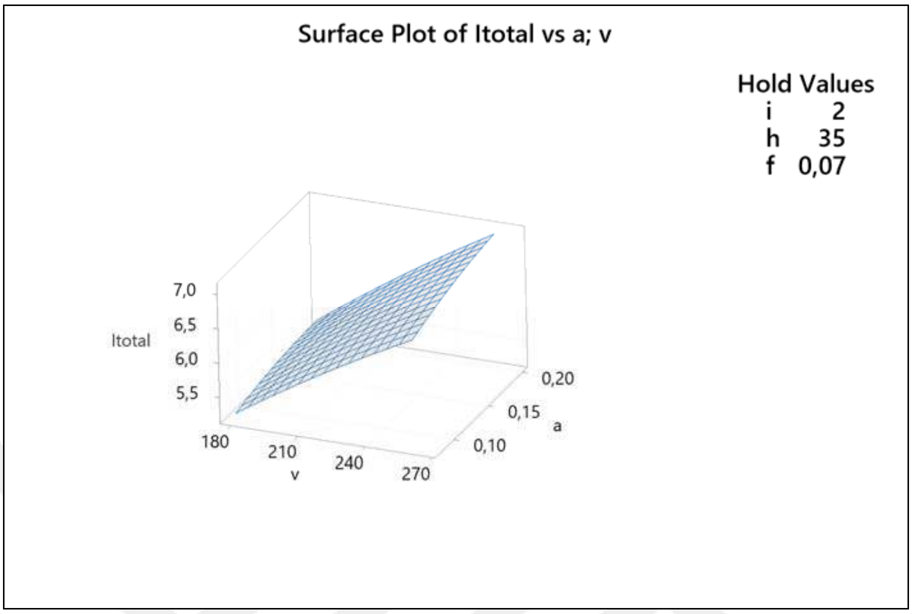


Figure 4.58. Surface plot of $I_{total}$ vs a;v

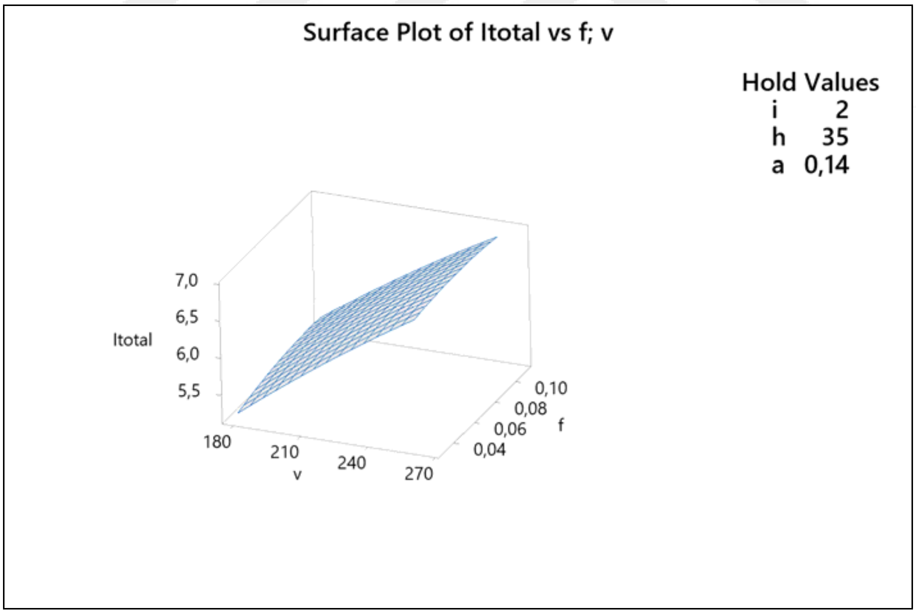


Figure 4.59. Surface plot of $I_{total}$ vs f;v

Surface Plots of $I_{total}$ against a;h, f;h, and v;h are presented in Figures 4.60-4.62. It is observed from the Figures that as feed rate, depth of cut, cutting speed, and hardness levels rise, $I_{total}$ value generally increases. It can be said that the highest $I_{total}$ value occurs when the hardness (40 HRC) and cutting speed (260 m/min) is highest as shown in Figure 4.62.

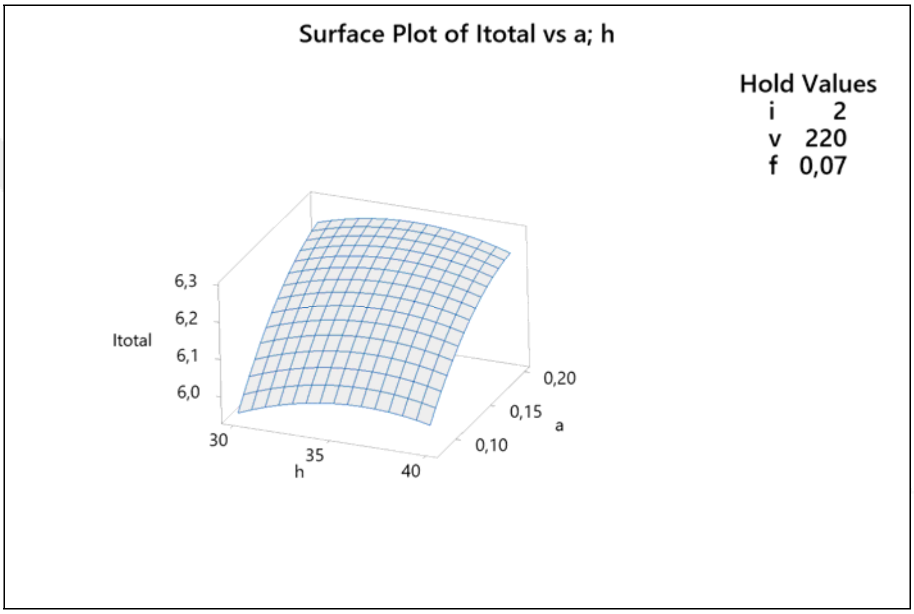


Figure 4.60. Surface plot of $I_{total}$ vs a;h

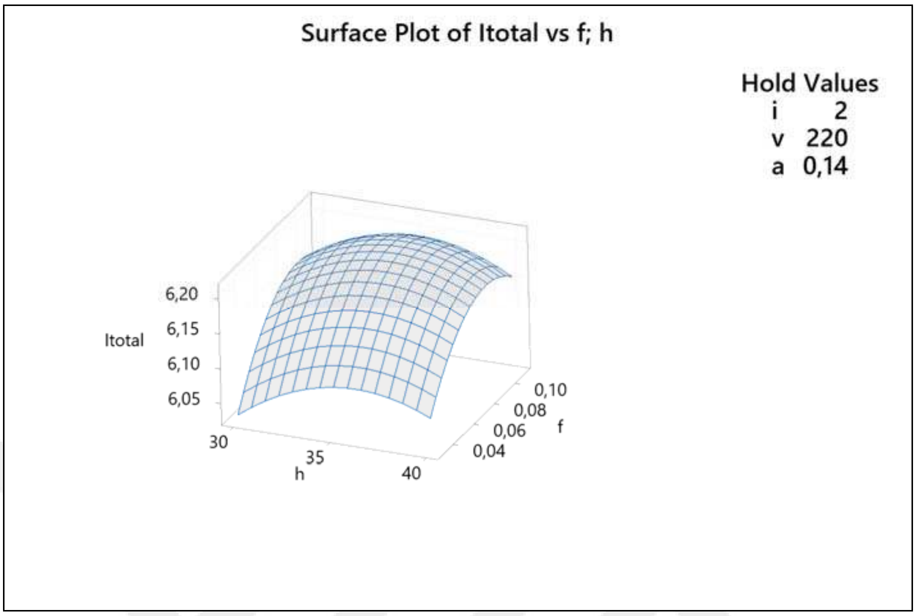


Figure 4.61. Surface plot of $I_{total}$ vs f;h

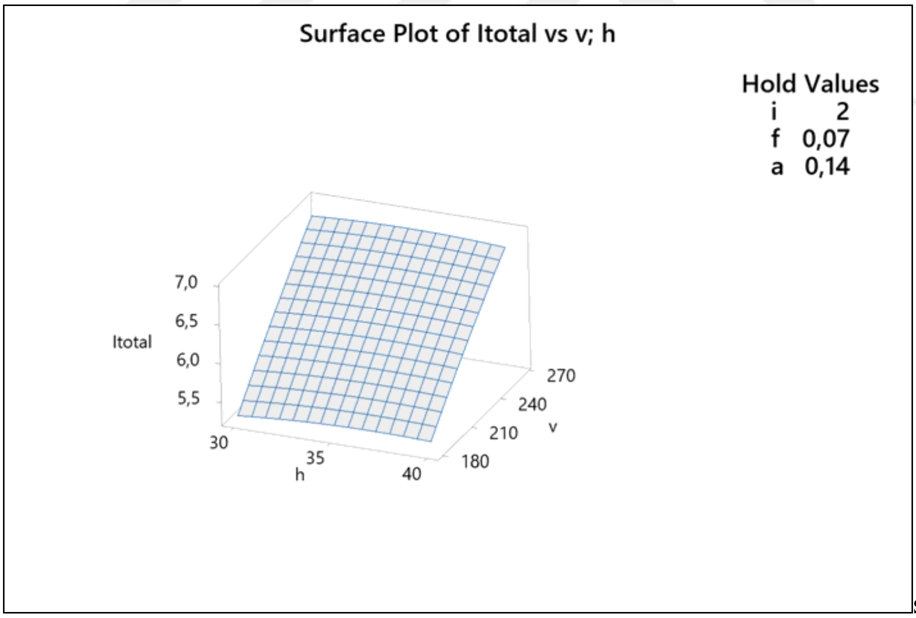


s

Figure 4.62. Surface plot of $I_{total}$ vs v;h

Surface Plots of $I_{total}$ against a;i, f;i, v;i, an h;i are presented in Figures 4.63-4.66. When the formula of P = F*v is considered, the cutting force is directly proportional to the power. In other words, it is directly proportional to the electric current. From cutting forces (Fx, Fy, Fz) surface plots, it can be seen that the lowest cutting forces (Fx, Fy, Fz) happened using ceramic insert. Therefore, from the surface graphs presented below, lower $I_{total}$ values may have been observed when ceramic inserts were used instead of carbide and CBN inserts.

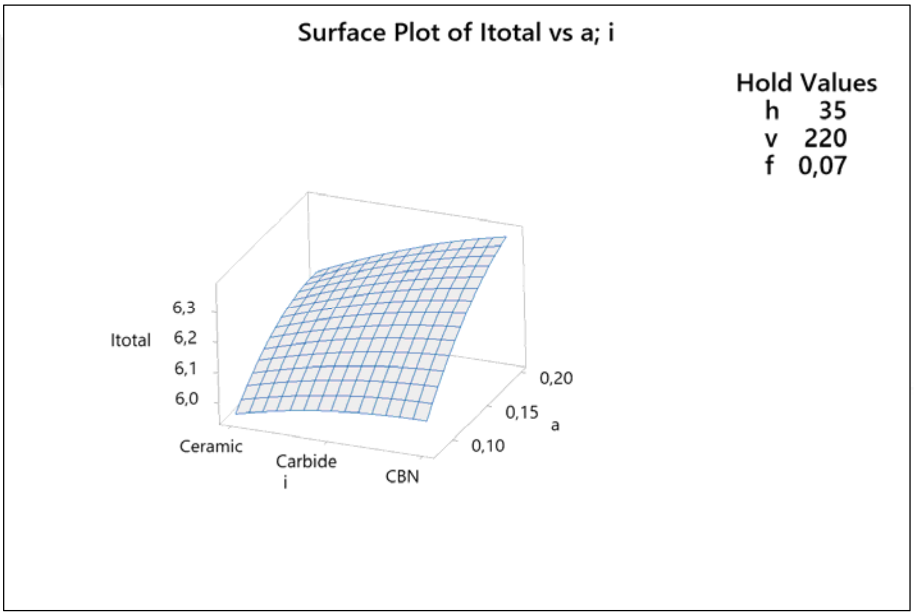


Figure 4.63. Surface plot of $I_{total}$ vs a;i

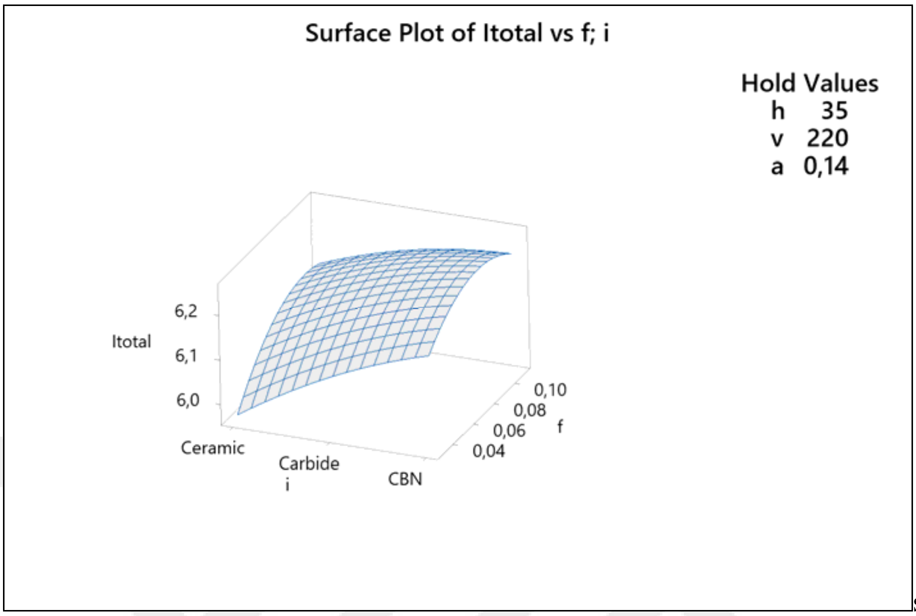


Figure 4.64. Surface plot of $I_{total}$ vs f;i

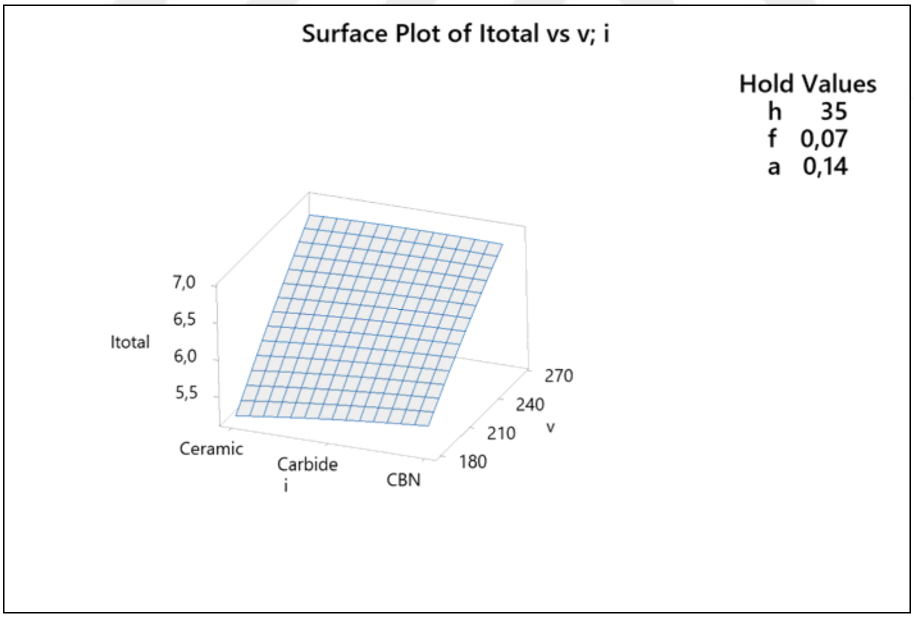


Figure 4.65. Surface plot of $I_{total}$ vs v;i

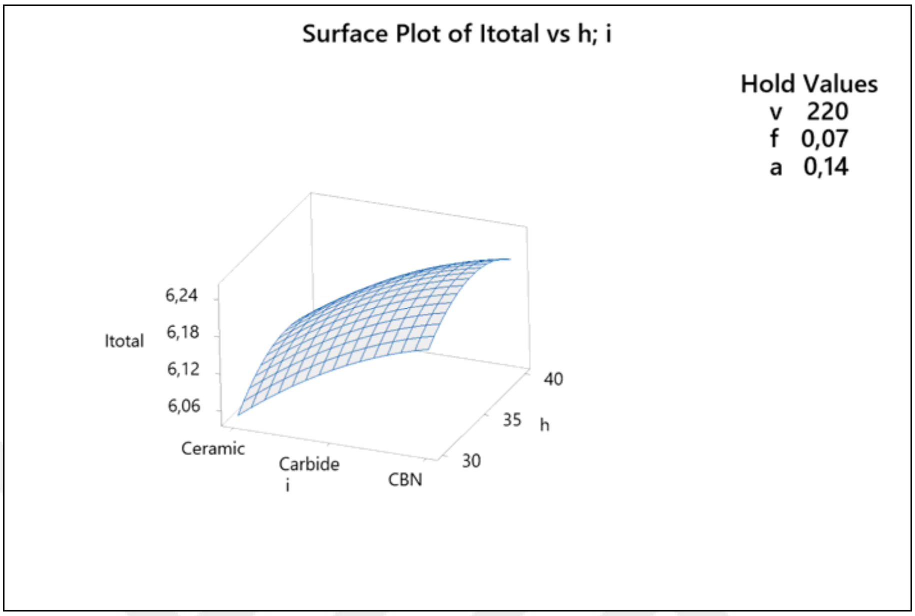


Figure 4.66. Surface plot of $I_{total}$ vs h;i

SN ratios belonging to $I_{total}$ are shown in the following Figure 4.67. The Main Effects Plot for SN ratio of $I_{total}$ indicates that cutting speed has the largest effect on the Signal-to-Noise ratio. The levels of the factors giving the optimum $I_{total}$ value are seen as v1 (Level 1), a1 (Level 1), h1 (Level 1), f1 (Level 1), and i1 (Level 1). That is to say, the optimum $I_{total}$ value is found with 180 m/min cutting speed (v1), 0,08 mm depth of cut (a1), 30 HRC hardness (h1), 0,03 mm/rev feed rate (f1), and ceramic insert (i1).

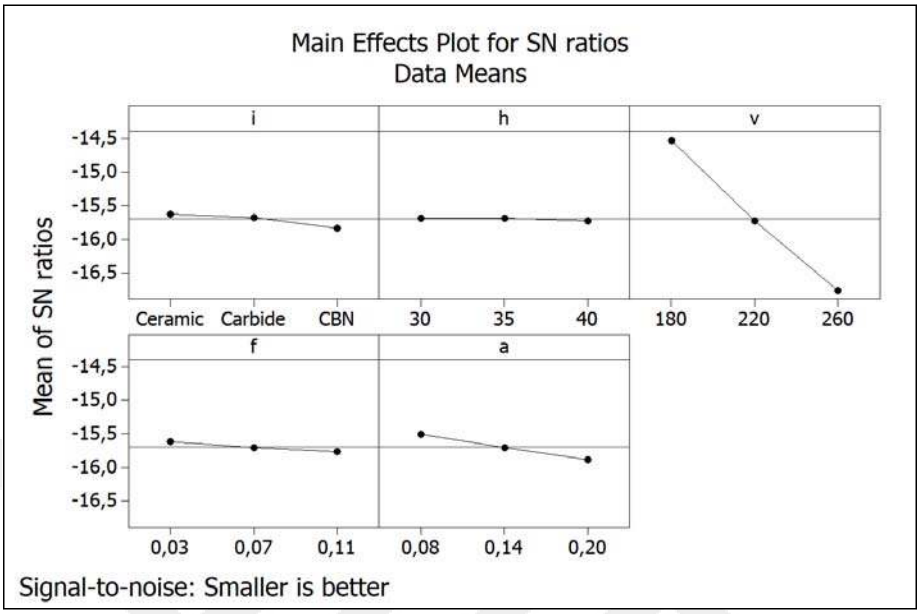


Figure 4.67. Main effects plot for SN ratios of $I_{total}$

After optimum parameters are read from Main effects plot for SN ratios of $I_{total}$, optimization Plot is run for optimum level (A1B1C1D1E1) of $I_{total}$ as shown in Figure 4.68. The optimum value of $I_{total}$ is predicted as 4,83 A.

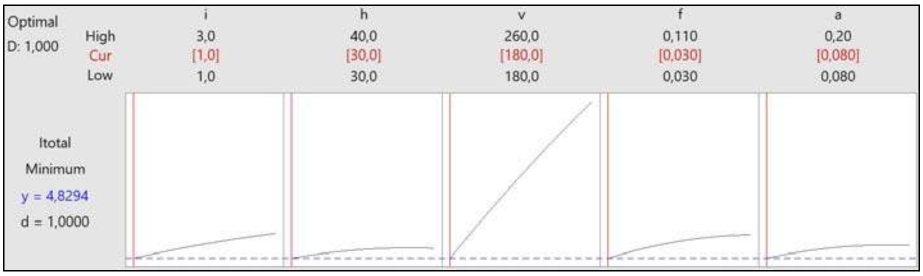


Figure 4.68. Optimization plot for $I_{total}$

An experimental modeling equation has been developed via the relationship between $I_{total}$ and machining parameters (i, h, v, f, a). Experimental modeling equations of $I_{total}$ in coded and uncoded formats are given in Equation 4.13 and Equation 4.14, respectively.

$$I_{total} = + 6,2 + 0,073 A + 0,01187 B + 0,78063 C + 0,05063 D + 0,135 E - 0,02021 A*A - 0,04187 B*B - 0,05021 C*C - 0,05854 D*D - 0,05104 E*E - 0,005 A*B - 0,065 A*C - 0,0275 A*D + 0,035 A*E - 0,0175 B*C - 0,0075 B*D - 0,0125 B*E - 0,04 C*D + 0,045 C*E - 0,0025 D*E \quad (4.13)$$

$$I_{total} = - 4,34 + 0,513 i + 0,1493 h + 0,03876 v + 14,72 f + 2,46 a - 0,0202 i*i - 0,001675 h*h - 0,000031 v*v - 36,6 f*f - 14,18 a*a - 0,00100 i*h - 0,001625 i*v - 0,688 i*f + 0,583 i*a - 0,000087 h*v - 0,037 h*f - 0,0417 h*a - 0,0250 v*f + 0,0187 v*a - 1,0 f*a \quad (4.14)$$

A comparison of experimental and predicted $I_{total}$ values is shown in Table 4.14. $I_{total}$ is found using developed experimental modeling equation. Maximum error (%) between the experimental and predicted $I_{total}$ values are obtained as 1,64.

Table 4.14. Comparison of experimental and predicted results for $I_{total}$

| Runs | Experimental value | Predicted value | Error (%) |
|---|---|---|---|
| **1** | 6 | 6,05 | 0,83 |
| **2** | 6,17 | 6,20 | 0,49 |
| **3** | 6,12 | 6,08 | 0,65 |
| **4** | 6,27 | 6,22 | 0,80 |
| **5** | 5,2 | 5,22 | 0,38 |
| **6** | 6,89 | 6,86 | 0,44 |
| **7** | 5,42 | 5,40 | 0,37 |
| **8** | 6,95 | 6,88 | 1,01 |
| **9** | 5,98 | 5,95 | 0,50 |
| **10** | 6 | 6,00 | 0,00 |
| **11** | 6,28 | 6,24 | 0,64 |
| **12** | 6,25 | 6,24 | 0,16 |
| **13** | 5,26 | 5,21 | 0,95 |
| **14** | 5,48 | 5,49 | 0,18 |
| **15** | 6,94 | 6,90 | 0,58 |
| **16** | 6,9 | 6,92 | 0,29 |
| **17** | 5,93 | 5,90 | 0,51 |
| **18** | 5,95 | 6,01 | 1,01 |
| **19** | 6,2 | 6,18 | 0,32 |
| **20** | 6,21 | 6,27 | 0,97 |
| **21** | 5,32 | 5,30 | 0,38 |
| **22** | 5,35 | 5,36 | 0,19 |
| **23** | 6,83 | 6,89 | 0,88 |
| **24** | 6,79 | 6,88 | 1,33 |
| **25** | 5,95 | 5,97 | 0,34 |
| **26** | 6,2 | 6,17 | 0,48 |
| **27** | 6,06 | 6,13 | 1,16 |
| **28** | 6,2 | 6,22 | 0,32 |
| **29** | 5,18 | 5,23 | 0,97 |
| **30** | 6,7 | 6,70 | 0,00 |
| **31** | 5,4 | 5,41 | 0,19 |
| **32** | 7,1 | 7,06 | 0,56 |
| **33** | 5,98 | 5,96 | 0,33 |
| **34** | 6,05 | 6,03 | 0,33 |
| **35** | 6,14 | 6,16 | 0,33 |
| **36** | 6,35 | 6,37 | 0,31 |
| **37** | 6,01 | 6,03 | 0,33 |
| **38** | 6,02 | 6,07 | 0,83 |
| **39** | 6,22 | 6,15 | 1,13 |
| **40** | 6,2 | 6,15 | 0,81 |
| **41** | 6,29 | 6,20 | 1,43 |
| **42** | 6,1 | 6,20 | 1,64 |
| **43** | 6,22 | 6,20 | 0,32 |
| **44** | 6,19 | 6,20 | 0,16 |
| **45** | 6,18 | 6,20 | 0,32 |
| **46** | 6,22 | 6,20 | 0,32 |

### 4.1.6. Total Sound ($S_{total}$= $S_{machine}$+ $S_{cutting}$) Analysis

Percentage contributions of parameters on $S_{total}$ are shown in Table 4.15. Percentage contributions of insert (i), hardness (h), cutting speed (v), feed rate (f), and depth of cut (a) on $S_{total}$ were found to be 0,06%, 1,75%, 86,71%, 2,14%, and 0,09%, respectively. It appears that cutting speed is the most significant parameter. In addition to these, other contributions on $S_{total}$ are square, interaction, and residual error. These are 2,04, 6,12, and 1,10 percent, respectively.

Table 4.15. Analysis of variance for $S_{total}$

| Source | DF | Seq SS | Adj SS | Adj MS | F | P | % Cont. |
|---|---|---|---|---|---|---|---|
| **Regression** | 20 | 365,463 | 365,463 | 18,273 | 112,12 | 0,000 | 98,90 |
| **Linear** | 5 | 335,331 | 335,331 | 67,066 | 411,50 | 0,000 | 90,74 |
| **i** | 1 | 0,214 | 0,214 | 0,214 | 1,31 | 0,263 | 0,06 |
| **h** | 1 | 6,477 | 6,477 | 6,477 | 39,74 | 0,000 | 1,75 |
| **v** | 1 | 320,410 | 320,410 | 320,410 | 1965,94 | 0,000 | 86,71 |
| **f** | 1 | 7,896 | 7,896 | 7,896 | 48,45 | 0,000 | 2,14 |
| **a** | 1 | 0,334 | 0,334 | 0,334 | 2,05 | 0,165 | 0,09 |
| **Square** | 5 | 7,525 | 7,525 | 1,505 | 9,23 | 0,000 | 2,04 |
| **i*i** | 1 | 0,631 | 0,631 | 1,264 | 7,76 | 0,010 | 0,17 |
| **h*h** | 1 | 0,187 | 0,187 | 0,003 | 0,02 | 0,886 | 0,05 |
| **v*v** | 1 | 0,273 | 0,273 | 0,003 | 0,02 | 0,896 | 0,07 |
| **f*f** | 1 | 6,428 | 6,428 | 6,058 | 37,17 | 0,000 | 1,74 |
| **a*a** | 1 | 0,007 | 0,007 | 0,007 | 0,04 | 0,843 | 0,00 |
| **Interaction** | 10 | 22,607 | 22,607 | 2,261 | 13,87 | 0,000 | 6,12 |
| **i*h** | 1 | 0,141 | 0,141 | 0,141 | 0,86 | 0,362 | 0,04 |
| **i*v** | 1 | 0,002 | 0,002 | 0,002 | 0,02 | 0,902 | 0,00 |
| **i*f** | 1 | 1,210 | 1,210 | 1,210 | 7,42 | 0,012 | 0,33 |
| **i*a** | 1 | 0,010 | 0,010 | 0,010 | 0,06 | 0,806 | 0,00 |
| **h*v** | 1 | 0,040 | 0,040 | 0,040 | 0,25 | 0,625 | 0,01 |
| **h*f** | 1 | 15,484 | 15,484 | 15,484 | 95,01 | 0,000 | 4,19 |
| **h*a** | 1 | 0,122 | 0,122 | 0,122 | 0,75 | 0,394 | 0,03 |
| **v*f** | 1 | 0,490 | 0,490 | 0,490 | 3,01 | 0,095 | 0,13 |
| **v*a** | 1 | 0,022 | 0,022 | 0,022 | 0,14 | 0,713 | 0,01 |
| **f*a** | 1 | 5,085 | 5,085 | 5,085 | 31,20 | 0,000 | 1,38 |
| **Residual Error** | 25 | 4,075 | 4,075 | 0,163 | | | 1,10 |
| **Lack-of-Fit** | 20 | 3,881 | 3,881 | 0,194 | 5,02 | 0,041 | 1,05 |
| **Pure Error** | 5 | 0,193 | 0,193 | 0,039 | | | 0,05 |
| **Total** | 45 | 369,537 | | | | | 100,00 |
| **Model summary**<br>S = 0,403708, R-Sq = 98,90%, R-Sq(pred) = 95,72%, R-Sq(adj) = 98,02% | | | | | | | |

As shown of Residual plots for $S_{total}$ in Figure 4.69, the residuals are normally distributed if the points on the normal probability plot form an approximately linear line. The residuals have constant variance because of the fact that residuals scattered randomly around zero on the Versus Fits graph. In this case, the model has been found to be valid. The Histogram chart is used to evaluate the shape and spread of data. The Histogram chart below shows that the data is normally distributed such as bell shape. Ideally, the residuals on Versus Order plot should occur randomly around zero line. The residuals in this plot are appeared to fluctuate in a down and up around the zero line. From investigation the Residual Plots of $S_{total}$, it is concluded that the model has the ability to accurately predict $S_{total}$.

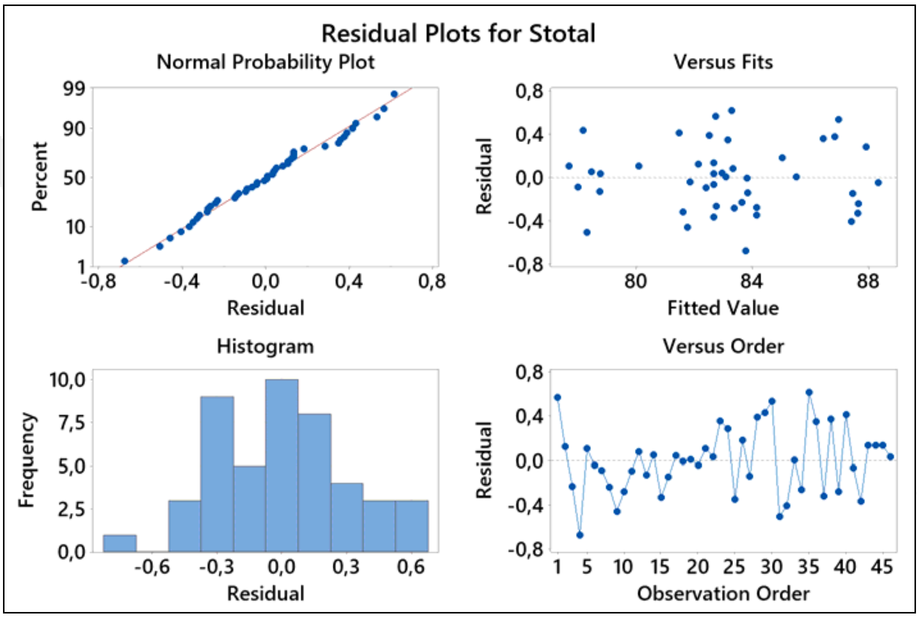

Figure 4.69. Residual plot for $S_{total}$

Chatter vibrations are the most common vibrations growing up to breakage of the workpiece due to dynamic displacements between the tool and the workpiece. Chatter can be determined with continuous monitoring of the amplitude of sound spectrum measured through the microphone (Altintas, 2012). Also, machining vibrations generated during turning operations are called chatter (Prasad and Babu, 2017). To measure the vibration level of CNC machine structure during machining, it has been seen that displacement values measured by the vibration meter and sound signal values measured by microphone have the same character (Bejaxhin and Paulraj, 2019). $S_{total}$ intensity is a value that gives information about cutting parameters, vibration, surface roughness, current, and cutting forces. Out of this, $S_{total}$ intensity can be easily measured with a sound level meter (Şahinoğlu et al., 2017). Surface Plots of interactions of $S_{total}$ are shown in Figures 4.70-4.79. From the Figures related to cutting speed and feed rate against $S_{total}$, it could be seen that when the level of cutting speed and feed rate rise, $S_{total}$ value increases. Likewise, $S_{total}$ value changes depending on the interaction of depth of cut. In the first case, $S_{total}$ value increases as depth of cut and cutting speed level rises during interaction of depth of cut and cutting speed. In the second case, $S_{total}$ value decreases as depth of cut and feed rate level rise during interaction of depth of cut and feed rate. There may have been different reasons for this. This situation can be explained by the effect of BUE formation during machining. As the cutting speed and feed rate increase, the cutting force increases. In this way, the load on the cutting tool holder increases. Then, it results in greater vibrational amplitude and more $S_{total}$ (Deshpande et al., 2017). This result can also be explained from another aspect. When levels of cutting speed and feed rate rise, friction between insert and workpiece happens. Later on, vibration increases with the existence of BUE formation. As a result of the increase in vibration, $S_{total}$ rise occurs (Swain et al., 2020; Fang et al., 2010). Present results are identical to the findings of previous studies (Al-Shayea et al., 2020; Aslan, 2020; Şahinoğlu et al., 2017).

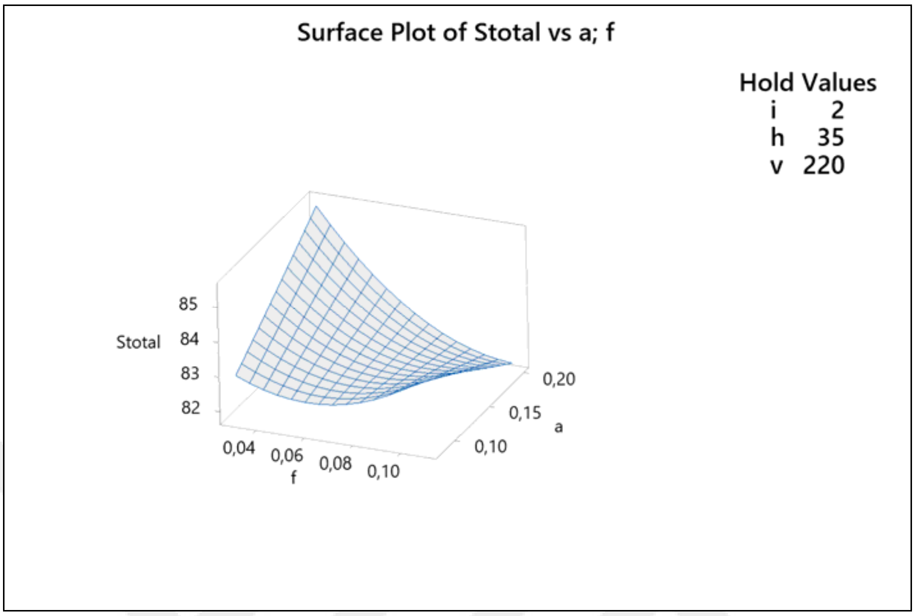


Figure 4.70. Surface plot of $S_{total}$ vs a;f

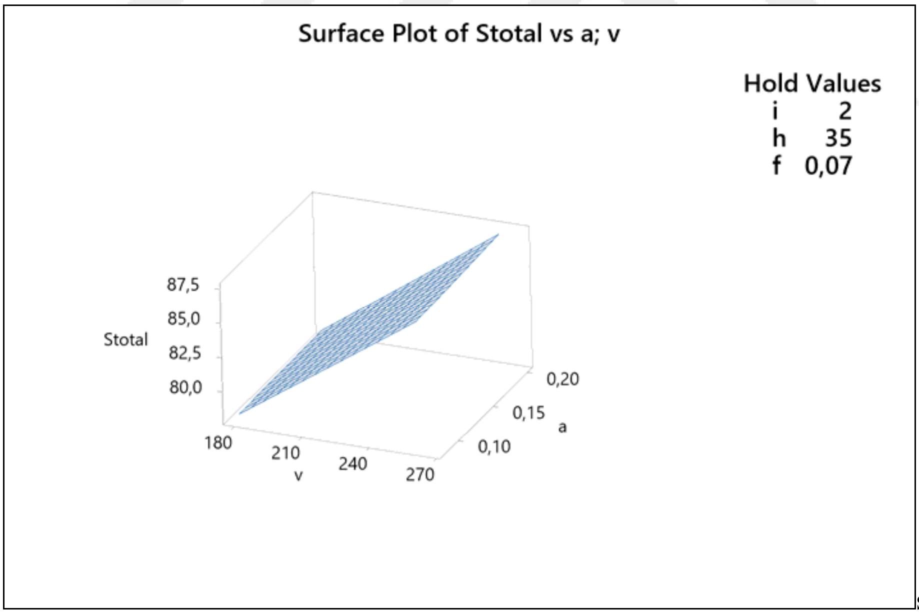


Figure 4.71. Surface plot of $S_{total}$ vs a;v

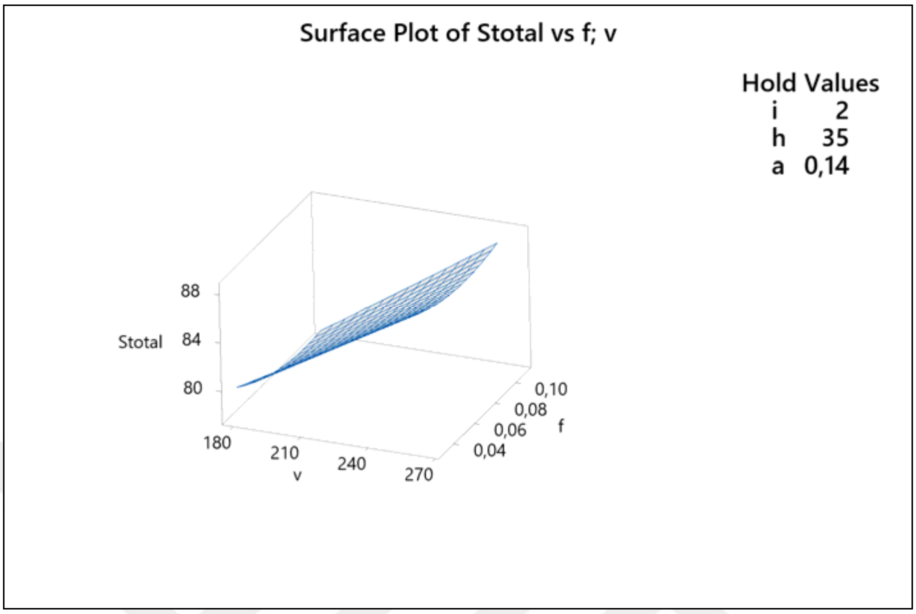


Figure 4.72. Surface plot of $S_{total}$ vs f;v

3D Surface Plots given in Figures 4.73-4.75 show the relationship between hardness (h) and three variables (a, f, and v). It is seen from the Figures that the lowest $S_{total}$ level on the plot occurs at h1 (30 HRC).

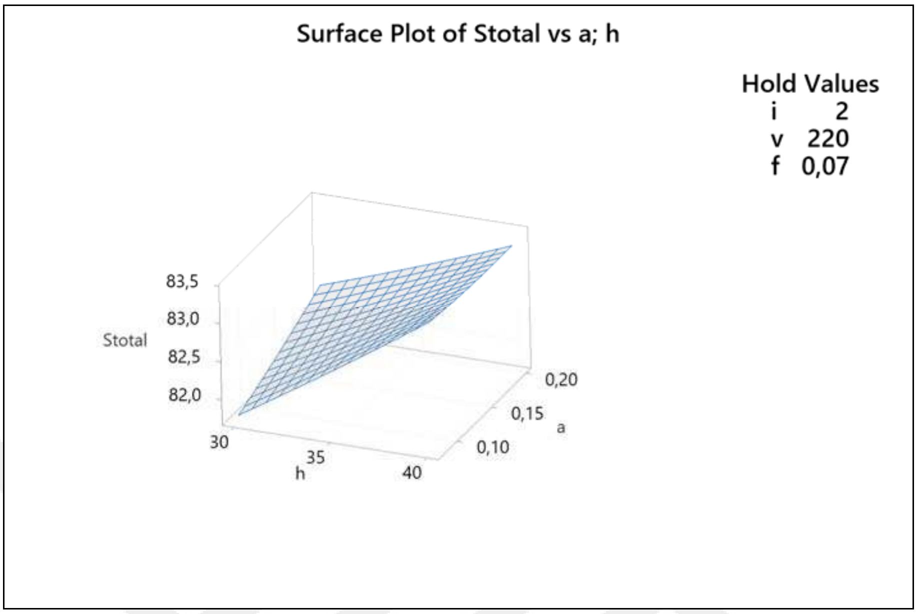


Figure 4.73. Surface plot of $S_{total}$ vs a;h

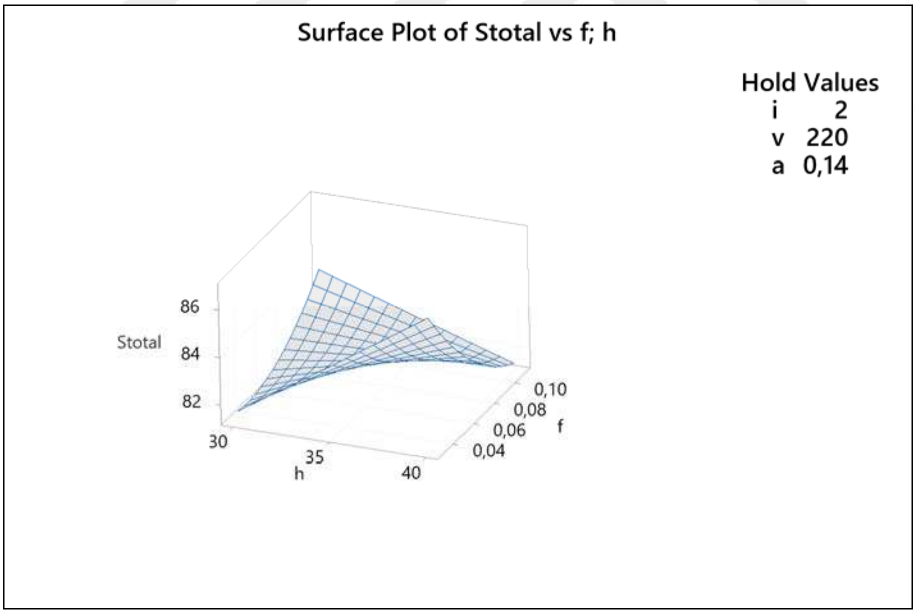


Figure 4.74. Surface plot of $S_{total}$ vs f;h

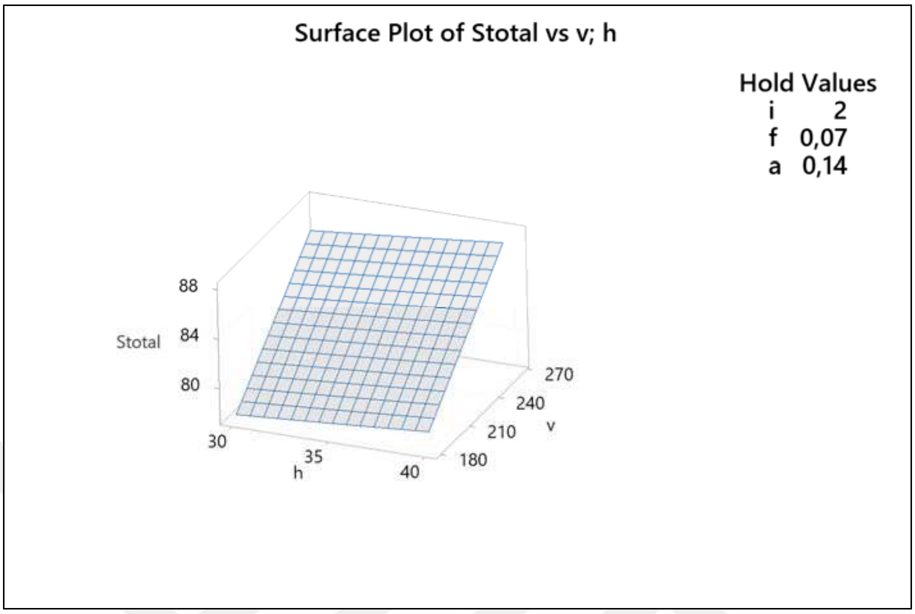


Figure 4.75. Surface plot of $S_{total}$ vs v;h

The following 3D Surface Plots given in Figures 4.76- 4.79 show the effect of depth of cut, feed rate, cutting speed, and hardness on $S_{total}$.

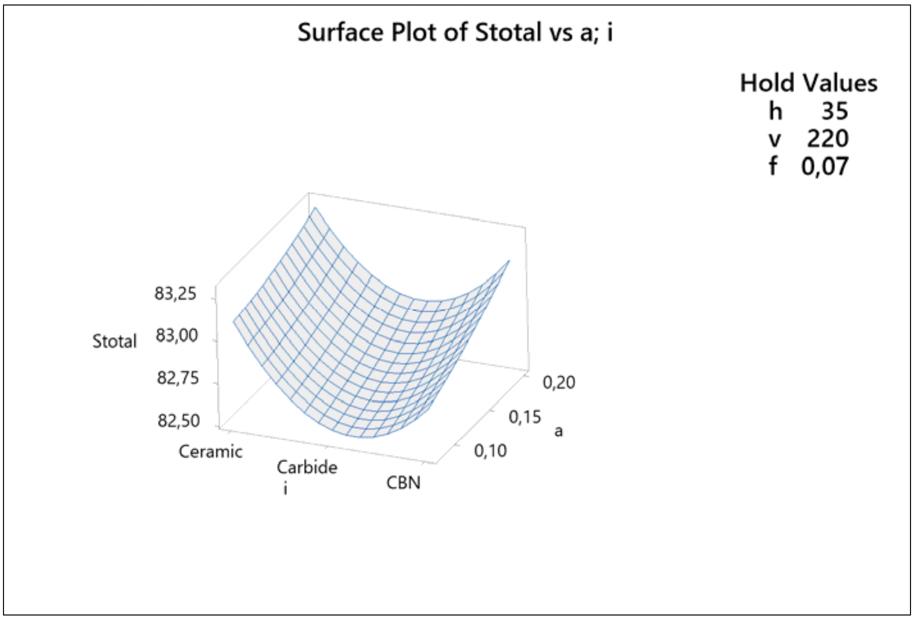


Figure 4.76. Surface plot of $S_{total}$ vs a;i

It is seen from Figures that the lowest $S_{total}$ level on the plot occurs at approximately insert = 2 (carbide). Moreover, as shown in Figure 4.76, the highest $S_{total}$ level is performed when ceramic insert is used. This situation can be explained by toughness of insert material. Toughness represents pressure and impact resistance that correlate with a tool's ability to withstand high feed rates, big depths of cut. Cutting tools (inserts) are subjected to different types of loading, unloading, vibration, and other interfering factors. CBN tool is in the form of a cubic boron nitride coating on a carbide plate. When there are impact loads during cutting, high toughness of a material is necessary to decrease vibrations. That is, the higher the toughness, the higher the vibration absorbing ability. The carbide insert has the highest toughness and the ceramic insert has the least toughness. Therefore, the carbide insert may have caused decreasing of the $S_{total}$ by absorbing vibration due to its highest toughness feature.

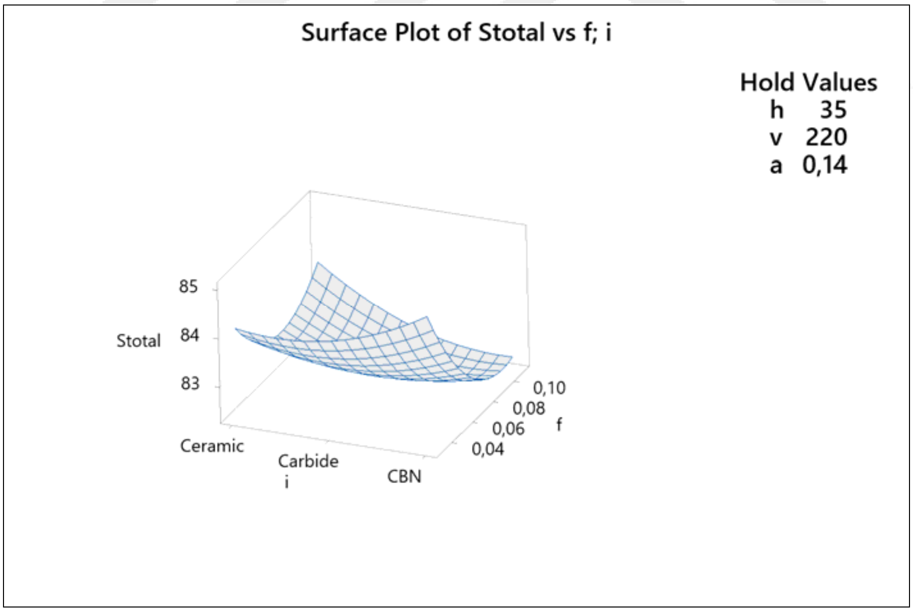


Figure 4.77. Surface plot of $S_{total}$ vs f;i

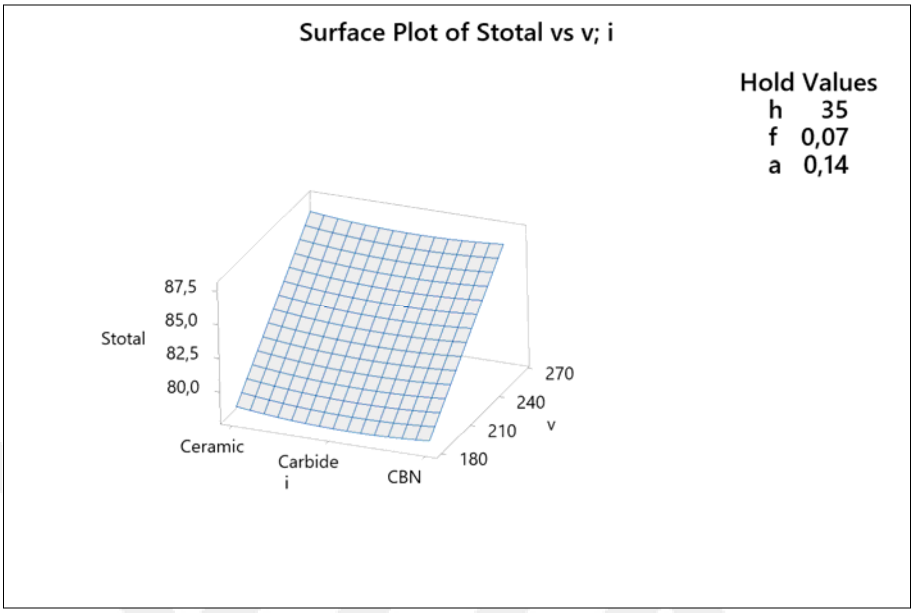


Figure 4.78. Surface plot of $S_{total}$ vs v;i

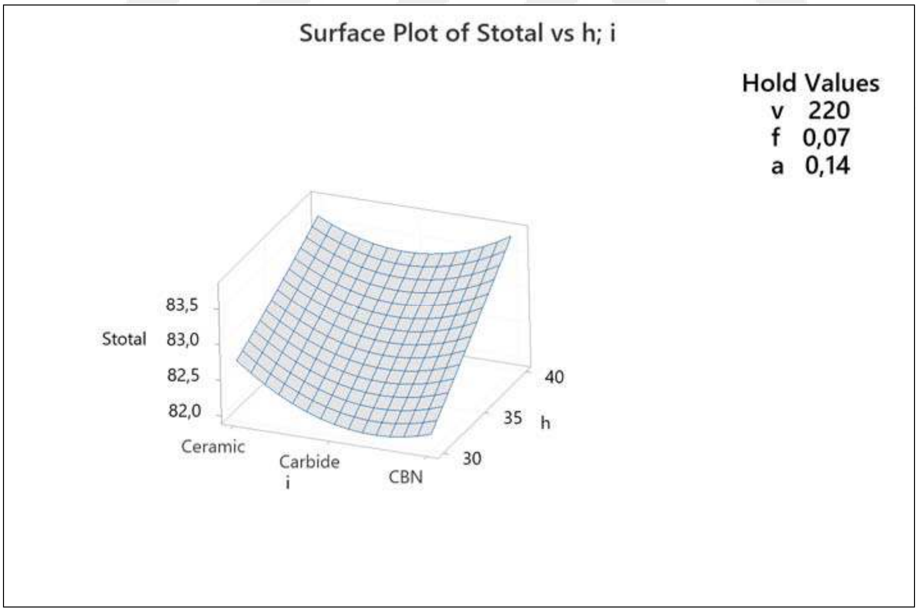


Figure 4.79. Surface plot of $S_{total}$ vs h;i

As shown in Figure 4.67, the Main Effects Plot for SN ratio of $S_{total}$ indicates that cutting speed has the largest effect on $S_{total}$. The levels of the factors giving the optimum $S_{total}$ value are seen as v1 (Level 1), f2 (Level 2), h1 (Level 1), a1 (Level 1), and i2 (Level 2). That is, the optimum $S_{total}$ value is found taking 180 m/min cutting speed (v1), 0,07 mm/rev feed rate (f2), 30 HRC hardness (h1), 0,08 mm depth of cut (a1), and carbide insert (i2) parameters.

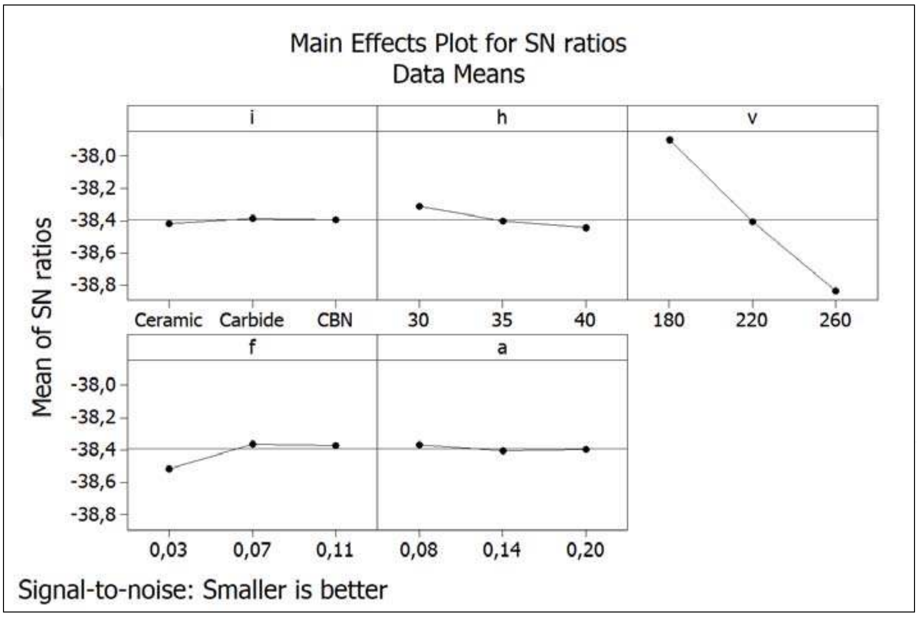


Figure 4.80. Main effects plot for SN ratios of $S_{total}$


Figure 4.81. Optimization plot for $S_{total}$

After optimum parameters are read from the Main effects plot for SN ratios of $S_{total}$, optimization Plot is run for optimum level (A2B1C1D2E1) of $S_{total}$ as shown in Figure 4.81. The optimum value of $S_{total}$ is predicted as 77,48 dB.

Experimental modelling equation has been developed via the relationship between $S_{total}$ and machining parameters (i, h, v, f, a). Experimental modeling equations of $S_{total}$ in coded and uncoded formats are given in Equation 4.15 and Equation 4.16, respectively.

$$S_{total} = 82{,}6667 - 0{,}1156\,A + 0{,}6363\,B + 4{,}4750\,C - 0{,}7025\,D + 0{,}1444\,E + 0{,}3806\,A*A + 0{,}0198\,B*B + 0{,}0181\,C*C + 0{,}8331\,D*D + 0{,}0273\,E*E + 0{,}1875\,A*B + 0{,}0250\,A*C - 0{,}5500\,A*D + 0{,}0500\,A*E + 0{,}1000\,B*C - 1{,}9675\,B*D - 0{,}1750\,B*E + 0{,}3500\,C*D + 0{,}0750\,C*E - 1{,}1275\,D*E \qquad (4.15)$$

$$S_{total} = 38{,}3 - 2{,}24\,i + 0{,}657\,h + 0{,}0685\,v + 299{,}0\,f + 45{,}0\,a + 0{,}381\,i*i + 0{,}00079\,h*h + 0{,}000011\,v*v + 520{,}7\,f*f + 7{,}6\,a*a + 0{,}0375\,i*h + 0{,}00062\,i*v - 13{,}75\,i*f + 0{,}83\,i*a + 0{,}00050\,h*v - 9{,}84\,h*f - 0{,}583\,h*a + 0{,}219\,v*f + 0{,}0312\,v*a - 469{,}8\,f*a \qquad (4.16)$$

The developed model is valuable for works done under present cases because of the high costs and difficulties executing of machining experiments (Kuntoğlu, 2020). A comparison of experimental and predicted $S_{total}$ values is shown in Table 4.16. $S_{total}$ is found using developed experimental modelling equation. Maximum error (%) between the experimental and predicted $S_{total}$ values are obtained as 0,81. Results indicated that predicted values are in close relation with experimental values.

Table 4.16. Comparison of experimental and predicted results for $S_{total}$

| Runs | Experimental Value | Predicted Value | Error (%) |
|---|---|---|---|
| 1 | 83,3 | 82,73 | 0,68 |
| 2 | 82,25 | 82,13 | 0,15 |
| 3 | 83,4 | 83,63 | 0,28 |
| 4 | 83,1 | 83,78 | 0,81 |
| 5 | 80,2 | 80,10 | 0,13 |
| 6 | 88,3 | 88,35 | 0,05 |
| 7 | 77,9 | 77,99 | 0,12 |
| 8 | 87,4 | 87,64 | 0,28 |
| 9 | 81,3 | 81,76 | 0,56 |
| 10 | 83,1 | 83,38 | 0,34 |
| 11 | 82,3 | 82,40 | 0,12 |
| 12 | 83,4 | 83,32 | 0,10 |
| 13 | 78,6 | 78,73 | 0,17 |
| 14 | 78,5 | 78,45 | 0,06 |
| 15 | 87,3 | 87,63 | 0,38 |
| 16 | 87,3 | 87,45 | 0,17 |
| 17 | 83 | 82,96 | 0,05 |
| 18 | 83,8 | 83,81 | 0,01 |
| 19 | 85,51 | 85,50 | 0,01 |
| 20 | 81,8 | 81,84 | 0,05 |
| 21 | 77,8 | 77,69 | 0,14 |
| 22 | 78,8 | 78,77 | 0,04 |
| 23 | 86,8 | 86,44 | 0,41 |
| 24 | 88,2 | 87,92 | 0,32 |
| 25 | 83,8 | 84,15 | 0,42 |
| 26 | 85,2 | 85,02 | 0,21 |
| 27 | 83,7 | 83,84 | 0,17 |
| 28 | 82,9 | 82,51 | 0,47 |
| 29 | 78,6 | 78,17 | 0,55 |
| 30 | 87,5 | 86,97 | 0,61 |
| 31 | 77,8 | 78,31 | 0,65 |
| 32 | 87 | 87,41 | 0,47 |
| 33 | 83,1 | 83,10 | 0,01 |
| 34 | 82,5 | 82,76 | 0,32 |
| 35 | 83,9 | 83,28 | 0,73 |
| 36 | 83,5 | 83,15 | 0,42 |
| 37 | 81,3 | 81,62 | 0,39 |
| 38 | 87,2 | 86,83 | 0,43 |
| 39 | 83,87 | 84,15 | 0,33 |
| 40 | 81,9 | 81,49 | 0,51 |
| 41 | 82,6 | 82,67 | 0,08 |
| 42 | 82,3 | 82,67 | 0,45 |
| 43 | 82,8 | 82,67 | 0,16 |
| 44 | 82,8 | 82,67 | 0,16 |
| 45 | 82,8 | 82,67 | 0,16 |
| 46 | 82,7 | 82,67 | 0,04 |

#### 4.1.7. Total Power Consumption ($P_{total}$=$P_{unloaded}$+$P_{cutting}$) Analysis

The analysis of variance and percentage contribution of process parameters for $P_{total}$ are presented in Table 4.17. Table 4.17 shows that percentage contributions of insert (i), hardness (h), cutting speed (v), feed rate (f), and depth of cut (a) on $P_{total}$ were found to be 0,83%, 0,02%, 94,23%, 0,40%, and 2,82%, respectively. Following this, cutting speed is seen as the most influencing parameter on $P_{total}$. In addition to these, other contributions on $P_{total}$ are square, interaction, and residual error. These are 0,50; 0,40; and 0,81 percent, respectively.

Table 4.17. Analysis of variance for $P_{total}$

| Source | DF | Seq SS | Adj SS | Adj MS | F | P | % Cont. |
|---|---|---|---|---|---|---|---|
| **Regression** | 20 | 4446139 | 4446139 | 222307 | 153,00 | 0,000 | 99,19 |
| **Linear** | 5 | 4405828 | 4405828 | 881166 | 606,44 | 0,000 | 98,29 |
| **i** | 1 | 37063 | 37063 | 37063 | 25,51 | 0,000 | 0,83 |
| **h** | 1 | 977 | 977 | 977 | 0,67 | 0,420 | 0,02 |
| **v** | 1 | 4223703 | 4223703 | 4223703 | 2906,83 | 0,000 | 94,23 |
| **f** | 1 | 17764 | 17764 | 17764 | 12,23 | 0,002 | 0,40 |
| **a** | 1 | 126321 | 126321 | 126321 | 86,94 | 0,000 | 2,82 |
| **Square** | 5 | 22322 | 22322 | 4464 | 3,07 | 0,027 | 0,50 |
| **i*i** | 1 | 1544 | 1544 | 1544 | 1,06 | 0,313 | 0,03 |
| **h*h** | 1 | 6629 | 6629 | 6629 | 4,56 | 0,043 | 0,15 |
| **v*v** | 1 | 9531 | 9531 | 9531 | 6,56 | 0,017 | 0,21 |
| **f*f** | 1 | 12957 | 12957 | 12957 | 8,92 | 0,006 | 0,29 |
| **a*a** | 1 | 9850 | 9850 | 9850 | 6,78 | 0,015 | 0,22 |
| **Interaction** | 10 | 17989 | 17989 | 1799 | 1,24 | 0,316 | 0,40 |
| **i*h** | 1 | 43 | 43 | 43 | 0,03 | 0,864 | 0,00 |
| **i*v** | 1 | 7321 | 7321 | 7321 | 5,04 | 0,034 | 0,16 |
| **i*f** | 1 | 1310 | 1310 | 1310 | 0,90 | 0,351 | 0,03 |
| **i*a** | 1 | 2123 | 2123 | 2123 | 1,46 | 0,238 | 0,05 |
| **h*v** | 1 | 531 | 531 | 531 | 0,37 | 0,551 | 0,01 |
| **h*f** | 1 | 97 | 97 | 97 | 0,07 | 0,798 | 0,00 |
| **h*a** | 1 | 271 | 271 | 271 | 0,19 | 0,670 | 0,01 |
| **v*f** | 1 | 2772 | 2772 | 2772 | 1,91 | 0,179 | 0,06 |
| **v*a** | 1 | 3509 | 3509 | 3509 | 2,41 | 0,133 | 0,08 |
| **f*a** | 1 | 11 | 11 | 11 | 0,01 | 0,932 | 0,00 |
| **Residual Error** | 25 | 36326 | 36326 | 1453 | | | 0,81 |
| **Lack-of-Fit** | 20 | 27922 | 27922 | 1396 | 0,83 | 0,657 | 0,62 |
| **Pure Error** | 5 | 8404 | 8404 | 1681 | | | 0,19 |
| **Total** | 45 | 4482464 | | | | | 100,00 |
| **Model summary**<br>S = 38,1186, R-Sq = 99,19%, R-Sq(pred) = 97,24%, R-Sq(adj) = 98,54% | | | | | | | |

From the residual plot (Normal Probability Plot) for $P_{total}$ given in Figure 4.82 (top left), it can be said that the residual error is much less because the data points are on an approximately linear line. The Versus Fits chart (top right) indicates the error terms against the fitted values. The data points appear to be distributed equally at the top and bottom sides of line zero. The Histogram chart (bottom left) exhibits a bell-shaped curve. The Versus Order chart (bottom right) depicts that residuals bounce randomly around the 0 line. Thus, this behavior typically indicates that the model is appropriate to predict $P_{total}$.

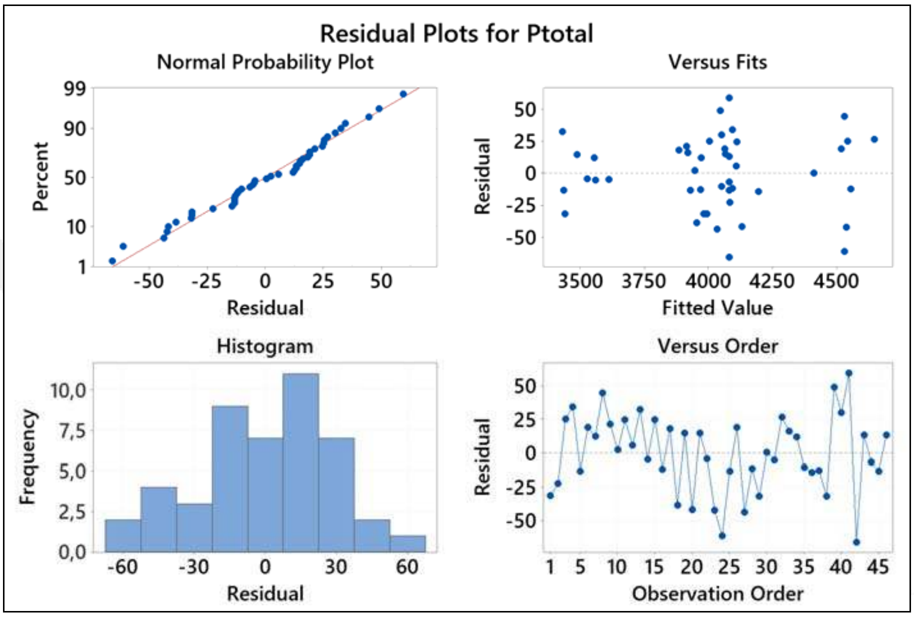


Figure 4.82. Residual plot for $P_{total}$

From Figure 4.83-4.85 it is shown that minimum $P_{total}$ is achieved at the interaction of lowest feed rate and lowest cutting speed.

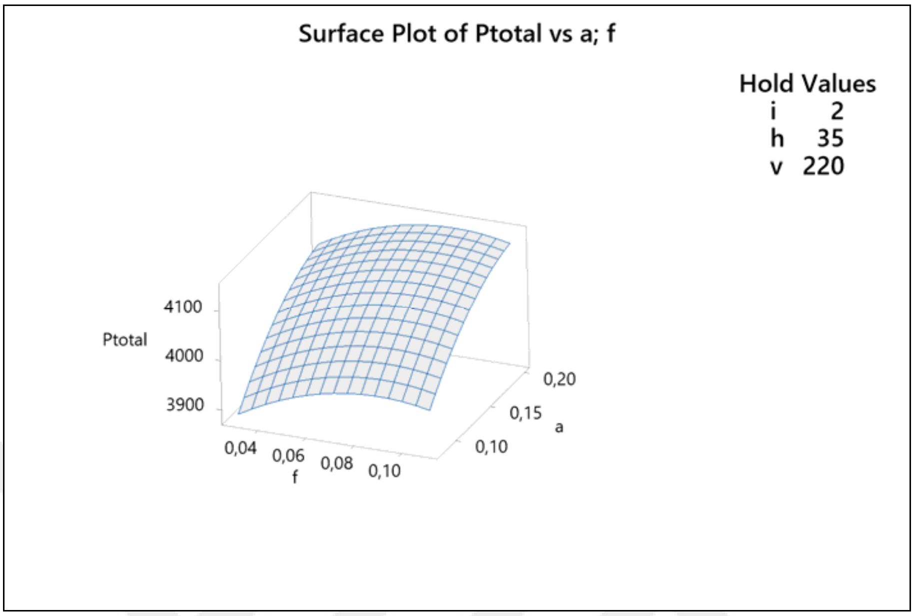


Figure 4.83. Surface plot of $P_{total}$ vs a;f

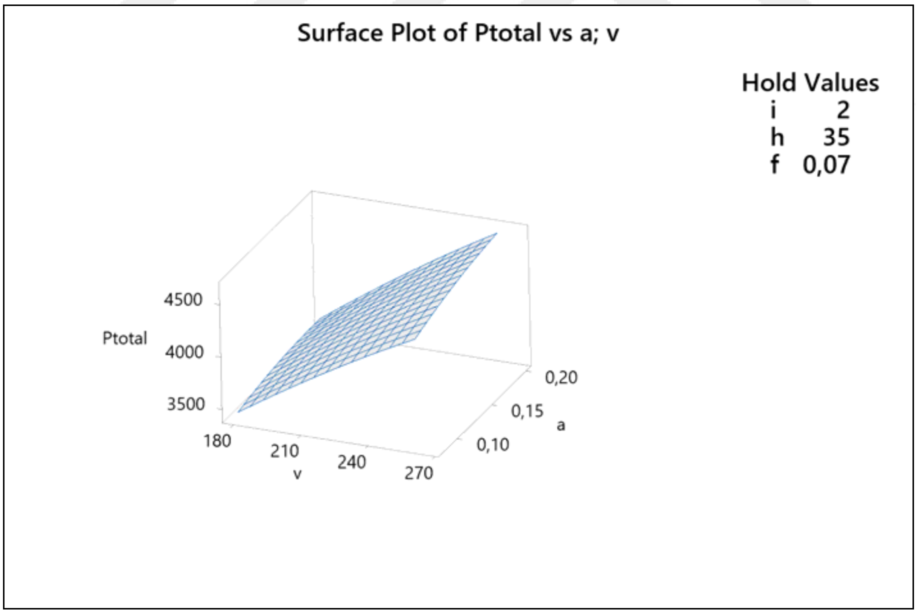


Figure 4.84. Surface plot of $P_{total}$ vs a;v

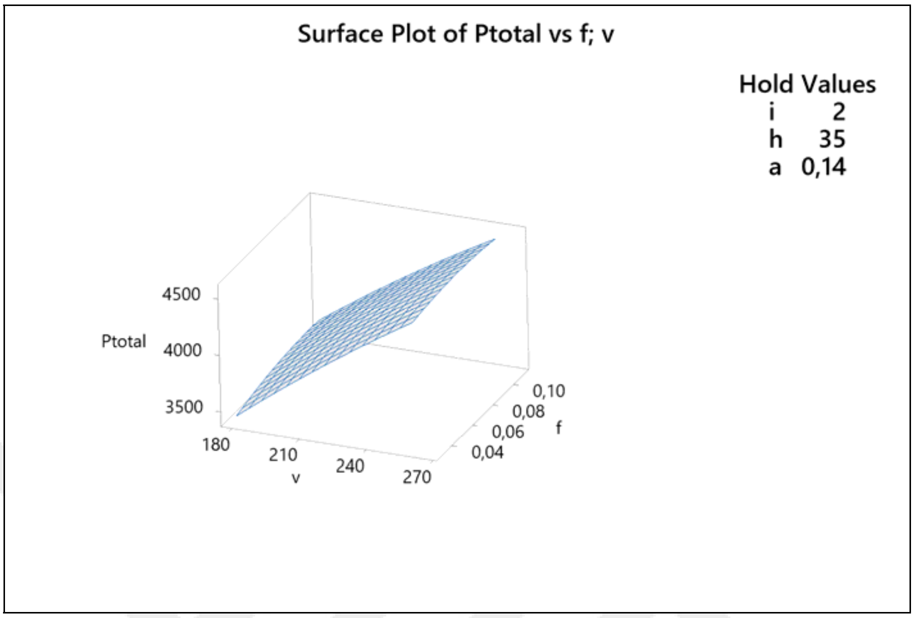


Figure 4.85. Surface plot of $P_{total}$ vs f;v

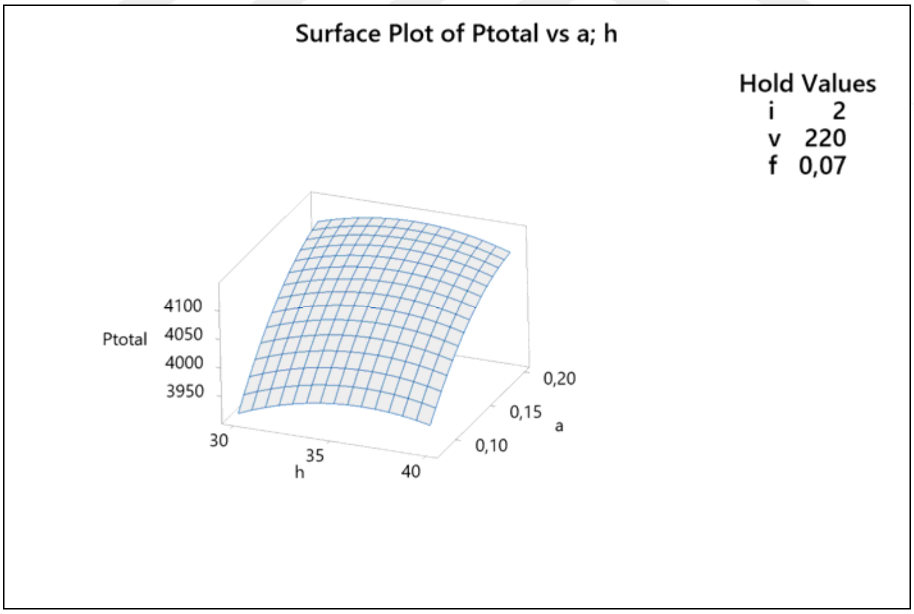


Figure 4.86. Surface plot of $P_{total}$ vs a;h

It is apparent from Figures 4.86-4.88 that there is the increase in $P_{total}$ with an increase in hardness, depth of cut, feed rate, and cutting speed. Also, Figures 4.89-4.92 show $P_{total}$ variation with i, h, v, f, and a.

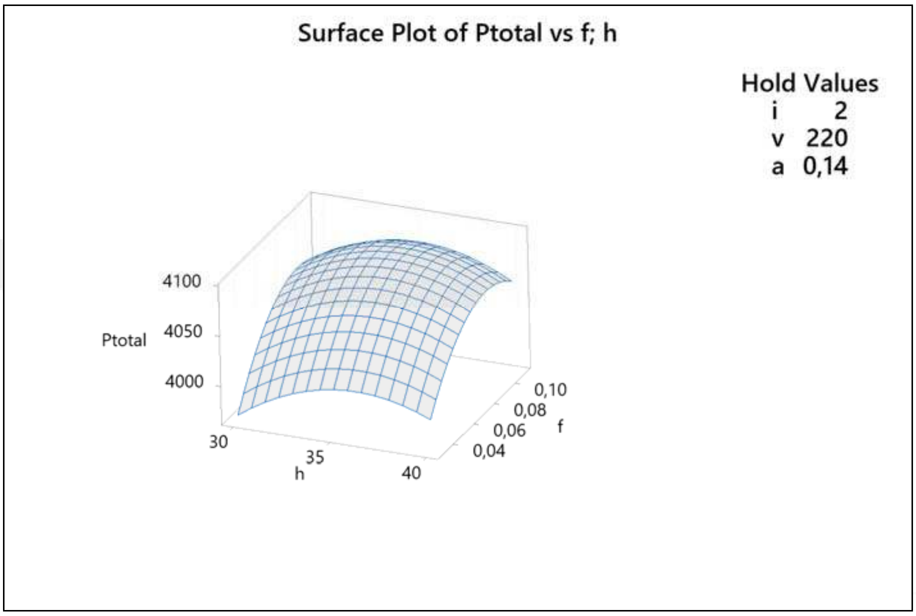


Figure 4.87. Surface plot of $P_{total}$ vs f;h

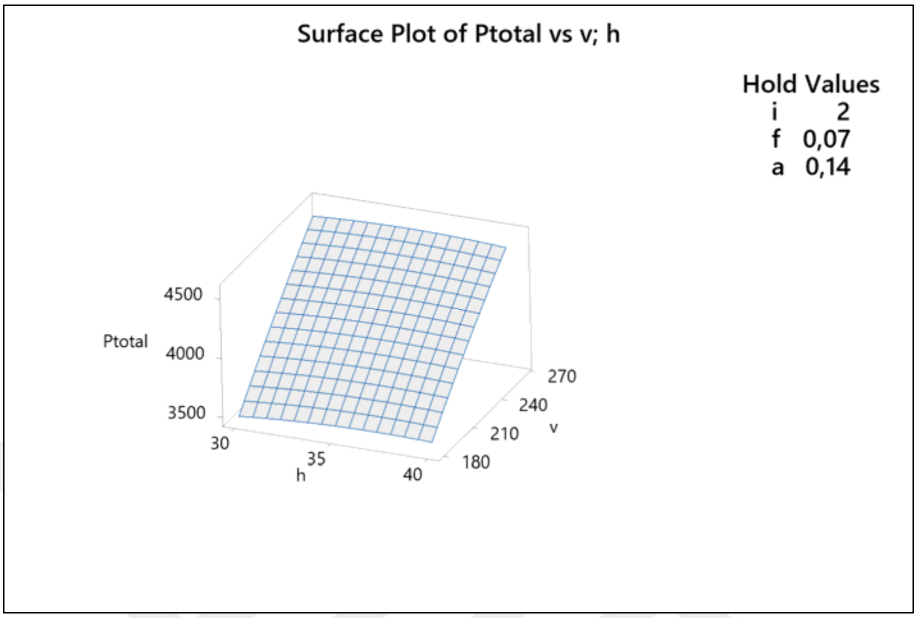


Figure 4.88. Surface plot of $P_{total}$ vs v;h

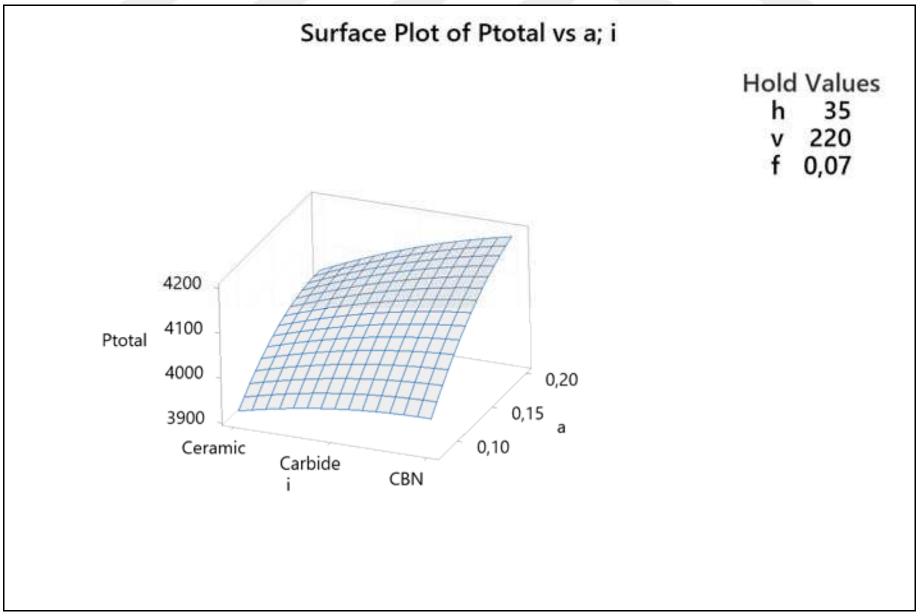


Figure 4.89. Surface plot of $P_{total}$ vs a;i

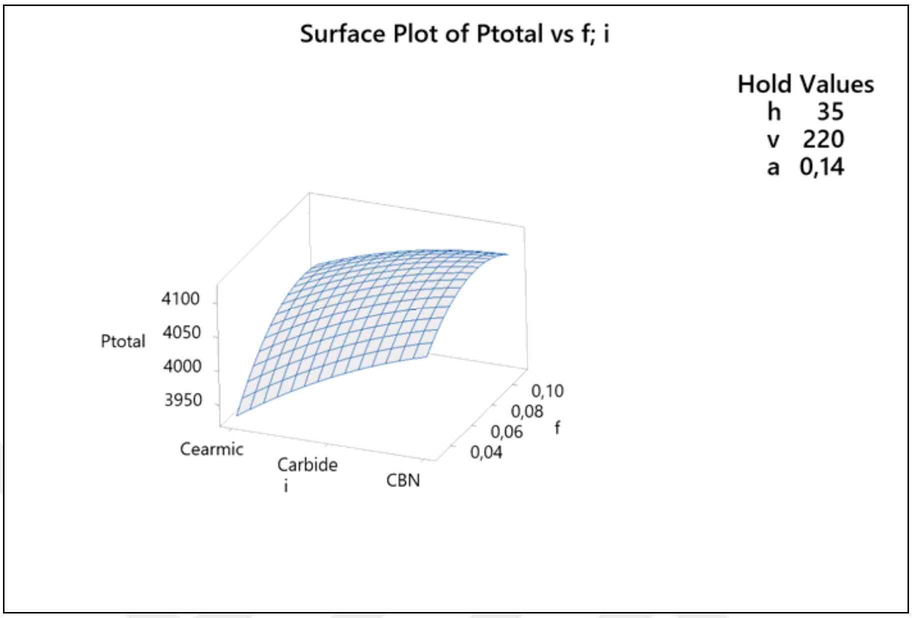


Figure 4.90. Surface plot of $P_{total}$ vs f;i

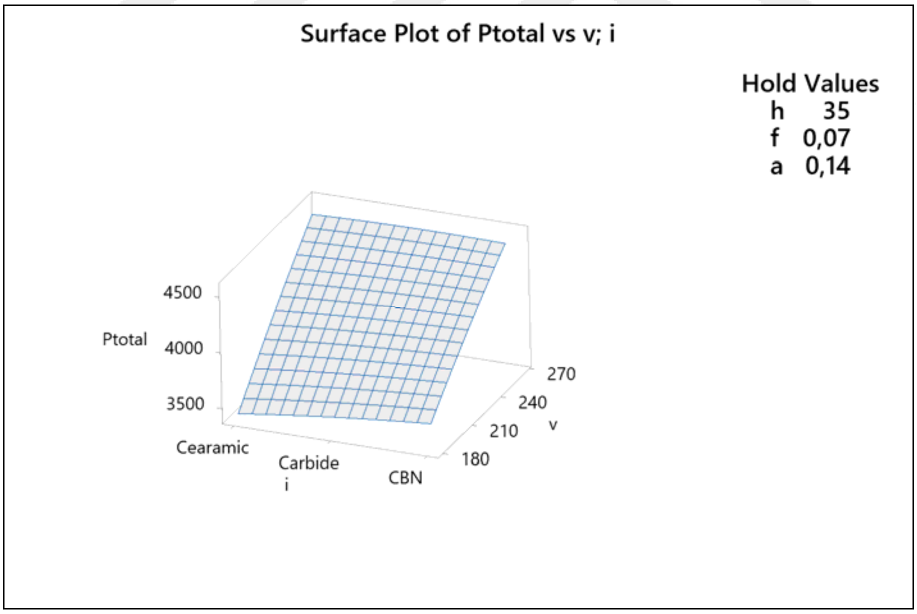


Figure 4.91. Surface plot of $P_{total}$ vs v;i

Figures show that maximum $P_{total}$ is performed as shown in Figure 4.91 when CBN insert (3) and the highest cutting speed (270 m/min) are used.

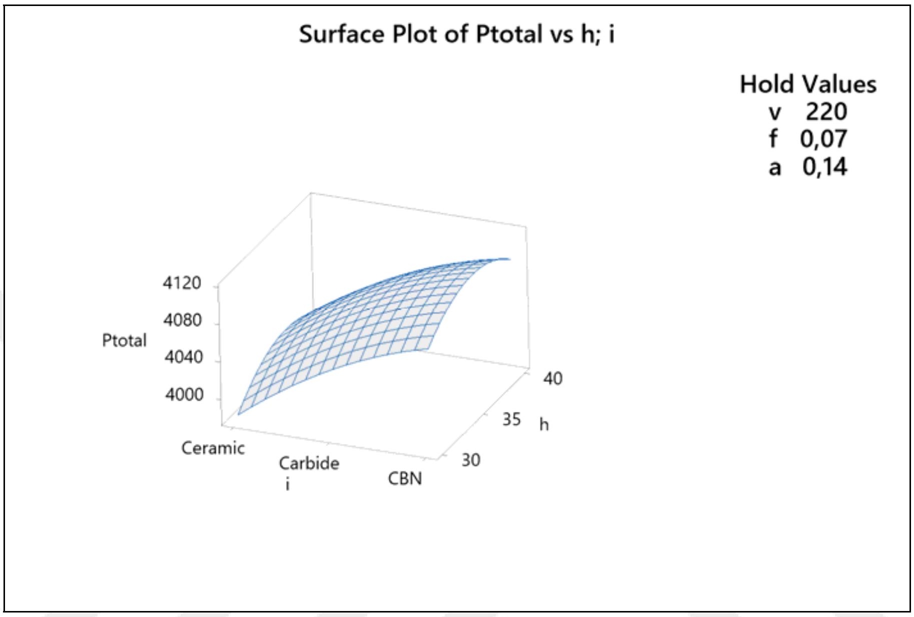


Figure 4.92. Surface plot of $P_{total}$ vs h;i

The Main Effects Plot for SN ratios of $P_{total}$ indicates that cutting speed has the largest effect on the Signal-to-Noise ratio as shown in Figure 4.93. The levels of the factors giving the optimum $P_{total}$ value are seen as v1 (Level 1), a1 (Level 1), h1 (Level 1), f1 (Level 1), and i1 (Level 1). That is to say, the optimum $P_{total}$ value is found with ceramic insert (i1), 30 HRC hardness (h1), 180 m/min cutting speed (v1), 0,03 mm/rev feed rate (f1), and 0,08 mm depth of cut (a1).

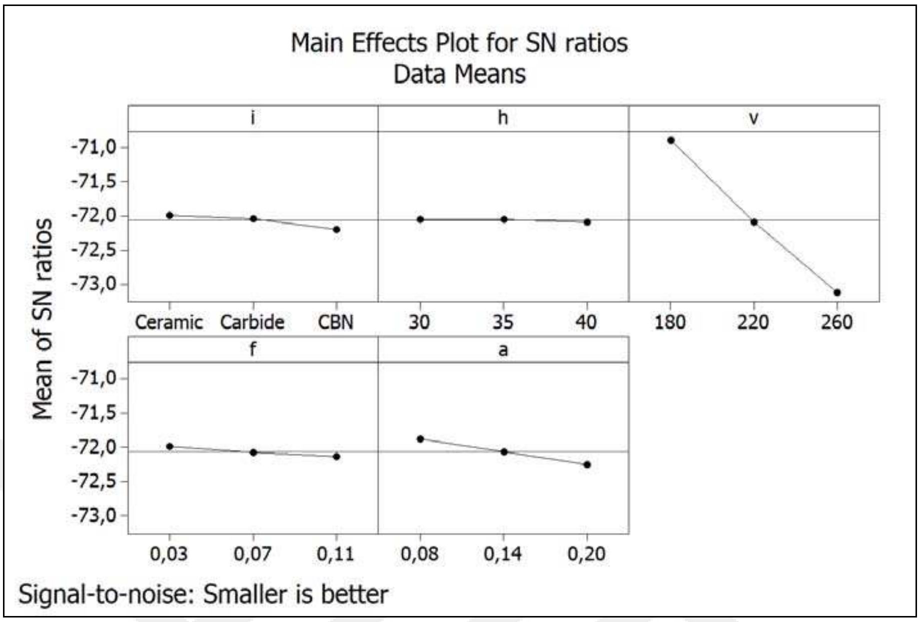


Figure 4.93. Main effects plot for SN ratios of $P_{total}$

The aim is to minimize $P_{total}$ value. To this end, optimum parameters are read from the Main effects plot for SN ratios of $P_{total}$. Optimization Plot is run for optimum level (A1B1C1D1E1) of $P_{total}$ as shown in Figure 4.94. The optimum value of $P_{total}$ is predicted as 3178,60 W.

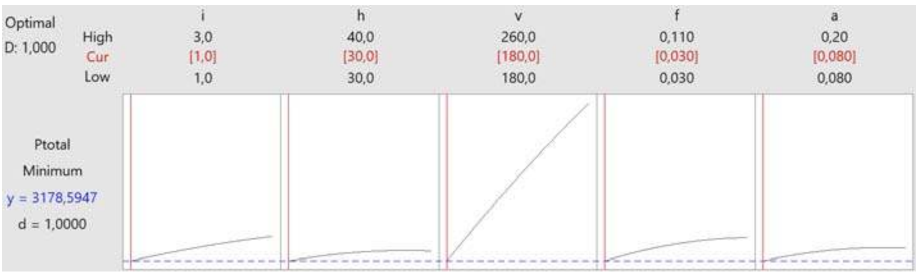


Figure 4.94. Optimization plot for $P_{total}$

Experimental modelling equation has been developed via the relationship between $P_{total}$ and machining parameters (i, h, v, f, a). Experimental modeling equations of $P_{total}$ in coded and uncoded formats are given in Equation 4.17 and Equation 4.18, respectively.

$$P_{total} = 4080,71 + 48,13\ A + 7,82\ B + 513,79\ C + 33,32\ D + 88,85\ E - 13,30\ A*A - 27,56\ B*B - 33,05\ C*C - 38,53\ D*D - 33,59\ E*E - 3,29\ A*B - 42,78\ A*C - 18,10\ A*D + 23,04\ A*E - 11,52\ B*C - 4,94\ B*D - 8,23\ B*E - 26,33\ C*D + 29,62\ C*E - 1,65\ D*E \quad (4.17)$$

$$P_{total} = - 2857 + 338\ i + 98,3\ h + 25,51\ v + 9689\ f + 1619\ a - 13,3\ i*i - 1,102\ h*h - 0,02065\ v*v - 24082\ f*f - 9332\ a*a - 0,66\ i*h - 1,070\ i*v - 452\ i*f + 384\ i*a - 0,0576\ h*v - 24,7\ h*f - 27,4\ h*a - 16,5\ v*f + 12,34\ v*a - 686\ f*a \quad (4.18)$$

A comparison of calculated and predicted $P_{total}$ values is shown in Table 4.18. $P_{total}$ is predicted using developed experimental modelling equation. Maximum error (%) between the calculated and predicted $P_{total}$ values are found as 1,64.

Table 4.18. Comparison of calculated and predicted results for $P_{total}$

| Runs | Calculated value | Predicted value | Error (%) |
|---|---|---|---|
| **1** | 3949,08 | 3980,61 | 0,80 |
| **2** | 4060,97 | 4083,45 | 0,55 |
| **3** | 4028,06 | 4002,83 | 0,63 |
| **4** | 4126,78 | 4092,50 | 0,83 |
| **5** | 3422,53 | 3435,70 | 0,38 |
| **6** | 4534,86 | 4515,93 | 0,42 |
| **7** | 3567,33 | 3554,99 | 0,35 |
| **8** | 4574,35 | 4529,92 | 0,97 |
| **9** | 3935,91 | 3914,66 | 0,54 |
| **10** | 3949,08 | 3946,74 | 0,06 |
| **11** | 4133,37 | 4108,82 | 0,59 |
| **12** | 4113,62 | 4108,00 | 0,14 |
| **13** | 3462,02 | 3429,66 | 0,93 |
| **14** | 3606,82 | 3611,48 | 0,13 |
| **15** | 4567,76 | 4542,81 | 0,55 |
| **16** | 4541,44 | 4553,50 | 0,27 |
| **17** | 3903,00 | 3884,77 | 0,47 |
| **18** | 3916,17 | 3954,70 | 0,98 |
| **19** | 4080,71 | 4065,77 | 0,37 |
| **20** | 4087,29 | 4129,12 | 1,02 |
| **21** | 3501,51 | 3486,98 | 0,42 |
| **22** | 3521,26 | 3525,65 | 0,12 |
| **23** | 4495,36 | 4537,60 | 0,94 |
| **24** | 4469,04 | 4530,19 | 1,37 |
| **25** | 3916,17 | 3929,33 | 0,34 |
| **26** | 4080,71 | 4061,79 | 0,46 |
| **27** | 3988,57 | 4032,17 | 1,09 |
| **28** | 4080,71 | 4092,23 | 0,28 |
| **29** | 3409,37 | 3441,04 | 0,93 |
| **30** | 4409,80 | 4409,39 | 0,01 |
| **31** | 3554,17 | 3559,52 | 0,15 |
| **32** | 4673,07 | 4646,33 | 0,57 |
| **33** | 3935,91 | 3919,87 | 0,41 |
| **34** | 3981,98 | 3970,06 | 0,30 |
| **35** | 4041,22 | 4051,50 | 0,25 |
| **36** | 4179,44 | 4193,84 | 0,34 |
| **37** | 3955,66 | 3968,55 | 0,33 |
| **38** | 3962,24 | 3994,05 | 0,80 |
| **39** | 4093,88 | 4045,06 | 1,19 |
| **40** | 4080,71 | 4050,82 | 0,73 |
| **41** | 4139,95 | 4080,71 | 1,43 |
| **42** | 4014,89 | 4080,71 | 1,64 |
| **43** | 4093,88 | 4080,71 | 0,32 |
| **44** | 4074,13 | 4080,71 | 0,16 |
| **45** | 4067,55 | 4080,71 | 0,32 |
| **46** | 4093,88 | 4080,71 | 0,32 |

## 4.2. Comparison of Dynamometer Cutting Power and Electric Cutting Power during the Turning Process

The power consumpted during the turning process can be found approximately with the help of some devices. These are Ammeter, Dynamometer, Wattmeter, Powermeter, and Power Quality Analyzer. According to $P_{total}$ experimental results, cutting speed in the turning process in this study is the most important factor with a contribution rate of 94,23 percent. Thus, the power loss of the motor spindle of CNC lathe can be approximately equal to the unloaded spindle power at operating cutting speeds. Cutting power found by means of dynamometer can be calculated with $P_{cuttingD}$ = F*v formula given in Equation 4.22 using the fundamental physical relationship between power and force. In addition, the power found through the electric current can be calculated with the formula of $P_{cuttingE}$ = 1,73*V*$I_{cutting}$*cosφ given in Equation 4.23. The electric cutting current during turning can be found by the formula of $I_{cutting}$ = $I_{total}$ - $I_{unloaded}$ given in Equation 4.21. $I_{unloaded}$ currents were measured without cutting workpiece for certain cutting speeds (180, 220, and 260 m/min) subject to the diameter of stock size as shown in Figure 4.95. The equations used related to power are given below.

$$P_{total} = P_{unloaded} + P_{cutting} \tag{4.19}$$

$$P_{total} = \sqrt{3} * V * I_{total} * \cos\varphi \tag{4.20}$$

$$I_{cutting} = I_{total} - I_{unloaded} \tag{4.21}$$

$$P_{cuttingD} = F * v \text{ (dynamometer cutting power)} \tag{4.22}$$

$$P_{cuttingE} = \sqrt{3} * V * I_{cutting} * \cos\varphi \quad \text{(electric cutting power)} \qquad (4.23)$$

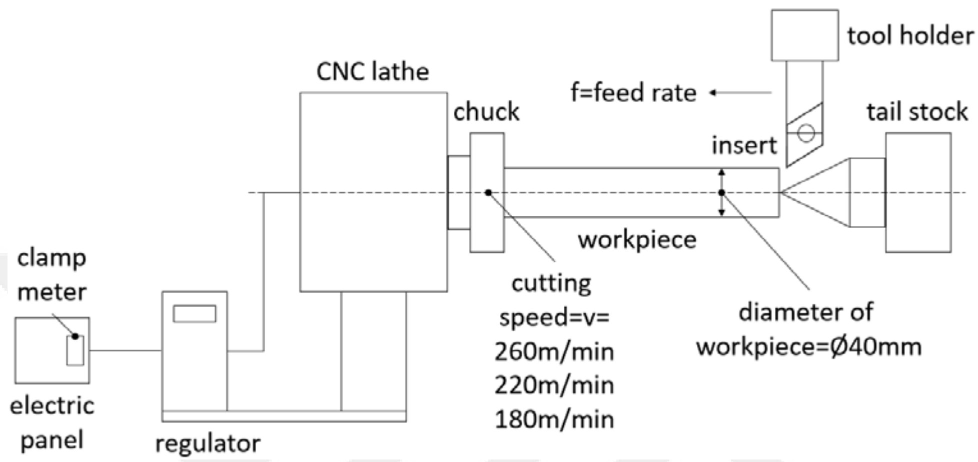


Figure 4.95. Symbolic schematic design of the turning process

Power consumed during the cutting process is calculated by cutting force dynamometer and amperemeter. Table 4.19 shows the calculated results. Deviations between $P_{cuttingD}$ and $P_{cuttingE}$ are seen when Table 4.19 is investigated. Error (%) is seen in the range 1,94-33,00. Voltage values change between 370 volts and 400 volts in Yozgat (city in Turkey) electric line. At the same time, deviation of voltage or current waveform from standard value is known as power quality problem. This situation can be explained by the deviation of voltage or current waveform from the standard value. Hence, it can conclude that if the direct measurement of power during the turning process provides with a powermeter or power quality analyzer, more accurate results can happen.

Table 4.19. Comparison of calculated dynamometer cutting power ($P_{cuttingD}$) and calculated electric cutting power ($P_{cuttingE}$)

| Runs | $I_{total}$= $I_{unloaded}$+$I_{cutting}$ (A) | $I_{unloaded}$ (A) | $I_{cutting}$ (A) | F (Resultant force) (N) | $P_{cuttingD}$ (w) | $P_{cuttingE}$ (w) | Error (%) |
|---|---|---|---|---|---|---|---|
| **1** | 6,00 | 5,70 | 0,30 | 66,96 | 245,52 | 197,45 | 19,58 |
| **2** | 6,17 | 5,70 | 0,47 | 100,91 | 370,00 | 309,34 | 16,39 |
| **3** | 6,12 | 5,70 | 0,42 | 79,10 | 290,03 | 276,44 | 4,69 |
| **4** | 6,27 | 5,70 | 0,57 | 109,61 | 401,90 | 375,16 | 6,65 |
| **5** | 5,20 | 5,00 | 0,20 | 56,70 | 170,10 | 131,64 | 22,61 |
| **6** | 6,89 | 6,40 | 0,49 | 62,46 | 270,66 | 322,51 | 19,16 |
| **7** | 5,42 | 5,00 | 0,42 | 98,80 | 296,40 | 276,44 | 6,74 |
| **8** | 6,95 | 6,40 | 0,55 | 98,48 | 426,75 | 362,00 | 15,17 |
| **9** | 5,98 | 5,70 | 0,28 | 48,36 | 177,32 | 184,29 | 3,93 |
| **10** | 6,00 | 5,70 | 0,30 | 65,06 | 238,55 | 197,45 | 17,23 |
| **11** | 6,28 | 5,70 | 0,58 | 91,15 | 334,22 | 381,74 | 14,22 |
| **12** | 6,25 | 5,70 | 0,55 | 105,37 | 386,36 | 362,00 | 6,30 |
| **13** | 5,26 | 5,00 | 0,26 | 74,17 | 222,51 | 171,13 | 23,09 |
| **14** | 5,48 | 5,00 | 0,48 | 107,39 | 322,17 | 315,93 | 1,94 |
| **15** | 6,94 | 6,40 | 0,54 | 73,23 | 317,33 | 355,42 | 12,00 |
| **16** | 6,90 | 6,40 | 0,50 | 101,70 | 440,70 | 329,09 | 25,33 |
| **17** | 5,93 | 5,70 | 0,23 | 44,89 | 164,60 | 151,38 | 8,03 |
| **18** | 5,95 | 5,70 | 0,25 | 65,35 | 239,62 | 164,54 | 31,33 |
| **19** | 6,20 | 5,70 | 0,50 | 68,50 | 251,17 | 329,09 | 31,02 |
| **20** | 6,21 | 5,70 | 0,51 | 124,48 | 456,43 | 335,67 | 26,46 |
| **21** | 5,32 | 5,00 | 0,32 | 73,93 | 221,79 | 210,62 | 5,04 |
| **22** | 5,35 | 5,00 | 0,35 | 85,50 | 256,50 | 230,36 | 10,19 |
| **23** | 6,83 | 6,40 | 0,43 | 71,22 | 308,62 | 283,02 | 8,30 |
| **24** | 6,79 | 6,40 | 0,39 | 88,41 | 383,11 | 256,69 | 33,00 |
| **25** | 5,95 | 5,70 | 0,25 | 52,99 | 194,30 | 164,54 | 15,31 |
| **26** | 6,20 | 5,70 | 0,50 | 75,87 | 278,19 | 329,09 | 18,30 |
| **27** | 6,06 | 5,70 | 0,36 | 87,59 | 321,16 | 236,94 | 26,22 |
| **28** | 6,20 | 5,70 | 0,50 | 128,90 | 472,63 | 329,09 | 30,37 |
| **29** | 5,18 | 5,00 | 0,18 | 50,59 | 151,77 | 118,47 | 21,94 |
| **30** | 6,70 | 6,40 | 0,30 | 57,94 | 251,07 | 197,45 | 21,36 |
| **31** | 5,40 | 5,00 | 0,40 | 96,18 | 288,54 | 263,27 | 8,76 |
| **32** | 7,10 | 6,40 | 0,70 | 98,64 | 427,44 | 460,73 | 7,79 |
| **33** | 5,98 | 5,70 | 0,28 | 52,94 | 194,11 | 184,29 | 5,06 |
| **34** | 6,05 | 5,70 | 0,35 | 69,61 | 255,24 | 230,36 | 9,75 |
| **35** | 6,14 | 5,70 | 0,44 | 92,72 | 339,97 | 289,60 | 14,82 |
| **36** | 6,35 | 5,70 | 0,65 | 134,98 | 494,93 | 427,82 | 13,56 |
| **37** | 6,01 | 5,70 | 0,31 | 52,24 | 191,55 | 204,04 | 6,52 |
| **38** | 6,02 | 5,70 | 0,32 | 61,23 | 224,51 | 210,62 | 6,19 |
| **39** | 6,22 | 5,70 | 0,52 | 87,36 | 320,32 | 342,25 | 6,85 |
| **40** | 6,20 | 5,70 | 0,50 | 105,70 | 387,57 | 329,09 | 15,09 |
| **41** | 6,29 | 5,70 | 0,59 | 81,72 | 299,64 | 388,33 | 29,60 |
| **42** | 6,10 | 5,70 | 0,40 | 80,87 | 296,52 | 263,27 | 11,21 |
| **43** | 6,22 | 5,70 | 0,52 | 81,10 | 297,37 | 342,25 | 15,09 |
| **44** | 6,19 | 5,70 | 0,49 | 80,00 | 293,33 | 322,51 | 9,95 |
| **45** | 6,18 | 5,70 | 0,48 | 80,19 | 294,03 | 315,93 | 7,45 |
| **46** | 6,22 | 5,70 | 0,52 | 80,47 | 295,06 | 342,25 | 16,00 |

**4.3. Comparison of Experimental and FEM Cutting Forces**

Experimental studies were executed in Yozgat Bozok University CNC laboratory of Mechanical Engineering Department. Cutting experiments of cylindrical bar and cylindrical tube specimens were conducted using Goodway 260Y high rigidly CNC lathe with 15 kW spindle power (P) and spindle speed (n) of 4000 rpm.

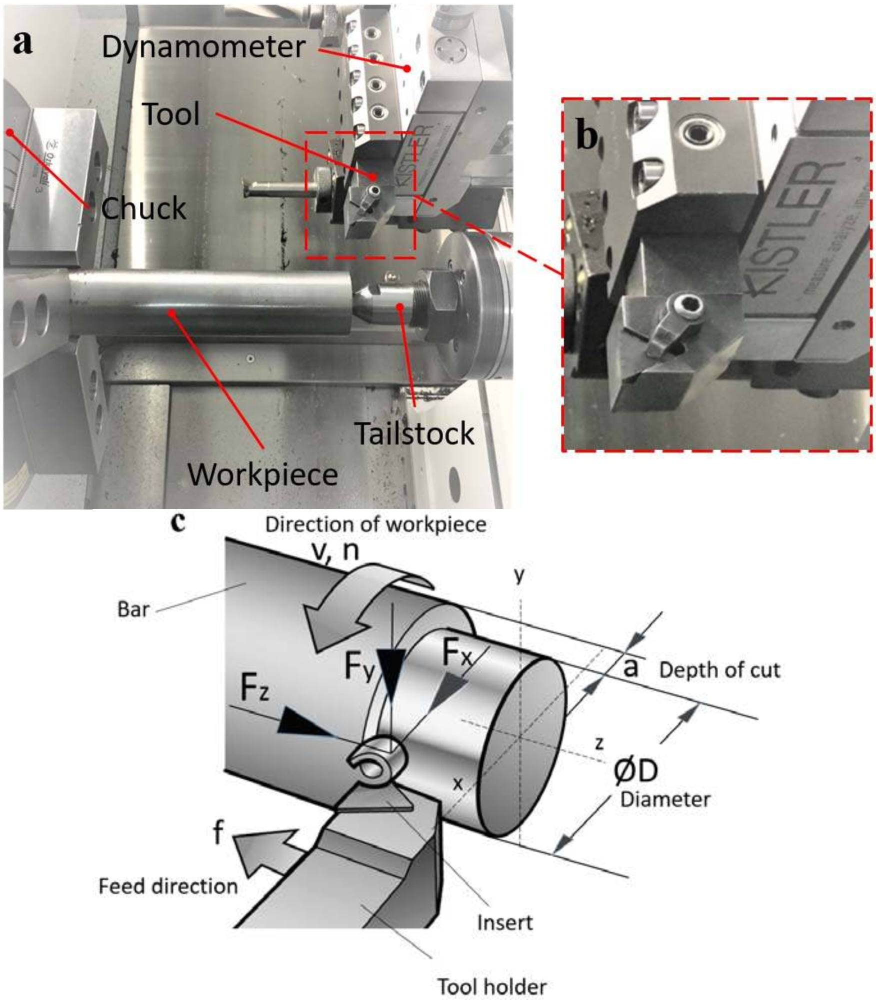


Figure 4.96. Turning process of cylindrical bar specimens; a) Experimental setup, b) Close-up, c) Depicted schema

From Kennametal catalogue, PVD AlTiN coating carbide insert (coded TPGN160304 KC5010) and tool holder (coded CTGPL2525M16) was selected. AISI 4340 alloy steel with Ø40x250 mm of dimension was used in machining experiments. Turning tests of cylindrical bar and cylindrical tube specimens were conducted under dry cutting conditions. Additional to this, cylindrical bar tests were performed at a fixed depth of cut of 0,5 mm for 0,1; 0,2; and 0,3 mm/rev feed rates. Tube wall thickness (t) was taken 2,17 mm; 2,20 mm; and 2,30 mm for 0,1; 0,2; and 0,3 mm/rev feed rates, respectively. Experimental setup and force measurement system used to realize tests are illustrated in Figures 4.96-4.98.

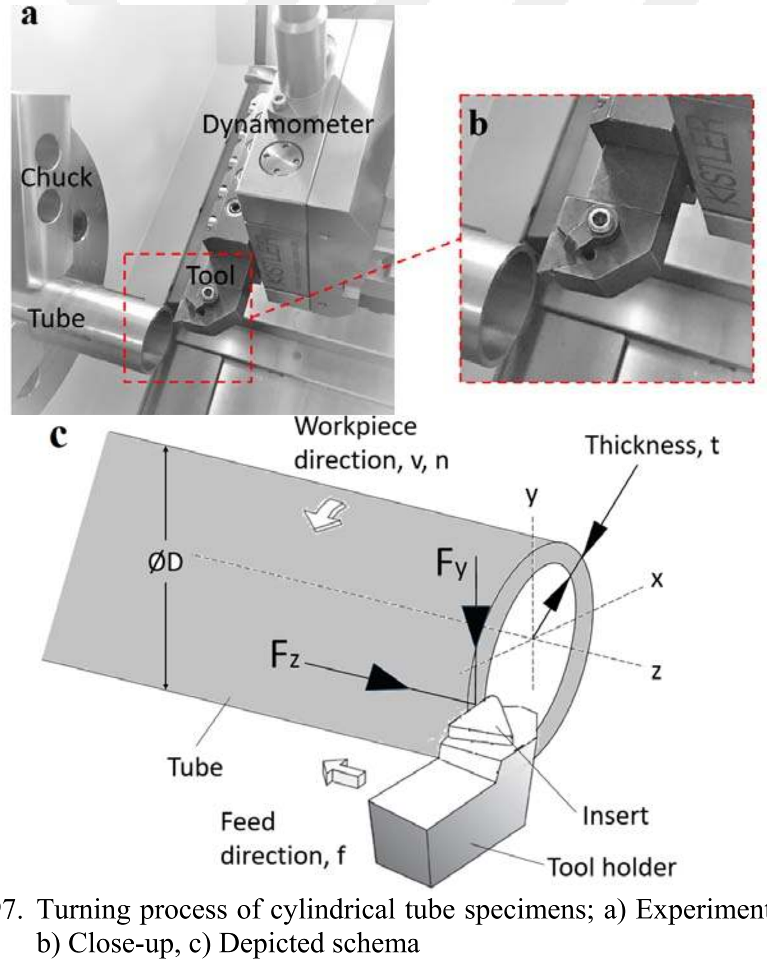


Figure 4.97. Turning process of cylindrical tube specimens; a) Experimental setup, b) Close-up, c) Depicted schema

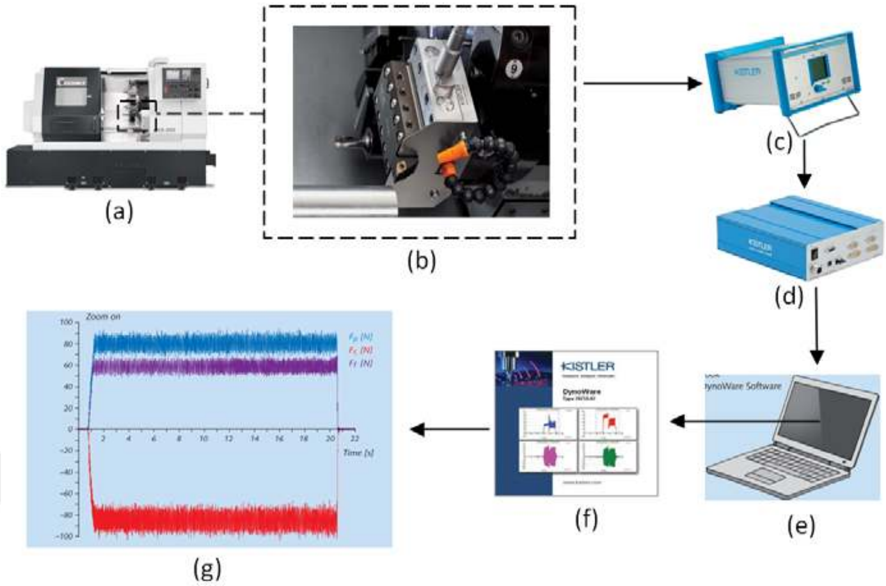


Figure 4.98. Force measurement system used in this study; a) Goodway 260Y CNC Lathe, b) Kistler 9129AA model piezoelectric dynamometer, c) Kistler 5070 model amplifier, d) Kistler 5697 model data acquisition box, e) Computer, f) Dynoware software, g) Screenshot of cutting forces

Experimental data for cylindrical bar and tubular materials are presented in Figure 4.99 and Figure 4.100, respectively. Here, stable force signals between two dashed lines are considered.

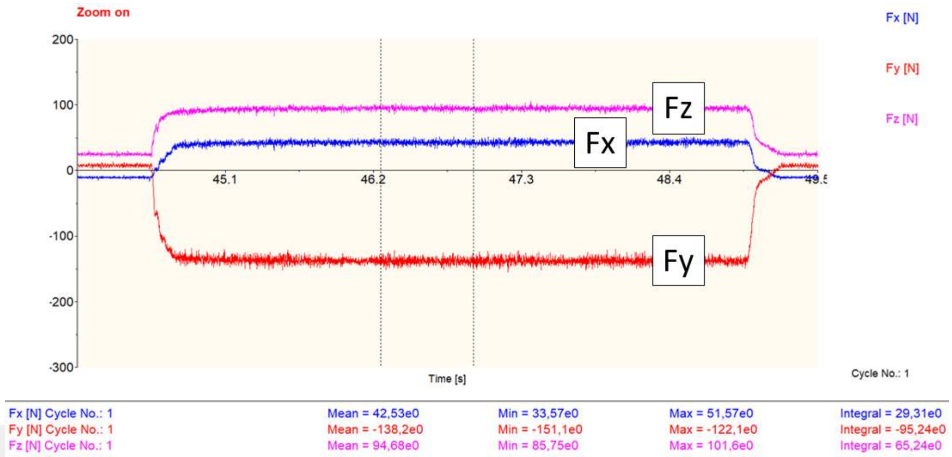


Figure 4.99. Measured feed, radial, and tangential force components for a cylindrical bar specimen

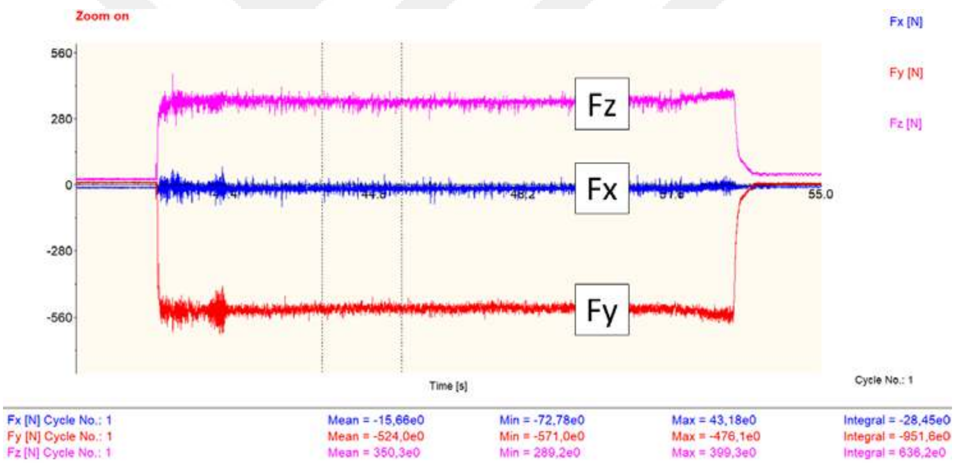


Figure 4.100. Measured feed, radial, and tangential force components for a cylindrical tube specimen

Altair HyperWorks (Altair HyperMesh) and Dassault systemes (Simula ABAQUS) software were utilized (Abaqus, 2021; HyperMesh, 2021). Finite element models are created in ABAQUS/Explicit in order to simulate 3D machining processes using cylindrical bar and cylindrical tube materials. ABAQUS/Explicit provides a dynamic fracture model for Johnson-Cook plasticity model. Johnson-Cook (JC) model is the most forceful amongst well-known plastic strain models. Therefore, it was decided to use this model in this study. JC model can be expressed as given in Equation 4.24. Here, $\sigma$, ε, $\dot{\varepsilon}$, $\dot{\varepsilon}_o$, $T$, $T_m$ and $T_r$ are material flow stress, plastic strain, strain rate, reference strain rate, temperature of a material, melting point of the material, and room temperature, respectively. A, B, C, n, and m empirical constants are yield stress, pre-exponential factor, strain rate factor, work-hardening exponent, and thermal softening exponent, respectively. Johnson–Cook specifications of AISI 4340 material with 30 HRC are given in the following Tables 4.20-4.23 (Guo and Yen, 2004; Arrazola and Özel, 2010; Johnson and Cook, 1985). Thermal effects are not considered in this study.

$$\sigma = \underbrace{\left(A + B\varepsilon^n\right)}_{Elasto-plastic\,deformation} \underbrace{\left[1 + C ln \frac{\dot{\varepsilon}}{\dot{\varepsilon}_o}\right]}_{Viscosity\,deformation} \underbrace{\left[1 - \left(\frac{T - T_r}{T_m - T_r}\right)^m\right]}_{Thermal\,softening} \tag{4.24}$$

Table 4.20. Physical properties for AISI 4340 steel with 30 HRC

| **Elastic Modulus, E** | **Poisson's ratio, υ** | **Density, ρ** |
|---|---|---|
| 200 GPa | 0,29 | 7830 kg/m$^3$ |

Table 4.21. Strength constants for AISI 4340 steel with 30 HRC

| **A** | **B** | **n** | **C** | **m** |
|---|---|---|---|---|
| 792 MPa | 510 MPa | 0,26 | 0,014 | 1,03 |

Table 4.22. Fracture constants for AISI4340 steel with 30 HRC

| **D1** | **D2** | **D3** | **D4** | **D5** |
|---|---|---|---|---|
| 0,05 | 3,44 | -2,12 | 0,002 | 0,61 |

Table 4.23. Physical properties for cutting tool (Carbide insert)

| **Elastic Modulus, E** | **Poisson's ratio, υ** | **Density, ρ** |
|---|---|---|
| 800 GPa | 0,20 | 15000 kg/m$^3$ |

Friction coefficient (μ) extensively affects cutting forces, cutting power, cutting temperature, and plastic strain. Nevertheless, the friction coefficient cannot be evaluated with sensitivity and it requires to be iterated. Hence, several iterations on friction coefficients were established (Maranhão and Davim, 2010; Asad et al., 2014). There are three contact constraint enforcement methods available in Abaqus/Standard. These are a direct method, penalty method, and augmented Lagrange method. With this method, the contact force is proportional to the penetration distance, so some degree of penetration will occur. The penalty method can significantly reduce solver cost in terms of CPU (central processing unit) time and is easier to treat over constraints (Abaqus, 2021). So, friction formulation is a penalty chosen in ABAQUS/Explicit. As described above, iteration is required to determine of friction coefficient. Therefore, tests were performed to investigate effect of various friction coefficients on resultant force (F) for values of f = 0,1 mm, v = 100 m/min, a = 0,5 mm. These results are given in Figure 4.101. The results showed that the values closest to the measured value was predicted when friction coefficient was taken 0,5 in the simulation study. To this end, the friction coefficient was accepted 0,5 in ABAQUS/Explicit.

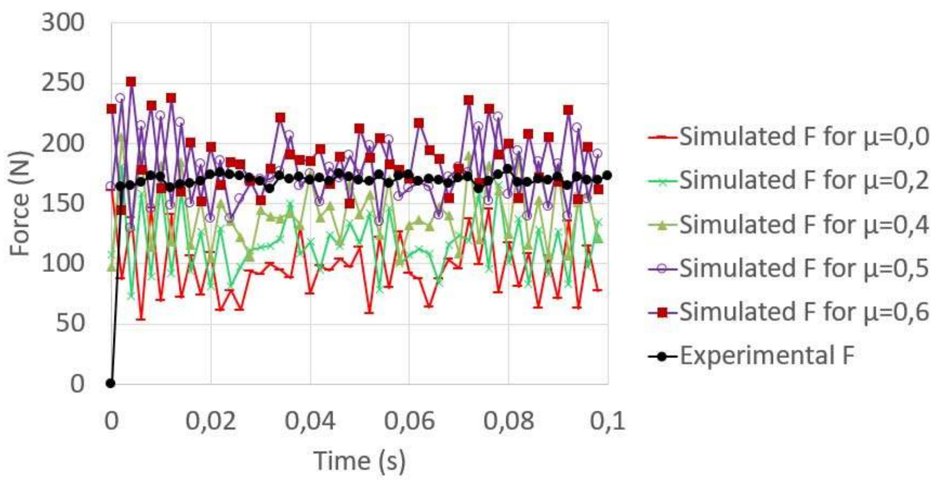


Figure 4.101. Iteration of friction coefficient for F

Interaction between cutting tool (insert) and workpiece was considered as general contact. Workpiece and cutting tool were meshed using HyperMesh. Then the input file was run in ABAQUS/Explicit. After the model of the workpiece and cutting tool were made, they were mounted and placed as per the real experimental setup. The workpiece was fixed and set to rotate clockwise. The tool moved in the cutting direction during the cutting operation. Contact algorithm between tool and workpiece was described as master and slave in ABAQUS/Explicit. Cutting tool and workpiece models were selected as master and slave elements, respectively. Schematics of FEM are indicated in Figures 4.102 and 4.103. The model has been partitioned into three sections: un-machined region of workpiece, damageable region, and chip separation region (Asad et al., 2014; Asad, 2019). The workpiece was meshed using eight-node C3D8R (8-node brick element with reduced integration) elements. The tool was assumed to be a rigid three-dimensional body and was meshed using C3D8R elements. The cylindrical bar model contains 76970 nodes and 67160 elements. The element deletion technique is used to provide chip separation formation. Mesh quality was enhanced using Arbitrary Lagrangian-Eulerian (ALE) formulation (Sadeghifar et al., 2018). Besides, the cylindrical tube model contained 11838 nodes and 9090 elements. To obtain reasonable results, a thinner element size was created in places close to the cutting zone, and a coarser mesh structure was created in places far from the cutting zone.

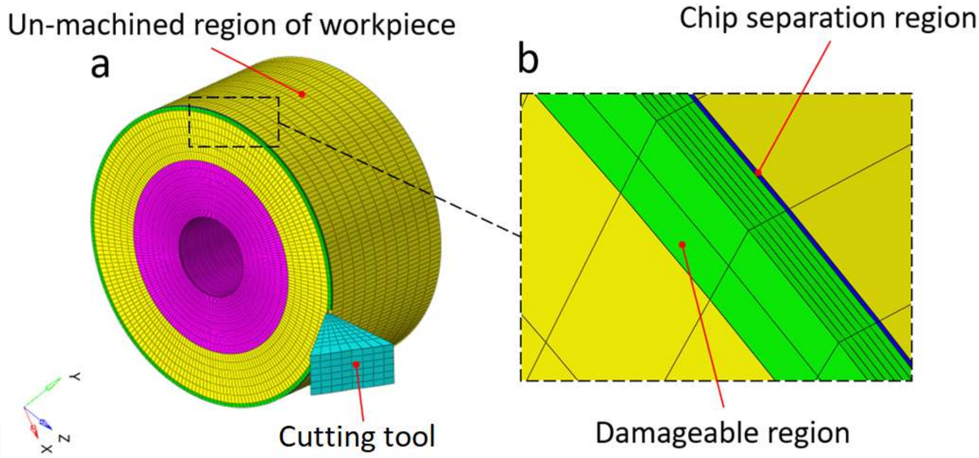


Figure 4.102. Finite element model of cylindrical bar workpiece prepared by means of HyperMesh software; a) Full image, b) Close-up

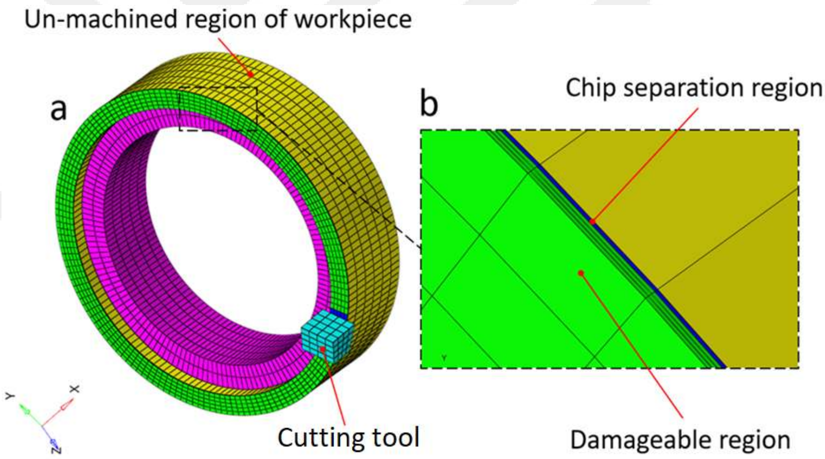


Figure 4.103. Finite element model of cylindrical tube workpiece prepared by means of HyperMesh software; a) Full image, b) Close-up

Mass scaling feature has been applied to reduce the run time in 3D simulation analysis. Nevertheless, each simulation took approximately 4 days using a computer that has Intel (R) Core (TM) i7-7500U CPU 2.7 GHz processor.

Von-Mises Stress Contours of the cylindrical bar and tube specimens are shown in Figures 4.104-4.107.

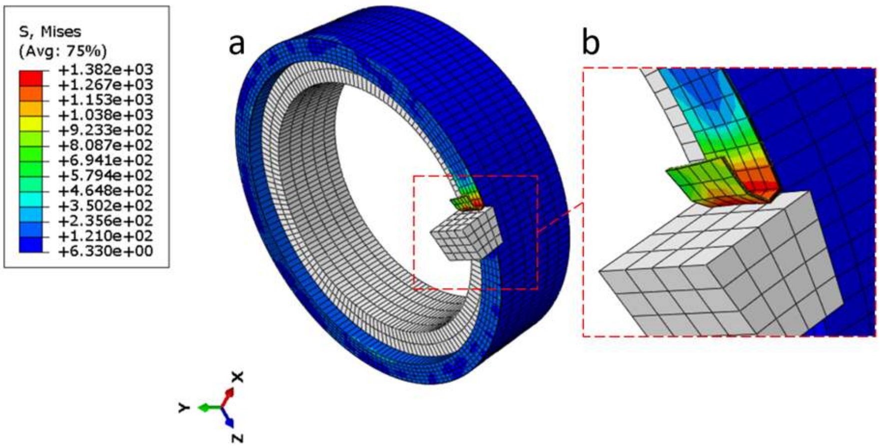


Figure 4.104. First step of Von-Mises Stress Contour in ABAQUS/Explicit for 3D cylindrical tube (feed rate: 0,1 mm/rev); a) Full image, b) Close-up

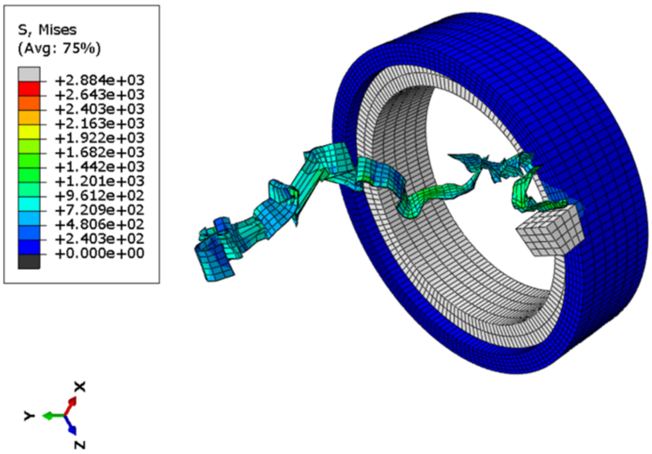


Figure 4.105. Final step of Von-Mises Stress Contour in ABAQUS/Explicit for 3D cylindrical tube (feed rate: 0,1 mm/rev)

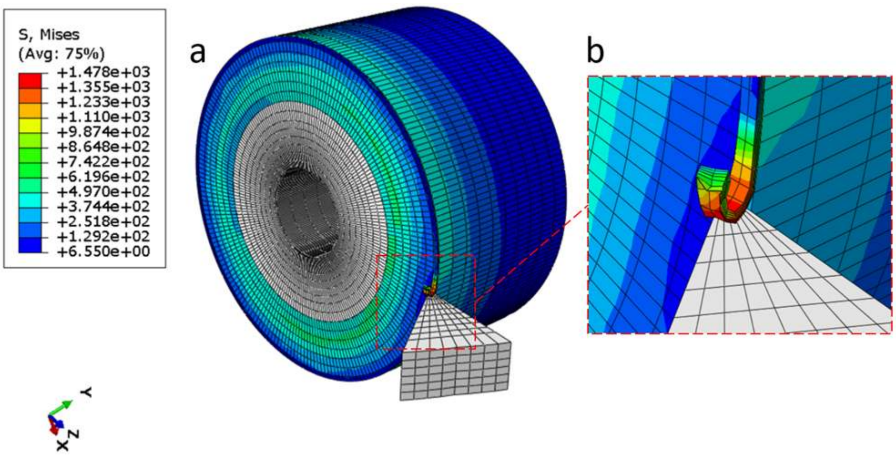


Figure 4.106. First step of Von-Mises Stress Contour in ABAQUS/Explicit for 3D cylindrical bar (feed rate: 0,2 mm/rev) ; a) Full image, b) Close-up

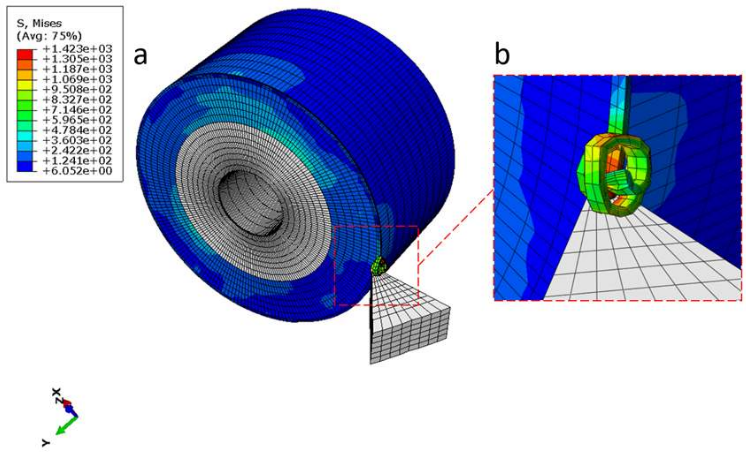


Figure 4.107. Final step of Von-Mises Stress Contour in ABAQUS/Explicit for 3D cylindrical bar (feed rate: 0,2 mm/rev); a) Full image, b) Close-up.

Comparisons of experimental and simulated cutting forces of cylindrical tubes for feed rates of 0,1; 0,2; and 0,3 mm/rev are shown in Figures 4.108-4.110 and Table 4.24.

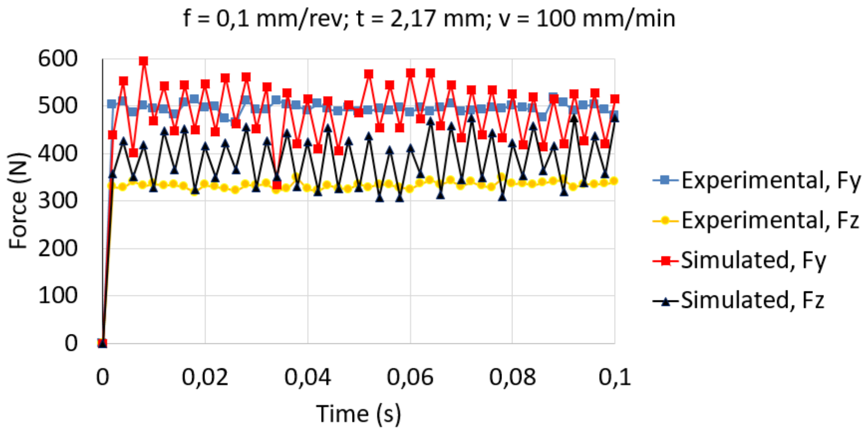


Figure 4.108. Comparison of experimental and simulated forces on the cylindrical tube for feed rate of 0,1 mm/rev during the turning process

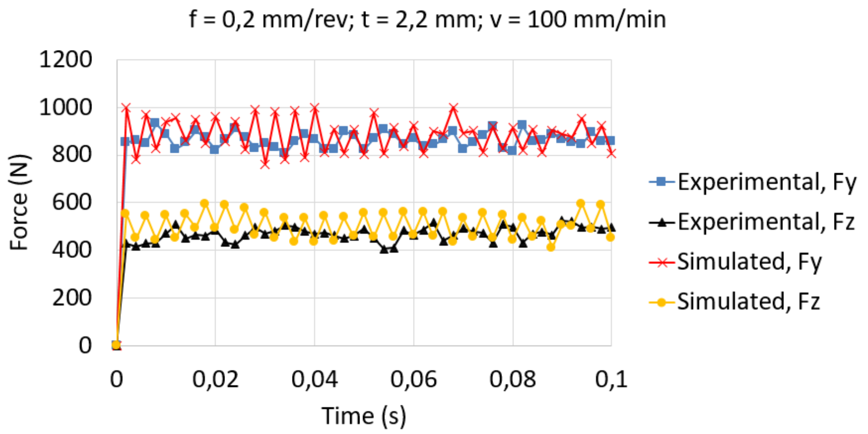


Figure 4.109. Comparison of experimental and simulated forces on the cylindrical tube for feed rate of 0,2 mm/rev during the turning process

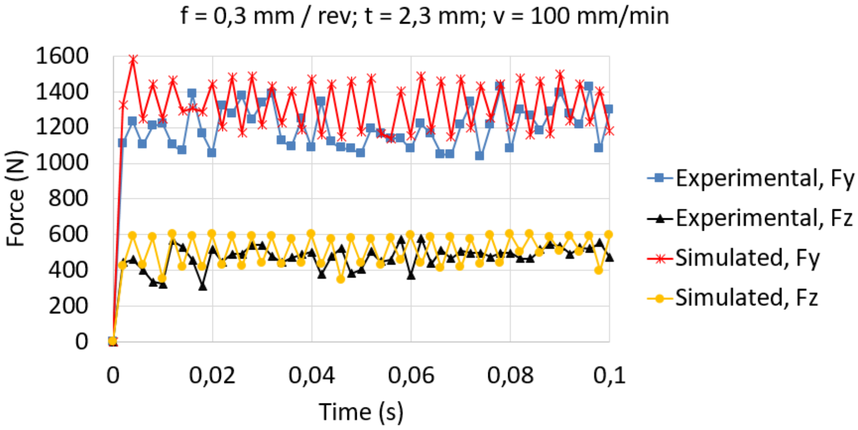


Figure 4.110. Comparison of experimental and simulated forces on the cylindrical tube for feed rate of 0,3 mm/rev during the turning process

Table 4.24. Experimental and simulated forces on cylindrical tubes

| Comparison | Fy, Tangential (N) | | | Fz, Feed (N) | | |
|---|---|---|---|---|---|---|
| Tube wall thickness, t (mm) | 2,17 | 2,20 | 2,30 | 2,17 | 2,20 | 2,30 |
| Feed rate, f (mm/rev) | 0,10 | 0,20 | 0,30 | 0,10 | 0,20 | 0,30 |
| Experimental force | 496 | 863 | 1201 | 333 | 470 | 477 |
| Simulated force | 488 | 886 | 1325 | 389 | 505 | 511 |
| Error (%) | 2 | 3 | 10 | 17 | 8 | 7 |

Comparisons of experimental and simulated cutting forces of cylindrical bars for feed rates of 0,1; 0,2; and 0,3 mm/rev are shown in Figures 4.111-4.113 and Table 4.25.

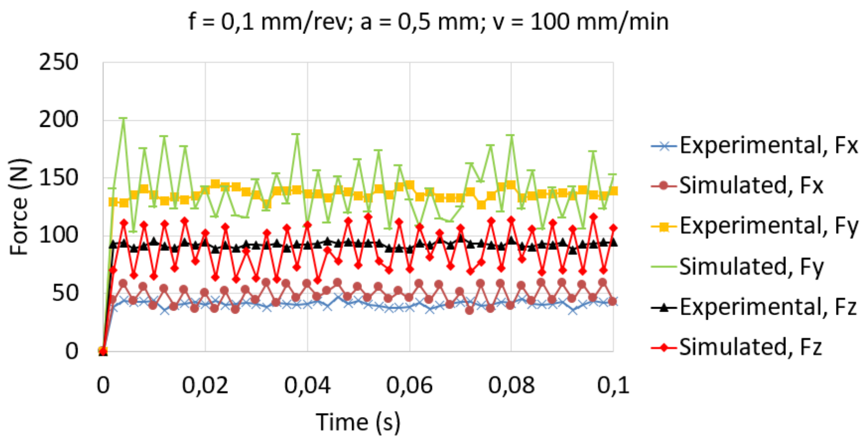


Figure 4.111. Comparison of experimental and simulated forces on the cylindrical bar for feed rate of 0,1 mm/rev during the turning process

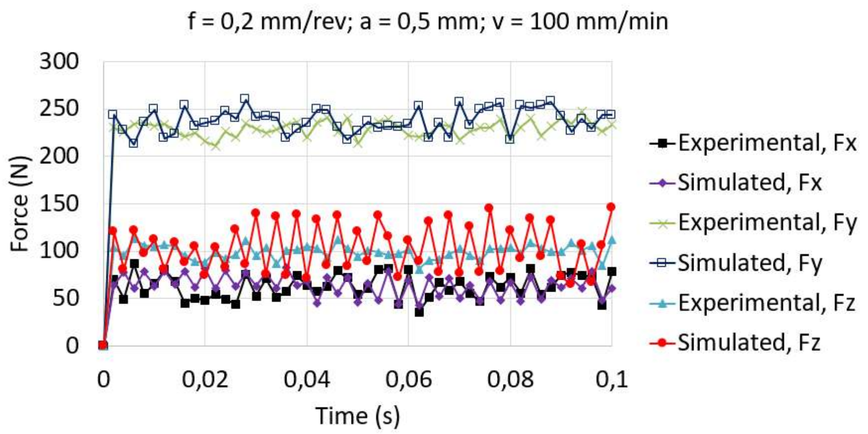


Figure 4.112. Comparison of experimental and simulated forces on the cylindrical bar for feed rate of 0,2 mm/rev during the turning process

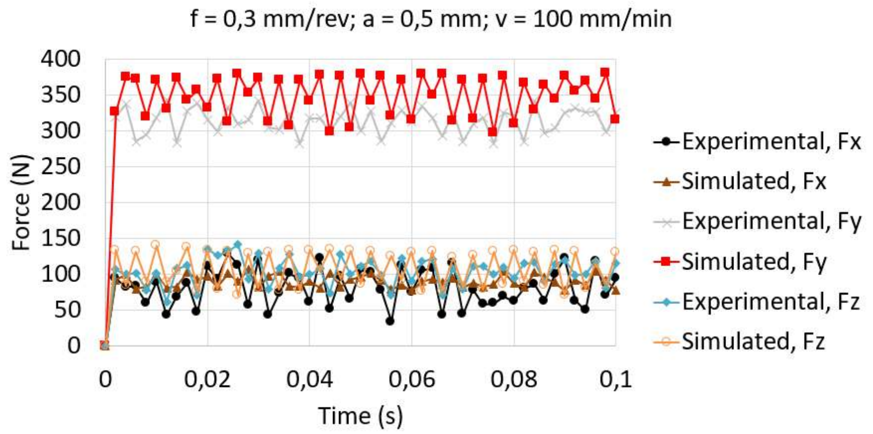


Figure 4.113. Comparison of experimental and simulated forces on the cylindrical bar for feed rate of 0,3 mm/rev during the turning process

Table 4.25. Experimental and simulated cutting forces results for cylindrical bars

| Comparison | Fy, Tangential (N) | | | Fx, Radial (N) | | | Fz, Feed (N) | | |
|---|---|---|---|---|---|---|---|---|---|
| Depth of cut, a (mm) | 0,5 | | | 0,5 | | | 0,5 | | |
| Feed rate, f (mm/rev) | 0,10 | 0,20 | 0,30 | 0,10 | 0,20 | 0,30 | 0,10 | 0,20 | 0,30 |
| Experimental force | 136 | 229 | 314 | 41 | 62 | 81 | 92 | 99 | 105 |
| Simulated force | 139 | 237 | 349 | 49 | 64 | 90 | 88 | 104 | 110 |
| Error (%) | 2 | 4 | 11 | 20 | 3 | 11 | 4 | 5 | 5 |

If computer simulation technology is used very efficiently, the cost and time allocated in experiments can be reduced. In this study, simulation of 3D turning of the cylindrical bar and cylindrical tube materials was discussed using ABAQUS/Explicit FEM software. Then simulation accuracy was controlled. A maximum of 20 percent error was found between experimental forces and simulated forces. Simulated values were found to be similar to experimental values. In this context, ABAQUS/Explicit based process simulation can reduce money and time spent on experimental studies.

# 5. CONCLUSIONS AND RECOMMENDATIONS FOR FUTURE WORK

## 5.1. Conclusions

The main objective of this dissertation is to provide optimization of machining parameters to achieve minimum $P_{total}$, Fx, Fy, Fz, $S_{total}$, $I_{total}$, and Ra during turning of AISI 4340 alloy steel using different inserts materials and workpiece materials with different hardness. First of all, an experiment plan was prepared with Respond Surface Method taking input machining parameters (i, h, v, f, a), and their levels. At the same time, output machining parameters ($P_{total}$, Fx, Fy, Fz, $S_{total}$, $I_{total}$, Ra) were determined. Then experimental setup was performed to measure Fx, Fy, Fz, $S_{total}$, $I_{total}$, and Ra. Afterward, optimum cutting parameters were obtained using SN ratios according to the smaller the better characteristic in Taguchi Method to obtain minimum values of output (response) parameters. In addition, ABAQUS/Explicit FEM software was used to find cutting forces that are important for power consumption. In this way, it can be reduced the time and cost spent in experimental studies using FEM. The literature survey showed that researchers have benefited from different methods such as RSM, Taguchi method, ANOVA method to generate optimal cutting conditions. Much of the literature research involves the surface roughness performance of workpieces taking into account materials of the same hardness and same inserts. It has been observed that there are very few studies related to finding the power consumption with the help of instantaneous current in the turning process using different insert types and materials of different hardness. The previous and present works revealed that a strong relationship between cutting parameters (insert, hardness, cutting speed, feed rate, depth of cut) and $P_{total}$, Fx, Fy, Fz, $S_{total}$, $I_{total}$, Ra. Because of this, further studies are required to be able to see the of effect cutting parameters on machining performance. In this thesis, obtained general data and done works are given below:

The experiment plan (machining parameters and their levels) was designed with 46 combinations (L46) using RSM in Minitab 16 software.

Taguchi and ANOVA methods have been used to determine the machining parameters leading to optimum $P_{total}$, Fx, Fy, Fz, $S_{total}$, $I_{total}$, and Ra.

Mathematical models using RSM have been developed to predict optimum $P_{total}$ (W), Fx (N), Fy (N), Fz (N), $S_{total}$ (dB), $I_{total}$ (A), Ra (mµ).

The results reveal that the developed mathematical model predicts $P_{total}$ with a maximum 1,64% error. Cutting speed is the most important factor influencing $P_{total}$ with 94,23% contribution. The contribution was followed by the depth of cut with 2,82%, insert with 0,83%, feed rate with 0,40%, and workpiece hardness with 0,02%. According to 3D surface plots, as the cutting speed increases, the $P_{total}$ increases linearly. Besides, as depth of cut and feed rate increase, $P_{total}$ usually increases. On the other hand, an increase in hardness values leads to a significant increase in $P_{total}$. Since there was not a big difference between the hardness grades (30, 35, 40 HRC), it was seen that the hardness did not have a great effect on the $P_{total}$. It is seen that ceramic is the most influential insert for minimum $P_{total}$. The optimization plot shows that the optimum $P_{total}$ of 3178,60 W is found at a hardness of 30 HRC, cutting speed of 180 m/min, feed rate of 0,03 mm/rev, depth of cut of 0,08 mm, and when insert uses ceramic.

It is seen that the developed mathematical model to find $S_{total}$ predicts with maximum 0,81% error. It was established that the main factor affecting Sound is cutting speed with a contribution of 86,71% according to ANOVA analyses. Contribution followed by feed rate with 2,14%, workpiece hardness with 1,75%, the depth of cut with 0,09%, and insert with 0,06%. According to surface plots, as the cutting speed increases, the $S_{total}$ level increases linearly. However, it can be negligible because the depth of cut and feed rate have little effect on the $S_{total}$ when it compared to the cutting speed. As hardness value that is another machining parameter rises, $S_{total}$ increases. In addition, the carbide insert revealed better performance than ceramic and CBN inserts, as it produced lower $S_{total}$ during turning. The optimization plot shows that the optimum $S_{total}$ (77,48 dB) is predicted at a cutting speed of 180 m/min, feed rate of 0,07 mm/rev, depth of cut of 0,08 mm, hardness of 30 HRC, and when insert uses carbide.

Results show that the developed mathematical model to find $I_{total}$ intensity predicts with a maximum 1,64% error. This study shows that the effects of insert, cutting speed, feed rate, and depth of cut on $I_{total}$ are statistically significant according to ANOVA results. It was established that the main factor affecting $I_{total}$ is cutting speed with a contribution of 94,23%. It followed by depth of cut with 2,82%, workpiece hardness with 0,02%, feed rate with 0,40%, and insert with 0,83%. According to surface plots, as the cutting speed increases, the $I_{total}$ increases linearly. It is generally seen that $I_{total}$ increases while feed rate and depth of cut levels rise. The slope of the surface plots shows that $I_{total}$ increases when the hardness level rise. In addition, ceramic and CBN inserts perform better than carbide inserts as they produce lower $I_{total}$ during turning. Optimization plot generated the minimum $I_{total}$ of 4,83 A when hardness of 30 HRC, cutting speed of 180 m/min, feed rate of 0,03 mm/rev, depth of cut of 0,08 mm, and ceramic insert use.

From this investigation, it is seen that the developed mathematical model to find Ra estimates in a range of 0,09-32,59% error. Although the cutting speed has an important effect on the surface roughness value, it has been determined that insert contributes more to the surface roughness of the workpiece in the working range of this thesis. ANOVA results established that insert is the dominating factor with a contribution of 51,52% to minimize Surface roughness. It was followed by hardness with 13,59%, feed rate with 1,86%, depth of cut with 0,47%, and cutting speed with 0,18%. It is apparent from surface plots that there is a considerable amount of increase in surface roughness with an increase in the feed rate, whilst the depth of cut has a rather changeable influence. Also, with the increase in cutting speed and hardness, the Surface roughness decreases. In addition, CBN inserts perform better than carbide and ceramic inserts as they produce lower surface roughness during turning. The optimization plot revealed the minimum Ra of 0,37 μm when the hardness of 40 HRC, cutting speed of 180 m/min, feed rate of 0,03 mm/rev, depth of cut of 0,08 mm, and CBN insert use.

Present results showed that the developed mathematical models to find Fx, Fy, and Fz estimated with a maximum 11,33%, 13,32%, and 4,00% error, respectively. One of the main goals of this study is to minimize Fx, Fy, and Fz. The ANOVA results found that the most important factor affecting Fx and Fy was feed rate. Furthermore, the most effective factor on Fz is the depth of cut. According to surface plots, Fx increased with rising cutting speed, feed rate, depth of cut, and hardness levels. The lowest Fx is formed when the ceramic insert is used. Fy increased almost linearly with the feed and depth of cut. But it showed different behavior with cutting speed. Cutting speed on Fy has negligible effect. Also, the lowest Fy is formed when the ceramic insert is used. Fz increased with the depth of feeding and cutting, but almost did not change with the increase in cutting speed. Generally, Fz increases as workpiece hardness increases. Besides, the lowest Fz is generated when the carbide insert is used. Optimization plot for Fx generated the minimum force of 9,51 N when hardness of 30 HRC, cutting speed of 180 m/min, feed rate of 0,03 mm/rev, depth of cut of 0,08 mm, and ceramic insert use. Optimization plot for Fy generated the minimum force of 15,72 N when hardness of 35 HRC, cutting speed of 220 m/min, feed rate of 0,03 mm/rev, depth of cut of 0,08 mm, and ceramic insert uses. Optimization plot for Fz generated the minimum force of 29,25 N when hardness of 30 HRC, cutting speed of 180 m/min, feed rate of 0,03 mm/rev, depth of cut of 0,08 mm, and carbide insert uses.

The 3D FEM simulation of Fx, Fy, and Fz forces was carried out with the Johnson-Cook constitutive model using ABAQUS/Explicit software. When experimental and simulated results of cylindrical bars compare, it is determined that maximum error for Fx, Fy, and Fz is 20%, 11%, and 5%, respectively. According to experimental works on cylindrical tubes, it is determined that maximum error for Fy and Fz is found 10% and 17%, respectively.

Table 5.1. Confirmation test results for Fx, Fy, Fz, Ra, $I_{total}$, $S_{total}$ and $P_{total}$

| Responses | | Results | | |
|---|---|---|---|---|
| | | Experimental/ Calculated | Predicted | Error (%) |
| $P_{total}$ (W) | A1 B1 C1 D1 E1 (optimum) | 3352,74 | 3178,60 | 5,19 |
| | A2 B1 C3 D3 E3 (random1) | 4766,15 | 4602,46 | 3,43 |
| | A1 B2 C2 D3 E1 (random2) | 3845,79 | 3934,40 | 2,30 |
| | A1 B2 C2 D3 E2 (random3) | 3865,51 | 4032,17 | 4,31 |
| Fx (N) | A1 B1 C1 D1 E1 (optimum) | 10,78 | 9,51 | 11,78 |
| | A2 B1 C3 D3 E3 (random1) | 61,91 | 66,61 | 7,59 |
| | A1 B2 C2 D3 E1 (random2) | 36,07 | 35,75 | 0,89 |
| | A1 B2 C2 D3 E2 (random3) | 58,35 | 54,28 | 6,98 |
| Fy (N) | A1 B2 C2 D1 E1 (optimum) | 13,47 | 15,72 | 16,70 |
| | A2 B1 C3 D3 E3 (random1) | 63,19 | 74,07 | 17,22 |
| | A1 B2 C2 D3 E1 (random2) | 32,89 | 30,40 | 7,57 |
| | A1 B2 C2 D3 E2 (random3) | 52,03 | 50,24 | 3,44 |
| Fz (N) | A2 B1 C1 D1 E1 (optimum) | 26,11 | 29,25 | 12,03 |
| | A2 B1 C3 D3 E3 (random1) | 52,80 | 56,02 | 6,10 |
| | A1 B2 C2 D3 E1 (random2) | 35,07 | 36,78 | 4,88 |
| | A1 B2 C2 D3 E2 (random3) | 47,55 | 46,31 | 2,61 |
| Ra (µm) | A3 B3 C1 D1 E1 (optimum) | 0,34 | 0,37 | 8,82 |
| | A2 B1 C3 D3 E3 (random1) | 0,69 | 0,68 | 1,45 |
| | A1 B2 C2 D3 E1 (random2) | 0,92 | 0,90 | 2,17 |
| | A1 B2 C2 D3 E2 (random3) | 0,90 | 0,85 | 5,56 |
| $S_{total}$ (dB) | A2 B1 C1 D2 E1 (optimum) | 74,10 | 77,48 | 4,56 |
| | A2 B1 C3 D3 E3 (random1) | 87,50 | 88,17 | 0,77 |
| | A1 B2 C2 D3 E1 (random2) | 83,80 | 84,90 | 1,31 |
| | A1 B2 C2 D3 E2 (random3) | 82,90 | 83,83 | 1,12 |
| $I_{total}$ (A) | A1 B1 C1 D1 E1 (optimum) | 5,10 | 4,83 | 5,29 |
| | A2 B1 C3 D3 E3 (random1) | 7,25 | 6,99 | 3,59 |
| | A1 B2 C2 D3 E1 (random2) | 5,85 | 5,98 | 2,22 |
| | A1 B2 C2 D3 E2 (random3) | 5,88 | 6,13 | 4,25 |

As a result of Taguchi optimization, the set of parameters that gives the optimum Fx, Fy, Fz, Ra, $I_{total}$, $S_{total}$ and $P_{total}$ can sometimes be any of the existing tests or be an experiment outside the tests. A smaller is better characteristic was selected as SN ratio in Taguchi optimization. The confirmation tests were performed using optimum and random machining parameters to validate the mathematical models. Optimum machining parameters were read from the SN ratios. The confirmation tests are presented in Table 5.1. Experimental/calculated results were compared with the results predicted by mathematical models. Errors between the experimental/calculated and the predicted results for $P_{total}$, Fx, Fy, Fz, Ra, $S_{total}$, and $I_{total}$ were found in the range of 2,30-5,19%; 0,89-11,78%; 3,44-17,72%; 2,61-12,03%; 1,45-8,82%; 0,77-4,56%; and 2,22-5,29%, respectively. Accordingly, it can be stated that the developed mathematical models confirm the relationship between the input and output parameters. As a result, these mathematical models developed have been found to be usable in industry.

**5.2. Recommendations for Future Studies**

This work presents the modeling of Fx, Fy, Fz, Ra, $I_{total}$, $S_{total}$, and $P_{total}$ for the turning operation of AISI 4340 alloy steel with different hardness. Effects of the hardness of workpiece, insert material, cutting speed, feed rate, and depth of cut parameters on Fx, Fy, Fz, Ra, $I_{total}$, $S_{total}$, and $P_{total}$ in the turning process are investigated. In conventional cutting theory, the main cutting force (tangential force) is the largest of the three-component forces (Fx, Fy, Fz). However, this relationship is different in this study. It was observed that the radial force component was larger than the tangential force during turning. Therefore, this situation can be investigated in more detail. Additionally, the effects of machining parameters such as insert geometry, insert coatings, coolants, cryogenic treatment of materials, etc. on Fx, Fy, Fz, Ra, $I_{total}$, $S_{total}$, and $P_{total}$ could be studied. Further, the effects of machining parameters on Material Removal Rate (MRR), Specific Cutting Energy (SCE), tool wear, tool life, and machining time can be analyzed. This work can be extended to comprise advanced materials like titanium alloys, powder metallurgy materials, and composites materials. Except for the above-mentioned cases, the results can also be investigated using other optimization techniques like Artificial Neural Networks (ANN), Full Factorial Design (FFD), Particle Swarm Optimization (PSO), and Genetic Algorithm (GA).

**REFERENCES**


Abaqus, 2021. Getting Started with Abaqus: Interactive Edition. Access date: 09.08.2021.
http://130.149.89.49:2080/v6.14/books/gsa/default.htm

Abbas, A. T., Gupta, M. K., Soliman, M. S., Mia, M., Hegab, H., Luqman, M., Pimenov, D. Y., 2019. Sustainability Assessment Associated with Surface Roughness and Power Consumption Characteristics in Nanofluid MQL-Assisted Turning of AISI 1045 Steel. The International Journal of Advanced Manufacturing Technology, 105: 1311-1327.
DOI: 10.1007/s00170-019-04325-6

Abbas, A. T., Anwar, S., Abdelnasser, E., Luqman, M., Qudeiri, J. E. A., Elkaseer, A., 2021. Effect of Different Cooling Strategies on Surface Quality and Power Consumption in Finishing End Milling of Stainless Steel 316. Materials, 14 (4): 903, 13 pages.
DOI: 10.3390/ma14040903

Abele, E., Sielaff, T., Schiffler, A., Rothenbücher, S., 2011. Analyzing Energy Consumption of Machine Tool Spindle Units and Identification of Potential for Improvements of Efficiency (J. Hesselbach and C. Herrmann, Editors). Glocalized Solutions for Sustainability in Manufacturing, Springer-Verlag, Berlin Heidelberg, German, pp. 280-285.
DOI: 10.1007/978-3-642-19692-8_49

Abhang, L. B. and Hameedullah, M., 2010. Power Prediction Model for Turning EN-31 Steel Using Response Surface Methodology. Journal of Engineering Science and Technology Review, 3 (1): 116-122.
DOI: 10.25103/jestr.031.20

Aggarwal, A., Singh, H., Kumar, P., Singh, M., 2008. Optimizing Power Consumption for CNC Turned Parts Using Response Surface Methodology and Taguchi's Technique—A Comparative Analysis. Journal of Materials Processing Technology, 200 (1-3): 373-384.
DOI: 10.1016/j.jmatprotec.2007.09.041

Ahilan, C., Kumanan, S., Sivakumara, N., Dhas, J. E. R., 2013. Modeling and Prediction of Machining Quality in CNC Turning Process Using Intelligent Hybrid Decision Making Tools. Applied Soft Computing, 13: 543-1551.
DOI: 10.1016/j.asoc.2012.03.071

Akgün, M. and Kara, F., 2021. Analysis and Optimization of Cutting Tool Coating Effects on Surface Roughness and Cutting Forces on Turning of AA 6061 Alloy. Advances in Materials Science and Engineering, ID: 6498261, 12 pages.
DOI: 10.1155/2021/6498261

Akhtar, W., Sun, J., Chen, W., 2014. Effect of Machining Parameters on Surface Integrity in High Speed Milling of Super Alloy GH4169/Inconel 718. Materials and Manufacturing Processes, 31 (5): 620-627.
DOI: 10.1080/10426914.2014.994769

AKKO, 2021. External Turning Toolholders. Access date: 09.08.2021.
https://www.akko.com.tr/urun_res/1602571239_teknik.pdf

Akkuş, H. and Yaka, H., 2021. Experimental and Statistical Investigation of the Effect of Cutting Parameters on Surface Roughness, Vibration and Energy Consumption in Machining of Titanium 6Al-4V ELI (grade 5) Alloy. Measurement, 167, ID: 108465, 9 pages.
DOI: 10.1016/j.measurement.2020.108465

Albayrak, S., Yeşildal, F., Yıldırım, C., 2020. Effects of Cutting Parameters on Volume Level and Surface Roughness of SAE 4140 Steel in Turning: Optimization of Parameters. Journal of the Institute of Science and Technology, 10 (4): 2759-2769.
DOI: 10.21597/jist.714810

Alimardani, M., Fallah, V., Khajepour, A., Toyserkani, E., 2010. The Effect of Localized Dynamic Surface Preheating in Laser Cladding of Stellite 1. Surface & Coatings Technology, 204: 3911-3919.
DOI: 10.1016/j.surfcoat.2010.05.009

Al-Shayea, A., Abdullah, F. M., Noman, M. A., Kaid, H., Nasr, E. A., 2020. Studying and Optimizing the Effect of Process Parameters on Machining Vibration in Turning Process of AISI 1040 Steel. Advances in Materials Science and Engineering, ID: 5480614, 15 pages.
DOI: 10.1155/2020/5480614

Al-Sulaiman, F. A., Baseer, M. A., Sheikh, A. K., 2005. Use of Electrical Power for Online Monitoring of Tool Condition. Journal of Materials Processing Technology, 166: 364-371.
DOI: 10.1016/j.jmatprotec.2004.07.104

Altintas, Y., 2012. Manufacturing Automation: Metal Cutting Mechanics, Machine Tool Vibrations, and CNC Design. Cambridge University Press, Second Edition, New York, USA, 380 pages.

Anand, Y., Gupta, A., Abrol, A., Gupta, A., Kumar, V. , Tyagi, S. K., Anand, S., 2016. Optimization of Machining Parameters for Green Manufacturing. Cogent Engineering, 3 (1), ID: 1153292.
DOI: 10.1080/23311916.2016.1153292

Anderberg, S. and Kara, S., 2009. Energy and Cost Efficiency in CNC Machining. In: The 7th CIRP Conference on Sustainable Manufacturing: Chennai, India, Digitala Vetenskapliga Arkivet (DIVA), ID: 42100338, 4 pages.
https://www.diva-portal.org/smash/get/diva2:287555/FULLTEXT01.pdf

Antony, J., 2003. Design of Experiments for Engineers and Scientists. Elsevier Ltd., 1st Edition, 156 pages.
DOI: 10.1016/B978-0-7506-4709-0.X5000-5

Aouici, H., Yallese, M. A., Chaoui, K., Mabrouki, T., Rigal, J.-F., 2012. Analysis of Surface Roughness and Cutting Force Components in Hard Turning with CBN tool: Prediction Model and Cutting Conditions Optimization. Measurement, 45: 344-353.
DOI: 10.1016/j.measurement.2011.11.011

Arrazola, P. J., 2011. Finite-Element Modeling and Simulation (J. P. Davim, Editor). Machining of Hard Materials, Springer-Verlag London, UK, p.143-175.

Arrazola, P. J. and Özel, T., 2010. Investigations on the Effects of Friction Modeling Infinite Element Simulation of Machining. International Journal of Mechanical Sciences, 52: 31-42.
DOI: 10.1016/j.ijmecsci.2009.10.001

Asad, M., Ijaz, H., A Khan, M., Mabrouki, T., Saleem, W., 2014. Turning Modeling and Simulation of an Aerospace Grade Aluminum Alloy Using Two-Dimensional and Three-Dimensional Finite Element Method. Proceedings of the Institution of Mechanical Engineers Part B Journal of Engineering Manufacture, 228 (3): 367-375.
DOI: 10.1177/0954405413501809

Asad, M., 2019. Effects of Tool Edge Geometry on Chip Segmentation and Exit Burr: A Finite Element Approach. Metals, 9 (11), 1234, 24 pages.
DOI: 10.3390/met9111234

Asiltürk, I. and Akkuş, H., 2011. Determining the Effect of Cutting Parameters on Surface Roughness in Hard Turning Using the Taguchi Method. Measurement, 44: 1697-1704.
DOI: 10.1016/j.measurement.2011.07.003

Aslan, A., 2020. Optimization and Analysis of Process Parameters for Flank Wear, Cutting Forces and Vibration in Turning of AISI 5140: A Comprehensive Study. Measurement, 163, ID: 107959, 16 pages.
DOI: 10.1016/j.measurement.2020.107959

ASTM Standard: E92-82, 2003. Standard Test Method for Vickers Hardness of Metallic Materials. ASTM International, West Conshohocken, PA, USA, 9 pages.

ASTM Standard: E18-15, 2015. Standard Test Methods for Rockwell Hardness of Metallic Materials. ASTM International, West Conshohocken, PA, USA, 38 pages.

ASTM Standard: E407-99, 1999. Standard Practice for Microetching Metals and Alloys. ASTM International, West Conshohocken, PA, USA, 21 pages.

ASTM Standard: E8/E8M-09, 2009. Standard Test Methods for Tension Testing of Metallic Materials. ASTM International, West Conshohocken, PA, USA, 27 pages.

Atlas Specialty Metals, 2005. Technical Handbook of Bar Products. Atlas Specialty Metals Technical Services Department, Colorado, USA, 136 pages.

Godoy, V. A. A. and Diniz, A. E., 2011. Turning of Interrupted and Continuous Hardened Steel Surfaces Using Ceramic and CBN Cutting Tools. Journal of Materials Processing Technology, 211: 1014-1025.
DOI: 10.1016/j.jmatprotec.2011.01.002

Azizi, M. W., Belhadi, S., Yallese, M. A., Mabrouki, T., Rigal, J. -F., 2012. Surface Roughness and Cutting Forces Modeling for Optimization of Machining Condition in Finish Hard Turning of AISI 52100 Steel. Journal of Mechanical Science and Technology, 26 (12): 4105-4114.
DOI: 10.1007/s12206-012-0885-6

Bagaber, S. A., and Yusoff, A. R., 2017. Multi-objective Optimization of Cutting Parameters to Minimize Power Consumption in Dry Turning of Stainless Steel 316. Journal of Cleaner Production, 157: 30-46.
DOI: 10.1016/j.jclepro.2017.03.231

Bagci, E., 2011. Monitoring and Analysis of MRR-based Feed rate Optimization Approach and Effects of Cutting Conditions using Acoustic Sound Pressure Level in Free-form Surface Milling. Scientific Research and Essays, 6 (2): 256-277.
DOI: 10.5897/SRE10.538

Bartarya, G. and Choudhury, S. K., 2012. Effect of Cutting Parameters on Cutting Force and Surface Roughness During Finish Hard Turning AISI52100 Grade Steel. Procedia CIRP, 1: 651-656.
DOI: 10.1016/j.procir.2012.04.116

Basmaci, G., 2018. Optimization of Machining Parameters for the Turning Process of AISI 316 L Stainless Steel and Taguchi Design. Acta Physica Polonica A, 134 (1): 260-264.
DOI: 10.12693/APhysPolA.134.260

Bejaxhin, A. B. H., and Paulraj, G., 2019. Experimental Investigation of Vibration Intensities of CNC Machining Centre by Microphone Signals with the Effect of TiN/epoxy Coated Tool Holder. Journal of Mechanical Science and Technology, 33 (3): 1321-1331.
DOI: 10.1007/s12206-018-1232-3

Bhattacharya, A., Das, S., Majumder, P., Batish, A., 2009. Estimating the Effect of Cutting Parameters on Surface Finish and Power Consumption During High Speed Machining of AISI 1045 Steel Using Taguchi Design and ANOVA. Research and Development, 3: 31-40.
DOI: 10.1007/s11740-008-0132-2

Bhushan, R. K., 2013. Optimization of Cutting Parameters for Minimizing Power Consumption and Maximizing Tool Life During Machining of Al Alloy SiC Particle Composites. Journal of Cleaner Production, 39: 242-254.
DOI: 10.1016/j.jclepro.2012.08.008

Bilga, P. S., Singh, S., Kumar, R., 2016. Optimization of Energy Consumption Response Parameters for Turning Operation Using Taguchi Method. Journal of Cleaner Production, 137: 1406-1417.
DOI: 10.1016/j.jclepro.2016.07.220

Black, S. C., Chiles, V., Lissaman, A. J., Martin, S. J., 1996. Principles of Engineering Manufacture. Butterworth-Heinemann Ltd., 3rd Edition London, UK, 656 pages.

Bouzid, L., Yallese, M. A., Chaoui, K., Mabrouki, T., Boulanouar, L., 2015. Mathematical Modeling for Turning on AISI 420 Stainless Steel Using Surface Response Methodology. Proceedings of the Institution of Mechanical Engineers, Part B: Journal of Engineering Manufacture, 229 (1): 45-61.
DOI: 10.1177/0954405414526385

bp, 2020. Statistical Review of World Energy. bp Report, 69th Edition, 12 pages.

Cakir, M. C., Ensarioglu, C., Demirayak, I., 2009. Mathematical Modeling of Surface Roughness for Evaluating the Effects of Cutting Parameters and Coating Material. Journal of Materials Processing Technology, 209 (1): 102-109.
DOI: 10.1016/j.jmatprotec.2008.01.050

Camposeco-Negrete, C., 2013. Optimization of Cutting Parameters for Minimizing Energy Consumption in Turning of AISI 6061 T6 Using Taguchi Methodology and ANOVA. Journal of Cleaner Production, 53: 195-203.
DOI: 10.1016/j.jclepro.2013.03.049

Campatelli, G., Lorenzini, L., Scippa, A., 2014. Optimization of Process Parameters Using a Response Surface Method for Minimizing Power Consumption in the Milling of Carbon Steel. Journal of Cleaner Production, 66: 309-316.
DOI: 10.1016/j.jclepro.2013.10.025

Camposeco-Negrete, C., 2015. Optimization of Cutting Parameters Using Response Surface Method for Minimizing Energy Consumption and Maximizing Cutting Quality in Turning of AISI 6061 T6 Aluminum. Journal of Cleaner Production, 91: 109-117.
DOI: 10.1016/j.jclepro.2014.12.017

Camposeco-Negrete, C., Nájera, J. D. C., Miranda-Valenzuela, J. C., 2016. Optimization of Cutting Parameters to Minimize Energy Consumption during Turning of AISI 1018 Steel at Constant Material Removal Rate using Robust Design. The International Journal of Advanced Manufacturing Technology, 83: 1341-1347.
DOI: 10.1007/s00170-015-7679-9

Cardoso, L. G., Madeira, D. S., Ricomini, T. E. P. A., Miranda, R. A., Brito, T. G., Paiva, E. J., 2021. Optimization of Machining Parameters Using Response Surface Methodology with Desirability Function in Turning Duplex Stainless Steel UNS S32760. The International Journal of Advanced Manufacturing Technology, 12 pages.
DOI: 10.1007/s00170-021-07690-3

Cica, D., Sredanovic, B., Tesic, S., Kramar, D., 2020. Optimisation of Turning Parameters for Minimising Specific Cutting Energy with Use of Different Cooling/lubricating Techniques. Int. J. Machining and Machinability of Materials, 22 (2): 153-164.
DOI: 10.1504/IJMMM.2020.105665

Cui, P., Shi, Z. Y., Li, X., Duan, N. M., 2019. Evaluation of Specific Cutting Energy Considering Effects of Cutting Tool Geometry During Micro-machining Process. The International Journal of Advanced Manufacturing Technology, 102: 1127-1139.
DOI: 10.1007/s00170-018-3125-0

Çelik, Y. H., Yildiz, H., Özek, C., 2016. Effect of Cutting Parameters on Workpiece and Tool Properties During Drilling of Ti-6Al-4V. Materials Testing, 58 (6): 519-525.
DOI: 10.3139/120.110886

Dahmus, J. B. and Gutowski, T. G., 2004. An Environmental Analysis of Machining. ASME 2004 International Mechanical Engineering Congress and Exposition, ID: 27625821, 11 pages.
DOI: 10.1115/IMECE2004-62600

Das, S. R., Panda, A., Dhupal, D., 2017. Experimental Investigation of Surface Roughness, Flank Wear, Chip Morphology and Cost Estimation During Machining of Hardened AISI 4340 Steel with Coated Carbide Insert. Mechanics of Advanced Materials and Modern Processes, 3, 9, 14 pages.
DOI: 10.1186/s40759-017-0025-1

Davim, J. P., 2011. Machining of Hard Materials. Springer-Verlag, London, UK, 225 pages.
DOI: 10.1007/978-1-84996-450-0

Davim, J. P. and Jackson, M. J., 2011. Manufacturing Technology Research. Nova Science Publishers, Inc., Volume 1, New York, USA, 335 pages.

Davis, R. and John, P., 2018. Application of Taguchi-Based Design of Experiments for Industrial Chemical Processes (V. Silva, Editor). 7th Edition, Statistical Approaches With Emphasis on Design of Experiments Applied to Chemical Processes, IntechOpen, pp. 137-155.
DOI: 10.5772/intechopen.69501

Davoodi, B. and Tazehkandi, A. H., 2014. Cutting Forces and Surface Roughness in Wet Machining of Inconel alloy 738 with Coated Carbide Tool. Proceedings of the Institution of Mechanical Engineers, Part B: Journal of Engineering Manufacture, 230 (2): 215-226.
DOI: 10.1177/0954405414542990

Deepak, D. and Rajendra, B., 2016. Optimization of Machining Parameters for Turning of Al6061 Using Robust Design Principle to Minimize the Surface Roughness. Procedia Technology, 24: 372-378.
DOI: 10.1016/j.protcy.2016.05.050

Deepanraj, B., Raman, L. A., Senthilkumar, N., Shivasankar, J., 2020. Investigation and Optimization of Machining Parameters Influence on Surface Roughness in Turning AISI 4340 Steel. FME Transactions, 48 (2): 383-390.
DOI: 10.5937/fme2002383B

Deshpande, Y., Andhare, A., Sahu, N. K., 2017. Estimation of Surface Roughness Using Cutting Parameters, Force, Sound, and Vibration in Turning of Inconel 718. Journal of the Brazilian Society of Mechanical Sciences and Engineering, 39: 5087-5096.
DOI: 10.1007/s40430-017-0819-4

Directive of the European Parliament and of the Council, 2003. Directive 2003/10/EC of the European Parliament and of the Council of 6 February 2003 on the Minimum Health and Safety Requirements regarding the Exposure of Workers to the Risks arising from Physical Agents (Noise). European Parliament and Council of the European Union, Access date: 09.08.2021.
https://eur-lex.europa.eu/legal-content/EN/ALL/?uri=CELEX%3A32003L0010

Dutta, S. and Narala, S. K. R., 2021. Optimizing Turning Parameters in the Machining of AM Alloy Using Taguchi Methodology. Measurement, 169: ID: 108340, 8 pages.
DOI: 10.1016/j.measurement.2020.108340

eia, 2013. Manufacturing Energy Consumption Survey. U.S. Energy Information Administration, Access date: 01.08.2021.
https://www.eia.gov/todayinenergy/detail.php?id=13431

Elsheikh, A. H., Elaziz, M. A., Das, S. R., Muthuramalingam, T., Lu, S., 2021. A New Optimized Predictive Model Based on Political Optimizer for Eco-friendly MQL-Turning of AISI 4340 Alloy with Nano-lubricants. Journal of Manufacturing Processes, 67: 562-578.
DOI: 10.1016/j.jmapro.2021.05.014

Fakir, R., Barka, N., Brousseau, J., 2018. Mechanical Properties Analysis of 4340 Steel Specimen Heat Treated in Oven and Quenching in Three Different Fluids. Metals and Materials International, 24: 981-991.
DOI: 10.1007/s12540-018-0120-9

Fang, N., Pai, P. S., Mosquea, S., 2010. The Effect of Built-Up Edge on the Cutting Vibrations in Machining 2024-T351 Aluminum alloy. The International Journal of Advanced Manufacturing Technology, 49 (1): 63-71.
DOI: 10.1007/s00170-009-2394-z

Frifita, W., Salem, S. B., Haddad, A., Yallese, M. A., 2020. Optimization of Machining Parameters in Turning of Inconel 718 Nickel-base Super Alloy. Mechanics & Industry, 21 (2), 203, 20 pages.
DOI: 10.1051/meca/2020001

Frigieri, E. P., Ynoguti, C. A., Paiva, A. P., 2017. Correlation Analysis Among Audible Sound Emissions and Machining Parameters in Hardened Steel Turning. Journal of Intelligent Manufacturing, 30: 1753-1764.
DOI: 10.1007/s10845-017-1356-9

Gaitonde, V. N., Karnik, S. R., Davim, J. P., 2009. Multiperformance Optimization in Turning of Free-Machining Steel Using Taguchi Method and Utility Concept. Journal of Materials Engineering and Performance, 18: 231-236.
DOI: 10.1007/s11665-008-9269-6

Garg, G. K., Garg, S., Sangwan, K. S., 2018. Development of an Empirical Model for Optimization of Machining Parameters to Minimize Power Consumption. IOP Conference Series: Materials Science and Engineering, 346 (1), ID: 012078, 11 pages.
DOI: 10.1088/1757-899X/346/1/012078

Gok, A., Gologlu, C., Demir, I. H., Kurt, M., 2012. Determination of Surface Qualities on Inclined Surface Machining with Acoustic Sound Pressure. Strojniški vestnik - Journal of Mechanical Engineering, 58 (10): 587-597. DOI: 10.5545/sv-jme.2012.352

Government gazette, 2013. Directive on the Protection of Workers from the Risks related to Exposure to Noise at Work. T.C. Presidential Legislation Information System, Access date: 09.08.2021. https://www.resmigazete.gov.tr/eskiler/2013/07/20130728-11.htm

Groover, M. P., 2010. Fundamentals of Modern Manufacturing: Materials, Processes, and Systems. John Wiley & Sons, Inc., 4th Edition, Hoboken, New Jersey, USA, 1028 pages.

Guo, Y., Loenders, J. Duflou, Lauwers, B., 2012. Optimization of Energy Consumption and Surface Quality in Finish Turning. Procedia CIRP, 1: 512-517. DOI: 10.1016/j.procir.2012.04.091

Guo, Y. B. and Yen, D. W., 2004. A FEM Study on Mechanisms of Discontinuous Chip Formation in Hard Machining. Journal of Materials Processing Technology, 155-156: 1350-1356. DOI: 10.1016/j.jmatprotec.2004.04.210

Gutowski, T., Murphy, C., Allen, D., Bauer, D., Bras, B., Piwonka, T., Sheng, P., Sutherland, J., Thurston D., Wolff, E., 2005. Environmentally Benign Manufacturing: Observations from Japan, Europe and the United States. Journal of Cleaner Production, 13: 1-17. DOI: 10.1016/j.jclepro.2003.10.004

Gutowski, T., Dahmus, J., Thiriez, A., 2006. Electrical Energy Requirements for Manufacturing Processes. Conference publication: Proceedings of 13th CIRP International Conference on Life Cycle Engineering, May 31st-June 2nd, Lueven, Belgium.

Gürbüz, H. and Gönülaçar, Y. E., 2020. Optimization and Evaluation of Dry and Minimum Quantity Lubricating Methods on Machinability of AISI 4140 Using Taguchi Design and ANOVA. Proceedings of the Institution of Mechanical Engineers, Part C: Journal of Mechanical Engineering Science, 235 (7): 1211-1227.
DOI: 10.1177/0954406220939609

He, Y., Liu, F., Wu, T., Zhong, F. -P., Peng, B., 2011. Analysis and Estimation of Energy Consumption for Numerical Control Machining. Proceedings of the Institution of Mechanical Engineers, Part B: Journal of Engineering Manufacture, 226 (2): 255-266.
DOI: 10.1177/0954405411417673

Helu, M., Rühl, J., Dornfeld, D., Werner, P., Lanza, G., 2011. Evaluating Trade-Offs Between Sustainability, Performance, and Cost of Green Machining Technologies. Editors: J. Hesselbach and C. Herrmann, Glocalized Solutions for Sustainability in Manufacturing, Springer-Verlag, Berlin Heidelberg, German, pp. 195-200.
DOI: 10.1007/978-3-642-19692-8_34

Herrmann, C., Suh, S.-H., Bogdanski, G., Zein, A., Cha, J.-M., Um, J., Jeong, S., Guzman, A., 2011. Context-Aware Analysis Approach to Enhance Industrial Smart Metering (J. Hesselbach and C. Herrmann, Editors). Glocalized Solutions for Sustainability in Manufacturing, Springer-Verlag, Berlin Heidelberg, German, pp. 323-328.
DOI: 10.1007/978-3-642-19692-8_56

Hypermesh, 2021. Getting Started with HyperMesh. Access date: 09.08.2021.
https://connect.altair.com/CP/SA/training/self_paced/aero_v13/PDF/chapter1_demonstration.pdf

Jiang, Z., Gao, D., Lu, Y., Kong, L., Shang, Z., 2018. Electrical Energy Consumption of CNC Machine Tools based on Empirical Modeling. The International Journal of Advanced Manufacturing Technology, 100: 2255-2267.
DOI: 10.1007/s00170-018-2808-x

Johnson, G. R. and Cook, W. H., 1985. Fracture Characteristics of Three Metals Subjected to Various Strains, Strain Rates, Temperatures and Pressures. Engineering Fracture Mechanics, 21 (1): 31-48.
DOI: 10.1016/0013-7944(85)90052-9

Józwik, J., Wac-Włodarczyk, A., Michałowska, J., Kłoczko, M., 2018. Monitoring of the Noise Emitted by Machine Tools in Industrial Conditions. Journal of Ecological Engineering, 19 (1): 83-93.
DOI: 10.12911/22998993/79447

Kaladhar, M., 2020. Modeling and Optimization for Surface Roughness and Tool Flank Wear in Hard Turning of AISI 4340 Steel (35 HRC) Using TiSiN-TiAlN Nanolaminate Coated Insert. Multidiscipline Modeling in Materials and Structures, 17 (2): 337-359.
DOI: 10.1108/MMMS-12-2019-0217

Kalpakjian, S. and Schmid, S. R., 2010. Manufacturing Engineering and Technology. Pearson Education, Inc., 6th Edition, New Jersey, USA, 1205 pages.

Kambagowni, V., Chitla, R., Challa, S., 2018. Determining the Effect of Material Hardness during the Hard Turning of AISI4340 Steel. Journal of the Institution of Engineers, 99: 185-192.
DOI: 10.1007/s40033-018-0160-9

Kant, G. and Sangwan, K. S., 2015. Predictive Modelling for Energy Consumption in Machining using Artificial Neural Network. Procedia CIRP, 37: 205-210.
DOI: 10.1016/j.procir.2015.08.081

Kant, G. and Sangwan, K. S., 2015. Predictive Modeling for Power Consumption in Machining using Artificial Intelligence Techniques. Procedia CIRP, 26: 403-407.
DOI: 10.1016/j.procir.2014.07.072

Kant, G. and Sangwan, K. S., 2014. Prediction and Optimization of Machining Parameters for Minimizing Power Consumption and Surface Roughness in Machining. Journal of Cleaner Production, 83: 151-164.
DOI: 10.1016/j.jclepro.2014.07.073

Kara, S., Bogdanski, G., Li, W., 2011. Electricity Metering and Monitoring in Manufacturing Systems (J. Hesselbach and C. Herrmann, Editors). Glocalized Solutions for Sustainability in Manufacturing, Springer-Verlag, Berlin Heidelberg, German, pp. 1-10.
DOI: 10.1007/978-3-642-19692-8_1

Karaaslan, F. and Şahinoğlu, A., 2020. Determination of Ideal Cutting Conditions for Maximum Surface Quality and Minimum Power Consumption During Hard Turning of AISI 4140 Steel Using TOPSIS Method Based on Fuzzy Distance. Arabian Journal for Science and Engineering, 45: 9145-9157.
DOI: 10.1007/s13369-020-04635-y

Karabulut, Ş. and Şahinoğlu, A., 2018. Effect of the Cutting Parameters on Surface Roughness, Power Consumption and Machine Noise in Machining of R260 Steel. Journal of Polytechnic, 21 (1): 237-244.
DOI: 10.2339/politeknik.371299

Kaufmann, J. and Schering, A. G., 2014. Analysis of Variance ANOVA. Wiley Online Library, John Wiley & Sons, Inc., 12 pages.
DOI: 10.1002/9781118445112.stat06938

Kechagias, J. D., Aslani, K. -E., Fountas, N. A., Vaxevanidis, N. M., Manolakos, D. E., 2020. A Comparative Investigation of Taguchi and Full Factorial Design for Machinability Prediction in Turning of a Titanium Alloy. Measurement, 151, ID: 107213, 20 pages.
DOI: 10.1016/j.measurement.2019.107213

Kennametal, 2018. Turning Tools. Master Catalogue, Volume One, 988 pages, Access date: 09.08.2021. https://catalogs.kennametal.com/Master-Catalog-2018-Vol-1-Turning-Tools-English-Metric/C/

Khan, M. A., Jaffery, S. H. I., Khan, M., Younas, M., Butt, S. I., Ahmad, R., Sagheer Warsi, S., 2019. Statistical Analysis of Energy Consumption, Tool Wear and Surface Roughness in Machining of Titanium Alloy (Ti-6Al-4V) under Dry, Wet and Cryogenic Conditions. Mechanical. Sciences, 10: 561-573.
DOI: 10.5194/ms-10-561-2019

Khanna, N., Agrawal, C., Dogra, M., Pruncu, C. I., 2020. Evaluation of Tool Wear, Energy Consumption, and Surface Roughness During Turning of Inconel 718 Using Sustainable Machining Technique. Journal of Materials Research and Technology, 9 (3): 5794-5804.
DOI: 10.1016/j.jmrt.2020.03.104

Khanna, N., Airao, J., Gupta, M. K., Song, Q., Liu, Z., Mia, M., Maruda, R., Krolczyk, G., 2019. Optimization of Power Consumption Associated with Surface Roughness in Ultrasonic Assisted Turning of Nimonic-90 Using Hybrid Particle Swarm-Simplex Method. Materials, 12 (20), 3418, 20 pages.
DOI: 10.3390/ma12203418

Khatir, F. A., Sadeghi, M. H., Akar, S., 2021. Investigation of Surface Integrity in the Laser-assisted Turning of AISI 4340 Hardened Steel. Journal of Manufacturing Processes, 61: 173-189.
DOI: 10.1016/j.jmapro.2020.09.073

Kıvak, T., 2014. Optimization of Surface Roughness and flank wear using the Taguchi method in milling of Hadfield steel with PVD and CVD coated inserts. Measurement, 50: 19-28.
DOI: 10.1016/j.measurement.2013.12.017

Kistler, 2021. Cutting Force Measurements in Research and Development. Access date: 09.08.2021. https://www.kistler.com/files/download/960-002e.pdf?callee=frontend

Korkmaz, M. E. and Günay, M., 2018. Finite Element Modelling of Cutting Forces and Power Consumption in Turning of AISI 420 Martensitic Stainless Steel. Arabian Journal for Science and Engineering, 43: 4863-4870. DOI: 10.1007/s13369-018-3204-4

Kumar, P., Chauhan, S. R., Aggarwal, A., 2020. Effects of Cutting Conditions, Tool Geometry and Material Hardness on Machinability of AISI H13 using CBN tool. Materials Today: Proceedings, 46 (1), 6 pages. DOI: 10.1016/j.matpr.2020.01.406

Kumar, P., Chauhan, S. R., Pruncu, C. L., Gupta, M. K., Pimenov, D. Y., Mia, M., Gill, H. S., 2019. Influence of Different Grades of CBN Inserts on Cutting Force and Surface Roughness of AISI H13 Die Tool Steel during Hard Turning Operation. Materials, 12, 177, 21 pages. DOI: 10.3390/ma12010177

Kumar, R., Bilga, P. S., Singh, S., 2021. An Investigation of Energy Efficiency in Finish Turning of EN 353 Alloy Steel. Procedia CIRP, 98: 654-659. DOI: 10.1016/j.procir.2021.01.170

Kuntoğlu, M., Aslan, A., Pimenov, D. Y., Giasin, K., Mikolajczyk, T., Sharma, S., 2020. Modeling of Cutting Parameters and Tool Geometry for Multi-Criteria Optimization of Surface Roughness and Vibration via Response Surface Methodology in Turning of AISI 5140 Steel. Materials, 13, 4242, 21 pages. DOI: 10.3390/ma13194242

Kuntoğlu, M., Acar, O., Gupta, M. K., Sağlam, H., Sarikaya, M., Giasin, K., Pimenov, D. Y., 2021. Parametric Optimization for Cutting Forces and Material Removal Rate in the Turning of AISI 5140. Machines, 9 (5), 90, 20 pages. DOI: 10.3390/machines9050090

Kuntoğlu, M., Aslan, A., Sağlam, H., Pimenov, D. Y., Giasin, K., Mikolajczyk, T., 2020. Optimization and Analysis of Surface Roughness, Flank Wear and 5 Different Sensorial Data via Tool Condition Monitoring System in Turning of AISI 5140. Sensors, 20 (16), 4377, 20 pages.
DOI: 10.3390/s20164377

Laghari, R. A., Li, J., Mia, M., 2020. Effects of Turning Parameters and Parametric Optimization of the Cutting Forces in Machining SiCp/Al 45 wt% Composite. Metals, 10 (6), 840, 21 pages.
DOI: 10.3390/met10060840

Lalwani, D. I., Mehta, N. K., Jain, P. K., 2008. Experimental Investigations of Cutting Parameters Influence on Cutting forces and surface Roughness in Finish Hard Turning of MDN250 Steel. Journal of materials processing technology, 206: 167-179.
DOI: 10.1016/j.jmatprotec.2007.12.018

Lee, W. S. and Su, T. T., 1999. Mechanical Properties and Microstructural Features of AISI 4340 High-Strength Alloy Steel under Quenched and Tempered Conditions. Journal of Materials Processing Technology, 87: 198-206.
DOI: 10.1016/S0924-0136(98)00351-3

Li, C., Xiao, Q., Tang, Y., Li, L., 2016. A Method Integrating Taguchi, RSM and MOPSO to CNC Machining Parameters Optimization for Energy Saving. Journal of Cleaner Production, 135: 263-275.
DOI: 10.1016/j.jclepro.2016.06.097

Li, L., Li, C., Tang, Y., Yi, Q., 2017. Influence Factors and Operational Strategies for Energy Efficiency Improvement of CNC Machining. Journal of Cleaner Production, 161: 220-238.
DOI: 10.1016/j.jclepro.2017.05.084

Li, W. and Kara, S., 2014. An Empirical Model for Predicting Energy Consumption of Manufacturing Processes: A Case of Turning Process. Proceedings of the Institution of Mechanical Engineers, Part B: Journal of Engineering Manufacture, 225 (9): 1636-1646.
DOI: 10.1177/2041297511398541

Li, W., Zein, A., Kara, S., Herrmann, C., 2011. An Investigation into Fixed Energy Consumption of Machine Tools (J. Hesselbach and C. Herrmann, Editors). Glocalized Solutions for Sustainability in Manufacturing, Springer-Verlag, Berlin Heidelberg, German, pp. 268-273.
DOI: 10.1007/978-3-642-19692-8_47

Li, Y., He, Y., Wang, Y., Yan, P., Liu, X., 2015. A Framework for Characterising Energy Consumption of Machining Manufacturing Systems. International Journal of Production Research, 52 (2): 314-325.
DOI: 10.1080/00207543.2013.813983

Liang, R., Huang, C., Hao, H., Liu, F., Liu, F., Song, M., Ke, L., 2020. Microstructure and Mechanical Properties of 34CrNiMo6 Steel Repaired by Laser Remelting. Journal of Materials Research and Technology, 9 (6): 13870-13878.
DOI: 10.1016/j.jmrt.2020.09.100

Liu, N., Wang, S. B., Zhang, Y. F., Lu, W. F., 2016. A Novel Approach to Predicting Surface Roughness based on Specific Cutting Energy Consumption When Slot Milling Al-7075. International Journal of Mechanical Sciences, 118: 13-20.
DOI: 10.1016/j.ijmecsci.2016.09.002

LMalghan, R., Rao M. C. K., ArunKumar S., Rao, S. S., Herbert, M. A., 2018. Machining Parameters Optimization of AA6061 Using Response Surface Methodology and Particle Swarm Optimization. International Journal of Precision Engineering and Manufacturing, 19 (5): 695-704.
DOI: 10.1007/s12541-018-0083-2

Luan, X., Zhang, S., Cai, G., 2016. Optimal Cutting Parameters to Reduce Power Consumption in Face Milling of a Cast Iron Alloy for Environmental Sustainability (R. J. Howlett and L. C. Jain, Editors). Sustainable Design and Manufacturing, Springer International Publishing, Switzerland, pp. 135-148.
DOI: 10.1007/978-3-319-32098-4_12

Lv, J., Tang, R., Tang, W., Jia, S., Liu, Y., Cao, Y., 2018. An Investigation into Methods for Predicting Material Removal Energy Consumption in Turning. Journal of Cleaner Production, 193: 128-139.
DOI: 10.1016/j.jclepro.2018.05.035

Lv, L., Deng, Z., Yan, C., Liu, T., Wan, L., Gu, Q., 2020. Modelling and Analysis for Processing Energy Consumption of Mechanism and Data Integrated Machine Tool. International Journal of Production Research, 58 (23): 7078-7093.
DOI: 10.1080/00207543.2020.1756508

Lv, J., Tang, R., Jia, S., Liu, Y., 2015. Experimental Study on Energy Consumption of Computer Numerical Control Machine Tools. Journal of Cleaner Production, 112 (5): 3864-3874.
DOI: 10.1016/j.jclepro.2015.07.040

Maranhão, C., Davim, J. P., 2010. Finite Element Modelling of Machining of AISI 316 Steel: Numerical Simulation and Experimental Validation. Simulation Modelling Practice and Theory, 18: 139-156.
DOI: 10.1016/j.simpat.2009.10.001

Mason, R. L., Gunst, R. F., Hest, J. L., 2003. Statistical Design and Analysis of Experiments. John Wiley & Sons, Inc., Second Edition, Hoboken, New Jersey, USA, 752 pages.

Mativenga, P. T. and Rajemi, M. F., 2011. Calculation of Optimum Cutting Parameters based on Minimum Energy Footprint. CIRP Annals - Manufacturing Technology, 60: 149-152.
DOI: 10.1016/j.cirp.2011.03.088

Meng, L., Zhou, M., Zhang, C., Tian, G., 2016. A New Model for Predicting Power Consumption of Machining Processes: A Turning Case. 2016 IEEE International Conference on Automation Science and Engineering (CASE), ID: 16467498, 1289-1294.
DOI: 10.1109/COASE.2016.7743556

Mia, M., Khan, M. A., Dhar, N. R., 2017. Study of Surface Roughness and Cutting Forces Using ANN, RSM, and ANOVA in Turning of Ti-6Al-4Vunder Cryogenic Jets Applied at Flank and Rake Faces of Coated WC Tool. The International Journal of Advanced Manufacturing Technology, 93: 975-991.
DOI: 10.1007/s00170-017-0566-9

Minitab, 2021. Getting Started with Minitab Statistical Software, Access date: 09.08.2021.
https://www.minitab.com/content/dam/www/en/uploadedfiles/documents/getting-started/MinitabGettingStarted_EN.pdf

Montgomery, D. C., 2001. Design and Analysis of Experiments. John Wiley & Sons, Inc., Fifty Edition, Hoboken, New Jersey, USA, 299 pages.

Moradnazhad, M. and Unver, H. O., 2016. Energy Efficiency of Machining Operations: A Review. Proceedings of the Institution of Mechanical Engineers, Part B: Journal of Engineering Manufacture, 231 (11): 1871-1889.
DOI: 10.1177/0954405415619345

Moradnazhad, M. and Unver, H. O., 2016. Energy Consumption Characteristics of Turn-mill Machining. The International Journal of Advanced Manufacturing Technology, 91: 1991-2016.
DOI: 10.1007/s00170-016-9868-6

Mori, T., 2011. Taguchi Methods Benefits, Impacts, Mathematics, Statistics, and Applications. ASME, New York, USA, 857 pages.

Motorcu, A. R., 2011. Tool Life Performances, Wear Mechanisms and Surface Roughness Characteristics When Turning Austenised and Quenched AISI 52100 Bearing Steel with Ceramics and CBN/TiC Cutting Tools. Indian Journal of Engineering and Materials Sciences, 18 (2): 137-146, Access Date: 09.08.2021.
http://nopr.niscair.res.in/bitstream/123456789/11682/1/IJEMS%2018(2)%20137-146.pdf

Myers, R. H., Montgomery, D. C., Anderson-Cook, C., M., 2016. Response Surface Methodology: Process and Product Optimization Using Designed Experiments. John Wiley & Sons, Inc., Fourth Edition, Hoboken, New Jersey, USA, 855 pages.

Ng, E. -G. and Aspinwall, D. K., 2002. The Effect of Workpiece Hardness and Cutting Speed on the Machinability of AISI H13 Hot Work Die Steel When Using PCBN Tooling. Transactions of the ASME, 124: 588-594.
DOI: 10.1115/1.1452749

Nguyen, T. -T., 2019. Prediction and Optimization of Machining Energy, Surface Roughness, and Production Rate in SKD61 Milling. Measurement, 136: 525-544.
DOI: 10.1016/j.measurement.2019.01.009

Nur, R., Noordin, M. Y., Izman, S., Kurniawan, D., 2015. Machining Parameters Effect in Dry Durning of AISI 316L Stainless Steel Using Coated Carbide Tools. Proceedings of the Institution of Mechanical Engineers, Part E: Journal of Process Mechanical Engineering, 231 (4): 676-683.
DOI: 10.1177/0954408915624861

Nur, R., Noordin, M. Y., Izman, S., Kurniawan, D., 2015. Optimizing Power Consumption for Sustainable Dry Turning of Treated Aluminum Alloy. Procedia Manufacturing, 2: 558-562.
DOI: 10.1016/j.promfg.2015.07.096

Nur, R., Yusof, N. M., Sudin, I., Nor, F. M., Kurniawan, D., 2021. Determination of Energy Consumption during Turning of Hardened Stainless Steel Using Resultant Cutting Force. Metals, 11 (4), 565, 14 pages.
DOI: 10.3390/met11040565

Nur, R., Noordin, M. Y., Izman, S. , Kurniawan, D., 2014. The Effect of Cutting Parameters on Power Consumption during Turning Nickel Based Alloy. Advanced Materials Research, 845: 799-802.
DOI: 10.4028/www.scientific.net/AMR.845.799

Nur, R., Suyuti, M. A., Susanto, T. A., 2017. Optimizing Cutting Conditions on Sustainable Machining of Aluminum Alloy to Minimize Power consumption. AIP Conference Proceedings, 1855 (1), 020002, 7 pages.
DOI: 10.1063/1.4985447

Ozturk, B., 2019. Investigation of Effects of Inverter Frequency Changes on the Specific Energy Consumption of Pipe Threading using Response Surface Methodology. Measurement, 152, ID: 107296.
DOI: 10.1016/j.measurement.2019.107296

Özdemir, M., Kaya, M. T., Akyıldız, H. K., 2020. Analysis of Surface Roughness and Cutting Forces in Hard Turning of 42CrMo4 Steel using Taguchi and RSM Method. MECHANIKA, 26 (3): 231-241.
DOI: 10.5755/j01.mech.26.3.23600

Özdemir, M., 2019. Analysis of the Effect Rates of Cutting Parameters on Surface Roughness Using Surface Response Method. Gazi University Journal of Science Part C: Design and Technology, 7 (3): 639-648.
DOI: 10.29109/gujsc.595722

Özdemir, M., 2019. Optimization with Taguchi Method of Influences on Surface Roughness of Cutting Parameters in CNC Turning Processing. MECHANIKA, 25 (5): 397-405.
DOI: 10.5755/j01.mech.25.5.23005

Özdemir, M., 2020. Modelling and Prediction of Effect of Machining Parameters on Surface Roughness in Turning Operations. Tehnički vjesnik, 27 (3): 751-760.
DOI: 10.17559/TV-20190320104114

Öztürk, B. and Kara, F., 2020. Calculation and Estimation of Surface Roughness and Energy Consumption in Milling of 6061 Alloy. Advances in Materials Science and Engineering, ID: 5687951, 12 pages.
DOI: 10.1155/2020/5687951

Panda, A., Das, S. R., Dhupal, D., 2019. Statistical Analysis of Surface Roughness Using RSM in Hard Turning of AISI 4340 Steel with Ceramic Tool (K. Shanker, R. Shankar, R. Sindhwani, Editors). Advances in Industrial and Production Engineering, Springer Nature Singapore Pte Ltd., Singapore, pp. 17-26.
DOI: 10.1007/978-981-13-6412-9_3

Pawanr, S., Garg, G. H., Routroy, S., 2021. Modelling of Variable Energy Consumption for CNC Machine Tools. Procedia CIRP, 98: 247-251.
DOI: 10.1016/j.procir.2021.01.038

Pervaiz, S., Deiab, I., Kishawy, H., 2016. A Finite Element Based Energy Consumption Analysis for Machining AISI 1045 Carbon Steel Using Uncoated Carbide Tool. Advances in Materials and Processing Technologies, 2 (1): 83-92.
DOI: 10.1080/2374068X.2016.1159033

Phate, M. R. and Tatwawadi, V. H., 2015. Mathematical Models of Material Removal Rate & Power Consumption for Dry Turning of Ferrous Material using Dimensional Analysis in Indian Prospective. Jordan Journal of Mechanical and Industrial Engineering, 9 (1): 27-38,
Access date: 09.08.2021.
http://www.jjmie.hu.edu.jo/vol9-1/JJMIE_-25-14-01%20Proof%20Reading.pdf

Prasad, B. S. and Babu, M. P., 2017. Correlation Between Vibration Amplitude and Tool Wear in Turning: Numerical and Experimental Analysis. Engineering Science and Technology, an International Journal, 20, 197-211. DOI: 10.1016/j.jestch.2016.06.011

Qasim, A., Nisar, S., Shah, A., Khalid, M. S., Sheikh, M. S., 2015. Optimization of Process Parameters for Machining of AISI-1045 Steel Using Taguchi Design and ANOVA. Simulation Modelling Practice and Theory, 59: 36-51. DOI: 10.1016/j.simpat.2015.08.004

Rafighi, M., Özdemir, M., Shehabi, S. A., Kaya, M. T., 2021. Sustainable Hard Turning of High Chromium AISI D2 Tool Steel Using CBN and Ceramic Inserts. Transactions of the Indian Institute of Metals, 74:1639-1653. DOI: 10.1007/s12666-021-02245-2

Rajemi, M. F., Mativenga, P. T., Aramcharoen, A., 2010. Sustainable Machining: Selection of Optimum Turning Conditions based on Minimum Energy Considerations. Journal of Cleaner Production, 18: 1059-1065. DOI: 10.1016/j.jclepro.2010.01.025

Raman, R. S., Kukreja, N., Singh, N., 2021. Process Parameters Optimization Through Taguchi and ANOVA Analysis - A Review. IOP Conference Series: Materials Science and Engineering, 1116, 012090, 8 pages. DOI: 10.1088/1757-899X/1116/1/012090

Rao, C. J., Rao, D. N., Srihari, P., 2013. Influence of Cutting Parameters on Cutting Force and Surface Finish in Turning Operation. Procedia Engineering, 64: 1405-1415. DOI: 10.1016/j.proeng.2013.09.222

Rawat, U. M. and Potdar, V. V., 2014. A Review on Optimization of Cutting Parameters in Machining Using Taguchi Method. International Journal of Innovative Research in Advanced Engineering (IJIRAE), 1 (11), ISSN: 2349-2163, pp. 21-24, Access date: 09.08.2021. https://www.ijirae.com/volumes/vol1/issue11/04.NVME10102.pdf

Rech, J., Dumont, F., Le Bot, A., Arrazola, P. J., 2017. Reduction of Noise During Milling Operations. CIRP Journal of Manufacturing Science and Technology, 18: 39-44.
DOI: 10.1016/j.cirpj.2016.09.001

Rutherford, A., 2011. ANOVA and ANCOVA A GLM Approach. John Wiley & Sons, Inc., Second Edition, Hoboken, New Jersey, USA, 360 pages.

Sadeghifar, M., Sedaghati, R., Jomaa, W., Songmene, V., 2018. A Comprehensive Review of Finite Element Modeling of Orthogonal Machining Process: Chip Formation and Surface Integrity Predictions. The International Journal of Advanced Manufacturing Technology, 96: 3747-3791.
DOI: 10.1007/s00170-018-1759-6

Saeidi, N., and Ekrami, A., 2003. Comparison of Mechanical Properties of Martensite/Ferrite and Bainite/Ferrite Dual Phase 4340 Steels. Materials Science and Engineering A, 523:125-129.
DOI: 10.1016/j.msea.2009.06.057

Sahoo, A. K. and Sahoo, B., 2013. Performance Studies of Multilayer Hard Surface Coatings (TiN/TiCN/Al2O3/TiN) of Indexable Carbide Inserts in Hard Machining: Part-II (RSM, Grey Relational and Techno Economical Approach). Measurement, 46: 2868-2884.
DOI: 10.1016/j.measurement.2012.09.023

Sahu, N. K. and Andhare, A. B., 2017. Modelling and Multiobjective Optimization for Productivity Improvement in High Speed Milling of Ti–6Al–4V Using RSM and GA. Journal of the Brazilian Society of Mechanical Sciences and Engineering, 39: 5069-5085.
DOI: 10.1007/s40430-017-0804-y

Sangwan, K. S. and Kant, G., 2017. Optimization of Machining Parameters for Improving Energy Efficiency using Integrated Response Surface Methodology and Genetic Algorithm Approach. Procedia CIRP, 61: 517-522.
DOI: 10.1016/j.procir.2016.11.162

Sarıkaya, M. and Güllü, A., 2014. Taguchi Design and Response Surface Methodology based Analysis of Machining Parameters in CNC Turning under MQL. Journal of Cleaner Production, 65: 604-616. DOI: 10.1016/j.jclepro.2013.08.040

Seçkin, Ö., 2021. Multi-objective Optimization of Ms58 Brass Machining Operation by Multi-axis CNC Lathe. Arabian Journal for Science and Engineering, 46: 2133-2145. DOI: 10.1007/s13369-020-04984-8

Seemuang, N., McLeay, T., Slatter, T., 2016. Using Spindle Noise to Monitor Tool Wear in a Turning Process. The International Journal of Advanced Manufacturing Technology, 86: 9-12. DOI: 10.1007/s00170-015-8303-8

Selvamuthu, D. and Das, D., 2018. Introduction to Statistical Methods, Design of Experiments and Statistical Quality Control. Springer Nature Singapore Pte Ltd., New Delhi, India, 445 pages. DOI: 10.1007/978-981-13-1736-1

Serin, G., Ozbayoglu, M., Unver, H. O., 2019. Integrated Energy-efficient Machining of Rotary Impellers and Multi-objective Optimization. Materials and Manufacturing Processes, 35 (4): 478-490. DOI: 10.1080/10426914.2019.1605177

Shin, S. -J., Woo, J., Rachuri, S., 2014. Predictive Analytics Model for Power Consumption in Manufacturing. Procedia CIRP, 15: 153-158. DOI: 10.1016/j.procir.2014.06.036

Shobaa, C., Prasad, D. S., Sucharita, A., Abishek M., Koundinya, M. S., 2018. Investigations of Surface roughness, Power Consumption, MRR and Tool Wear While Turning Hybrid Composites. Materials Today: Proceedings, 5: 16565-16574. DOI: 10.1016/j.matpr.2018.06.012

Shokoohi,Y., Khosrojerdi, E., Shiadhi, B. h. R., 2015. Machining and Ecological Effects of a New Developed Cutting Fluid in Combination with Different Cooling Techniques on Turning Operation. Journal of Cleaner Production, 94: 330-339.
DOI: 10.1016/j.jclepro.2015.01.055

Siddhpura, M. and Paurobally, R., 2012. A review of Chatter Vibration Research in Turning. International Journal of Machine Tools & Manufacture, 61: 27-47.
DOI: 10.1016/j.ijmachtools.2012.05.007

Smith, G. T., 2008. Cutting Tool Technology: Industrial Handbook. Springer Verlag, London, UK, 606 pages.
DOI: 10.1007/978-1-84800-205-0

Subbaiah, K. V., Raju, C., Suresh, C., 2020. Parametric Analysis and Optimization of Hard Turning at Different Levels of Hardness Using Wiper Ceramic Insert. Measurement, 158, ID: 107712, 13 pages.
DOI: 10.1016/j.measurement.2020.107712

Sumardiyanto, D., Susilowati, S. E., Cahyo, A., 2018. Effect of Cutting Parameter on Surface Roughness Carbon Steel S45C. Journal of Mechanical Engineering and Automation, 8 (1): 1-6.
DOI: 10.5923/j.jmea.20180801.01

Sumitomo, 2021. Performance cutting Tools. Cutting Tools General Catalogue, Access date: 09.08.2021.
https://www.sumitomotool.com/fileadmin/user_upload/Catalogues_Download/Sumitomo_Catalogue_2020-2021_EN.pdf

Suresh, R., Basavarajappa, S., Gaitonde, V. N., Samuel, G. L., 2012. Machinability Investigations on Hardened AISI 4340 Steel Using Coated Carbide Insert. International Journal of Refractory Metals and Hard Materials, 33: 75-86.
DOI: 10.1016/j.ijrmhm.2012.02.019

Swain, S., Panigrahi, I., Sahoo, A. K., Panda, A., Kumar, R., 2020. Effect of Tool Vibration on Flank Wear and Surface Roughness During High-Speed Machining of 1040 Steel. Journal of Failure Analysis and Prevention, 20: 976-994.
DOI: 10.1007/s11668-020-00905-x

Şahinoğlu, A., Güllü, A., Dönertaş, M. A., 2017. Investigation of Surface Roughness, Sound Level, Vibration During the Turning of GGG50 Material. Sinop University journal of natural sciences, 2 (1): 67-79, Access Date: 09.08.2021.
https://www.researchgate.net/profile/Abidin-Sahinoglu/publication/330683626_Arastirma_Makalesi_GGG50_Malzemenin_Torna_Tezgahinda_Islenmesinde_Kesme_Parametrelerinin_Titresim_Ses_Siddeti_ve_Yuzey_Puruzlulugu_Uzerinde_Etkisinin_Arastirilmasi_Investigation_of_Surface_Roughness_S/links/5d7a648d92851ca36810c499/Arastirma-Makalesi-GGG50-Malzemenin-Torna-Tezgahinda-Islenmesinde-Kesme-Parametrelerinin-Titresim-Ses-Siddeti-ve-Yuezey-Pueruezlueluegue-Uezerinde-Etkisinin-Arastirilmasi-Investigation-of-Surface-Rou.pdf

Şahinoğlu, A., Karabulut, Ş., Güllü, A., 2017. Study on Spindle Vibration and Surface Finish in Turning of Al 7075. Solid State Phenomena, 261: 321-327.
DOI: 10.4028/www.scientific.net/SSP.261.321

Şahinoğlu, A. and Ulas, E., 2020. An investigation of Cutting Parameters Effect on Sound level, Surface roughness, and Power Consumption during Machining of Hardened AISI 4140. Mechanics & Industry, 21, 523, 12 pages.
DOI: 10.1051/meca/2020068

Şahinoğlu, A., Güllü, A., Çifçi, İ., 2009. Analysis of Surface Roughness, Sound Level, Vibration and Current When Machining AISI 1040 Steel. Sigma Journal of Engineering and Natural Sciences, 37 (2): 423-437, Access Date: 09.08.2021.
https://eds.yildiz.edu.tr/ArticleContent/Journal/sigma/Volumes/2019/Issues/4/YTUJENS-2019-37-2.4643.pdf

Şahinoğlu, A. and Güllü, A., 2019. Investigation of the Relationship Between Current, Sound Intensity, Vibration and Surface Roughness in Machining of CuZn39Pb3 Material on Lathe Machine. Journal of Polytechnic, 23 (3): 615-624.
DOI: 10.2339/politeknik.426106

Şahinoğlu, A. and Rafighi, M., 2020. Investigation of Vibration, Sound Intensity, Machine Current and Surface Roughness Values of AISI 4140 During Machining on the Lathe. Arabian Journal for Science and Engineering, 45: 765-778.
DOI: 10.1007/s13369-019-04124-x

Şahinoğlu, A. and Rafighi, M., 2019. Optimization of Cutting Parameters with Respect to Roughness for Machining of Hardened AISI 1040 Steel. Materials Testing, 62 (1): 85-95.
DOI: 10.3139/120.111458

Tamang, S. K., Chandrasekaran, M., Sahoo, A. K., 2018. Sustainable Machining: An Experimental Investigation and Optimization of Machining Inconel 825 with Dry and MQL Approach. Journal of the Brazilian Society of Mechanical Sciences and Engineering, 40, 374, 18 pages.
DOI: 10.1007/s40430-018-1294-2

Tanikić, D. and Marinković, V., 2012. Modelling and Optimization of the Surface Roughness in the Dry Turning of the Cold Rolled Alloyed Steel Using Regression Analysis. Journal of the Brazilian Society of Mechanical Sciences and Engineering, 34 (1), 41-48.
DOI: 10.1590/S1678-58782012000100006

Tekiner, Z. and Yeşilyurt, S., 2004. Investigation of the Cutting Parameters Depending on Process Sound during Turning of AISI 304 Austenitic Stainless Steel. Materials and Design, 25: 507-513.
DOI: 10.1016/j.matdes.2003.12.011

Valera, H. Y. and Bhavsar, S. N., 2014. Experimental Investigation of Surface Roughness and Power Consumption in Turning Operation of EN 31 Alloy Steel. Procedia Technology, 14: 528-534.
DOI: 10.1016/j.protcy.2014.08.067

Velchev, S., Kolev, I., Ivanov, K., Gechevski, S., 2014. Empirical Models for Specific Energy Consumption and Optimization of Cutting Parameters for Minimizing Energy Consumption During Turning. Journal of Cleaner Production, 80: 139-149.
DOI: 10.1016/j.jclepro.2014.05.099

Warsi, S. S., Jaffery, S. H. I, Ahmad, R., Khan, M., Ali, L., Agha, M. H., Akram, S., 2017. Development of Energy Consumption Map for Orthogonal Machining of Al 6061-T6 Alloy. Proceedings of the Institution of Mechanical Engineers, Part B: Journal of Engineering Manufacture, 232 (14): 2510-2522.
DOI: 10.1177/0954405417703424

Warsi, S. S., Jaffery, H. I., Ahmad, R., Khan, M., Akram, S., 2015. Analysis of Power and Specific Cutting Energy Consumption in Orthogonal Machining of Al 6061-T6 Alloys at Transitional Cutting Speeds. Proceedings of the ASME 2015 International Mechanical Engineering Congress & Exposition, IMECE2015 November 13-19, Houston, Texas, USA.
DOI: 10.1115/IMECE2015-53290

Warsi, S. S., Ahmad, R., Jaffery, S. H. I., Agha, M. H., Khan, M., 2020. Development of Specific Cutting Energy Map for Sustainable Turning: a Study of Al 6061 T6 from Conventional to High Cutting Speeds. The International Journal of Advanced Manufacturing Technology, 106: 2949-2960.
DOI: 10.1007/s00170-019-04836-2

Wirtz, A., Meißner, M., Wiederkehr, P., Biermann, D., Myrzik, J., 2019. Evaluation of Cutting Processes Using Geometric Physically-based Process Simulations in View of the Electric Power Consumption of Machine Tools. Procedia CIRP, 79: 602-607.
DOI: 10.1016/j.procir.2019.02.083

Yallese, M. A., Rigal, J.-F., Chaoui, K., Boulanouar, L., 2005. The Effects of Cutting Conditions on Mixed Ceramic and Cubic Boron Nitride Tool Wear and on Surface Roughness During Machining of X200Cr12 Steel (60 HRC). Proceedings of the Institution of Mechanical Engineers Part B Journal of Engineering Manufacture, 219 (1): 35-55.
DOI: 10.1243/095440505X8082

Yao, C., Zhou, Z., Zhang, J., Wu, D., Tan, L., 2017. Experimental Study on Cutting Force of Face-Turning Inconel718 with Ceramic Tools and Carbide Tools. Advances in Mechanical Engineering, 9: (7), 1-9.
DOI: 10.1177/1687814017716620

Yang, W. H. and Tarng, Y. S., 1998. Design Optimization of Cutting Parameters for Turning Operations Based on the Taguchi Method. Journal of Materials Processing Technology, 84: 122-129.
DOI: 10.1016/S0924-0136(98)00079-X

Zhang, C., Li, W., Jiang, P., Gu, P., 2017. Experimental Investigation and Multi-objective Optimization Approach for Low-carbon Milling Operation of Aluminum. Proceedings of the Institution of Mechanical Engineers, Part C: Journal of Mechanical Engineering Science, 231 (15): 2753-2772.
DOI: 10.1177/0954406216640574

Zhang, L., Jiang, P., Gu, P., Li, W., 2013. A Methodology to Estimate Power Consumption of Numerical Control Machining. 2013 IEEE International Symposium on Assembly and Manufacturing (ISAM), ID: 33816142, pp. 219-221.
DOI: 10.1109/ISAM.2013.6643531

Zhang, W., He, F., Wu, T., Du, C., Liu, H., 2016. 3D Numerical Simulation on Thermal-Stress Distribution of Hardened Steels Workpiece Assembled with Different Hardness. International Journal on Interactive Design and Manufacturing (IJIDeM), 11 (3), 10 pages.
DOI: 10.1007/s12008-016-0317-4

Zhao, G. Y., Liu, Z. Y., He, Y., Cao, H. J., Guo, Y. B., 2017. Energy Consumption in Machining: Classification, Prediction, and Reduction Strategy. Energy, 133: 142-157.
DOI: 10.1016/j.energy.2017.05.110

Zhao, G., Hou, C., Qiao, J., Cheng, X., 2016. Energy Consumption Characteristics Evaluation Method in Turning. Advances in Mechanical Engineering, 8: (11), 1-8.
DOI: 10.1177/1687814016680737

Zhong, Q., Tang, R., Lv, J., Jia, S. Jin, M., 2015. Evaluation on Models of Calculating Energy Consumption in Metal Cutting Processes: A Case of External Turning Process. The International Journal of Advanced Manufacturing Technology, 82 (9-12): 2087-2099.
DOI: 10.1007/s00170-015-7477-4

Zhou, L., Li, J., Li, F., Meng, Q., Li, J., Xu, X., 2015. Energy Consumption Model and Energy Efficiency of Machine Tools: A Comprehensive Literature Review. Journal of Cleaner Production, 112: 3721-3734.
DOI: 10.1016/j.jclepro.2015.05.093

**CURRICULUM VITAE (CV)**

Oğur İYNEN. He enrolled Department of Mechanical Engineering in Harran University in 1998. He graduated from Harran University in 2002 and obtained B.Sc. degree in Mechanical Engineering. In 2005, he started his M.Sc. degree at Çukurova University. Then he achieved M.Sc. degree at Department of Construction & Manufacturing in 2009. And later on, he started his Ph.D. degree at Çukurova University in 2009. Also, he has been working as a Lecturer in Mechanical Engineering Department at University of Yozgat Bozok since 2009. He is married and has two children.

# APPENDIX

### A.1. Calibration Certifications for Kistler Turning Dynamometer

KISTLER
measure. analyze. innovate.

## Kalibrierschein
Calibration Certificate

Type **Kistler 9129AA** Serial No. **4510446**

| Kalibriert durch / Calibration Technician | Datum / Date | |
|---|---|---|
| S. Mogavero | 23. Jul. 2013 | |

| Referenzgeräte / Reference Equipment | Typ / Type | Serien-Nr. / Serial No. |
|---|---|---|
| Gebrauchsnormal / Working Standard | Kistler 9067 | 474351 |
| | Kistler 9068 | 107070 |
| | Kistler 9068 | 128643 |
| Ladungskalibrator / Charge Calibrator | Kistler 5395A | 605262 |

| Umgebungstemperatur / Ambient Temperature °C | Relative Feuchte / Relative Humidity % |
|---|---|
| 27 | 38 |

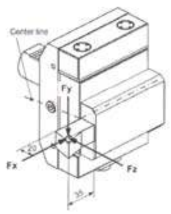


## Messergebnisse Results of Measurement

| Kalibrierter Bereich / Calibrated Range kN | | Empfindlichkeit / Sensitivity pC / N | Linearität / Linearity ≤ ± %FSO | Übersprechen / Cross talk % | % |
|---|---|---|---|---|---|
| Fx | 0 ... 5 | -8,067 | 0,03 | Fx → Fy -0,1 | Fx → Fz 0,2 |
| Fx | 0 ... 0,5 | -8,049 | 0,08 | Fx → Fy 0,0 | Fx → Fz 0,4 |
| Fy | 0 ... 8 | -4,162 | 0,04 | Fy → Fx 0,6 | Fy → Fz 0,4 |
| Fy | 0 ... 0.8 | -4,137 | 0,03 | Fy → Fx 0,6 | Fy → Fz 0,3 |
| Fz | 0 ... 5 | -8,086 | 0,08 | Fz → Fx -0,4 | Fz → Fy 0,6 |
| Fz | 0 ... 0,5 | -8,074 | 0,02 | Fz → Fx -0,4 | Fz → Fy 0,8 |

**Messverfahren** Kontinuierliche Kalibrierung, Vergleichsverfahren
Measurement Procedure Continuous Calibration, Comparison Method

Kistler betreibt die SCS Kalibrierstelle Nr. 049, akkreditiert nach ISO 17025. SCS Kalibrierzertifikate sind auf Bestellung erhältlich.
Kistler operates the SCS Calibration Laboratory No. 049, which is accredited per ISO 17025. SCS Calibration Certificates are available on request.

## Bestätigung Confirmation

Das oben durch die Seriennummer identifizierte Gerät entspricht der Vereinbarung der Bestellung und hält die Herstelltoleranzen gemäss den Spezifikationen der Datenblätter ein. Dieses Dokument erfüllt die Anforderungen von EN 10204 Abnahmeprüfzeugnis "3.1". Alle Messmittel sind auf nationale Normale rückverfolgbar. Das Kistler Qualitätsmanagement System ist nach ISO 9001 zertifiziert. Dieses Dokument ist ohne Unterschrift gültig.
The equipment mentioned above and identified by Serial Number complies with the agreement of the order and meets the manufacturing tolerances specified in the data sheets. This document fulfils the requirements of EN 10204 Inspection Certificate "3.1". All measuring devices are traceable to national standards. The Kistler Quality Management System is certified per ISO 9001. This document is valid without a signature.


**Kistler Instrumente AG**
Eulachstrasse 22
PO Box
CH-8408 Wintherthur
Tel. +41 52 224 11 11
Fax +41 52 224 14 14
info@kistler.com
ZKB Winterthur BC 732
Swift: ZKBKCHZZ80A
Account: 1132-0374.628
IBAN: CH67 0070 0113 2003 7462 8
VAT: 229 713
ISO 9001 certified
www.kistler.com


Seite page 1 / 1

Figure A.1.1. 3-Component system for measuring cutting forces up to 8 kN during turning

KISTLER
measure. analyze. innovate.

# Kalibrierschein
## Calibration Certificate

Type **Kistler 9129AA** Serial No. **4510446**

| Kalibriert durch / Calibration Technician | Datum / Date |
|---|---|
| S. Mogavero | 24. Jul. 2013 |

| Referenzgeräte / Reference Equipment | Typ / Type | Serien-Nr. / Serial No. |
|---|---|---|
| Gebrauchsnormal / Working Standard | Kistler 9067 | 474351 |
| | Kistler 9068 | 107070 |
| | Kistler 9068 | 128643 |
| Ladungskalibrator / Charge Calibrator | Kistler 5395A | 605262 |

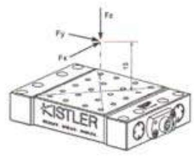


| Umgebungstemperatur / Ambient Temperature °C | Relative Feuchte / Relative Humidity % |
|---|---|
| 25 | 42 |

## Messergebnisse Results of Measurement

| Kalibrierter Bereich / Calibrated Range kN | | Empfindlichkeit / Sensitivity pC / N | Linearität / Linearity ≤ ± %FSO | Übersprechen / Cross talk % | % |
|---|---|---|---|---|---|
| Fx | 0 ... 10 | -8,079 | 0,04 | Fx → Fy -0,5 | Fx → Fz 0,2 |
| Fx | 0 ... 1 | -8,043 | 0,05 | Fx → Fy -0,5 | Fx → Fz 0,2 |
| Fx | 0 ... 0,1 | -8,039 | 0,06 | Fx → Fy -0,5 | Fx → Fz 0,2 |
| Fy | 0 ... 10 | -4,145 | 0,02 | Fy → Fx 1,0 | Fy → Fz 0,4 |
| Fy | 0 ... 1 | -4,125 | 0,07 | Fy → Fx 1,0 | Fy → Fz 0,3 |
| Fy | 0 ... 0,1 | -4,124 | 0,08 | Fy → Fx 1,0 | Fy → Fz 0,3 |
| Fz | 0 ... 10 | -8,072 | 0,02 | Fz → Fx 0,2 | Fz → Fy 0,1 |
| Fz | 0 ... 1 | -8,033 | 0,02 | Fz → Fx 0,2 | Fz → Fy 0,0 |
| Fz | 0 ... 0,1 | -8,027 | 0,07 | Fz → Fx 0,2 | Fz → Fy 0,0 |

**Messverfahren** Measurement Procedure — **Kontinuierliche Kalibrierung, Vergleichsverfahren** Continuous Calibration, Comparison Method

Kistler betreibt die SCS Kalibrierstelle Nr. 049, akkreditiert nach ISO 17025. SCS Kalibrierzertifikate sind auf Bestellung erhältlich.
Kistler operates the SCS Calibration Laboratory No. 049, which is accredited per ISO 17025. SCS Calibration Certificates are available on request.

## Bestätigung Confirmation

Das oben durch die Seriennummer identifizierte Gerät entspricht der Vereinbarung der Bestellung und hält die Herstelltoleranzen gemäss den Spezifikationen der Datenblätter ein. Dieses Dokument erfüllt die Anforderungen von EN 10204 Abnahmeprüfzeugnis "3.1". Alle Messmittel sind auf nationale Normale rückverfolgbar. Das Kistler Qualitätsmanagement System ist nach ISO 9001 zertifiziert. Dieses Dokument ist ohne Unterschrift gültig.
The equipment mentioned above and identified by Serial Number complies with the agreement of the order and meets the manufacturing tolerances specified in the data sheets. This document fulfils the requirements of EN 10204 inspection Certificate "3.1". All measuring devices are traceable to national standards. The Kistler Quality Management System is certified per ISO 9001. This document is valid without a signature.

**Kistler Instrumente AG**
Eulachstrasse 22
PO Box
CH-8408 Wintherthur
Tel. +41 52 224 11 11
Fax +41 52 224 14 14
info@kistler.com
ZKB Winterthur BC 732
Swift: ZKBKCHZZ80A
Account: 1132-0374.628
IBAN: CH67 0070 0113 2003 7462 8
VAT: 229 713
ISO 9001 certified
www.kistler.com

Seite page 1 / 1

Figure A.1.2. Multi-component dynamometer with top Plate 90x105 mm up to 10 kN

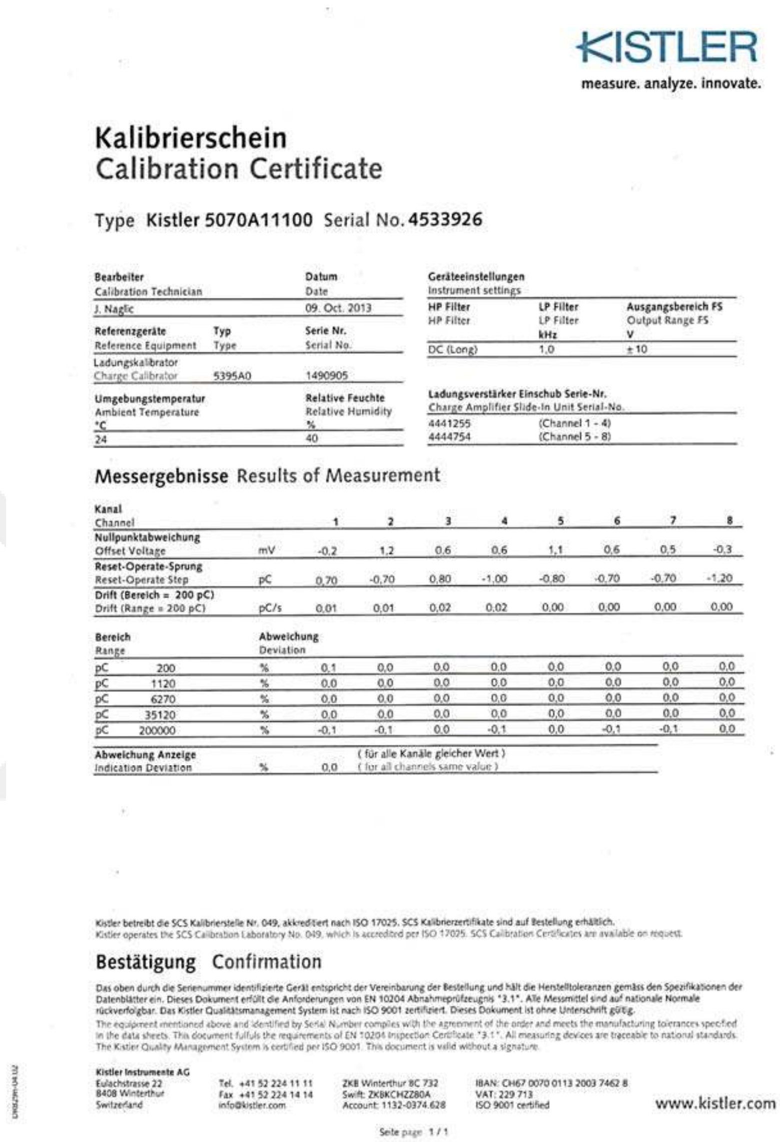

KISTLER
measure. analyze. innovate.

# Kalibrierschein
# Calibration Certificate

Type Kistler 5070A11100 Serial No. 4533926

| Bearbeiter / Calibration Technician | | Datum / Date |
|---|---|---|
| J. Naglic | | 09. Oct. 2013 |
| **Referenzgeräte** / Reference Equipment | **Typ** / Type | **Serie Nr.** / Serial No. |
| Ladungskalibrator / Charge Calibrator | 5395A0 | 1490905 |

| Umgebungstemperatur / Ambient Temperature °C | Relative Feuchte / Relative Humidity % |
|---|---|
| 24 | 40 |

Geräteeinstellungen / Instrument settings

| HP Filter / HP Filter | LP Filter / LP Filter kHz | Ausgangsbereich FS / Output Range FS V |
|---|---|---|
| DC (Long) | 1,0 | ± 10 |

Ladungsverstärker Einschub Serie-Nr. / Charge Amplifier Slide-In Unit Serial-No.

| | |
|---|---|
| 4441255 | (Channel 1 - 4) |
| 4444754 | (Channel 5 - 8) |

## Messergebnisse Results of Measurement

| Kanal / Channel | | 1 | 2 | 3 | 4 | 5 | 6 | 7 | 8 |
|---|---|---|---|---|---|---|---|---|---|
| Nullpunktabweichung / Offset Voltage | mV | -0,2 | 1,2 | 0,6 | 0,6 | 1,1 | 0,6 | 0,5 | -0,3 |
| Reset-Operate-Sprung / Reset-Operate Step | pC | 0,70 | -0,70 | 0,80 | -1,00 | -0,80 | -0,70 | -0,70 | -1,20 |
| Drift (Bereich = 200 pC) / Drift (Range = 200 pC) | pC/s | 0,01 | 0,01 | 0,02 | 0,02 | 0,00 | 0,00 | 0,00 | 0,00 |

| Bereich / Range | Abweichung / Deviation | | | | | | | | |
|---|---|---|---|---|---|---|---|---|---|
| pC 200 | % | 0,1 | 0,0 | 0,0 | 0,0 | 0,0 | 0,0 | 0,0 | 0,0 |
| pC 1120 | % | 0,0 | 0,0 | 0,0 | 0,0 | 0,0 | 0,0 | 0,0 | 0,0 |
| pC 6270 | % | 0,0 | 0,0 | 0,0 | 0,0 | 0,0 | 0,0 | 0,0 | 0,0 |
| pC 35120 | % | 0,0 | 0,0 | 0,0 | 0,0 | 0,0 | 0,0 | 0,0 | 0,0 |
| pC 200000 | % | -0,1 | -0,1 | 0,0 | -0,1 | 0,0 | -0,1 | -0,1 | 0,0 |

| Abweichung Anzeige / Indication Deviation | % | 0,0 | ( für alle Kanäle gleicher Wert ) / ( for all channels same value ) |
|---|---|---|---|

Kistler betreibt die SCS Kalibrierstelle Nr. 049, akkreditiert nach ISO 17025. SCS Kalibrierzertifikate sind auf Bestellung erhältlich.
Kistler operates the SCS Calibration Laboratory No. 049, which is accredited per ISO 17025. SCS Calibration Certificates are available on request.

## Bestätigung Confirmation

Das oben durch die Seriennummer identifizierte Gerät entspricht der Vereinbarung der Bestellung und hält die Herstelltoleranzen gemäss den Spezifikationen der Datenblätter ein. Dieses Dokument erfüllt die Anforderungen von EN 10204 Abnahmeprüfzeugnis "3.1". Alle Messmittel sind auf nationale Normale rückverfolgbar. Das Kistler Qualitätsmanagement System ist nach ISO 9001 zertifiziert. Dieses Dokument ist ohne Unterschrift gültig.
The equipment mentioned above and identified by Serial Number complies with the agreement of the order and meets the manufacturing tolerances specified in the data sheets. This document fulfuls the requirements of EN 10204 Inspection Certificate "3.1". All measuring devices are traceable to national standards. The Kistler Quality Management System is certified per ISO 9001. This document is valid without a signature.

Kistler Instrumente AG
Eulachstrasse 22
8408 Winterthur
Switzerland

Tel. +41 52 224 11 11
Fax +41 52 224 14 14
info@kistler.com

ZKB Winterthur BC 732
Swift: ZKBKCHZZ80A
Account: 1132-0374.628

IBAN: CH67 0070 0113 2003 7462 8
VAT: 229 713
ISO 9001 certified

www.kistler.com

Seite page 1 / 1

Figure A.1.3. Multi-channel charge amplifier for multi-component force measurement

### A.2. Properties of Kistler Turning Dynamometer

**3-Component System for Measuring Cutting Forces up to 8 kN During Turning**

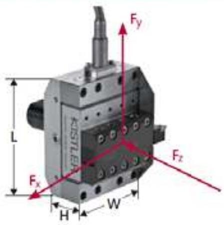


*Type 9129A...*

| Specifications | | | Type 9129A... |
|---|---|---|---|
| Measuring range, max. allowable | $F_x$, $F_z$<br>$F_y$ | kN<br>kN | –5 ... 5 *)<br>–8 ... 8 *) |
| Calibrated measuring ranges | $F_x$, $F_z$<br>$F_y$ | N<br>N | 0 ... 5; 0 ... 0,5<br>0 ... 8; 0 ... 0,8 |
| Sensitivity | $F_x$, $F_z$<br>$F_y$ | pC/N<br>pC/N | ≈–8<br>≈–4,1 |
| Natural frequency | $f_nx$<br>$f_ny$<br>$f_nz$ | kHz<br>kHz<br>kHz | ≈1,5 **)<br>≈1,5 **)<br>≈2,5 **) |
| Operating temperature range | | °C | 0 ... 70 |
| Clamping surface | | mm | 90x105 |
| LxWxH | | mm | 150x107x63 *) |
| Weight | | kg | 7,6 *) |
| Degree of protection IEC/EN 60529 | | | IP67 with connected cable |
| Connection | | | Fischer Flange 9-pole neg. |

*This sensor is calibrated and ready for measurement.*

**Characteristics**
This is a modular measuring system based on the dynamometers Type 9129AA with a large measuring range. Its special mounting arrangement ensures a small temperature error. The lathe adapter is readily mounted on the dynamometer. The available toolholders for lathe tools and boring bars are equally easily mounted.

**Applications**
Measuring cutting forces during turning on turret lathes.

**Accessories**
- Lathe adapter with straight shank (VDI) Type 9129AB...
- Lathe adapter with Capto C6 Type 9129AC6
- Lathe adapter with clamping wedge Type 9129AD...
- Toolholder for lathe tool Type 9129AE...
- Toolholder for boring bar Type 9129AF40
- Connecting cable Type 1687B5/1689B5 (3-Comp.)

**Data sheet** 9129A_000-710

*) Depending on adapter
**) Applies to dynamometer Type 9129AA with lathe type 9129AB40 and toolholder Type 9129AE25, without tool

Figure A.2.1. 3-Component system for measuring cutting forces up to 8 kN during turning

## Stationary Dynamometer

**Multi-Component Dynamometer with Top Plate 90x105 mm up to 10 kN**

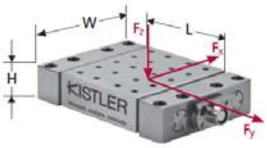


*Type 9129AA*

| Specifications | | | Type 9129AA |
|---|---|---|---|
| Measuring range | $F_x$, $F_y$, $F_z$ | kN | –10 ... 10 |
| Calibrated measuring ranges | $F_x$, $F_y$, $F_z$ | kN<br>kN<br>kN | 0 ... 0,1<br>0 ... 1<br>0 ... 10 |
| Sensitivity | $F_x$, $F_z$<br>$F_y$ | pC/N<br>pC/N | ≈–8<br>≈–4,1 |
| Natural frequency | $f_nx$<br>$f_ny$<br>$f_nz$ | kHz<br>kHz<br>kHz | ≈3,5<br>≈4,5<br>≈3,5 |
| Operating temperature range | | °C | 0 ... 70 |
| LxWxH | | mm | 90x105x32 |
| Weight | | kg | 3,2 |
| Degree of Protection IEC/EN 60529 | | | IP67 with connected cable |
| Connection | | | Fischer Flange 9-pole neg. |

*This sensor is calibrated and ready for measurement.*

**Characteristics**
The low profile, large measuring range and small temperature error make this dynamometer the ideal instrument for measurements on precision machinery. Its design ensures high natural frequencies in all three force directions.

**Applications**
Measuring cutting forces involved in milling and grinding.

**Accessories**
- Connecting cable
  - Type 1687B5/1689B5 (3-Comp.)
  - Type 1677A5/1679A5 (6-Comp.)

**Data sheet** 9129AA_000-709

Figure A.2.2. Multi-component dynamometer with top plate 90x105 mm up to 10 kN

## Charge Amplifier

**Multi-Channel Charge Amplifier for Multi-component Force Measurement**


*Type 5070A...*

| **Technical data** | | **5070Ax0xxx** | **5070Ax1xxx** | **5070Ax2xxx** |
|---|---|---|---|---|
| Number of channels | | 4 | 8 | 8 with 6-component summing calculator |

| **General technical data** | | | |
|---|---|---|---|
| Measuring ranges FS | pC | optional | ±200 ... 200 000<br>±600 ... 600 000 |
| Measuring range adjustment | | continous | |
| Frequency range (–3 dB) | kHz | ≈0 ... 45 | |
| Output signal | V | ±10 | |
| Supply voltage | VAC | 100 ... 240 | |
| Input signal | Type/connector | piezoelectric, optional with<br>• BNC neg.<br>• Fischer 9-pole neg. | |
| Degree of Protection to IEC/EN 60529 | | IP40 | |
| Interface | | optional | • RS-232C<br>• RS-232C and IEEE-488 |
| Case | | optional | • 19" cassette for rack mounting<br>• Desktop unit with support bracket<br>• 19" cassette with panel mounting set |
| **Other features** | | | |
| | | • Display of peak values<br>• Display of mechanical measurands | |

*The parameters of this charge amplifier can be quickly and easily configured with the DynoWare software package for the PC.*

**Characteristics**
This amplifier is ideal for multicomponent force-torque measurement with piezoelectric dynamometers or force plates for cutting force measurement.

**Application**
The 4-channel amplifier is effective for measuring cutting forces with Kistler dynamometers. The 8-channel amplifier is suitable for 6-component force-torque measurement in laboratories, research and development.

**Accessories**
- RS-232C null modem cable, l = 5 m, D-Sub 9-pole pos. / D-Sub 9-pole neg. Type 1200A27
- Connecting cable for signal outputs from charge amp to data acquisition card, l = 2 m, D-Sub 15-pole pos./D-Sub 37-pole neg. Type 1500B15
- Connecting cable for signal outputs from 6-component summing calculator to data acquisition card, l = 2 m, D-Sub 15-pole pos. / D-Sub 37-pole neg. Type 1500A7
- Inductive proximity swith Type 2233B

**Data sheet** 5070A_000-485

Figure A.2.3. Multi-channel charge amplifier for multi-component force measurement

## Software

### DynoWare Type 2825A...


*Type 2825A*

| Technical data | Windows® Software for Data Acquisition and Evaluation |
|---|---|
| Supported charge amplifier: | Type 5011/5015A.../5018A...<br>Type 5017/5019<br>Type 5070A...<br>Type 5080A... |
| Supported Signal Conditioners (for rotating dynamometers) | Type 5223B...<br>Type 5237A... |
| More information | see data sheet |

**Characteristics**
Simple operation, configuration and control of Kistler measuring instruments via RS-232C interface, high-performance graphics, useful signal evaluation and calculation functions, simultaneous recording of measuring channels. Is also ideal for acquisition and evaluation of any physical measurands.

**Applications**
Windows® software for data acquisition and evaluation. All-purpose, operator-friendly software, especially effective for force measurement with dynamometers and single- or multicomponent force sensors. For signal analysis DynoWare provides an online display of measurement curves as well as useful calculation and graphics functions. In addition to easy configuration of the most important measuring instruments, DynoWare supports individual documentation of the measurement process as well as storage of configuration and measurement data.

**Options**
None

**Accessories**
- Data acquisition card PCIM-DAS 1602/16 Type 2855A4
- Data acquisition card PC-Card-DAS 16/16 Typ 2855A5
- Data acquisition box Type 5697
- Connecting cable Type 1500B15
- Connecting cable Type 1500A67
- Connecting cable Type 1500B69
- USB-RS232C converter Type 2867

**Data sheet** 2825A_000-371

Figure A.2.4. Dynoware Type 2825A

### Cables, High Insulation, Temperature Range –5 ... 70 °C

*Type 1677A5*

| Specifications | | Type 1677A5 |
|---|---|---|
| Connection | | Fischer 9-pole pos.<br>Fischer 9-pole pos. |
| Length | m | 5 |
| Diameter | mm | 12,3 (metal sheath) |
| Number of conductors | | 8 |
| Used for | | 6-component measurement |

Figure A.2.5. Cables, high insulation, temperature range -5…70 ºC

## Cable

### Cables, Low-resistance

*Type 1500A7*

| Specifications | | Type 1500A7 |
|---|---|---|
| Connection | | D-Sub 15-pole pos.<br>D-Sub 37-pole pos. |
| Length | m | 2 |
| Diameter | mm | 7 |
| Number of conductors | | 9 |
| Used for | | Connection of summing amplifiers Type 5070Ax2xxx to Type 2855A4 |

Figure A.2.6. Cables, low-resistance

## Distributing Box, Fischer 9-pole neg. – 8 x BNC neg.

*Type 5405A*

| Specifications | | Type 5405A |
|---|---|---|
| Input signal | | Fischer 9-pole neg. |
| Output signal | | 8 x BNC neg. |
| Dimensions LxWxH | mm | 73x99x33 |

Figure A.2.7. Distributing box, fischer 9-pole neg.-8xBNC neg

## Data Acquisition Card

*Type 2855A4*

| Specifications | | Type 2855A4, PCIM-DAS 1602/16 |
|---|---|---|
| Number of measuring channels | | 8 differential |
| PC bus | | PCI |
| Resolution | Bit | 16 |
| Sampling rate, max. | kS/s | 100 |
| Connection | | D-Sub 37-pole pos. |

**Data sheet** 2825A_000-371

Figure A.2.8. Data acquisition card

## Data Acquisition Box

*Type 5697*

| Specifications | | Type 5697 |
|---|---|---|
| Number of measuring channels | | 32 |
| Resolution | Bit | 16 |
| Sampling rate, max. | | (continuously adjustable in DynoWare) |
| with 1 channel | kS/s | 1 000 |
| with 8 channels | kS/s | 125 |
| with 16 channels | kS/s | 62,5 |
| Interface to PC | | USB 2.0 Type B, female |
| Dimensions | mm | 208x70x250 |
| Weight | kg | 2,5 |

Available from 02/2010

**Data sheet** 5697_000-745

Figure A.2.9. Data acquisition box

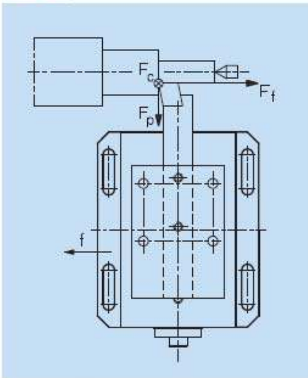


*Forces during longitudinal cylindrical turning*


*Turning with dynamometer Type 9129A...*

Turning is machining with a geometrically defined cutting edge and a circular cutting motion. Normally the workpiece carries out the rotational movement. The single-point tool (turning tool) is firmly clamped on the dynamometer for cutting force measurement.

The machining force produced by the turning process is resolved directly into three significant components by the multi-component dynamometer.

**Forces Measurable During Turning**

- Main cutting force $F_c$
- Feed force $F_f$
- Passive force $F_p$

Cylindrical turning is the model situation of machining with a geometrically determined cutting edge, and is particularly suitable for determining the specific machining force $k_{i1,1}$ of materials. With universal lathes, stationary bench dynamometers are mounted on the tool slide in place of the tool holder. The tool edge must be accurately set to the workpiece center.

For lathes with a turret-head style tool holder, the the 3-component measuring system Type 9129A... is used. The exact position of the tool edge is ensured by the tool holder fixture on the turret head. The modular measuring system Type 9129A... accommodates different combinations of lathe adapters and toolholders. All of the popular types and sizes of adapter as well as toolholders for boring and outside turning tools are available.

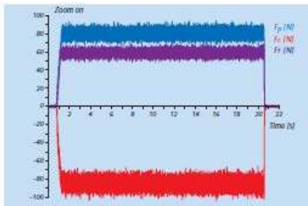


*Measured turning data*

| | |
|---|---|
| Material | C45E |
| $v_c$ | 495 m/min |
| f | 0,05 mm/rev. |
| $a_p$ | 0,5 mm |
| Dynamometer | Type 9129A... |

Figure A.2.10. Cutting force measurement during turning

## A.3. Published Articles



# Experimental and numerical investigation of cutting forces during turning of cylindrical AISI 4340 steel specimens

*Oğur İynen, Yozgat, Abdul Kadir Ekşi, Adana, Mustafa Özdemir, Yozgat and Hamza Kemal Akyıldız, Yozgat, Turkey*

Cutting forces play a significant role in machining because they directly affect the mechanics of machining, the energy requirements, and the tool stability required. In this study, the cutting forces occurring during the turning of AISI 4340 material with 30 Rockwell C hardness scale have been analyzed both experimentally and numerically. Many types of research have been conducted via 2-D simulation using the finite element analysis method. In other words, in most studies, the workpiece was modeled as a flat specimen. Therefore, this paper presents a real 3-D turning simulation model using cylindrical specimens. The cutting forces were measured using a Kistler 9129AA model piezoelectric dynamometer. The ABAQUS/Explicit finite element method was used, and a model by Johnson and Cook was assigned as a material model in the numerical analysis. A new PVD AlTiN coated carbide insert was incorporated to prevent wear. Experimental results obtained from cutting tests were compared with numerical results to establish the accuracy of the FEM. It was observed that experimental and numerical results overlapped each other. Thus, this method can be used directly in the industry to reduce high processing costs.

***Article Information***

***Correspondence Address***
*Associate Prof. Dr. Mustafa Özdemir*
*Machine and Metal Technology Department*
*Vocational High School*
*Bozok University*
*Esentepe Campus*
*66200 Yozgat, Turkey*
*E-mail: mustafa.ozdemir@bozok.edu.tr*

***Keywords***
*Turning, cutting forces, AISI 4340, FEM*

AISI 4340 alloy is a heat treatable steel. High toughness, good ductility and low brittleness are achieved when subjected to heat treatment. Mostly it is used in typical applications like producing crankshafts, piston connecting rods, shafts, aircraft parts, gears, valves, pins [1, 2]. Interest on the part of various industries with respect to cutting is mainly due to a need to reduce costs while maintaining a high-quality product standard. As a result, the scientific community always focuses on cutting, developing research on several topics concerning cutting operations. As a consequence, it is possible to find articles in the literature often dealing with numerical models. These models became popular due to the high cost of cutting tools, workpieces, measuring devices, and energy consumption in the experimental study. However, several aspects are not completely clear yet and need to be investigated [3, 4]. More recently, the finite element method (FEM) has been effectively used in cutting process applications. Simulation results found without experimental tests supply useful information that can be used by researchers and tool manufacturers. In addition, these results can serve as a guide for designing tools and optimizing the cutting process [5, 6]. ABAQUS is widely used as a FEM simulation software in most studies. It can be applied to solve linear and nonlinear problems [7]. Because conducting experiments can be expensive and take time [8], in various works different numerical analysis software based on FEM such as ABAQUS have reported that complex structures can be solved easily.

Maranhão and Davim [9] conducted a numerical analysis for the machining of AISI 316 steel by finite element modeling. The authors used AdvantedgeTM software for establishing a machining simulation. They stated that the friction coefficient has an important effect while cutting forces are being determined during the FEM cutting process. Thus, the cutting forces change significantly with a change in the friction coefficient. The friction coefficient calculated by the Coulomb model for use in the



Figure A.3.1. Article titled "Experimental and Numerical Investigation of Cutting Forces During Turning of Cylindrical AISI 4340 Steel Specimens"

Journal of the Brazilian Society of Mechanical Sciences and Engineering (2021) 43:374
https://doi.org/10.1007/s40430-021-03075-5

TECHNICAL PAPER

# Real 3D turning simulation of materials with cylindrical shapes using ABAQUS/Explicit

Oğur İynen[1] · Abdul Kadir Ekşi[2] · Hamza Kemal Akyıldız[1] · Mustafa Özdemir[3]

Received: 1 August 2020 / Accepted: 9 June 2021


**Abstract**
In this study, cutting forces and chip shapes formed by turning cylindrical materials were researched experimentally and numerically. AISI 4340 steel alloy with a hardness of about 30 Rockwell C scale was chosen as workpiece material. Most of the turning simulations performed by finite element method (FEM) have been conducted 2D (two-dimensional) because 3D (three-dimensional) is very difficult and time-consuming and mechanics of more complex 3D cutting operations are usually evaluated by using geometrical and kinematic transformation models applied to the 2D cutting Process. In other words, the workpiece was modeled as a flat specimen. Nevertheless, 3D (three-dimensional) simulation using cylindrical models are more nearer to practical process. For this reason, to get the actual cutting process, this paper aims to present a real 3D (three-dimensional) turning simulation model using ABAQUS/ Explicit software using tube and bar specimens with a cylindrical shape. Cutting forces were measured utilizing the Kistler 9129AA model piezoelectric dynamometer. Cutting forces and chip shapes obtained by making FEM simulations were compared. Simulation results were determined to be in high proximity with experimental results. Also, realistic chip shapes were simulated by FEM. Therefore, this method could be used as reliable in the industry.

**Keywords** Turning · Cutting forces · FEM · ABAQUS · Chip morphology

## 1 Introduction

AISI 4340 alloys are commonly used in production. These steels are cheaper than their equivalent. It is utilized in aircraft, automobile and engine parts, camshafts and crankshafts, steering parts, and gears. It is also a material suitable for surface hardening. It is steel with high toughness properties [1–3]. These are the main reasons that led numerous researchers to carry out various studies aiming to examine the machinability of this type of material. Forces formed in the metal cutting process have great importance in the manufacturing sector because these forces provide information about the power requirements of the machine. In this way, by determining the best cutting process parameters, an essential energy economy is provided during processing [4–6]. Also, metal turning is an important part of cutting machining and has a wide range on market. Therefore, this cutting process is explored by experimental, analytical, and numerical methods. Because the mechanism of the cutting process has a sophisticated structure, it is rather hard to work out them analytically. The experimental method takes a high cost and a long time. However, this difficult and sophisticated structure can be solved easier with help of finite element method (FEM), which is a numerical analysis program [7]. Recently, the finite element method has been used in cutting operations and very effective results have been obtained. The finite element method can be a guideway for machine manufacturers, tool designers, and researchers [8–11]. A large budget and time are required to perform experimental studies only in cutting operations. Therefore, the use of different FEM software applications such as ABAQUS, AdvantEdge, ANSYS, and DEFORM has increased [12–14]. ABAQUS is a very strong FEM simulation software for solutions of linear and nonlinear problems [15]. Hence, it was preferred

✉ Mustafa Özdemir
mustafa.ozdemir@bozok.edu.tr

1 Department of Mechanical Engineering, Yozgat Bozok University, Yozgat 66900, Turkey

2 Department of Mechanical Engineering, Çukurova University, Adana 01330, Turkey

3 Vocational School of Technical Sciences, Yozgat Bozok University, Yozgat 66200, Turkey

Published online: 07 July 2021 Springer

Figure A.3.2. Article titled "Real 3D Turning Simulation of Materials with Cylindrical Shapes Using ABAQUS/Explicit"